Investigation of the Transport Phenomena within the Liquid Phase of a Methanol Pool Fire

by

Alireza Vali

A thesis submitted in partial fulfillment of the requirements for the degree of

Doctor of Philosophy

Department of Mechanical Engineering

University of Alberta

Abstract

A 90 mm diameter methanol pool fire was investigated experimentally and analytically. Aiming for well-defined experiments and understanding the physics of the involved transport processes, the liquid-side boundary conditions including the pool's bottom temperature the wall thermal conductivity and depth were controlled. Bottom temperature was changed from 0ºC to 50ºC, wall material was altered to copper, stainless steel, and quartz, and the pool depth was varied to 6, 12, and 18 mm. Burning rate, flame height, liquid and wall temperatures, and liquid velocity fields were measured under steady-state and quiescent environment conditions.

The experimental results showed that the burning characteristics of pool fire (burning rate and flame height) were affected by the liquid-side boundary conditions. The temperature profiles along the pool walls also altered from uniform distributions for the copper pool to significantly non-uniform for the quartz pool. The generally observed liquid thermal structure (a uniform-temperature layer above a steep temperature gradient layer) was influenced by the bottom temperature especially when the wall thermal conductivity increased or the pool became shallower. The velocity measurements within the liquid pool revealed the existence of large-scale mixing motions which profoundly contributed to energy transport from the pool wall into the liquid fuel.

An energy model was developed to quantify different heat pathways from the flame to the liquid pool and energy changes within the liquid fuel, which predicted the fuel burning rate within ±10% of the measured values. This analysis showed that the heat transfer from the wall to the liquid pool depended strongly on the wall thermal conductivity. The liquid temperature distributions within the pool were also modeled as a constant-temperature region at the top and an exponentially-decreasing-temperature region in the lower part of the liquid pool. It was shown that when the pool became shallower or its bottom became colder, more energy was required for the liquid sensible energy change and less became available for the fuel evaporation. The experimental results and energy models presented in this study suggested that in order to achieve an accurate energy balance for pool fire, the liquid phase phenomena and boundary conditions were important and should be included.

Preface

Part of this thesis has been published as A. Vali, D.S. Nobes, and L.W. Kostiuk, 2013. "Effects of altering the liquid phase boundary conditions of methanol pool" fires. *Exp. Therm. Fluid Sci.,* vol. 44, 786-791 and A. Vali, D.S. Nobes, and L.W. Kostiuk, 2014. "Transport Phenomena within the Liquid Phase of a Laboratory-Scale Circular Methanol Pool Fire". *Combust. Flame,* vol. 161, 1076-1084. I was responsible for the data collection, data analysis, and preparing the manuscripts. Dr. D.S. Nobes and Dr. L.W. Kostiuk were the supervisory authers and contributed to manuscript composition.

This dissertation is dedicated to my father and mother for their endless love and support throughout my life.

Acknowledgments

I would like to express my deep appreciation to my supervisors Dr. Larry Kostiuk and Dr. David Nobes. Thank you for your help and inspiration throughout this research. It would not be possible to accomplish this work without your support and guidance.

I also would like to deeply thank Bernie Faulkner, Andrew Coward, and Rick Conrad for their technical assistance with the design and construction of my experimental setup.

This research was funded by Alberta Ingenuity Fund, the Natural Sciences and Research Council (NSERC) of Canada, and the Canadian Foundation for Innovation (CFI).

Contents

List of Tables

List of Figures

Nomenclature

English Symbols

A	Area (m^2)
Bi	Biot number
c_p	Heat capacity [kJ/(gK)]
d	Diameter (m) or (mm)
$F\#$	F-number
Fr	Froude number
g	Gravitational acceleration (m/s^2)
Gr	Grashof number
h	Enthalpy [kJ/(gK)]
ΔH_c	Heat of combustion (kJ/g)
ΔH_v	Heat of evaporation (kJ/g)
k	Thermal conductivity [kW/(mK)]
L	Pool depth (mm)
l	Height (mm)
$\dot{m}$	Mass flow rate (g/s)
$\dot{m}''$	Mass flux [g/(m^{2}s)]
N	Combustion number
Pe	Peclet number
$\dot{Q}$	Heat transfer rate (kW)
$\dot{Q}'''$	Heat generation (kW/m^3)
$\dot{q}''$	Heat flux (kW/m^2)
R	Thermal resistance [(m^{2}K)/kW]
r	fuel/air stoichiometric mass ratio
T	Temperature (ºC)
t	Time (s)
U	Characteristic velocity (m/s)
u	Horizontal velocity component (mm/s)
V	Volume (m^3)
$\dot{V}$	Volumetric flow rate (ml/min)
v	Vertical velocity component (mm/s)
W	Width (mm)
x	Horizontal coordinate (mm)
y	Vertical coordinate (mm)
y^*	Dimensionless vertical location
y^+	Dimensionless vertical location

Greek Symbols

α	Constant
β	Constant
ε	Error, difference
θ	Dimensionless temperature
μ	Viscosity
ρ	Density
τ	Sampling time
χ	Fraction

ω	Vorticity

Subscripts

a	Actual
b	Burning
bath	Bath
bot	Bottom
c	Combustion
cond	Conduction
conv	Convection
gas	Gasification
f	Flame
fs	Flame to pool surface
i	Inlet
l	Liquid
max	Maximum
o	Outlet
p	Pool
r	Radiative
rad	Radiation
s	Surface
w	Wall

Miscellaneous

Δ	Difference
$< >$	Average
∇	Divergence

1. Introduction

1.1 Motivation

The ubiquitous presence of flammable liquids found in modern society either as fuels, solvents or for cooking has dampened the respect they deserve during handling and storage. Therefore, their accidental ignition can be completely devastating. For example, based on a simple calculation it can be found that a typical compact car with 40 liters of gasoline carries the equivalent energy to 1400 sticks of dynamite.

Fire accidents can occur in various stages of production, storage, transportation, and application of flammable liquids. Among the numerous examples, one notable incident involving burning liquid fuels was at the Buncefield Oil Depot, Hemel Hempstead, Hertfordshire, UK, (December 11, 2005) that injured over 40 people and significantly damaged both commercial and residential properties [1]. There is also on-average one fire accident involving liquid fuel storage tanks every year in China [2]. Another example could be the fatal incident that happened recently in Lac-Mégantic, QC, Canada on July 6, 2013 [3]. During crude oil transportation, a 74-car train ran into the town and fire destroyed almost half of the downtown area and left 47 victims.

For domestic instances, 11% of fire accidents that happened in the province of Alberta in 2012 involved flammable liquid ignition. These resulted in 69 cases of death and injury and 50 million dollars of property losses [4]. In the same year, 19% of the residential fires in Alberta, Canada were caused by cooking [4], and the ignition of overheated pots of cooking oil was reported as the most frequent reason [5]. When cooking oil is heated to a high temperature, it releases flammable vapors that can be ignited. The lack of understanding of this phenomenon results in millions of dollars property loss in Alberta alone every year.

The demand for safe processing and application of flammable liquids has led the regulating authorities to lay down strict regulations to mitigate fire disasters. Therefore, fire protection standards and guidelines [6, 7] have been issued for safe practices in the workplace especially where large quantities of liquid fuels are produced and refined, such as Alberta. There are also standards for the development of firefighting systems and evacuation strategies in case of fires in industrial facilities and commercial and residential buildings [8-10]. It is clear that the fire protection engineers require reliable prediction of fire processes in order to develop effective standards to mitigate potentioal fire damage or to establish cause and responsibility should such events occur.

The need for immediate solutions to the fire threat and the complexity of the fire problem has led researchers in the fire community to look for practical engineering solutions for the prediction of fire development and control. Common fire scenarios encountered with flammable liquids ranging from the industrial and transportation incidents such as fuel spills and storage tank fires to pan fires can be classified as pool fires [11]. This class of fire includes the burning of the gases and vapors emitted from a horizontal layer of flammable liquid [12]. The large number of studies on both fundamental and practical aspects of this subject during the past few decades reflects the importance of pool fires to the fire safety engineering community [13]. This is one of the most basic forms of fuel combustion often present in accidental fires [14]. Therefore, pool fires have been investigated analytically, experimentally and recently numerically with each approach having its own advantages and disadvantages.

In general, analytical models [15, 16] cannot capture the complexity of these phenomena since they often use one or several simplifying assumptions such as ignoring some forms of transport phenomena or use of constant flame temperature or species concentrations. However, these models are still appreciated as they can estimate the effects of different phenomena and help to provide general understanding.

Experimental studies were mostly conducted in the past to achieve realistic solutions. It was shown that pool fires are affected by a large number of coupled parameters such as pool geometry, fuel type, ambient condition, and etc. [13, 17]. For example, in the classical work of Blinov and Khudyakov [18], the rate of fuel burning was measured for different hydrocarbon fuels for a range of pool diameters. It was reported that the local fuel evaporation rate was maximum at the center of the pool and decreased toward the wall. This particular finding has not been universally observed and others [19] have stated that the maximum local evaporation rate was at the wall and decreased toward the pool center.

The reasons for these different observations have not been extensively discussed in the literature, but connections have been made to the relative importance of different mechanisms (*i.e.*, conduction, convection and radiation) that bring the energy necessary to evaporate the fuel from the flame and combustion products to the liquid. For example, soot producing fuels, such as heptane, emit high levels of thermal radiation to become a key pathway of heat feedback from the flame to the liquid fuel along with convection and conduction [20]. In general, radiation is seen as the dominant heat transfer mechanism for highly luminous fires, especially for large-scale pools [12]. Energy radiated to the fuel surface has been observed to be the highest at the center [21] and is attributed to creating the maximum local evaporation rate at that location. In contrast, for small-scale non-luminous pool fires, the heat transfer from the pool's wall to the liquid is seen as dominant [17, 19, 22] and results in the highest local evaporation rate being at the wall. This perspective on the local evaporation rate focuses on where the energy enters the pool, but does not address any subsequent phenomena associated with its redistribution within the liquid, which is the topic central to the current research.

In summary, a significant barrier to developing a comprehensive and quantitatively relevant phenomenological model of pool fires from experiments is the large number of coupled parameters involved in establishing the burning of liquid pools. As a result, numerical modeling of pool fires is often seen as the more robust tool for predicting the key characteristics of pool fires, especially for large-scale pools.

However, it is widely recognized that the reliability of numerical model's predictions necessarily depends upon the quality and amount of knowledge about the processes involved. As an instance, in developing numerical models, a key decision is the establishing of an appropriate region of interest or computational domain. Some models essentially ignored the liquid phase and only solved the reacting gas flow for a prescribed fuel mass flow rate being emitted from the pool surface at their computational boundary [23]. However, this mass flow should be determined by the requirement that the liquid fuel must evaporate before it burns, and that energy for evaporation comes from the flame and product gases. Therefore, the flow of fuel vapor at the inlet boundary is itself a part of the solution, and some numerical models coupled it to the heat feedback from the flame to the fuel surface [24]. In this particular case, the solution domain remained restricted to the gas phase and it was assumed that all the energy transferred to the liquid was used to create an average evaporation rate without respecting spatial variations and redistribution within the pool's depth.

More complete numerical models have been developed including the liquid phase in the solution domain [25-27]. They determined the rate of fuel evaporation from liquid-vapor equilibrium at the fuel surface temperature. In these models, the liquid layer has been treated as a thermally-thick solid with one-dimensional heat conduction in the direction normal to the liquid surface [25, 26]. Prasad et al. [27-29] modeled the pool fire numerically and applied their simulation to develop a water mist fire suppression system. They modeled the liquid phase as columns of liquid traveling only in the direction normal to the surface at a constant velocity from inlet to the interface as required by the local surface evaporation rate. They set the velocity component parallel to the interface equal to zero. The effects of such assumptions on the model must be investigated when it is used to design a system that is supposed to be reliable in the case of fire emergency.

In general, there is a lack of information about the liquid phase in pool fires that has forced modelers to use simplifying assumptions. These assumptions are sometimes inaccurate or unrealistic, such as using an infinitely deep or a stationary liquid layer. It is important to assess the assumptions and models used for the liquid phase. Therefore, a good understanding of the liquid phase phenomena can improve the quality of the pool fire models by answering to two main concerns. First is the importance of the liquid side phenomena on the burning characteristic of pool fires. In other words, it is required to investigate if excluding the liquid phase from the analysis does not result in inaccuracy. Second is the process involved in the transport of energy and momentum within the liquid phase. That is, what are the processes which redistribute energy within the liquid phase? The liquid evaporation rate as the source of the fuel for pool fire burning is a coupling of liquid and gas phase phenomena. Investigation of these two specific subjects is the main objective of this thesis. The findings of the current study may help to develop more realistic predictive tools for various pool fire scenarios.

1.2 Thesis Objective and Outline

The main objective of this study is to contribute to the overall understanding of liquid pool fires by investigating the processes involved in the liquid phase. This study is aimed to characterize the energy transfer to the liquid pool from the flame and the processes that distribute this energy within the liquid fuel. It is worth emphasizing that although the results of this research may be useful for fire safety applications, a fundamental perspective is used here to understand the transport phenomena within the liquid phase of a laboratory-scale pool fire.

In the following chapter, Chapter 2, a more formal review of the literature associated with pool fires is presented to provide the necessary background to the current work. Then, well-defined and highly controlled experimental setups and procedures which are applied to advance the understanding of this problem are described in detail in Chapter 3. The variables of interest in this study are: fuel burning rate, liquid fuel and pool wall temperatures, flow field within the liquid, flame structure and heat feedback from the flame and products to the liquid fuel. Data are acquired under steady-state steady-flow conditions associated with maintaining the fuel level at the top edge of the pool. Quiescent ambient conditions and controlled lower fuel boundary temperatures are also imposed during the experiments. The pool wall materials and depth are changed as test parameters to investigate their effects on pool fire burning.

The results for measured variables are presented and described in Chapter 4 and the energy transfer processes in the liquid phase are quantified in Chapter 5. Eventually, a set of conclusions are drawn from the experimental results and their analysis in Chapter 6, and new ideas and directions are proposed for further investigation of the problem in the future. The results and analysis of this study have been also published in [30, 31] and presented in two more journal papers which are currently under review.

At the end, it should be noted that the laboratory-scale pool fire results cannot be used directly for large-scale pools which may be more appealing to fire protection engineers. However, they can provide a solid basis for the understanding of the physics of the problem since several major characteristics of pool fires (*e.g.*, the coupling between the liquid and gas phase) are conserved in laboratory-scale pools. In addition to the findings of this study, the experimental data presented here can be used for numerical model assessment and justification.

2. Pool Fire Dynamics

2.1 Overview

The ignition of fuel vapor emitted from a horizontal layer of combustible liquids results in a pool fire. This class of diffusion flames can be either laminar or turbulent depending on its buoyant interactions with the surroundings and ambient air motion [13]. In general, pool fires are complex due to the coupling between numerous parameters of the problem that includes a combination of combustion, heat and mass transfer, and fluid dynamics in a multi-phase (gas, liquid, and solid) system.

For example, the liquid fuel burning rate, expressed as the mass loss rate of fuel or in other word its usual surrogate quantity of fuel evaporation rate from the pool ($\dot{m}_b$), requires an analysis of the transport phenomena of the overall system. The liquid fuel must be evaporated before burning, which requires energy. The source of this energy is primarily the heat transfer from the flame and the hot combustion products to the liquid fuel through radiation, convection, and conduction pathways [20]. To determine the flame heat feedback, in general, flow and thermal structures of the flame, aerosol (soot) and gaseous product compositions, and thermal energy generation in the flame are required. The conduction pathway, which indeed involves convection from the vessel wall into the liquid [22], requires the temperature field of the solid wall. Transport phenomena within the liquid phase impose how the energy re-distributes itself within the liquid phase and how much of the received energy will be available for the fuel evaporation. Remembering that the rate of thermal energy generation in the flame itself is a strong function of the burning rate, $\dot{m}_b$, the associated complexity of the system can be realized in a highly coupled problem. In summary, in order to have reasonably accurate estimations of pool fire characteristics, *e.g.*, burning rate, the overall system should be considered.

The practical and fundamental aspects of pool fire behavior have been the subject of a considerable amount of research since the 1950s. Some of the pool fire studies up to the 1990s were summarized in Refs. [13, 21, 32]. The interesting characteristics of pool fires included flame structure, the entrainment of air, pulsation frequency, soot formation, flame spread rate, effects of cross-flow air, flame heat feedback, flame radiation and mass burning rate of fuel. In this chapter a brief review of the abundant research on pool fires is presented.

2.2 Burning of Fuels

Fire involves chemical reaction between combustible species and oxygen. The combustion reaction is exothermic and releases thermal energy. The emitted gaseous species are known generally as products. A global description of this reaction can be expressed as:

$$\text{Fuel} + \text{Oxygen} \rightarrow \text{Products} + \text{Thermal Energy} \tag{2.1}$$

The fuel must mix with oxygen in order to be combusted, so the fuel must be in the form of a gas or vapor. The burning of gaseous fuel is usually partitioned into two different flame regimes: premix and diffusion flames. In the premixed regime fuel and oxygen mix together and then this mixture burns in a flame (*i.e.*, a thermal/chemical structure embedded in the fluid where the exothermic reaction occurs). In a diffusion flame, fuel and oxygen are initially separate and they mix together through entrainment and diffusion, and burn in the spatial region where the fuel/oxygen (or air) is within the mixture flammability limits [12].

Zabetakis [33] performed an extensive investigation on the flammability of the gas and vapor fuels. According to [33] for methanol (vaporized), which is the fuel used in this study, the lower (lean) flammability limit is 6.7% and the upper (rich) flammability limit is 36%, which are the minimum and maximum volumetric concentrations of the fuel vapor in a flammable fuel/air mixture (*i.e.*, the ratio of the volume of the fuel in the total volume of mixture) . That is, below and above these limits the fuel/air mixture is non-flammable. Of course the mentioned values are subject to change depending on temperature and pressure, however further discussion on this subject is not in scope of this study (because ambient temperature and pressure are constant) and readers are referred to [34] for more information.

For premixed flames the mass flow rate of the gas fuel and air oxygen can be set to insure that the fuel/air mixture is within the flammability limits. In contrast, in diffusion flames, the rates that the fuel and air are transported from independent sources are not the same throughout the reacting zone and depend on numerous parameters such as air entrainment, environment, fuel type, and fuel flow rate. In the region near the fuel inlet, which is rich in fuel, the fuel concentration is above upper flammability limit. In the region near the air inlet, which is rich in oxygen, the fuel concentration is below the lower flammability limit. The combustion can only be initiated in the middle of these two aforementioned regions, which is called the flammable region. Once ignited, diffusion flames locate themselves spatially where they have access to the required rates of fuel and oxygen to sustain combustion.

However, there is a gradient in the fuel and oxygen concentrations within the flammable region and the reaction may be different spatially. There is a specific fuel/air mixture composition within the flammability limit known as stoichiometric mixture at which both the fuel and oxygen are completely consumed by combustion [34]. For methanol, the stoichiometric mixture corresponds to 12.24% volumetric concentration of vaporized methanol in the fuel/air mixture [34]. When combustion is complete (*i.e.*, burning of stoichiometric fuel/air mixture) the products in Eq. (2.1) only contain carbon dioxide and water vapor. If the fuel concentration is above the stoichiometric mixture (*e.g.*, for the case of methanol, when the vaporized fuel concentration in fuel/air mixture is between 12.24% and 36%), the mixture is called fuel-rich. In this case, the oxygen rate is sufficient for fuel burning but not for complete combustion. As a result, there is some unburned fuel in the products. At the opposite side of the stoichiometric mixture (*e.g.*, when the vaporized methanol concentration in fuel/air mixture is between 6.7% and 12.24%) the oxygen rate is more than that required for the complete combustion. This region is called fuel-lean where unburned oxygen can be found in the combustion products.

In the diffusion flames of gaseous fuel, the fuel flow rate is an independent parameter from combustion and can be controlled directly (*e.g.*, jet fires). However, for burning of liquid and solid fuels, the rate of fuel vaporization from the fuel bed that supplies the fuel for combustion is related to the heat feedback from the flame. That is, under a certain burning condition a specific rate of gasified fuel is emitted from the fuel surface and it only changes if the energy received by the fuel surface is altered. Therefore, the volatility and enthalpy of vaporization of the liquid fuel are the key characteristics when it burns. As a result, fire protection engineers assess the associated risks of liquid fuels from their ability to supply fuel vapor.

Liquid fuels are classified according to their flashpoint defined as the lowest temperature at which the fuel vapor concentration above the liquid surface is within the flammability fuel/air mixture limit [8]. The mole fraction of the fuel vapor, X_{fuel}, above an evaporating fuel surface can be determined from the fuel vapor partial pressure P_{fuel} as:

$$X_{fuel} = \frac{P_{fuel}}{P} \tag{2.2}$$

where *P* is total pressure. At equilibrium, the vapor partial pressure at the surface of a liquid fuel bed at temperature T_{fuel} can be determined from the Clausius–Clapeyron relationship as [27]:

$$P_{fuel} = P_0 \exp\left[-\frac{\Delta H_v}{R}\left(\frac{1}{T_{fuel}} - \frac{1}{T_0}\right)\right] \tag{2.3}$$

where ΔH_v is the heat of evaporation, *R* is the gas constant, and T_0 is the fuel saturation temperature at pressure P_0. When the liquid fuel is cold, the vaporized fuel concentration is not enough to form a flammable mixture above the liquid surface. The fuel volumetric fraction increases as the fuel temperature increases, and the temperature at which it becomes sufficient to compose a flammable fuel/air mixture is known as the flashpoint.

The lower the liquid flashpoint with respect to the ambient temperature, the greater is the fuel volatility and the higher is its flammability. A flashpoint of

~11ºC and a boiling point of ~64.5ºC [35], put methanol in the Class IB of flammable liquids category which includes the second most hazardous liquids according to the National Fire Protection Association [8]. Liquids with a flashpoint lower than the ambient temperature (*i.e.*, surroundings) are potentially dangerous, because they can be ignited by providing a small amount of energy (~few mJ) known as ignition (spark) energy to the flammable fuel/air mixture [12].

2.2.1 Combustion and Heat Release

When vaporized methanol is burning with air in a stoichiometric mixture the single step combustion reaction is:

$$CH_3OH + 1.5\ O_2 + 5.67\ N_2 \rightarrow CO_2 + H_2O_{(g)} + 5.67\ N_2 \tag{2.4}$$

As aforementioned, the products of the complete combustion of a stoichiometric mixture are water vapor and carbon dioxide (from an energy perspective nitrogen is considered completely inert). This exothermic reaction generates thermal energy, which when expressed as a rate is often called "heat release rate", $\dot{Q}_c$ (kW). Within the fire protection engineering community this parameter is seen as the most important variable [36] as it determines the severity of the fire hazards [37]. Thus, one of the main objectives in fire studies is to determine the fire heat release rate, and different methods have been used to do so.

The heat release rate per unit volume in the reacting zone can be determined from chemical kinetics as:

$$\dot{Q}_c''' = \sum_{i=1}^{N} h_i W_i \dot{\omega}_i \tag{2.5}$$

where W_i (g/mol) is the molecular weight, h_i (kJ/g) is the specific enthalpy of ith species, N is the total number of species involved in combustion and $\dot{\omega}_i$ (mol/(m^{3}s)) is the rate of production/consumption of ith species in combustion process.

In order to have an accurate estimation from Eq. (2.5), it is necessary to know how fuels react with oxygen when they combust. Although the combustion of fuels is commonly expressed as a single-step reaction such as Eq. (2.4), the fuel does not oxidize in a single-step reaction, and burning in reality involves a set of elementary reactions and species. The burning of methanol, for example, involves 326 elementary steps and 52 species [38]. Smooke [39] used a 78-reaction and 26-species mechanism for modeling of a methane diffusion flame.

The combustion mechanism is a set of K chemical reactions which generally can be expressed as [34]:

$$\sum_{i=1}^{N} \nu_i' M_i \leftrightarrow \sum_{i=1}^{N} \nu_i'' M_i \tag{2.6}$$

where M_i represents the chemical symbol for species i, ν_i' and ν_i'' are the coefficients for species i when it appears as a reactant and product, respectively. The symbol ↔ is indicating that the chemical reactions, in general, occur in both forward and reverse directions. The production rate of species i, $\dot{\omega}_i$, can be determined for the set of K reactions as [39]:

$$\dot{\omega}_i = \sum_{j=1}^{K} \left(\nu''_{ji} - \nu'_{ji}\right) \left[k_j^f \prod_{i=1}^{N} \left(\frac{\rho Y_i}{W_i}\right)^{\nu'_{ji}} - k_j^r \prod_{i=1}^{N} \left(\frac{\rho Y_i}{W_i}\right)^{\nu''_{ji}} \right] \tag{2.7}$$

where Y_i is the mass fraction of species i, k_j^f and k_j^r are the specific-rate constants for forward and reverse jth reaction expressed as [34]:

$$k_j = A_j T^b \exp\left(-E_j / RT\right) \tag{2.8}$$

where for any reaction, AT^b is the collision frequency and the exponential term is the fractions of collisions that have energy level greater than the activation energy E (kJ/mol). A list of A , b, and E for a wide range of reactions can be found in [40].

The chemical kinetics approach is mostly used in numerical models, and in order to have an accurate estimation, all the reactions and species in addition to soot formation models should be taken into account, which often takes hundreds of hours of calculation time [39]. Therefore, several studies investigated reduced mechanisms that can be used for practical computations. For example, the detailed mechanism of 326 reactions for methanol burning was reduced to 19-step [38], five-step [41] and single-step [42, 43] mechanisms. The approach in these works was to empirically find the best coefficients of Eq. (2.8) for those limited number of reactions to make the set a reasonable representation of the detailed mechanism.

Assuming complete combustion, the ideal heat release can be determined with having the fuel flow rate and heat of combustion as:

$$\dot{Q}_c = \dot{m}_b \Delta H_c \tag{2.9}$$

where $\dot{m}_b$ (g/s) is the burning rate (or mass flow rate of fuel) and ΔH_c (kJ/g) is the heat of combustion. In pool fire studies, the heat release rate and burning rate are typically expressed per unit area of the pool in kW/m^2 and $g/(m^2s)$, respectively.

The actual fire heat release rate, $\dot{Q}_a$, was measured directly with a calorimetry technique [37, 44-48] and was related to the ideal value by using a coefficient known as combustion efficiency, χ_a (≤ 1). This quantity accounts for the incompleteness of combustion in diffusion flames [37]. Thus,

$$\dot{Q}_a = \chi_a \dot{Q}_c \tag{2.10}$$

Combustion efficiency is related to the fire tendency to produce soot. In the case of complete combustion stable gaseous products (*e.g.*, water vapor and carbon dioxide) are generated. However, in most pool fires, especially burning of hydrocarbon fuels (*e.g.*, heptane) in diffusion flame, in the regions that oxygen concentration is low the combustion of the gasified fuel forms unsaturated molecular species (radicals). These radicals undergo several reactions and convert into soot particles [49]. The existences of these soot particles that radiate energy in a diffusion flame results in its yellow color. The soot particles have a size of 10-100 nm and after production may burn in the flame, but when they escape the high temperature flame region, they come together and form chains and clusters of an overall size of 1 μm [12] that eventually become smoke.

The minimum distance from the liquid fuel surface upward to the point at which smoke is first generated is known as the fuel smoke point [50]. This quantity is used to assess the completeness of combustion, χ_a. A large value for the smoke point means the combustion is complete and its efficiency is close to unity [50]. For methanol, the smoke point has not been measured accurately but it is expected to be extremely large [21]. The translucent blue color of the non-luminous flame generated by methanol pool fire depicts very low tendency of methanol to generate soot. Therefore, the combustion efficiency for methanol pool fires is usually taken as unity [21]. On the other hand, for soot-producing combustibles, the smoke point is smaller. The smoke point for liquid PMMA (polymethyl methacrylate) is ~0.11 m [50], meaning 11 cm above the combustible bed the smoke first appears. This gives PMMA pool fire a combustion efficiency of 0.85 [51].

2.2.2 *Diffusion Flames*

A diffusion flame can be established over the vaporizing combustible liquid in pool fires. Diffusion flames can be classified as jet flames or buoyancy (natural) flames, and the Froude number (Fr) may be used as a criterion of classification defined as:

$$Fr = U^2 / gd \tag{2.11}$$

where U (m/s) is the characteristic fuel velocity, d (m) is the characteristic length scale of the burner (diameter), and g (m/s^2) is the gravitational acceleration. That is, the type of fire is determined based on the relative importance of momentum to buoyancy effects.

For gaseous fuels the characteristic velocity, U, is equal to the gas average velocity at the fuel inlet, gas jet velocity. When the fuel flow rate is low and Reynolds number at the origin is less than ~2000 (which is equivalent to $1 < Fr < 10^2$), the resulting jet flame is laminar [12]. Turbulence starts to initiate at the tip of the flame as the flow rate increases until the jet flame becomes fully turbulent at a nozzle Reynolds number significantly greater than 2000 [52] and when $Fr > 10^5$ [12].

The burning of condensed fuels (solids and liquids), on the other hand, involves buoyant flame (natural fire) which is dominated by buoyancy and the momentum of the fuel vapor from the surface is relatively small ($Fr < 1$). The degree of flame turbulence for this type of fires is determined by the diameter (characteristic dimension), d, of the fuel bed (in this case pool diameter). In pool fires, if $d < 0.1$ m, the flame will be laminar also known as small-scale pool fire, the flame transition to turbulent occurs within 0.1 < d < 1 m, which is called the medium-scale pool fire regime, and for d > 1 m the buoyant diffusion flame is fully turbulent classified as large-scale pool fires [17, 18].

As for buoyancy flames above liquid and solid fuels, the initial velocity of the fuel vapor is unknown and is dependent on fire heat release (and portion thereof that vaporizes the fuel), the *Fr* number is usually modified in fire studies based on the velocity derived as

$$U = \frac{\dot{Q}_c}{\Delta H_c \rho \left(\pi d^2 / 4 \right)} \tag{2.12}$$

Substituting U from Eq. (2.12) into the *Fr* number definition shows that *Fr* is proportional to $\dot{Q}_c^{\,2} / d^5$. For pool fire studies, a more common dimensionless number of $\dot{Q}^*$ was introduced in [53] as:

$$\dot{Q}^* = \frac{\dot{Q}_c}{\rho_\infty c_p T_\infty d^2 \sqrt{gd}} \tag{2.13}$$

$\dot{Q}^*$ is commonly used for fire classification, models, and correlations [54]. The turbulent pool fires are associated to the case when $\dot{Q}^* \leq 1$ [55].

The buoyancy-driven (natural) fires sometimes have been studied using porous bed gas burners [53, 56, 57]. For research purposes, these burners have an advantage over fires involving combustible solids or liquids. The fuel flow rate, which is related to the heat feedback from the flame in natural fires, becomes an independent variable when porous bed gas burners are used. Low gas fuel initial momentums were prescribed in these burners to establish purely buoyant diffusion flames. However, these burners cannot simulate the interaction between the flame and the liquid fuel or the characteristics of the region just above the liquid surface [14].

2.3 Burning Characteristics of Pool Fires

Pool fires mainly involve two interactive phases: the flammable liquid (liquid phase) and the fire plume (gas phase). As it will be explained in Sec. 2.4, for small pool fires, energy transfer through the confining wall is also important, which adds another phase (solid phase) to the problem.

Each individual phase of pool fires and its interactions with the others have been investigated in the literature through controlling parameters such as pool diameter [58]. The main pool fire characteristics in those studies are: heat release rate, fuel burning rate, flame height, flame temperature and velocity, air entrainment, reactant and product concentrations, soot (smoke) production rate, flame radiation and heat feedback. In this section, those characteristics that are most relevant to the current study or help general understanding of the problem are discussed.

2.3.1 Flame Features

The pool flame is strongly influenced by buoyancy effects [14]. The fire plume structure is usually divided into three regions as shown in Fig. 2.1 [59]. The first zone, immediately above the liquid fuel surface, is the "Persistent Flame Zone". This zone involves a flame envelope around a central region that is rich in fuel vapor. The combustion reaction mostly occurs at the outer boundaries of this zone where enough oxygen exists to make a flammable mixture. This zone has a rather constant conical shape.

Second is the "Intermittent Zone" where the fire instability and turbulence occurs. Therefore, this part of the fire structure may also be called the "Pulsation Zone". Chemical reactions are still important in this region especially at the beginning of this zone where the amount of diffused fuel vapor could be within the flammability limits and the combustion is more probable (shown as flammable volume in Fig. 2.1). However, as the fuel diffuses away from the pool surface it burns and the combustion probability decreases. It should be noted that the visible fire that is commonly known as the visible flame contains these two regions (*i.e.*, persistent flame and intermittent zones) [60] as shown in Fig. 2.1.

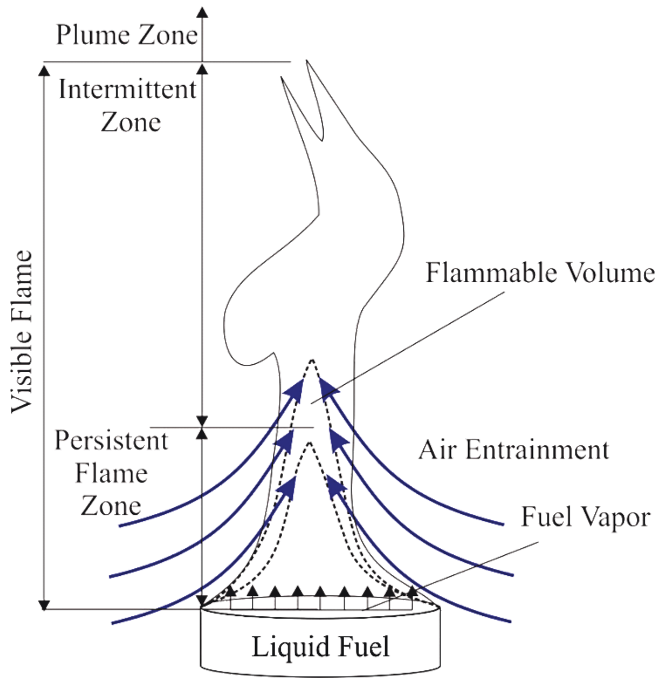

Fig. 2.1 Schematic diagram of different zones of the pool fire structure

For methane buoyant diffusion flames above a 0.3 m square porous burner, a combustion intensity map was presented in [61]. It was shown in [61] that the combustion may occur in the persistent flame and the intermittent zones, and it was most probable (presented more than 50% of the time) in the persistent flame zone especially near the edge of the burner where a large mass flow rate of ambient air could entrain into the reacting zone [14]. The findings were in agreement with [62] that proposed the same result from temperature and concentration measurements above a 0.15 m diameter kerosene pool fire. Due to the low combustion probability in the central area of the persistent flame zone a fuel-rich region was observed immediately above the central area of the pool.

The last region is a non-reacting buoyant plume known as the “Plume Zone”. This region is mostly turbulent where the hot combustion products move upward as a result of buoyancy forces. The study of this zone is mostly of interest for safety engineers for fire detection, building evacuation, and control of fire toxicity and smoke movement.

A schematic illustration of the fire typically established over the liquid pool is shown in Fig. 2.2. Volatiles from the liquid pool mix with surrounding air and burn in the reacting zones (*i.e.*, persistent flame and intermittent) when the local temperature and species concentrations are appropriate. The temperature of the gases increases by combustion heat generation. Then, due to the buoyancy forces, the hot gases rise with respect to their surroundings and generate a buoyant plume. The upward buoyant flow is resisted by viscous stress within the stagnant atmosphere. The ratio of buoyancy to viscous forces can be expressed by the Grashof number, *Gr* [63]. Due to the conservation of mass, the vertical flow of the gases in the fire plume causes air to be entrained from the surroundings inward [53, 56, 64]. The dashed lines, in Fig. 2.2a, show the boundary between the buoyant flow and the still surroundings. The mean flow profile within the region that contains buoyant flow of combustion products and entrained air is also apparent in Fig. 2.2a.

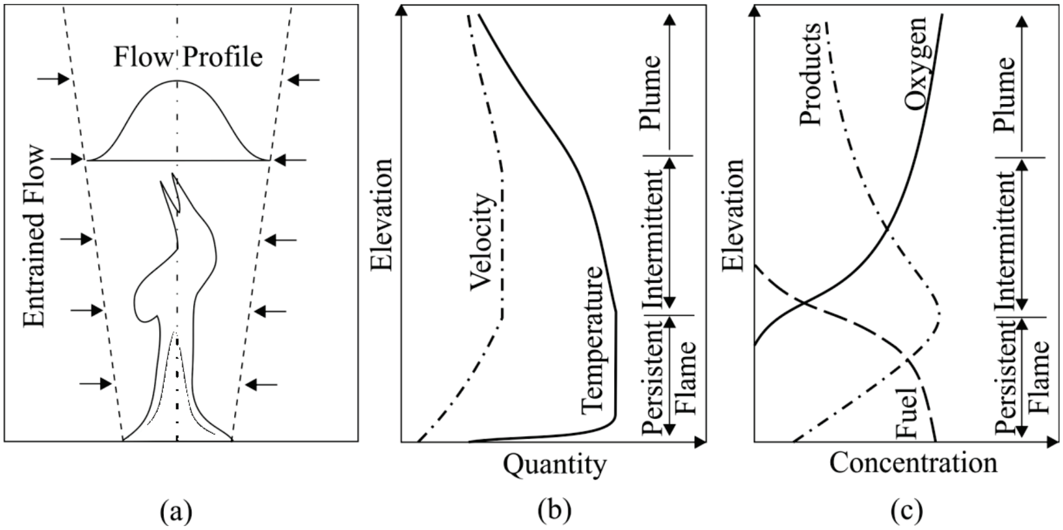

Fig. 2.2 Schematic diagrams of (a) fire structure and the qualitative upward variations of (b) mean temperature and vertical velocity and (c) mean species concentration along the flame centerline; this figure was derived based on information in [24, 29, 65-73]

The qualitative trends of mean velocity, temperature and species concentration variations on the centerline in respect to the vertical location are presented in Fig. 2.2, which are based on the data from the literature [24, 29, 65-

74]. Moving upward from the fuel surface, immediately above the liquid-gas interface is a region rich in fuel and due to the heat that comes from combustion, the temperature rises from the interface upwards. In the persistent flame zone, fuel and oxygen are consumed in combustion and products are generated. Thus, the gas temperature reaches a maximum value and remains almost constant to the end of this zone. It is important to note that the air entrainment constantly cools down the gases [13] and convects part of the combustion heat release upwards [75] (a description of pool fire heat transfer is presented in Sec. 2.4). Koseki [73] measured the gas maximum temperature in heptane pool fires of different diameters and showed that it increases as the pool get larger. The high temperature of the flame zone makes the gases accelerate in the flame zone, $Gr > 1$.

In the intermittent zone, the combustion probability reduces, so less heat is generated in this region and as a result of cool air entrainment, the temperature starts to decay. Therefore, the buoyancy and viscous forces become almost the same magnitude, $Gr \approx 1$, and the velocity remains constant at its maximum value within this zone. Lowered reaction probability in the intermittent zone causes a decrease in the product generation and oxygen consumption. Consequently, the product concentration decreases while the oxygen concentration increases.

In the non-reacting plume zone, the temperature decreases even faster due to the entrainment of cool air from the surroundings. The buoyancy forces decrease to lower than the viscous drag, which eventually results in a decrease of the vertical velocity. Product concentration decreases with elevation since more air entrains from the surrounding atmosphere to the fire plume progressively [76]. As a result of fresh air entrainment, the plume volume increases (shown in Fig. 2.2a), the products are diluted [75] and the oxygen concentration rises upwards.

Two-dimensional distributions of parameters presented in Fig. 2.2 can be found in [27, 28, 62, 70, 74, 77]. Fig. 2.3 shows the radial distributions of temperature and velocity, Fig. 2.3a, and different species concentration, Fig. 2.3b, in the persistent flame zone. This zone includes a central fuel-rich area in the middle and as a result of the combustion near the edge of the burner [61] the fuel concentration drops in the flame sheet [24] where the temperature is maximum [78-80]. The air is entrained from the surroundings radially inward and as it passes through the flame sheet the oxygen is consumed by the reaction. The radial distribution of the products (H_2O and CO_2) in the persistent flame zone is apparent in Fig. 2.3b [68]. The combustion products are generated in the flame sheet and advected by entrained flow mostly into the fire plume.

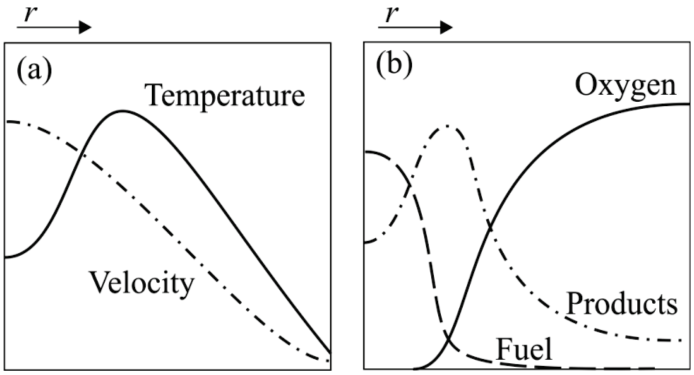

Fig. 2.3 (a) Qualitative radial mean temperature and vertical velocity variations and (b) radial mean species concentration variations within the persistent flame zone

The radial distribution of vertical velocity in the persistent flame zone is shown in Fig. 2.3a according to the data presented in [65]. However, at the base of the fire plume near the liquid fuel surface, the flow distribution is more complicated. On the fuel-rich side of the flame, the buoyancy is not large enough to counter the viscous effect of entrained flow through the flame sheet and a vortical structure is generated [62]. Venkatesh et al. [79] performed flow visualization in the base of pool fires and they confirmed the existence of the recirculating structures within the central region of the flame zone immediately above the fuel surface. The vortex generated by the entrained flow was directed inward at the top and outward at the lower part. Therefore, at the base of the flame, the vertical velocity profile is different from the one shown in Fig. 2.3a. The vertical velocity increases radially from the center to a maximum value (at the flame sheet location) and then deceases with radius [68].

In the plume zone, profiles of temperature, velocity and product concentration are Gaussian [75] as depicted in Fig. 2.4 [66]. No fuel remains in this region, so no reaction occurs, and as a result of air entrainment oxygen diffuses through the plume gases.

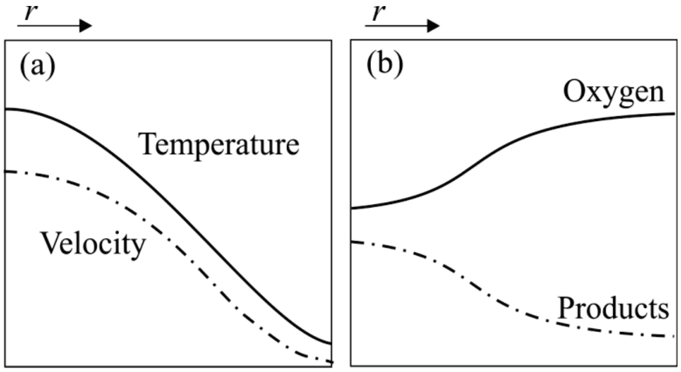

Fig. 2.4 Qualitative radial mean temperature and vertical velocity variations and (b) radial species concentration variations within the plume zone

Another feature of pool fires (similar to other natural fires) is that the visible flame fluctuates (fire puffing). For diffusion flame, the oscillations take place when the velocity at the fuel exit is above a certain velocity known as critical velocity (pool fires are classified based on their diameter). Below this the critical fuel velocity (diameter) the flame is laminar and flame puffing was not observed [81]. These flame oscillations interact with the air entrainment into the flame and its mixing with fuel [82], so the fire puffing has been studied by many researchers [83].

Initially it was believed that the puffing is a combustion-related phenomenon and involves the flame expansion to entrain required oxygen to burn the volatiles [83]. The existence of this oscillatory behavior in non-reacting buoyant plumes [84] and flow visualization of the flame [82] revealed that the flame puffing is a result of the fluid dynamics not the accessibility of the air for combustion. The mechanism of puffing was described and illustrated in [82, 83] as the buoyancy of combustion gases (or initial momentum in case of jet flame) in stagnant surroundings generating large toroidal vortices around the fuel base.

These vortical structures were noted in [85] and observed in [86]. The vortex moves upward and leaves a low pressure region behind itself that is filled with combustion gases. As a result, the flame sheet forms a convex upward bulge and is pulled up by the vortex. As the bulge rises, accumulation and acceleration of the buoyant gases inside the flame envelope forms another vortex at the flame base. The second vortex stretches the bulge by pushing the lower part of it radially outward and at the same time pushes the bulge vertically upward. The vortical structures shed (laterally expand) as a result of combustion completion when they travel along the fire plume [82].

There is large amount of research that has characterized the puffing frequency. A summary of these studies and puffing frequency correlations can be found in [81, 83, 87, 88]. It was shown that the puffing frequency was almost independent from the fuel type and flame heat release rate while it decreased with the pool diameter. The frequency was found to be proportional to $d^{-1/2}$ (d is pool diameter) over the range of 10^{-2} m $< d <$ 10^{2} m.

The flame pulsation may affect the heat transfer to the liquid pool and subsequently the burning rate (the relationship of burning rate to heat transfer is explained in Sec. 2.4). The flame instabilities can be removed by introducing a coaxial air jet around the burner (air co-flow) which pushes the vortical structures upward from the flame base [89].

2.3.2 Flame Height

In a diffusion flame, the location of the flame is limited by the amount of oxygen that is accessible for combustion. Air is entrained from the surroundings through the flame boundary and oxygen mixes with the fuel in the flame sheet. The vertical size of the flame, l_f, is an indication of the required time (or length of flame) for complete combustion [12]. That is, when the flame height is l_f and U is the characteristic vertical velocity of the volatiles, in the time interval of $t = l_f / U$ sufficient air is entrained through the plume boundaries to burn all the fuel issued from the burner [90].

The interpretation of the flame height requires the understanding of the mass transfer to the mixing process of the flame. This mixing in diffusion flames may occur in two ways: molecular diffusion and eddy diffusion (turbulent mixing) [52]. In laminar flames, the mixing is by molecular diffusion which is relatively slow. Therefore, an increase of fuel flow rate to the flame increases the size of the flame needed to provide the required time for sufficient oxygen to be diffused for complete combustion. In the case of a laminar jet flame, this happens as the gas fuel exit velocity increases and for buoyant flames (natural fires) it is associated with any effect that increases the fuel evaporation (*e.g.*, an increase in the fuel diameter or fire heat release).

Above a certain fuel jet velocity or pool diameter ($d > 0.1$ for pool fires [17]), indications of turbulence begin at the tip of the flame. The location along the flame where the flame turbulence starts is called the breakdown point [52]. The mixing process in the turbulent region mostly occurs by eddy diffusion which is more efficient than molecular diffusion. As a result, the formation of turbulence near the tip of the flame causes its height to decrease (less time is required for mixing). With an increase in the flow rate (or evaporation rate in natural fires), during the transition region, the breakdown point moves downward to the fuel inlet (never reaching the inlet though [12]) and a progressively larger portion of the flame becomes turbulent. Therefore, more eddy-mixing occurs instead of molecular diffusion mixing and the flame is shortened until the whole flame becomes turbulent (fully turbulent flame). In the fully turbulent regime (nozzle Reynolds number larger than 2000 for jet fires [52]) the flame height remains almost constant in response to the fuel flow rate increase and instead more eddies are generated [52].

The pool fire flame height is usually reported as a value normalized with the burner diameter, l_f/d [17, 18, 73]. The variation of the normalized flame height for a heptane pool fire was presented with respect to the burner diameter in [73] where l_f/d increases with diameter to $d = 1$ m and then it decreases. Blinov and Khudiakov [18] showed that the normalized flame height decreased with pool diameter and then remained constant for $d > 3$ m.

The size of the flame is also important for fire protection engineers as flame radiation, known as the most destructive characteristic of fires (ignition of the external objects depends on the received radiation from the flame), is related to the flame size. Thus, a large number of investigations have tried to characterize the flame height. This variable is usually measured as the distance from the burner exit to the tip of visible flame [57, 91-96]. This visible flame containing the combustion reactions [75] was commonly measured by photography or video recording of the fire in a darkened environment and against a black background. The reported results were based on different definition though. While most of the mentioned studies reported the time-averaged values, Zukoski et al. [94] applied a new definition based on the flame intermittency (the fraction of time that at least part of the flame lies above a certain elevation). Fig. 2.5 shows the variation of the flame intermittency with the elevation. The flame intermittency is one in the flame zone and it decreases upwards in the intermittent region to zero in the non-reacting plume zone. The flame height was defined as the distance from the fire source to the elevation where the flame intermittency declined to 0.5. That is, the length the flame is maintained for more than 50% of the time during the steady burning period. This definition gave visible flame heights 10-15% smaller than the ones obtained from averaging [94].

Another definition for flame height was presented in [97] as the elevation where the centerline gas temperature reaches a maximum. As mentioned in Sec 2.3.1 the radial temperature distributions in the flame zone showed that the maximum temperature is at the flame sheet location. The lateral distance of the flame sheet from the axis decreases upward forming a conical combustion zone from the pool rim at the base to a point where the flame sheet reaches to the axis. The vertical distance from the pool surface to this point at which sufficient oxygen could diffuse for combustion was called the combustion zone height [97].

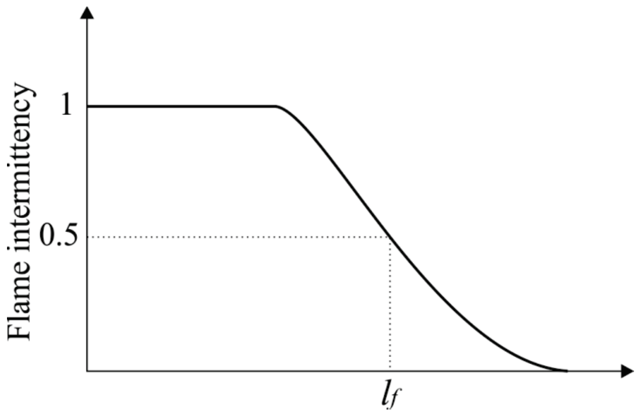

Fig. 2.5 Flame intermittency as a function of vertical distance above the fuel source and definition of mean flame height [94]

Functional relationships were presented in the literature to predict the flame height based on experimental data [57, 90, 92-94] or analytical models [69, 91, 95-98]. These correlations mostly related l_f / d (the ratio of the flame height to the burner diameter) to *Fr*, $\dot{Q}^*$ and another non-dimensional group known as the combustion number [95]:

$$N = \left(\frac{c_p T_\infty}{g \rho_\infty^2 \left(\Delta H_c / r \right)^3} \right) \frac{\dot{Q}_c^2}{d^5} \tag{2.14}$$

where *r* is the fuel/air stoichiometric mass ratio. Some of the flame height correlations are listed in Table 2.1.

McCaffrey [54] summarized the correlations for the normalized flame height as shown in Fig. 2.6 [75]. From Fig. 2.6, it is apparent that the flame height, in general, depends strongly on the burner diameter and the heat release rate but this dependency is not the same over the range of variables shown in the figure. It should be noted that $\dot{Q}^{*2/5} \approx 10$ is equivalent to $Fr \approx 1$, so on right side of the graph, the flame is momentum dominant (jet flame) while the left side belongs to buoyancy dominant flames (*e.g.*, pool fires).

Table 2.1 Selected correlations of the flame height presented in the literature

Ref.	Correlation		
[57]	$l_f/d = 15.1\dot{Q}^{*2}$	$0.13 < \dot{Q}^{*} < 0.28$	(2.15)
	$l_f/d = 3.2\dot{Q}^{*2}$	$0.28 < \dot{Q}^{*} < 0.55$	(2.16)
[65]	$l_f \approx 0.2\dot{Q}_c^{2/5}$		(2.17)
[92]	$l_f/d = 42\,\dot{Q}^{*0.61}$		(2.18)
[94]	$l_f/d = 3.3\dot{Q}^{*2/3}$	$\dot{Q}^{*} < 1$	(2.19)
	$l_f/d = 3.2\dot{Q}^{*2/5}$	$\dot{Q}^{*} \geq 1$	(2.20)
[95]	$\log\left(2l_f/d\right) = 0.2\log N + 1.21$		(2.21)
[97]	$l_c/d = (13.8 \pm 2.15)Fr^{2/3}$		(2.22)[a]
	$l_f/d = 15.5(1 \pm 0.095)Fr^{2/5}$		(2.23)
[98]	$l_f/d = 15.6N^{1/5} - 1.02$		(2.24)

[a] l_c is combustion zone height

For turbulent jet flames, l_f is independent from $\dot{Q}^{*}$ (which is an indication of fuel flow rate) so $\dot{Q}^{*}$ is not an appropriate scaling factor for this regime [55]. In the middle is the region where the flame is mostly laminar and the relationship between l_f/d and $\dot{Q}^{*2/5}$ is seen as a 45-degree line in Fig. 2.6 [54]. And finally are the turbulent buoyant flames (natural fires) that have heights of the same order of magnitude as the fire base diameter. According to [94] the dependence of the flame height on the source diameter and heat release rate changes at $\dot{Q}^{*} = 1$.

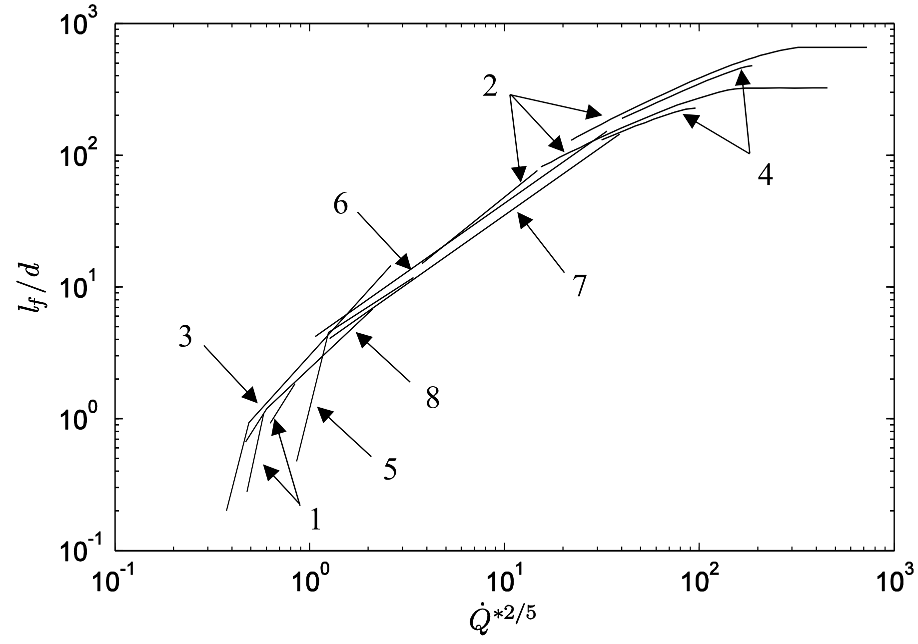

Fig. 2.6 Correlations for normalized diffusion flame height summarized by McCaffrey [54]. The numbers are 1: [57], 2: [91], 3: [92], 4: [93], 5: [94], 6: [95], 7: [96], and 8:[98]

2.3.3 Burning Rate

The pool burning rate is the rate at which the liquid fuel evaporates at the pool surface or in other words the rate that volatiles are issued from the liquid fuel. The burning rate is usually reported as fuel mass loss rate, $\dot{m}_b$ (g/s) [99], or per unit area of the pool as fuel mass flux, $\dot{m}''_b = \dot{m}_b / A_p$ (g/(m^{2}s)) [58] or as the average rate of fall of the liquid surface, regression rate, defined as $R = \dot{m}''_b / \rho_l$ (mm/min) [18].

According to the literature [12, 17, 18, 100, 101], the mass burning rate can be determined from the conservation of energy at the fuel interface as:

$$\dot{m}_b = \frac{\dot{Q}_{fs} - \dot{Q}_l}{\Delta H_v} \tag{2.25}$$

where $\dot{Q}_{fs}$ (kW) is the heat transfer from the flame to the fuel surface, $\dot{Q}_l$ (kW) is the heat that is lost from the pool surface to the bulk of the liquid fuel underneath, and ΔH_v (kJ/g) is the heat of evaporation. $\dot{Q}_{fs}$ is a portion of the total heat released from the combustion that made its way to the fuel source (this parameter will be described in more detail in Sec. 2.4), so burning rate is strongly dependent on the flame heat release rate.

In general, any parameter that affects terms on the right side of Eq. (2.25) can influence the burning rate. One of the most considered parameters of the pool is its diameter. The classic study of Blinove and Khudiakov [18] reported the regression rate of hydrocarbon pool fires over a wide range of diameters from 4 mm to 22.9 m. The experimental data of [18] was analyzed and compiled by Hottel [17] and the results were presented to illustrate the effects of the pool diameter on the burning rate. According to [17], in small-scale pools ($d \leq 0.1$ m) the regression rate decreased with increasing pool diameter, then it increased in the medium pool regime ($0.1 \text{ m} < d \leq 1$ m) and finally remained almost constant for large pools ($d > 1$ m). The constant value for large pools is usually known as the burning rate of an infinitely large pool, $\dot{m}''_{\max}$ [102]. Several studies showed a slight decrease in regression rate for very large pools ($d > 10$ m), which was related to incompletion of combustion and presence of smoke [58].

The burning rate also depends greatly on the fuel type. The variation of $\dot{m}''_{\max}$ with thermochemical properties of different fuels is illustrated in Fig. 2.7 (adapted from [102]). As it is apparent $\dot{m}''_{\max}$ increases with the ratio of fuel heat of combustion, ΔH_c, to the heat of evaporation, ΔH_v. That is, in general those fuels with lower heat of evaporation and those that generate more heat have higher burning rates [103]. The reason can be explained by the coupling between the fuel evaporation as the source of volatiles for combustion and flame heat release as the source of energy for sustaining the fuel evaporation.

The change in burning rate of different liquid fuels with pool diameter is not the same. Burgess et al. [104] measured the regression rate of different fuels burnt in pool fires with diameters in the range of 0.07-2.4 m (mostly excluding the small-scale pool regime). The results suggested that while the trend was similar the burning rate increased with pool diameter differently depending on the fuel type. While the burning rate of butane increased dramatically with diameter, this increase was relatively trivial in the case of methanol. The same was observed by Babrauskas [105] who compared the effect of the diameter on the mass flux of gasoline and methanol. The reason for such a variation is in the heat transfer mechanisms from the flame to the pool (this is explained in Sec. 2.4).

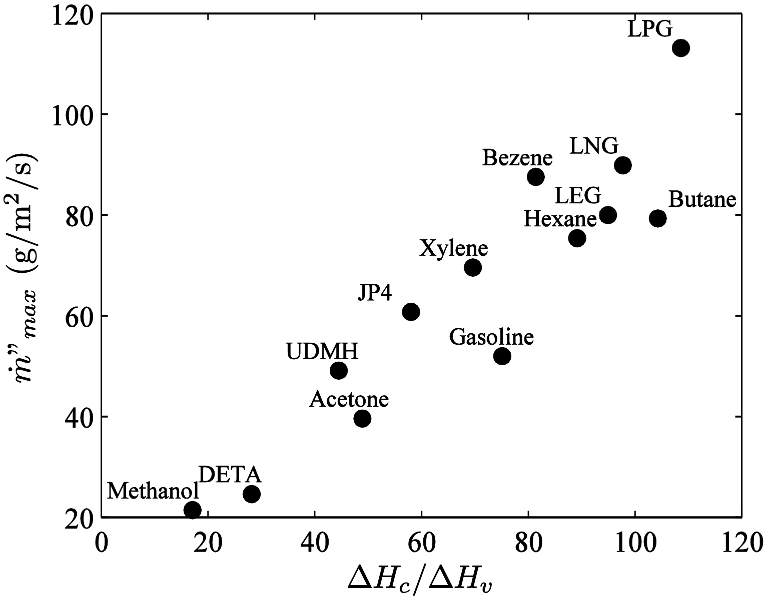

Fig. 2.7 Burning rate of very large pool fires with respect to thermochemical properties of fuels [102]

One of the parameters measured in this thesis is the pool fire burning rate, so a review of measurement techniques utilized by previous researchers is presented here. A list of selected works that measured the burning rate is shown in Table 2.2. Their fuels, pool geometries and pool dimensions are also included. The burning rate measurements can be divided into two major groups: ones that maintained the fuel surface at a constant level within the pool during the tests (steady) and those which burnt down a quantity of the liquid fuel in the pool without any control over the liquid level (unsteady). As presented in Table 2.2 both steady and unsteady pool fires have received great attention from researchers. While the analysis of the fire development and extinction could be conducted through the unsteady burning conditions which were more similar to the real fire scenario, systematic data was usually reported in the literature for the steady-state burning condition.

Table 2.2 List of the selected experimental studies on pool fire burning rate

Ref.	Test condition	Fuel	Geometry	Dimension (m)
[18]	Steady	Gasoline Kerosene Diesel oil Solar oil	Circular pool	0.004-30
[19]	Steady	Methanol	Circular pool	0.01-0.06
[67]	Unsteady	Methanol Heptane	Circular pool	1.22-2.44
[70]	Unsteady	Heptane	Square pool	2.7
[73]	Unsteady	Heptane Toluene Kerosene Gasoline	Circular pool Square pool	3-50 2.7
[100]	Unsteady	Heptane Kerosene Methanol	Circular pool	0.05
[101]	Unknown	Methanol	Circular pool	0.31-1.8
[103]	Steady	Toluene Heptane JP-8 Methanol Ethanol	Circular pool	0.1-2
[104]	Steady	Hexane Butane Benzene Xylene Methanol	Circular pool	0.07-2.4
[106]	Steady	Methanol	Circular pool	0.01-0.115
[107]	Steady	Methanol/Toluene	Circular pool	0.3-1.22
[108]	Steady	Methanol Kerosene	Circular pool	0.3
[109]	Steady	Methanol Ethanol	Circular pool	0.25-0.38
[110]	Steady	Kerosene	Circular pool	0.15
[111]	Unsteady	Heptane	Circular pool	0.3-6
[112]	Unsteady	Toluene Kerosene	Circular pool	1
[113]	Steady	Methanol Ethanol Heptane Toluene	Circular pool	0.046-1
[114]	Steady	Methanol	Rectangular pool	0.075-0.3
[115]	Unsteady	Gasoline Diesel oil	Circular pool	1.5-4
[116]	Steady Unsteady	Hex-11 Hex-12 Jet-A	Circular pool	0.3

Under unsteady testing conditions, the burning rate is not constant and can increase or decrease with time during the test period. This parameter is usually measured from the fuel surface regression rate [70, 73, 111, 112, 116] or weighing the pool [67, 100, 115] as the fuel is burning. Hayasaka [100] measured the burning rate, liquid and pool temperatures (at a single point) when the fuel level in the pool was not controlled. It was shown that after ignition the liquid fuel and the pool were heated up and burning rate increased and then became relatively constant at its "preheating" value. After a jump in the burning rate from the preheating value in the transition stage, boiling was observed in the liquid fuel. As a result, the liquid pool temperature remained constant and the burning rate reached and maintained a maximum value (called the boiling value) until it suddenly dropped as the fuel completely burnt out. The same trend was observed in [117] for a 0.2 m diameter *n*-heptane pool fire. Hayasaka [100] reported 60% and 30% increase in the burning rate of heptane and kerosene, respectively, from preheating to boiling stage while the burning rate was almost the same for a methanol pool fire after the warm up stage.

Different trends from those shown in [100] were presented by [116] for the unsteady regression rate of jet-A and hex-12 (these fuels are mixtures of different liquid fuels and their compositions can be found in [116]) with time. It was observed that in the preheating stage the regression rate increased to a maximum and then it decayed and finally remained constant for a while before it dropped rapidly upon the fuel burn out. It can be concluded based on [100, 116] that the variations of the burning rate with time under unsteady conditions also depends on the fuel type.

The steady burning rate includes monitoring the level of the liquid fuel in the pool and adding the fuel to the pool accordingly to cover the fuel mass loss due to the surface evaporation at the base of the fire. Therefore, the supply flow rate to the burner was usually considered as the steady state burning rate. The fuel level was monitored either by the use of level sensors [116] or through axillary variables such as: static pressure of the liquid layer [103, 107, 114] and the temperature difference of the liquid and gas phases at different sides of the fuel surface [104, 113, 118, 119].

Although all of the studies that established steady burning conditions kept the fuel level constant, this level was different from the edge of the pool. The vertical distance from the pool liquid surface to the edge of the container is known as the freeboard or lip height [120]. Depending on the burning conditions the freeboard could either enhance the heat transfer to the liquid pool [58] and consequently increase the burning rate, or decrease it as reported in [120] for small-scale ethanol pool fires. While some researchers maintained the fuel level at the pool rim (zero lip height) [19], some others allowed a prescribed lip height (*e.g.*, ~3-5 mm) [103, 107]. Another parameter that could affect the burning rate measurements is the ambient conditions such as pressure and wind effects, which will be discussed in Sec. 2.6.

2.4 Heat Transfer Mechanisms

Due to the combustion within the diffusion flame over the combustible liquid in pool fires, thermal energy is generated. The overall heat released in the flame , $\dot{Q}_a$, is radiated, $\dot{Q}_{f,rad}$, and convected, $\dot{Q}_{f,conv}$, from the flame to its surroundings. Also, a portion of this energy is the flame heat feedback to the liquid in the pool to vaporize the fuel, $\dot{Q}_{fs}$ [121]. The fractional amount of each of these energy pathways can be defined as:

$$\chi_{rad} = \dot{Q}_{f,rad} / \dot{Q}_c \tag{2.26}$$

$$\chi_{conv} = \dot{Q}_{f,conv} / \dot{Q}_c \tag{2.27}$$

$$\chi_{fs} = \dot{Q}_{fs} / \dot{Q}_c \tag{2.28}$$

It worth emphasizing that actual heat release rate, $\dot{Q}_a$, is smaller than $\dot{Q}_c$ especially for sooty fuels the combustion efficiency, χ_a, can be as low as 0.6 (for liquid polystyrene pool fire) [51].For non-smoky flames with a low tendency to produce soot, such as methanol pool fires, becomes approximately one [21]. It also important to note that the fractional values of energy transport from the flame strongly depend on the fuel type and burning conditions.

For liquid pool fires, the convective fraction of the total heat release rate, χ_{conv} , is mostly more than 0.6 to 0.7 [75, 122, 123]. This convective portion of heat release is carried away by the plume above the flames. The remainder of the total heat released is radiated away in all directions [75]. From a practical point of view, the ignition of an external target depends on the amount of heat received from the fire radiatively [102]. Therefore, the radiative heat from the pool fires has been investigated in numerous studies and their summary can be found in [14, 51, 102].

In order to determine the overall radiation output of pool fires, Hamins et al. [124] measured the radiative flux at a single point and assumed the fire radiation to be isotropic. A number of investigators [21, 119, 125] used radiometers at different distance from the burner to find profiles of the radiative flux as a function of location in the radial and vertical directions. The total radiant power output of the flame was then estimated from the integration of the radiative flux over the measurement regions [21, 126]. The results showed that the flame radiation of alcohol pools (*e.g.*, methanol) was more than an order of magnitude smaller than the radiation of hydrocarbon pool fires (*e.g.*, heptanes) [21].

Radiative emission of the flame is a strong function of the flame soot volume fraction. In fact, the characteristic yellow luminosity of the flame is a result of soot particles. Combustion gas products such as carbon dioxide, water vapor and carbon monoxide emit infrared radiation which is invisible [21]. Therefore, non-sooty flames such as the burning of H_2 are invisible; methanol flame is also noticeably blue in low light levels and almost invisible in natural light. In contrast, hydrocarbon fires are luminous due to the existence of soot particles in the flame which are in high temperature and therefore emit visible radiation [21].

Besides soot concentration, the flame radiation output is also a function of flame temperature [13]. The radiant fraction, χ_{rad} , was correlated as a function of fuel smoke point, actual heat release rate $\dot{Q}_a$, stoichiometric air to fuel mass ratio and the adiabatic flame temperature in [127-129]. Klassen and Gore [113] reported the radiative fraction, χ_{rad} , of around 0.2 for several alcohols (*e.g.*, methanol and ethanol) and around 0.3 for hydrocarbon fuels (*e.g.*, heptane and toluene) for 0.05-1 m pool diameter range. For very sooty liquid plastic 0.3 m pool fires the radiative fraction was reported as high as 0.4 [51]. An upper limit for radiant fraction was suggested as 0.43 in [127]. It was suggested in [129] that a radiative fraction of 0.3 was appropriate for most fire engineering applications.

Hamins et al. [121] simulated liquid pool fires with low initial-momentum gas porous burners and measured the different fractions of the heat release for a range of 0.1-1 m burner diameter and 0.4-200 kW heat release rate. The combustion efficiency for a smoky acetylene flame was around unity for lower mass fluxes and then decreased with the fuel mass flux to as low as 0.6. This quantity remained almost constant and approximately equal to unity for methane and propane. These trends were related to the fuel tendency to soot. Fuels such as acetylene typically yield smoke only for moderate and high fuel mass fluxes, so for large mass fluxes, large quantities of soot were formed in the flame and χ_a decreased. For methane and propane even at the large mass fluxes no evidence of emitted visible smoke was observed. Based on their findings, Hamins et al. [121] checked the validation of the flame height correlations available in the literature and suggested that those correlations were invalid for smoky flames. The correlations were proven for non-smoky flames though.

Hamins et al. [121] also showed that χ_{fs} was a relatively small term except for small mass fluxes (*i.e.*, $\dot{m}_b'' < 10$ g/(m^{2}s)). With an increase in fuel mass flux, the radiative fraction increased to 0.2-0.3. The convective fraction was almost constant at 0.7-0.8 for methane and propane when $\dot{m}_b'' > 10$ g/(m^{2}s) while for acetylene it was continuously reducing with $\dot{m}_b''$ increasing.

For non-smoky fuels the liquid fraction, χ_{fs} , may be estimated by the ratio of the heat of evaporation to the heat of combustion [21]. This ratio is 0.06 for methanol, which is in agreement with the measured value for χ_{fs} [37]. This means that 6% of the heat released from combustion in a methanol pool fire is transferred to the liquid methanol pool. The heat transfer from the flame to the pool surface, $\dot{Q}_{fs}$, occurs in forms of conduction, convection, and radiation [17, 20] as shown schematically in Fig. 2.8. Therefore, the heat feedback would be:

$$\dot{Q}_{fs} = \dot{Q}_{rad} + \dot{Q}_{conv} + \dot{Q}_{cond} \tag{2.29}$$

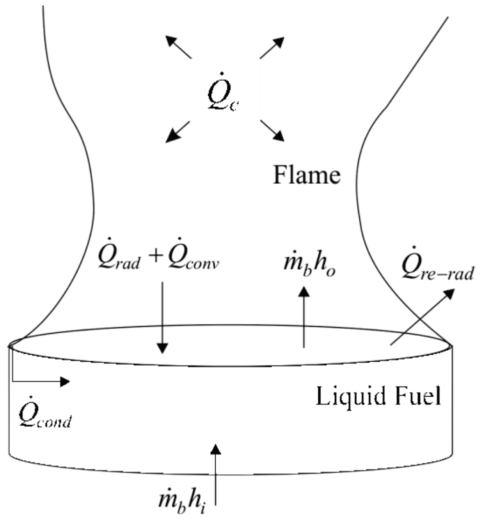

Fig. 2.8 Energy transfer mechanisms from the flame to the liquid pool

Different forms of flame heat feedback can be expressed in terms of the system parameters by the classical formulations developed in [17] as:

$$\dot{Q}_{rad} = \frac{\pi d^2}{4}\Gamma_1\left(T_f^4 - T_l^4\right)\left[1 - \exp\left(-\kappa d\right)\right] \tag{2.30}$$

$$\dot{Q}_{conv} = \frac{\pi d^2}{4}\Gamma_2\left(T_f - T_l\right) \tag{2.31}$$

$$\dot{Q}_{cond} = \pi d\, \Gamma_3\left(T_f - T_l\right) \tag{2.32}$$

In Eq. (2.30), Γ_1 is a coefficient that includes the Stefan-Boltzmann constant and the configuration factor for heat transfer from the flame to the liquid fuel surface, T_f and T_l are the representative flame and liquid temperatures, and $[1 - \exp(\kappa d)]$ is the flame emissivity [12]. In Eq. (2.31), Γ_2 is the convective heat transfer coefficient, and Γ_3, in Eq. (2.32), is a constant that is used for the conductive heat transfer in [17]. While the radiation and convection terms are the heat pathways directly from the flame to the fuel bed, the conduction is a pathway that includes the heat transfer from the flame to the pool wall and then into the liquid pool convectively [17, 22, 106]. The coefficients used in Eqs. (2.30)-(2.32) were described in another reference [130].

As shown in Fig. 2.8, a portion of the received heat from the flame in the form of radiation is re-radiated to the surroundings, $\dot{Q}_{re-rad}$. This term was estimated to be less than 10% for a kerosene pool fire [131]. The flame heat feedback minus the heat re-radiation from the surface is balanced with the heat required for fuel evaporation at the pool surface [14, 100, 119] as:

$$\dot{Q}_{fs} - \dot{Q}_{re-rad} = \dot{m}_b \left(c_{p,l} (T_s - T_i) + \Delta H_v \right) \tag{2.33}$$

This relationship can give the burning rate, so the determination of the different heat transfer fluxes to the pool surface are important. Although Eqs. (2.30)-(2.32) cannot accurately determine the different heat transfer pathways, they help in a general understanding of the problem. Neglecting the pool heat re-radiation and the temperature variations within the liquid and assuming that the flame is isothermal (according to the temperature distributions shown previously these assumptions are not valid but they are just for a qualitative explanation), the fuel mass flux at the pool surface can be estimated as:

$$\dot{m}''_b = \frac{\Gamma_1 \left(T_f^4 - T_l^4 \right) \left[1 - \exp\left(-\kappa d \right) \right] + \Gamma_2 \left(T_f - T_l \right) + \Gamma_3 \left(T_f - T_l \right) / d}{\Delta H_v} \tag{2.34}$$

In Eq. (2.34) the first term is the radiation, the second term is the convection and the last term is the rim conduction pathway. This expression can describe the variation of the fuel mass flux with the pool diameter as shown qualitatively in Fig. 2.9 [17]. It should be emphasized that in addition to the pool dimensions, the relative contributions of the heat transfer pathways to the liquid fuel evaporation depend on other system characteristics such as vessel properties, lip height, flame structure, soot volume fraction and temperature and species concentration distributions [20].

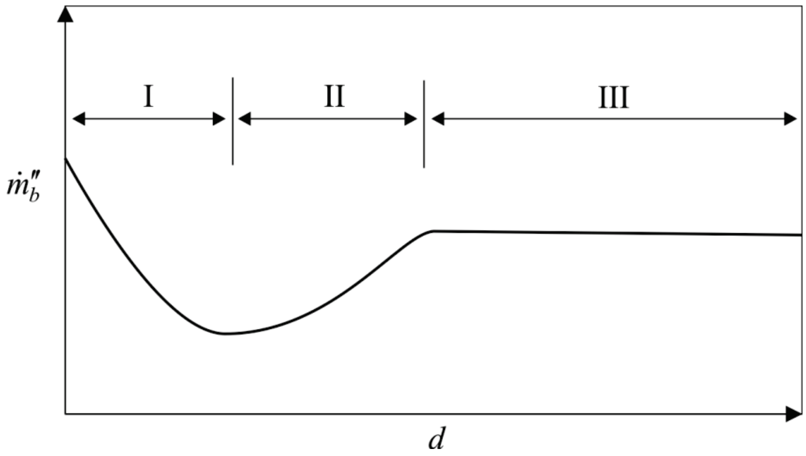

Fig. 2.9 Variation in fuel mass flux as a function of pool diameter [17]

In small pools, Region I, rim conduction dominates the heat feedback. Conduction is inversely proportional to the pool diameter, and as the pool gets larger the importance of conduction diminishes and convection dominates. In this region, the flame is laminar and convection also decreases with pool diameter [19, 130]. By decreasing the heat feedback, $\dot{m}''_b$ also decays with the pool diameter. After the laminar regime, convection is not a strong function of the pool diameter [103, 132] but with increasing pool diameter, in Region II, the flame emissivity increases and the radiation dominancy rises against convection. That is, in Region II, which is known as the medium pool regime, for smaller diameters convection is more important than radiation but radiation dominates as the pool become larger [103]. The radiation heat pathway increases with the pool diameter, as does the mass flux in Region II. Eventually, for very large pools, Region III, the radiative heat transfer becomes the principle heat feedback mechanism. In this regime, since the fire emissivity reaches its maximum value, the flame heat feedback becomes independent from the pool size and the mass flux remains constant.

Babrauskas [58] classified liquid pool fires to four burning modes as shown in Table 2.3 (the wall conduction was ignored). Based on Hottel's review [17] of Blinov and Khudlakov's data [18], Babrauskas [58] suggested that the pool fires may be either in radatively dominated burning for large diameters or convectively dominated burning for small diameters. Furthermore, the flow can be either laminar or turbulent in the convective regime, while in the radiative regime the flame may be optically thin or thick.

Table 2.3 Different liquid pool burning modes based on pool diameter [58]

Pool diameter (m)	Burning mode
< 0.05	convective, laminar
0.05-0.2	convective, turbulent
0.2-1	radiative, optically thin
> 1	radiative, optically thick

Another method [130] classified pool fires to different regimes in which the burning rates were controlled by convection and rim conduction for $d < 0.01$ m, convection for $0.01 < d < 0.2$ m, and by convection and radiation for $d > 0.2$ m. They proposed that the convection was changed from laminar to turbulent at $d = 0.1$ m. The influence of radiation also appeared to behave as though the gas between the radiating flame and the fuel surface was non-absorbing (optically thin) for $0.2 < d < 2$ m. For $d > 2$ m, combustion gases became optically thick and absorbed part of the incident radiation from flame to the liquid surface.

Each of the heat transfer mechanisms from flame to the pool surface has been investigated in an effort to accurately model mass evaporation rate of burning pools. Large pools which are controlled by radiative heat feedback are the most interesting for fire protection. For radiatively dominated pool fires ($d > 0.2$ m) the fuel mass flux can be estimated as [133]:

$$\dot{m}''_b = \dot{m}''_{\max}\left(1 - e^{-\kappa d}\right) \tag{2.35}$$

where $\dot{m}''_{\max}$ is the mass flux when the pool is very large and κ (m^{-1}) is the flame emission coefficient. The values of $\dot{m}''_{\max}$ and κ for different fuels can be found in the literature [58, 102].

For a 0.3 m pool fire, Rasbash et al. [108] determined the emission coefficients, κ, of 0.37 m^{-1} for non-sooty alcohol and 2-4 m^{-1} for sooty hydrocarbon fuels (*e.g.*, benzene and kerosene). They also showed that the temperature of the non-luminous alcohol flames was (1218ºC) much higher than that of hydrocarbon flames (*e.g.*, 921ºC for benzene). This was due to the considerable heat radiation from soot particles in the case of hydrocarbon fuels. In another study [51] the emission coefficients of very sooty liquid thermoplastic (*e.g.*, PMMA and polystyrene) pool fires with a diameter of 0.3 m were reported to be 1.3-5.3 m^{-1}.

The heat radiated to the pool surface was also estimated in [51, 108]. It was shown that 20% of the energy required for the fuel evaporation at the pool surface came from flame radiation for alcohol pool fires, while the estimated radiant heat feedback was even greater than the required heat for sustaining the steady burning for sooty fuels. For non-luminous pool fires, such as alcohol, the flame burns very close to the liquid surface so the rest of the required heat is provided by convection [12, 108]. In the case of hydrocarbon fuels the flame is further above the pool surface and there is a discernible vapor zone immediately above the liquid. This vapor zone absorbs part of the radiant flux to the liquid surface [108, 131, 134-136].

Flame height and shape were also shown to be important parameters in the estimation of radiative heat from the flame [21]. Orloff and de Ris [126] measured the radiative heat flux from the flame by using radiometers at different locations. They also developed an analytical expression for the flame shape, and assuming homogeneity and constant temperature for the flame, they estimated heat feedback to the fuel surface. Their algorithm adequately described the flame shape and energy balance at the fuel surface for a range of pool sizes of 0.1-0.7 m, different fuels, and different fuel flow rates. An empirical correlation was also presented in [103] to predict the heat feedback for various fuel (sooty and non-sooty) pool fires with 0.1-0.3 m diameter.

In convectively dominated pool fires, the convective heat feedback was reported to be proportional to d^n [130, 137]. The power, *n,* was zero when the flow was turbulent ($d > 0.1$ m), which meant the convective heat feedback was independent from the pool diameter while a value of $n = -0.5$ for laminar pools, made the convection inversely proportional to the roots square of pool diameter.

A dimensionless correlation was presented in [132] for pool fire burning rate based on a dimensionless number known as the mass transfer driving force (defined by Spalding [15]). The predictions of the correlations were in good agreement with the experimental data except for the laminar pools.

Akita and Yomoto [19] investigated methanol laminar pool fires experimentally. The rate of methanol burning and the flow field within the gas phase were investigated in their study. Particle tracking in the flame showed qualitatively that there was a symmetrical vortex along the liquid surface. The vortices were introduced as the characteristics of the laminar diffusion burning that transferred heat from the flame to the fuel surface. They also conducted experiments on concentric and single vessels of different sizes and showed that in small vessels with laminar burning the maximum burning rate was at the vessel rim next to the flame base and the burning rate decreased toward the center. However, this trend was not so readily observed in larger vessels. They proposed that the difference in burning rate could cause a longitudinal flow at the fuel surface but they did not present any supporting data. In small-scale pools, the rim conductive heat transfer is also important. Akita and Yomoto [19] reported that the ratio of conduction to convection at the base of the flame was 0.7 and suggested that the radiation heat feedback was negligible for small methanol pool fires.

Nakakuki [22] measured the burning rate and calculated the direct radiation from the flame to the fuel surface in the laminar region. It was shown that the radiative heat transfer was small. The heat convection from the flame to the liquid surface and the heat conducted through the vessel walls and then transferred to the liquid fuel convectively were proposed as the dominant heat transfer mechanisms in small pool fires. Nakakuki [106, 138] quantified the amount of heat transferred through the vessel walls to the liquid by developing a finite difference model. The burning rate and the wall temperature distributions were measured and calculated for vessels of different materials and thickness. The results from the numerical calculations showed good agreements with measured data when the vessel had low thermal conductivity or was thin. The calculated wall heat flux distributions with respect to the vertical position were presented. The quantitative values of the overall heat transfer from different pathways were not presented in [106]. However, it was concluded that in small pool fires (d = 0.01-0.02 m) the direct convective and radiative heats from the flame above the liquid surface were negligible in comparison to the wall heat transfer.

2.5 Liquid Phase of Pool Fires

The studies reviewed so far mostly tended to focus on combustion in the flame and transport phenomena within the gas phase. Comparing with the relatively large number of investigations on the gas phase of the pool fire, limited information can be found in the literature to characterize the motion and thermal structure within the liquid phase.

Several studies determined the liquid temperature distributions as shown in Fig. 2.10 [139, 140]. The thermal structure stabilized within relatively deep pools (so called "tank fires") included a hot zone below the fuel surface, and a steep gradient region followed by a relatively cold zone. The temperature within the hot zone was varying slightly, but it was considered to be uniform and be approximately equal to the pool surface temperature [139]. Inamura et al. [141] attributed the existence of the uniform hot zone below the fuel surface to the in-depth absorption of the flame radiation.

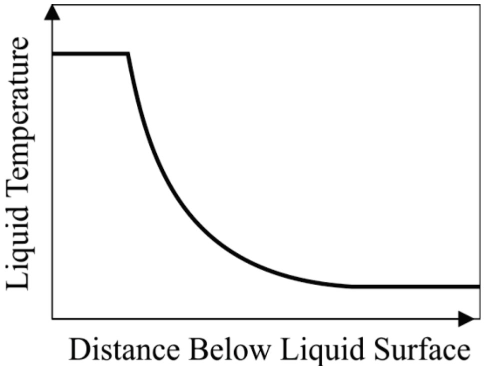

Fig. 2.10 Temperature within the liquid phase during steady burning [139]

The finite difference model developed in [106] was used in [142] for medium pool fires ($0.1 < d < 1$ m). It was found that the fuel heat loss/gain through the wall was not negligible in comparison with the direct heat feedback from the flame to the liquid surface. The existence of the hot zone below the burning surface was related to the heat transfer from the wall to the liquid fuel. It was observed that when the outer surface of the pool was cooled the hot-zone layer thickness decreased. The reason for an increase in the hot-zone layer (or isothermal layer) thickness reported in the unsteady burning of the pool fires [117] could also be explained by wall heat transfer. As the fuel level decreases a larger portion of the wall is exposed to the flame radiation and becomes hotter. This phenomenon results in a wall heat transfer enhancement and a thicker hot-zone layer [142].

Nakakuki [142] also showed that the exact heat balance of the overall system was not obtained unless the heat transfer from the pool wall and the rate of change of sensible heat in the liquid fuel were included in the analysis of heat transfer. Therefore, accurate models for the energy transfer within the liquid phase are required. Based on this, the accuracy of the assumptions numerical modelers used for the liquid phase of pool fires may be questionable where the liquid phase was either excluded from the analysis [24] or modelled unrealistically [25-27].

Inamura et al. [141] presented two models for the transient energy balance within the liquid phase. One of them included only conduction and the other included conduction and radiation absorption within the liquid phase. The temperature profiles calculated from these models were compared with measured liquid temperature distributions. It was shown that the radiation absorption through the liquid layer was important and had to be included in the liquid energy transfer analysis. However, even with accounting for in-depth radiation absorption, Inamura et al. [141] found discrepancies between the measured and the estimated temperature distributions within the liquid phase. They proposed that in order to improve the model accuracy, the effects of Rayleigh convection (buoyancy-driven natural convection) should also be included in the energy analysis. The convection was added to the energy model in [143, 144] and showed a better agreement with the experimental data.

Although the works presented in [143, 144] demonstrated the importance of convection currents within the liquid phase, the model they used for convection was one-dimensional with only a vertical component (normal to the liquid surface). There are evidences in the literature that the convection currents within the liquid phase might also have a horizontal component (parallel to the pool surface plane) and essentially be two-dimensional. For example, the wall heat transfer [142] from the side to the liquid pool is expected to have a horizontal component.

Gradients in the heat flux incident on the fuel surface and consequently the non-uniform surface mass flux $\dot{m}_b''$ [19-21] may result in temperature gradients within and on the surface of the liquid pool. The surface tension gradient due to the temperature variation may result in thermocapillary convection or Marangoni motion on the liquid surface [145]. The temperature gradients within the liquid may cause buoyancy-driven or Rayleigh convection [146]. These effects should be considered in the analysis of pool fires. For example, it was shown by [147] that only the thermocapillary effect can enhance the heat transfer in methanol by up to a factor of two in comparison with the case that this effect did not exist depending on the Marangoni number which is a measure of surface tension forces with respect to viscous forces.

The aforementioned mechanisms play an important role in the flame spread across the liquid fuel after ignition [148]. There are two major types of flame spread over liquid fuels, and the classification is based on the liquid fuel property and the initial liquid temperature before ignition. A summary of the research done on flame spread can be found in [148, 149]. The interesting properties here are liquid fuel flashpoint and firepoint. Flashpoint is the lowest temperature that the fuel vapor/air mixture above the liquid fuel is within the flammability limits [8]. When the vapor above the liquid is ignited a transient premix flame is generated that consumes all of the vapor/air mixture lying within the flammability limit. After this transient phase, the diffusion flame establishes above the liquid fuel bed only if the rate of fuel evaporation is sufficient to sustain the diffusion burning. The lowest temperature that liquid evaporation can support a sustained diffusion burning after the ignition is known as the firepoint [12].

While the flashpoint and the firepoint of volatile fuels like methanol are identical [148] there are some hydrocarbon fuels for which the firepoints are significantly greater than their flashpoints [12]. For example, the flashpoint is 12-14ºC and the firepoint is 20ºC for *n*-octane [148]. However, mostly the flashpoint is used to classify the flame spread patterns in the literature. If the liquid temperature is well below its firepoint the fire cannot survive since the flame heat loss to the fuel surface causes the extinction of fire. When the liquid fuel initial temperature is above its firepoint flame is spread over the liquid fuel with premix combustion propagation [148, 150].

The flame spread over a liquid fuel at a temperature below its firepoint (or sub-flash flame spread) occurs by surface tension driven flows (thermocapillary convection) [151]. The region beneath the flame is hotter than other regions and motion is induced by thermocapillary stresses on the fuel surface as a result of the temperature gradient. The surface tension decreases with temperature and the colder regions pull the liquid from the hotter region beneath the flame, so the flow is induced from hot to cold regions. This motion on the liquid surface results in the flame spread over the fuel bed in the same direction [148, 150-152]. The rate of flame spread is a function of liquid temperature [150]. It takes more time to preheat the colder liquid in front of the flame to its firepoint, so flame spread speed decreases as the initial liquid temperature decreases.

Although the starting force for the flow in the flame spread stage was well-known as a function of thermocapillary forces, the liquid convection in fact is driven by thermocapillary and buoyancy forces [153]. The existence of buoyancy in the liquid pool was considered controversial since the liquid was heated from above. However, there was an inherent coupling between thermocapillary effects and buoyancy [148]. Murad et al. [153] investigated the effects of these two forces on the convection in the liquid after ignition. They eliminated the thermocapillary effects by adding surfactant to the liquid and in a separate test they added viscosifier (*i.e.*, material that increased the liquid viscosity) to eliminate any convection within the liquid. They concluded that the flow may start due to the temperature gradient on the surface but it is maintained mainly by buoyancy forces.

Ross [152] found that the flame spread over the liquid pool was completely different in normal gravity and micro-gravity, which suggested that buoyancy was important in this phenomenon. The flame spread faster in normal gravity than in micro-gravity. It was also shown that under micro-gravity conditions heat could penetrate far deeper into the pool. The major effect of the buoyancy in the liquid phase was shown to be its stratification of the temperature field in normal gravity, and when the buoyancy effect was weakened by decreasing the gravity the thermal stratification became weaker and energy could convected further away from the pool surface in the vertical direction. The deeper penetration of heat from the surface into the liquid under micro-gravity conditions makes the surface preheating delay for flame spread longer, so the flame spreads slower than it does in normal gravity. For the same reason the rate of flame spread over liquid pools decreases with the pool depth [154]. The flame also spreads slower as the liquid surface tension increases since the flow takes the energy faster from the region in the vicinity of the flame and makes the surface preheating longer [153, 155, 156].

From numerical models and flow visualization in the liquid layer below a spreading flame, it was depicted that the convection currents within the pools were essentially two-dimensional. The liquid flowed away from the hot regions beneath the flame at the surface and towards it in the pool. This established a recirculating motion (*i.e.*, vortex) below the flame [152, 157-160].

In summary, the effects of surface-tension and buoyancy are important in developing convection currents within the liquid phase of pool fires during flame spread. There is evidence in the literature that the same driving forces may govern the steady-state flow distributions within the liquid layer [161]. Therefore, these mechanisms are reviewed here for two simpler cases that may be similar to the steady burning of pool fires. This review can help the understanding of the phenomena happening in the more complicated problem such as steady burning of pool fires. These simple cases are Case I: the flow induced by exposing the liquid layer to a point heat source (*e.g.*, hot wire or laser beam) from above, and Case II: the flow induced in a cavity with an adiabatic bottom when its side walls are kept at different temperatures.

The flow streamlines are shown in Fig. 2.11a for Case I [148]. The heat transfer from the point heat source to the surface is non-uniform. This scenario is similar to the non-uniform heat feedback from the flame [20]. By introducing this heat source to the liquid surface, at first a thin top surface layer streams outward from the point source as a result of thermocapillary forces. The flow turns downward when it encounters the wall and eventually returns up to the surface underneath the heat source. As a result, two counter-rotating vortices (the results were two-dimensional in [148] and the structure of the vortices could be toroidal in 3D), one on each side of the point source, are established. After this initial formation stage, buoyancy stabilizes and restricts these two main vortices to the near liquid surface. These main vortices maintain in steady-state condition but their size shrinks as a result of thermal (density) stratification by buoyancy [148].

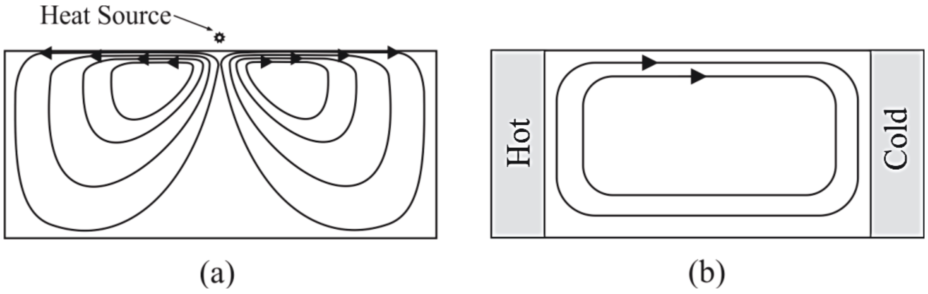

Fig. 2.11 Qualitative streamline maps within the liquid layer for (a) Case 1: when the liquid is heated from top by a point heat source and (b) Case II: when liquid is within a cavity with two side walls kept at different temperatures

The flow streamlines established in Case II are illustrated in Fig. 2.11b qualitatively [162]. This situation can be seen as similar to the flow within a liquid pool confined by a hot wall. This is a common scenario in pool fires given that the proximity of the wall to the flame makes the top of the wall hotter than the liquid in the center of the pool [106]. It was shown in [163] that the buoyancy by itself could result in a flow field similar to Fig. 2.11b and [162] showed that addition of surface tension to the problem resulted in fluid acceleration at the liquid surface. In both cases there was possibility for more convection cells to be generated depending on the problem parameters, but the other vortices were not as strong as the main vortices shown in Fig. 2.11.

In summary, it is worth emphasizing that although according to the information presented in the literature the general form of flow structure within the liquid phase may be speculated, no systematic experimental data for the pool fire situation was found. Therefore, one of the main goals of the current study is to conduct such an investigation.

2.6 Effects of Burning Conditions and Pool Parameters

The measureable variables (*e.g.*, burning rate) are established by the characteristics of the pool and burning conditions. While the effects of several parameters such as fuel type and pool diameter have been already described in the preceding sections, the influence of other parameters that may be important for the current study are discussed in this section.

Of the parameters that may affect the pool fire burning especially for small diameters are the pan material and its wall thickness. These have a great influence on the wall heat transfer (*i.e.*, conduction heat pathway) which is important for small and probably medium pools [17, 19, 22, 106, 138, 142]. Nakakuki developed a finite difference model [106] to study different pool burning scenarios such as deep pools, pools with different lip heights, flame spread, *etc*. However, of interest here are the effects of wall material and thickness. It was shown that for a full pool (*i.e.*, no freeboard) the burning rate reduced with increases in the wall thickness and thermal conductivity [22, 120]. However, this was strongly influenced by pool lip height. An opposite dependency of burning rate to the pool wall thickness and thermal conductivity can be observed if the liquid level drops below the pool wall top edge [106, 138, 142, 164, 165].

The next important pool parameter is the pool lip height (or freeboard height). The influences of the lip height in summary include affecting the convective heat transfer from the flame to the liquid surface, changing the temperature distribution of the pool wall and hence affecting the conduction heat transfer pathway, and increasing the flame volume and the flame radiation [58]. Each of the aforementioned effects is important for a particular pool regime and their coupling is not fully understood. As a result, the variations in the pool burning with lip height were reported differently in the past studies, and still there is not agreement on an empirical correlation between the ullage (another term for lip height and freeboard) and the pool fire attributes [165]. While a decrease in burning rate was reported with increasing lip height in [22, 165, 166] it was mentioned in [62] that the burning rate increased with the fuel level descending. The increase in the burning rate with lip height increase was also observed in [167] and in unsteady burning [117]. Relevant to the case studied here, it can be concluded from the literature that the pool fire burning characteristics are sensitive to the lip height. Furthermore, it is expected that the pool burning rate decreases with lip height and that the rate of burning rate reduction is a function of pool wall thermal conductivity and thickness [22, 164, 165].

Garo et al. [168] examined the effects of the liquid layer thickness on the burning rate of pool fires of different sizes. It was found that the burning rate of crude-oil reduced as the pool (*i.e.*, the volume occupied by the fuel) became shallower. In their experiment the fuel was floating on water and the burning rate reduction was explained with the increase in the heat loss from the fuel layer to the water substrate in shallower pools. They also showed that the heat sink effect of water lessened for deeper pools and at a certain depth depending on the pool size the burning rate remained invariant. There was no control over the fuel level in [168] though and no data could be found for steady pools. The liquid temperature has a proportional effect on the burning rate in both steady and unsteady pool fires [104, 169]. This result was due to the increase of fuel sensible energy at lower fuel initial temperatures.

Finally, the pool fire burning is also dependent on environmental conditions. A review of the studies on this subject can be found in [170] where the effects of temperature, pressure, and motion (wind) of the ambient air were described. The ambient temperature can affect the flammability limit and change the flame temperature. It was observed from the burning of pools at different ambient pressures [171, 172] that with increasing pressure the burning rate decreased and increased when the pool diameter was smaller and greater than 7 cm, respectively. It was also shown that at lower air pressure, the flame height and temperature increased while the radiant fraction decreased.

The effects of air flow (*i.e.*, wind) on pool fires have been investigated in more detail in the literature. It was found that wind enhanced convective heat transfer [173] and improved the mixing and combustion which finally raised the flame temperature [139]. Therefore, the first result of wind particularly observed for small pools, dominated by convective heat feedback, was an increase in the fuel burning rate [114, 174]. However, the effects of wind on large pool fires, controlled by radiation, are different. Wind reduces flame volume and tilts the flame to be less well-centered, which in overall decreases the radiative heat feedback to the pool [97, 102], and decreases the burning rate of radiatively dominated pools [32, 175].

2.7 Conclusion

An extensive literature review on different aspects of pool fires was presented in this chapter. Pool fire characteristics were studied and important problem parameters were identified. An understanding was also developed of the phenomena involved in the burning of pool fires. It was found that compared to the gas phase (flame), limited information was available on the liquid phase. Therefore, an experimental approach is developed and used in this thesis to investigate the transport phenomena within the liquid phase of pool fire.

3. Experimental Setup and Methodology

3.1 Overview

The main objective of this experimental study is to investigate the complex problem of the transport phenomena of pool fire especially within the liquid phase. In order to achieve this goal the key variables of the problem must be identified and obtained. Different pool fire characteristics were described in Chapter 2. Among those the parameters that were important for developing an understanding of the liquid phase of pool fires are:

- Burning rate (fuel mass loss rate): this may be the most important variable as it is directly related to the flame heat release which essentially is the source of heat feedback from the flame to the liquid fuel. From the liquid phase perspective, it is also an important quantity as an integral parameter that indicates the influence of the energy distribution within the liquid fuel. This variable may be described as the connecting factor between different phases of the pool fire as the relationship between the gas and liquid phases is through the rate at which the fuel vapor emits from the pool surface.
- Flame height: in order to illustrate the effects of the transport phenomena within the liquid phase on the gas phase (flame), this variable was examined. These effects have been mostly underestimated in the literature. For example, while the details of the process of the gas phase have been considered in the numerical models, the liquid phase have been neglected to reduce the computation time and cost.
- Pool wall temperature distribution: one of the heat pathways from the flame to the liquid phase is the heat transfer through the pool wall into the liquid fuel. This heat pathway is particularly important for small-scale pool fires such as the ones considered in this study. To quantify the heat

transfer from the wall to the liquid fuel the pool wall temperature was required.

- Temperature within the liquid phase: the energy distribution and transport (as well as heat transfer at the wall) cannot be characterized unless the thermal structure within the liquid phase is examined. The temperature at different locations within the pool was considered to understand the energy transfer patterns.
- Velocity field within the liquid fuel: the energy may be transferred within the liquid phase with fluid motion (convection). Due to the lack of information, this effect has been neglected in previous studies that assumed it to be trivial. The velocity field of the liquid phase was considered for a better investigation of the energy distribution and transport within the liquid layer and to examine the assumptions used in the past.

These variables should be measured under well-defined testing conditions. In general, in this study, the experiments were conducted under steady-state, steady-flow conditions, in a quiescent environment with no transverse airflow, and in a lab at atmospheric pressure and typical room temperature of 22°C. The steady-state, steady-flow conditions were associated with maintaining a constant fuel level in the pool. That is, during the fuel burning, the liquid fuel was continuously added to the pool to replace the fuel that was evaporated from the top of the pool for combustion.

It is also required to alter the liquid phase test parameters to achieve a comprehensive understanding of the transport phenomena. In a typical pool the liquid fuel is contained in a vessel. The material and the temperature of the vessel can play essential roles in the energy transfer to/from the liquid fuel. Therefore, highly controlled tests were planned by prescribing a constant temperature at the bottom of the pool. This bottom temperature was altered in the range of 0°C to 50°C as one of the test parameters. The vessel wall temperature was not controlled to avoid any interruption in the wall heat transfer. However, the other controllable test parameter was the vessel wall material that was specified as either copper, stainless steel or quartz. Finally, pool depth was changed to investigate the effects of this parameter on the variables of interest.

The meaningful quantities should be obtained with accurate experimental techniques that are affordable and practical for the problem of interest. The detailed description of the approaches used for the various measurements are given in the following sections. However, in short, the burning rate was measured from the fuel flow rate, the flame height was measured from the flame photography, different temperatures were measured by fine thermocouples, and the velocity field was determined by particle image velocimetry (PIV).

The measured quantities must be reported with their associated experimental uncertainty. The systematic (bias) errors were accounted for by the calibration of different measurement methods as explained for each individual method in the following sections. The ranges of measured values were also determined from the standard deviation of the data sample population and the methods presented in [176, 177].

3.2 Fuel

The fuel used in this study was methanol (methyl alcohol, CH_3OH) which under standard conditions (pressure of 101.325 kPa) has a flash point of 11°C and boiling point of 64.7°C [35]. Methanol was chosen as the fuel in this study due to its accessibility, cost, relatively low explosivity (compared to fuels such as gasoline) and low smoke production, which makes it a good option for laboratory-scale pool fire experiments. Besides, this fuel has been used in many pool fire studies such as [19-22], which means relatively more information about methanol pool fires can be found in the literature and makes this fuel an appealing alternative to other fuels.

At atmospheric pressure, the flames that are established above a methanol pool are translucent blue and emits low levels of thermal radiation compared to yellow soot-producing pool fires (*e.g.*, heptane) [21]. Therefore, small amount of radiative heat transfer from the flame to the liquid phase, especially when the pool is small (*e.g.*, the ones of interest in this study), allows it to be neglected [22], which can significantly simplify the pool fire heat transfer analysis presented later. A more comprehensive list of the properties of methanol can be found in Appendix A.

3.3 Burner

As the main component of the experimental apparatus, it was required to design and build a laboratory-scale burner that gave the capabilities of measuring the variables and controlling the test parameters. As it was planned to employ an optical diagnostic technique for measuring the velocity fields (*i.e.*, PIV) within the pool, the burner should provide some optical accessibility for flow visualization. Another design constraint was that the fuel inlet at the bottom of the pool should be at uniform temperature and with a uniform flow distribution to minimize the inlet flow effects on the thermal and flow structures within the liquid phase. Moreover, the burner bottom temperature and depth had to be controllable, and its side wall material had to be easily substitutable. Lastly, the design should be practical for manufacturing, affordable, safe and reliable for repetitive experiments.

Considering the aforementioned requirements, two burners, shown in Fig. 3.1, were designed by the author and built in the Mechanical Engineering Machine Shop, at the University of Alberta. The square and round burners are described in detail in this section, and their manufacturing drawings can be found in Appendix B.

Shown in Fig. 3.2a, the square pool had a width of 70 mm and a depth of 14 mm, and in Fig. 3.2b, the circular pool had an inner diameter of 90 mm with a depth of 12 mm. The coordinate system for the two pools associated with the presentation of results and data analysis are shown in Fig. 3.2. The axisymmetric geometry of the circular pool enabled the use of a 2D coordinate system [25-27]. It is important to note that the choice of coordinate system is only for convenience and does not affect the results or analysis presented in this study.

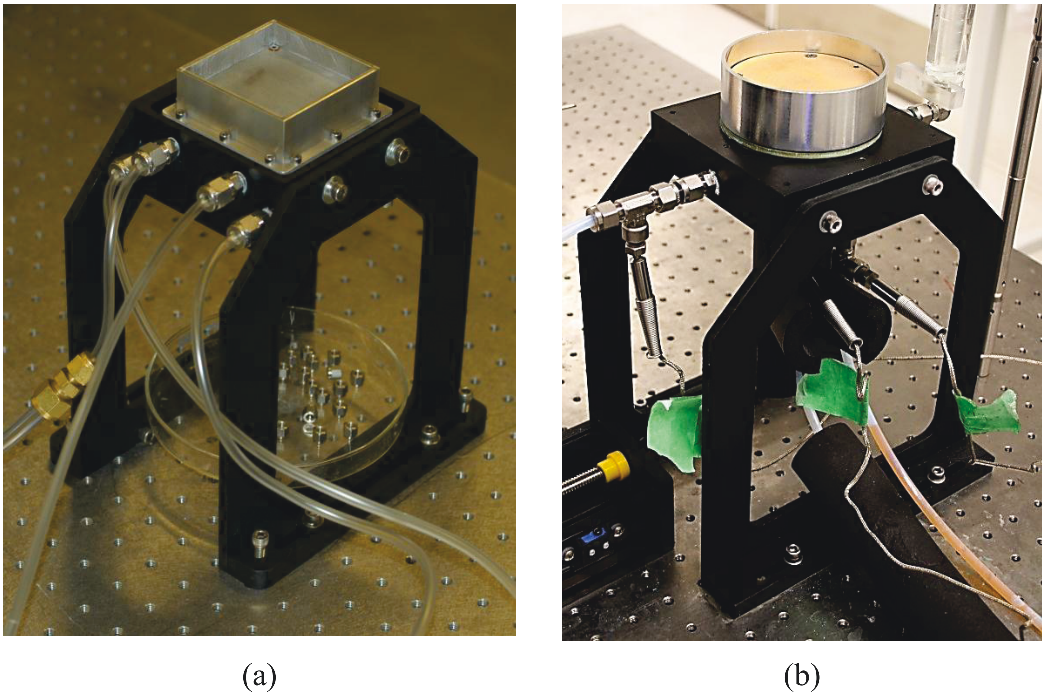

Fig. 3.1 (a) The square and (b) the circular burner

Exploded views of the square and round burners are shown in Fig. 3.3. The pools are essentially made of two main parts: the pool wall and its base. Such a structure for the burner made it possible to replace the wall material and height very easily and with minimum required modifications.

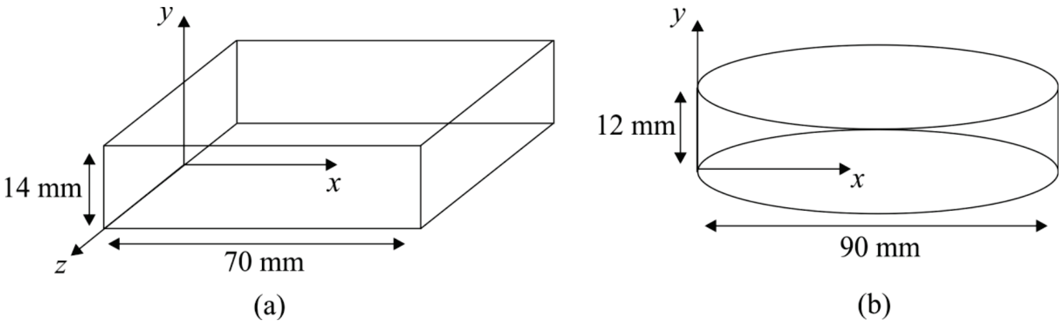

Fig. 3.2 Schematic diagram of the pool geometry, dimensions and the coordinate system for (a) square burner and (b) circular burner

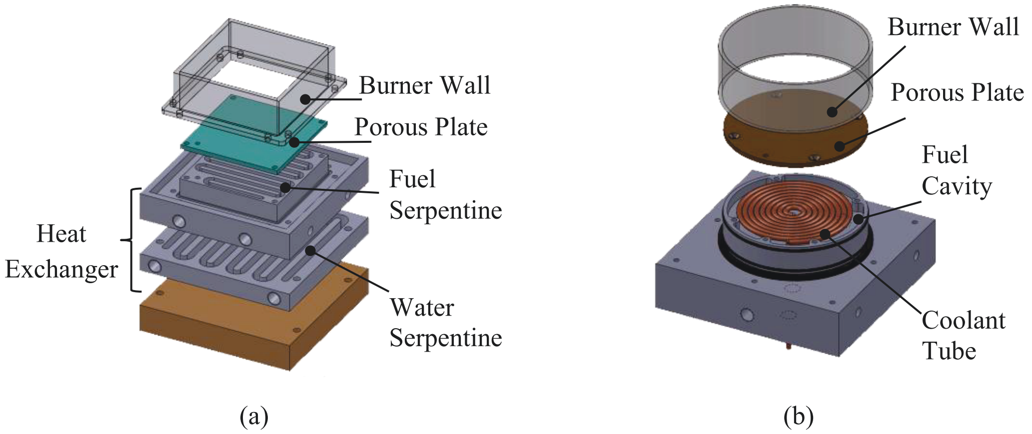

Fig. 3.3 Exploded views of (a) square and (b) circular burner

The confining walls were 2.5 mm thick for both burners and were subjected to the quiescent ambient at room temperature on their outer side. For the square pool, the wall was made of either quartz or aluminum, and the circular pool wall was made of copper, stainless steel, and quartz. The diversity of material was to investigate the effects of the wall thermal conductivity on the pool fire characteristics. The thermal conductivities of the materials used for the pool wall are tabulated in Table 3.1.

Table 3.1 Thermal conductivity of different wall materials

Material	Thermal Conductivity [W/(mK)]
Quartz	1.4
Stainless Steel (AISI 316)	13.4
Aluminum	237
Copper	401

The pool depth could be altered easily by changing the wall height. While the square pool had a constant depth of L = 14 mm (L is the pool depth), the quartz circular pool depth was changed from L = 12 mm to L = 6 mm and L = 18 mm by switching the wall with shorter and taller ones. From now on the circular quartz pools with different depths are denoted as shallow (L = 6 mm), medium (L = 12 mm), and deep (L = 18 mm). It should be noted that quartz was the only transparent material with optical accessibility for PIV. Also, only the quartz pool depth was changed, while for the cases of copper and stainless steel pools the depth was fixed at L = 12 mm.

The second main part of the burners was the base, which itself consisted of different components as illustrated in Fig. 3.3. In general, the base included a heat exchanger that was located under the pool to control the pool bottom temperature. The fuel in the pool was separated from this heat exchanger by a 3 mm thick porous plate. This porous plate was made of stainless steel (4 µm pore size, 1100-10-12-.125-2-A Sheet 316LSS, Mott Corperation) and bronze (10 µm pore size, SH6-8, Capstan California) for the square and circular pools respectively, and provided a uniform inlet fuel flow into the bottom of the pool.

For both burners, a cooling/heating fluid (referred to as the coolant, which was a 50% ethylene glycol 50% water solution) was circulated in the heat exchanger. Heat transferred from the liquid fuel and the bottom porous plate to the coolant when it was used to chill the fuel (the heat transfer direction would be opposite to heat the fuel). The coolant temperature was set by a water bath (Model 12111-21, Cole Parmer Canada Inc.) controllable between -10ºC and 50ºC.

The design of the heat exchanger was different in the square and circular pools as shown in Fig. 3.3. For square burner, the heat exchanger included two serpentine channels that were machined in an aluminum block. Either heated or chilled coolant was circulated through one of the heat exchanger's serpentines, while the fuel-side of the heat exchanger was a closed-end serpentine channel covered by the porous plate. The heat transfer between these two fluids occurred through the aluminum block which was in contact with the porous plate from the top. As a result, the temperature of both the fuel and pool bottom plate could be controlled. For the circular pool, the coolant was circulated in a flat spiral coil made of 6 mm diameter copper tube that passed through a cavity filled with liquid fuel beneath the porous plate. The spiral coil's top surface was also flattened and pushed against the porous plate underneath to establish a good thermal contact with the plate.

It should be noted that making two different burners was not intended in this study from the beginning. The first design was the square pool since its flat optical access made it more convenient for PIV. However, the difficulties of the square burner resulted in essential changes in the design. The main problem of the square burner was its requirement for custom-manufactured quartz walls that was expensive and could not be built on campus. The building and delivery of the quartz piece could take months. Also, the method that the quartz piece was joined to the base part put the quartz part at risk of breakage. The quartz wall in the square burner had to be bolted to the aluminum base. Due to the difference in the thermal expansions of these materials, the quartz piece was under tension (or contraction) especially at the location of the bolt holes where more stress was concentrated. Stress cracking of the square pool was problematic, and as a result there is a limited amount of data available for this burner, but it is included in this thesis as a point of comparison. Also, for the square pool, the lower part of the wall was in direct contact with the base (heat exchanger), which resulted in energy transport between the wall and the base. This phenomenon could affect the temperature distribution of the pool wall and consequently influence heat transfer from the wall to the liquid fuel.

The second burner (*i.e.*, the circular burner) was designed to eliminate the problems of the square pool. In the circular burner, the wall was made of a standard size quartz tube and was assembled on the top of the burner base without any bolted joints. The base diameter was 2 mm less than the inner diameter of the quartz tube and the pool was sealed by O-rings. There was also an air gap to prevent direct contact between the wall and the base, so the wall thermal structure was no longer specified at its lower edge (due to the wall and base contact in the square pool, the wall thermal structure was affected by altering the bottom temperature). Circular pools are also more common in pool fire studies. Due to its axisymmetric geometry, the problem is assumed two dimensional, which makes the future analysis much easier compared to the square pool. In summary, after preliminary but insightful work it was decided to stop the study on the square burner after building the circular pool. Consequently, most of the results and analysis presented here are associated to the circular pool.

3.4 Fuel Delivery System and Burning Rate Measurement

The fuel burning rate is the fuel mass that is consumed in the process of combustion per unit time. This quantity was measured with a fuel supply system that was designed to maintain a steady fuel level within the pool. Such a system is shown schematically in Fig. 3.4. The pool was kept full of liquid fuel to the top edge of the wall to eliminate any effects of ullage (*i.e.*, lip height effects) [22, 58, 165].

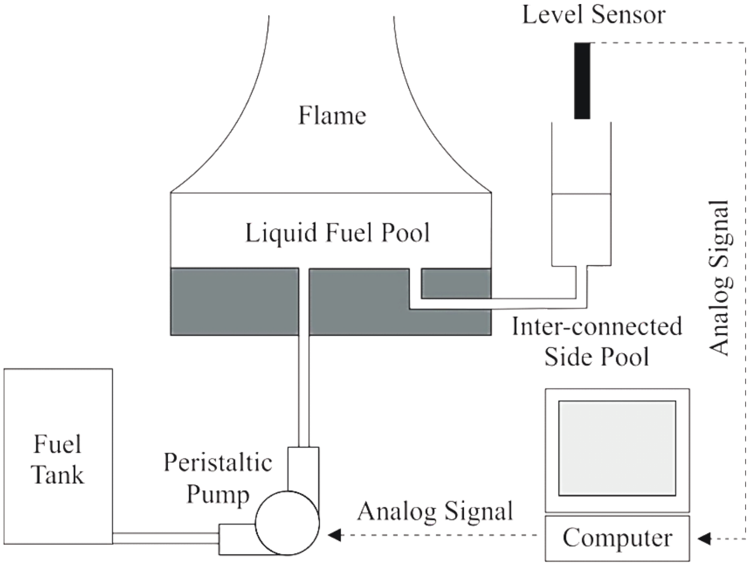

Fig. 3.4 Schematic diagram of the fuel delivery system

As shown in Fig. 3.4, the fuel delivery system took the methanol from an open atmospheric tank to the liquid pool, and it also consisted of a level sensor, a controller (shown as a computer in Fig. 3.4), and a pump. The ultrasonic level sensor (Model 098-10001, ML-101, Cosense Inc.) monitored the fuel level, l_l, with an accuracy of ±0.01 mm in a small (6 mm diameter) non-combusting, inter-connected shunt-pool located immediately adjacent to the main pool. Then, the fuel level readings were sent to a custom-designed software (LabWindows/CVI, National Instruments Corporation) controller every 0.01 s. The fuel level value was compared in the controller with the pool depth, L, since the pool must be filled with the liquid fuel to the top edge during the experiment. Finally, the peristaltic pump (MasterFlex L/S digital driver with Easy Load II head, Cole Parmer Canada Inc.) flow rate was set with an accuracy of ±0.01 ml/min accordingly to eliminate the difference between the pool depth and the fuel level. The pump flow rate was set by the controller as

$$\dot{V}_l(t+\Delta t) = \dot{V}_l(t) + \alpha(L - l_l(t+\Delta t)) \tag{3.1}$$

where $\dot{V}_l$ is the volumetric fuel flow rate to the pool and α is a constant coefficient found experimentally by tuning the controller to give a proper response to the fuel variations. Δt is the time interval of collecting a sample population of 10 fuel level data at 10 Hz. l_l is the mean value of this sample population that was used by the controller to update the pump flow rate. Analog voltage signals (conversion factor of 3 ml/min per volt) were sent from a computer controlled data acquisition system (miniLAB 1008^{TM}, Measurement Computing Corporation) to the pump every second to update the fuel flow rate.

Even with fuel level control, transient effects occur before steady state when the liquid pool was ignited. This stage was known as the warm-up (transient) period and was associated with the heat transfer to the liquid fuel and the pool to establish their steady thermal structures [58, 119]. While some researchers suggested that the pool fire could reach the steady-state burning rate in less than a minute [107] others proposed a relatively longer warm-up period of around 20 min [116]. Hamins et al. [20] reported that under constant-level conditions, the mass burning rate reached a nearly constant value after 10 min. Woods [178] found that the burning rate of a methanol pool fire of 0.3 m ×0.3 m ×0.01 m became independent from time after 200 s (*i.e.*, 3-4 min). The warm-up period must be related to the liquid volume in the pool as the larger liquid volume needs more time to be pre-heated. The largest fuel volume in this study belonged to the deep pool, which was one order of magnitude smaller than the one tested in [178]. However, here, the fuel flow rate transferred to the pool was recorded after 20 minutes following the pool ignition to ensure steady condition for burning rate.

Although the controller was intended to eliminate the discrepancies between the pool depth and the fuel level, for unclear reasons, the system could not achieve a constant pump flow rate after the transient period. The pump flow rate would fluctuate around a constant value however. The flow rate oscillations may be due to the flame pulsations [27] or instrument noise, which resulted in up to ±0.15 mm variation in the measured fuel level under steady-state conditions. Two minutes of typical variations in the steady-state pump flow rate and its associated level oscillation, $\varepsilon = L - l_l$, with respect to time are shown in Fig. 3.5. To eliminate the effects of these fluctuations, the burning rate was measured during a time period, τ, and the averaged pump flow rate was determined as:

$$\left\langle \dot{V}_l \right\rangle(\tau) = \int_0^{\tau} \dot{V}_l(t)\,dt \tag{3.2}$$

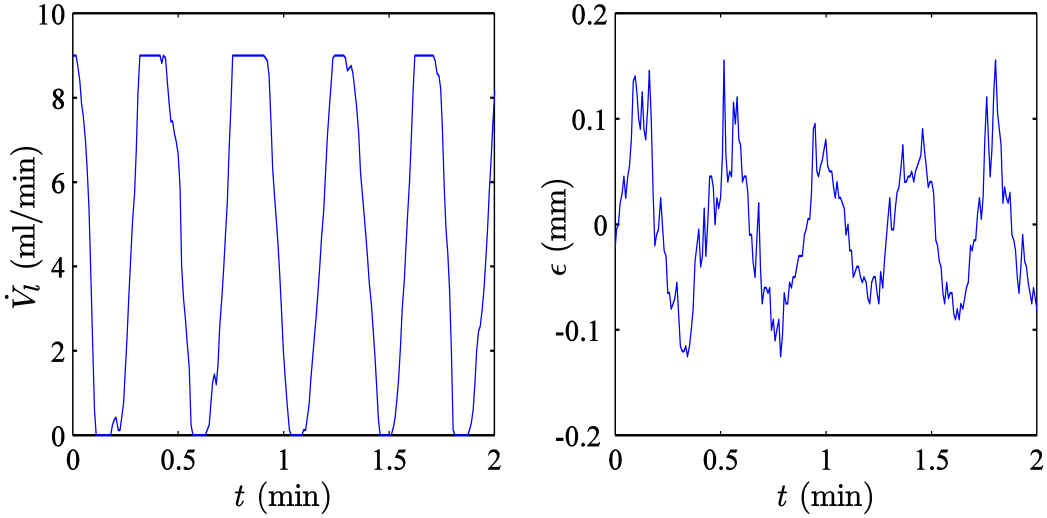

(a) (b)

Fig. 3.5 Two minutes of typical variations in (a) the pump flow rate and (b) the difference between the pool depth and the fuel level

To achieve temporally invariant burning rate values, the flow rate sampling was continued until the mean value, $\left\langle \dot{V}_l \right\rangle$, became independent from the sampling time, τ. The procedure included determining the average value of the entire flow rate sample population every 10 s during the data collection. Then, the data acquisition was carried on until the flow rate precision uncertainty (95%

confidence interval) [177] became less than 0.01 ml/min (*i.e.*, the accuracy of the pump). The variation of the averaged pump flow rate and its uncertainty with respect to time for a certain test (medium circular quartz pool) are shown in Fig. 3.6. After determining the averaged pump flow rate independent from sampling time, the fuel burning rate was determined as

$$\dot{m}_b = \rho_l \left\langle \dot{V}_l \right\rangle \tag{3.3}$$

where ρ_l is the liquid methanol density in room temperature (fuel tank is at room temperature). The mass burning rate in this study is expressed per unit area of the pool, $\dot{m}_b''$, (mass loss flux) in g/(m^{2}s).

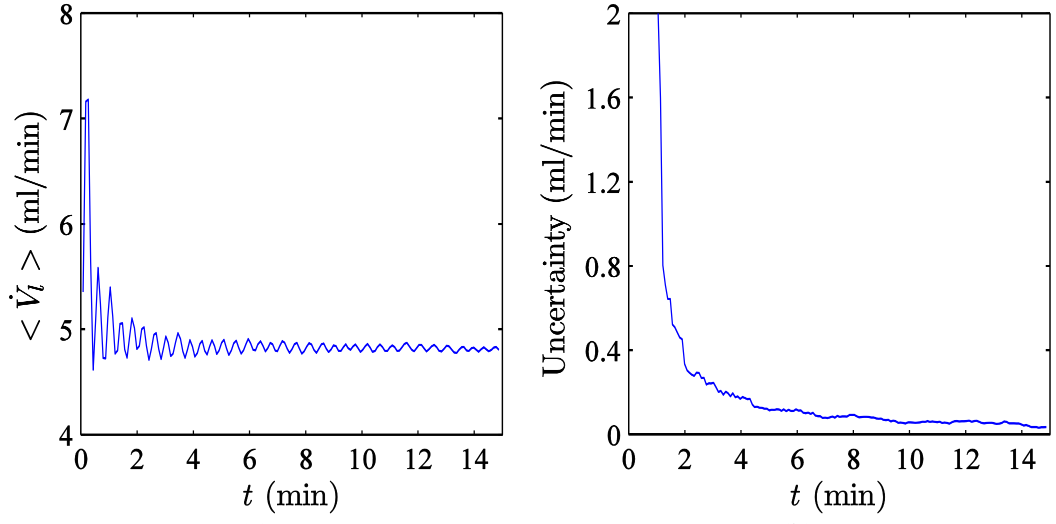

(a) (b)

Fig. 3.6 (a) The averaged pump flow rate and (b) its associated uncertainty with respect to time

The burning rate measurement setup was calibrated according to the pump manufacturer's instructions to eliminate the bias (systematic) error before collecting data. A volume of the fuel was collected in a graduated cylinder (with accuracy of 0.01 ml) in a known time period set internally by the device and the value was given to the pump in its calibration menu.

It should also be mentioned that while a slight fuel level fluctuation was inevitable in burning rate measurements, it was possible to narrow the range of oscillation in the controller software. This was done during the measurements of the other variables (*e.g.*, temperature and velocity) to eliminate the potential unsteadiness in those variables due to the flow rate variations. In other words, after measuring the burning rate under different test conditions with full range of flow rate variation (*i.e.*, 0-9 ml/min), the flow rate fluctuations were limited by decreasing the range for flow rate to the mean flow rate for that specific condition ±0.25 ml/min. Therefore, the flow rate remained almost constant during the tests and its fluctuation effects on the other variables could be ignored.

3.5 Flame Imaging and Flame Height Measurement

The flame height was measured from flame photography. For each test condition, 120 images were taken from the flame spaced 5 s apart by an 8-megapixel CCD camera (EOS 20D, 28-105 mm lens, Canon Inc.). The camera was positioned horizontally and normal to the flame in a darkened laboratory against a black background. The camera settings were: ISO 1600, aperture at F#=5.6 and shutter speed of 1/4 s.

The captured photographs of the flame were then processed individually according to the steps illustrated in Fig. 3.7. The flame images were converted into gray-scaled format. Then, they became binary (black and white) depending on the grey-scaled pixel value (intensity) and a threshold of 10% of the intensity of the white color. The flame height was determined from the black and white flame images as the distance above the rim of the pool to the tip of the visible flame. The tip of the flame in these images was located at a maximum vertical position with white color. The threshold criterion of 10% was arrived at by manual inspection of collected images to give the least error in estimating a visual length of the flame.

Due to unsteadiness (flame pulsation), the range of visible flame height values was broad in a sample population associated with a specific test condition. Therefore, the flame height, l_f, was determined as a statistical measure of the height that flame occurrences in the ensemble of images were greater than that 50% of the time [94]. The elevations that visible flames were maintained above them in 10% and 90% of the time were also recorded for a more comprehensive result presentation. These flame heights are illustrated schematically in Fig. 3.8 for comparison.

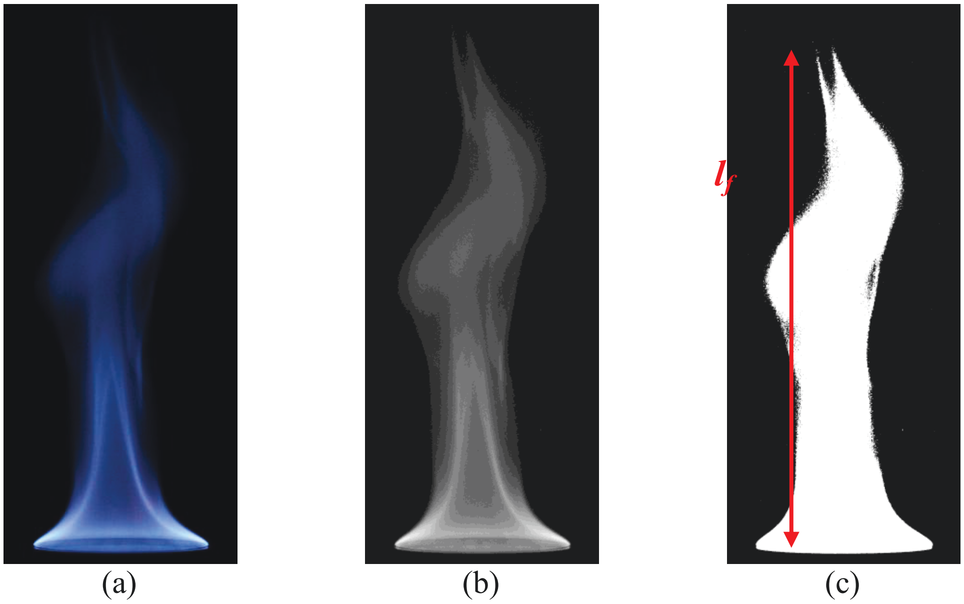

(a) (b) (c)

Fig. 3.7 Flame image processing steps: (a) original, (b) gray-scaled, and (c) black and white (based on the threshold of 10%) flame photos

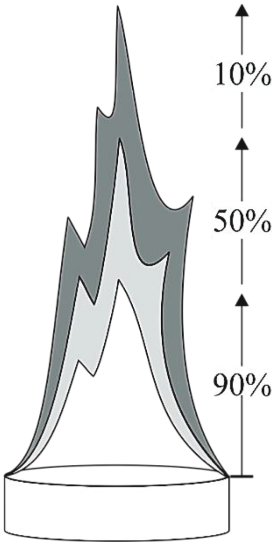

Fig. 3.8 Schematic diagram of the flame height definitions

3.6 Temperature Measurement

A schematic diagram of the setup used for the liquid temperature measurement is shown in Fig. 3.9. The temperature within the liquid fuel was measured with a Type-K thermocouple probe (TSS series, Omega Engineering Inc.) with an exposed 0.25 mm junction. This thermocouple was traversed by a 2-axis motorized stage (UniSlide model, Velmex Inc.) to measure 2D temperature distributions across the central cross-sectional plane from the pool wall to the center. The thermocouple motion within the liquid pool was controlled with a pair of stepper motors with a resolution of 0.005 mm/step.

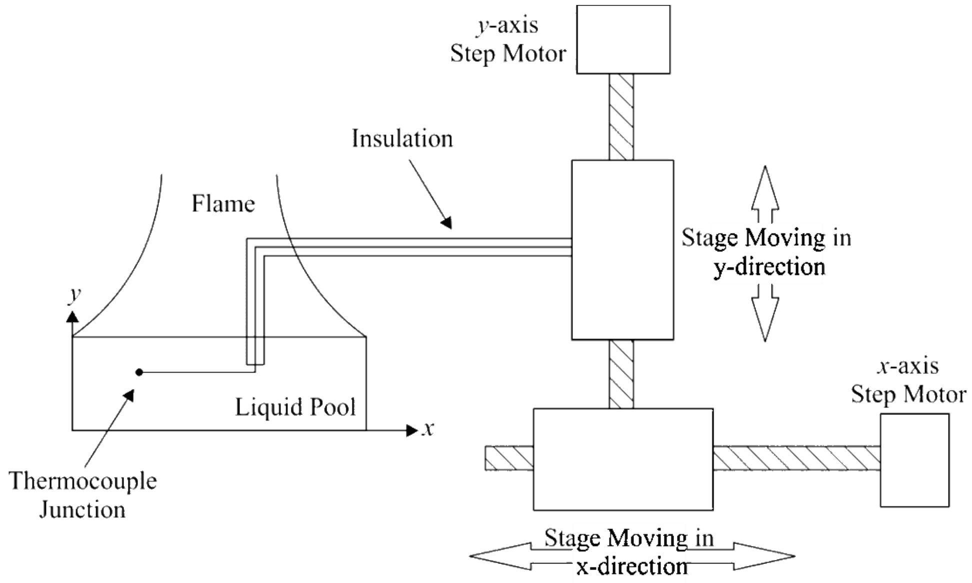

Fig. 3.9 Schematic diagram of the setup used for the liquid temperature measurement

The liquid temperature maps were measured in a marching pattern starting at $(x,y) = (0,0)$. One hundred temperature samples were recorded at each point after pausing 10 s to allow the thermocouple junction to reach the same temperature as the liquid local temperature (thermocouple response is less than 1 s). The data samples were collected using a computer controlled data acquisition system (Model NI 9219, National Instruments Corporation) at 10 Hz. To avoid heat conduction along the thermocouple probe and the associated uncertainty in the temperature readings, the probe was insulated and shaped in a way, as shown in Fig. 3.9, that the last 35 mm of its length was positioned at the same depth within the liquid pool. The temperature gradient in the *x*-direction was found to be insignificant with respect to affecting junction temperature in the preliminary observations.

The measurement grid pattern was similar to the one shown in Fig. 3.10 for the medium circular pool (the coordinate system was according to Fig. 3.2b). The temperature was measured every 1 mm and 1.5 mm in vertical and horizontal directions, respectively. To obtain higher resolution results, the spatial resolution in the vertical direction was increased within the 5 mm below the fuel surface. In this region it was expected that more profound transport phenomena would occur, so data was collected every 0.5 mm in the *y*-direction.

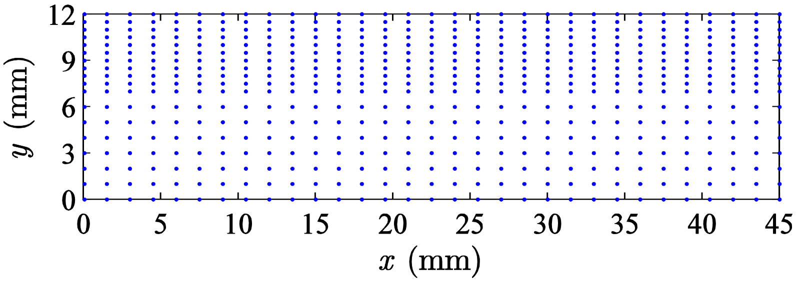

Fig. 3.10 Locations of temperature measurements within the medium circular pool

The steady-state liquid thermal structures were measured after a transient warm-up period. Hamins et al. [20] showed that although the mass burning rate could be considered constant 10 min after ignition for a 0.15 m deep pool with a 0.3 m diameter, the temperature inside the liquid was still changing. According to their results, the liquid was not thermally stabilized even 40 min after the ignition.

Before starting the data collection under steady-state conditions, an appropriate estimation transient time was required. It is important to note that the transient period is related to the energy required for preheating the liquid, which is essentially a function of the liquid volume and initial temperature at ignition moment. Therefore, the temperature was measured at several locations within the deep (18 mm) pool with a bottom temperature associated with the lowest bath temperature (*i.e.*, -10ºC). These preliminary data sets are illustrated in Fig. 3.11. According to Fig. 3.11, in this particular case that gave the maximum transient time for the cases of interest, the liquid temperature became essentially time-independent 20 min after ignition. As a result, to secure the steady condition, the thermocouple marching within the pool began 30 min after pool ignition. It should also be noted that collecting a full 2D map data set takes several hours (*e.g.*, four hours for the deep pool).

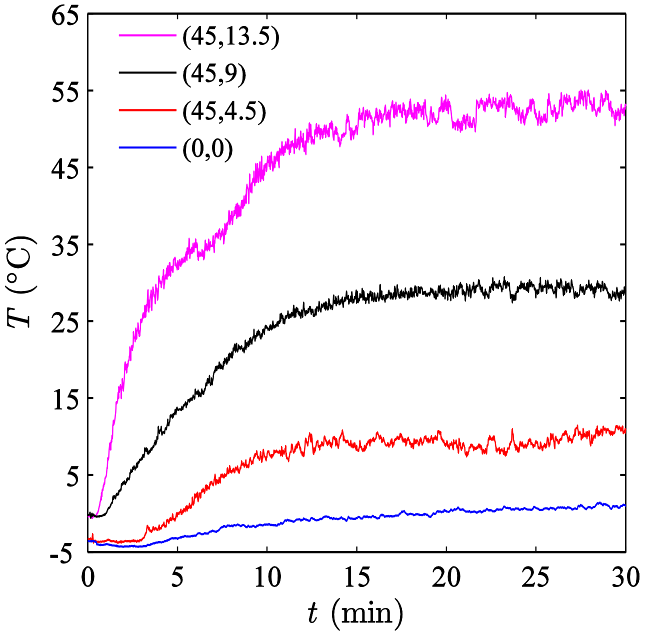

Fig. 3.11 Temperature variations with respect to time immediately after pool ignition measured at different locations within the liquid fuel; the numbers in the legend are the coordinate where the temperature was measured with respect to time

The temperature along the wall at different vertical positions was measured with a series of 12 Type-K fine wire thermocouples with 0.25 mm exposed junction. The thermocouples were placed in 2 mm deep holes in the wall (*i.e.*, 0.5 mm away from the inner surface) and 1 mm apart from each other in the vertical direction as shown in Fig. 3.12. It is apparent in Fig. 3.12 that the thermocouple holes in the pool wall were located at different azimuthal positions to avoid affecting the axisymmetric characteristic of the circular pool. This arrangement was also due to manufacturing convenience especially for the quartz pool.

The wall temperature data was collected by using a data acquisition system (Model SCXI-1000, National Instruments Corporation) at 10 Hz for 30 min from the pool ignition moment. Therefore, the transient variations of the wall temperature distributions were recorded in addition to the steady-state profiles. The stabilized wall temperature was determined by averaging over the last 10 min after reaching a constant value, which occurred in less than 10 min (the transient results are presented in Sec. 3.6).

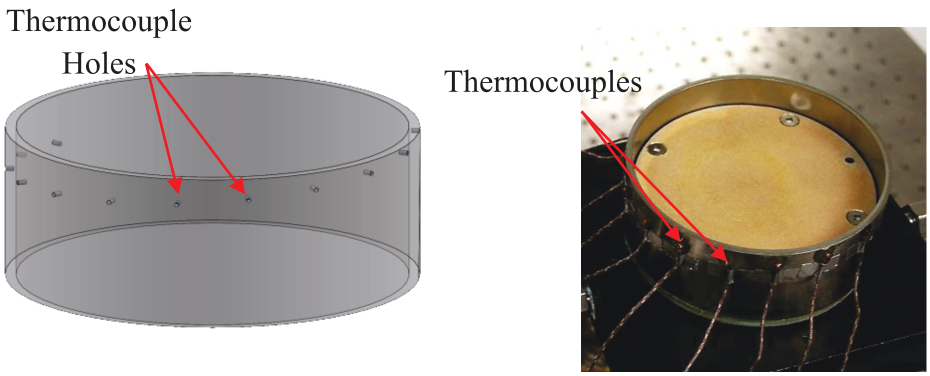

(a) (b)

Fig. 3.12 Thermocouple locations for the wall temperature measurements shown on (a) 3D model and (b) the burner with inserted thermocouples

The temperature measurement system including the thermocouples and their assigned data acquisition card channels were calibrated against water bath temperatures. The thermocouples were immersed in the bath maintained at a known temperature over the range of 0ºC to 65ºC and their readings were collected with the same measurement system. Then the calibration curves (*i.e.*, bath temperature versus measured temperature) were used to correct the collected data.

3.7 Velocity Measurement

The velocity field within the liquid fuel was determined by particle image velocimetry (PIV). This technique involves measuring the velocity of particles that are seeded in the liquid pool and move with the fluid. It is assumed that the particles exactly follow the flow motion [179]. In summary, in PIV, the fluid is seeded with particles and a light sheet is generated by an illumination source across the region of the fluid which is of interest. Then, the particles reflect light when they pass through this light sheet, and the reflected light is collected with a camera sensor. The displacement of the particles is determined from image processing of a pair of successive particle images and eventually knowing the time difference between those images the particle velocity is determined [180, 181].

The particles for PIV should be small enough to follow the fluid motion and large enough to scatter sufficient light to be detectable by the camera sensor. The density of the particles also should be near the fluid density [180]. In this study, the liquid fuel in the pool was seeded with 10 μm hollow glass sphere particles. The specific gravity of the particles was 1.1, which was slightly greater than the specific gravity of methanol, ~0.8. This difference in density was necessary to prevent particle accumulation on the pool surface due to the slow bulk motion of the methanol toward the liquid surface. The fuel was supplied to the pool from the bottom to maintain the liquid level in the pool.

As mentioned previously, PIV assumes that the fluid and particles motions are identical. This assumption must be evaluated by estimating the particles' "relaxation time" [180]. This is the time required for a particle to adjust its velocity to a new condition within the fluid (also known as particle lag). The particle (tracer) relaxation time, τ_t (s), can be determined as [180]:

$$\tau_t = d_t^2 \frac{\rho_t}{18 \mu_l} \tag{3.4}$$

where d_t(m) and ρ_t (kg/m^3) is the particle (tracer) diameter and density, respectively, and μ_l (Pa.s) is the liquid viscosity. The particles relaxation time was estimated as 1.1×10^{-5} s. This very small response time of the tracer particles allows them to follow the fluid motion.

The influence of the gravitational forces due to the difference between the liquid and particles density can be assessed from the particles settling velocity as:

$$U_g = d_t^2 \frac{(\rho_t - \rho_l)}{18\,\mu_l} g \tag{3.5}$$

where ρ_l (kg/m^3) is the liquid density and g (m^2/s) is the gravitational acceleration. The settling velocity of the particles was ~20 μm/s, which was on order of the typical liquid bulk motion from the bottom to the surface (~12.5 μm/s).

The PIV setup used in this study is illustrated in Fig. 3.13. The light sheet was produced by a scanning system composed of two mirrors of which one was fluctuating at 500 Hz and distributing the laser beam (LRS-0532-TF, 1.6 W, 532 nm, Laserglow Technologies) to illuminate the central cross-sectional plane within the pool. A lens located at its focal length from the fluctuating mirror was used to make a parallel and uniform light sheet that passed through the pool's center. A time series of 500 particle images were collected at 100 fps by a 1024×1024 pixel CMOS high speed camera (MV-D1024E-160, Photon Focus) equipped with an SLR camera lens (65 mm, F#=11, Nikon).

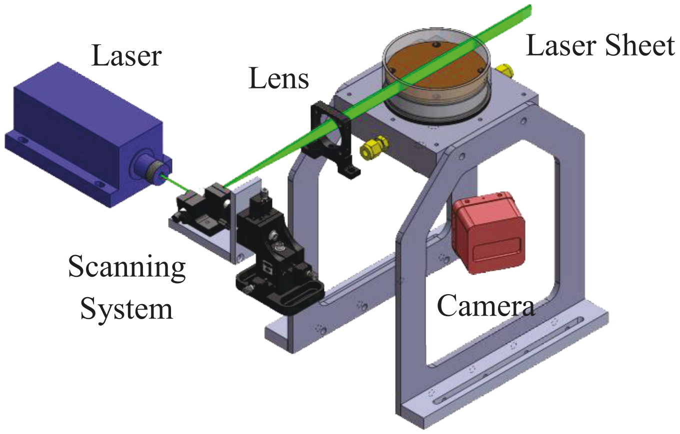

Fig. 3.13 PIV setup configuration

The field-of-view (FOV) for velocity measurements was 30 mm wide and as deep as the pool depth adjacent to the wall where the strongest fluid motion was expected due to the wall heat transfer. The strong image distortion of the circular pool resulted in a large uncertainty in the velocity measurements toward the pool's center. Therefore, the width of the FOV was restricted to the first 1/3 of the pool diameter as a tradeoff over having a large FOV from the wall to the center of the pool in order to reduce the results' uncertainty.

To consider the effects of the pool curvature on the images, the velocity measurements were corrected for image distortion. A custom-designed 2D calibration target was placed within the pool and aligned with the laser sheet location. The target was a 2D array of circular dots of known diameter (0.5 mm) located 1.5 mm apart from each other. The target images were processed using commercial software (DaVis 8.0.6, La Vision GmbH) and an algorithm detected the dots in the target images. Knowing the size and the distance of the dots, a third-order polynomial mapping function was calculated to de-warp the images. The root-mean-square error of the mapping function calculated from the imaged dots was 0.29 pixel was acceptable according to the software manual [181]. The location of the particles within the pool was determined on average by ±0.29 pixel which is equivalent to ±0.015 mm uncertainty in the particle location.

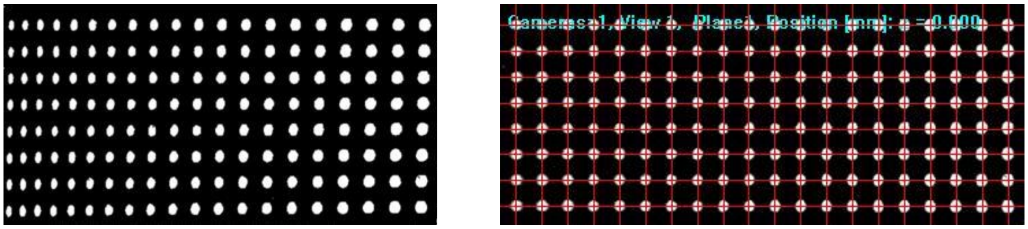

(a) (b)

Fig. 3.14 (a) Actual image compared to (b) de-warped image of the calibration target

The collected particle images were processed and the velocity vector fields were calculated using commercial software (DaVis 8.0.6, La Vision GmbH). Different stages of the image processing and PIV vector calculation are shown in Fig. 3.15. Prior to the velocity calculation, the images were de-warped according to the mapping function obtained from the calibration procedure. Then, they were pre-processed to improve the contrast between the light particles and the dark background. It was performed by subtracting the background light and sharpening the particle edges as shown in Fig. 3.15b. As a wide range of velocity scales was obtained in the preliminary observations (from near zero to up to 25 mm/s) especially near the wall, a multi-pass processing scheme was used. This method, first, calculated the instantaneous velocity vectors using a 32×32 pixel interrogation window with 50% overlapping. Then, the accuracy of the results was improved by refining the interrogation window size to a 12×12 pixel and window overlapping to 75%. Lastly, the mean velocity field was calculated from the averaging of 500 instantaneous vector fields.

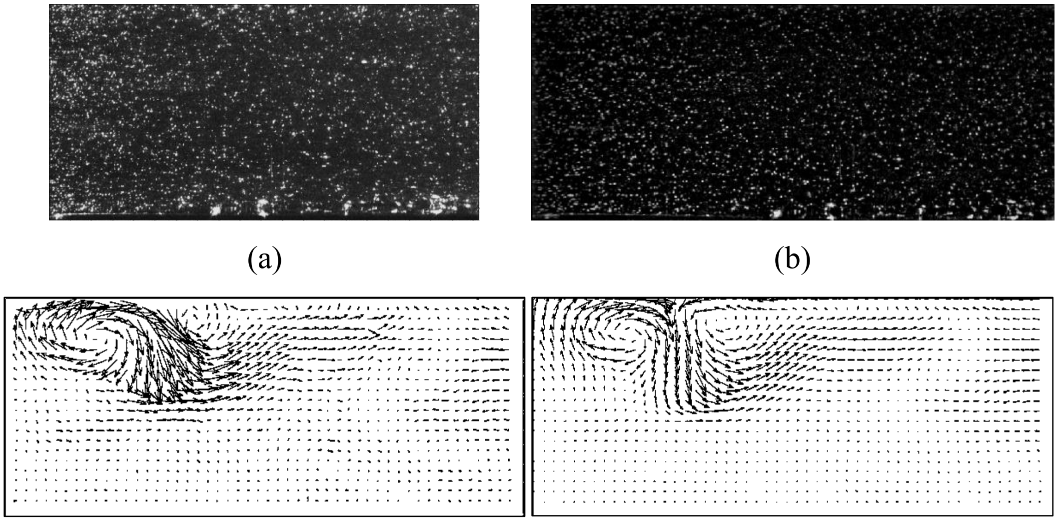

(a) (b)

(c) (d)

Fig. 3.15 PIV processing steps: (a) original image of particles within the liquid pool, (b) de-warped and pre-processed image, (c) instantaneous velocity vector field, and (d) averaged velocity vector field over 500 images

4. Experimental Results: Presentations and Discussions

4.1 Overview

The steady burning of a methanol pool fire was examined at different liquid bottom boundary temperatures under quiescent ambient condition. The tests were conducted in pools of different materials and depth when the fuel level was maintained at the pool rim during the data collection period. The methanol pool fire burning rate, flame height, wall and liquid temperature distributions, and mean velocity field within the liquid phase corresponding to each test condition were recorded and are presented here.

In measuring different characteristics of the pool fire, one of the test parameters was the liquid boundary temperature at the bottom of the pool, T_{bot}. The bath temperature, T_{bath}, was set from -10ºC to 50ºC in order to give a wide range of pool bottom temperatures through which the effects of T_{bot} could be investigated. However, the fuel temperature at the bottom of the pool was not the same as the bath temperature due to the heat loss/gain to the surroundings and the heat feedback from the flame to the liquid pool. Two cases of non-burning and burning pools are compared for the same bath temperature of 20ºC in Fig. 4.1. As shown without flame the bottom temperature is close to the bath temperature (difference less than 0.5ºC) and with flame there is a 3ºC temperature rise at the bottom of the pool. Also, the local bottom temperature is not constant throughout the bottom surface and typically increases 3-4ºC radially within the last 5 mm near the wall (located at $x = 0$ mm) from the pool center (located at $x = 45$ mm). Also, it should be noted that the tubes were not in contact with the porous plate at the bottom of the pool throughout the whole bottom surface area, and as it is apparent in Fig. 4.1 for the burning pool, the temperature increased 2-3ºC at the center. The temperature drop from 10 mm to 35 mm was due to the presence of tubes in contact with the bottom plate. The temperatures at the bottom of the pool were measured at different radial positions and a representative bottom temperature, T_{bot}, was found by area-averaging.

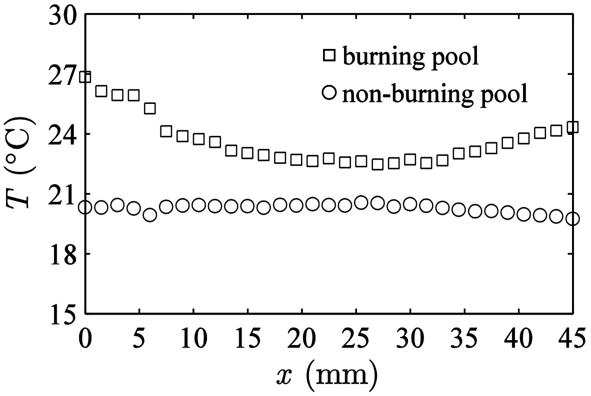

Fig. 4.1 Radial variation of liquid temperature at the bottom of the circular quartz pool when the water bath was set at T_{bath} =20ºC; pool wall and center are at $x = 0$ and 45 mm, respectively

It can be concluded from Fig. 4.1 that the temperature at the bottom of the pool may be related to the heat transfer to the liquid layer and the bottom plate from the flame. Shown later in this study, Chapter 5, the heat transfer to the liquid phase is not the same in different pools. Thus, for prescribed bath temperatures, T_{bath}, the area-averaged bottom temperatures, T_{bot}, of the square pool are listed in Table 4.1.

Table 4.1 Pools T_{bot} that resulted from setting the bath temperature for square pools of different materials

case	T_{bath}	T_{bot}	
		Quartz	Aluminum
1	10ºC	16ºC	20ºC
2	20ºC	24ºC	29ºC
3	40ºC	38ºC	42ºC

The T_{bot} that resulted from different bath temperatures for the circular pool test cases are presented in Table 4.2 for different pool materials (*i.e.*, copper, stainless steel and quartz) and in Table 4.3 for quartz pools of different depth (*i.e.*, shallow: L = 6 mm, medium: L = 12 mm, and deep: L = 18 mm). The information presented in Table 4.1, Table 4.2, and Table 4.3 is used for the result presentations in this chapter.

Table 4.2 Pools T_{bot} that resulted from setting the bath temperature for circular pools of different materials

case	T_{bath}	T_{bot}		
		Copper	SS	Quartz
1	-10ºC	5.8ºC	2.3ºC	-0.9ºC
2	0ºC	13.5ºC	9.9ºC	7.3ºC
3	10ºC	20.8ºC	18.2ºC	14.3ºC
4	20ºC	27.8ºC	25.3ºC	22.8ºC
5	30ºC	34.8ºC	32.6ºC	30.5ºC
6	40ºC	42.8ºC	41ºC	39.1ºC
7	50ºC	50.4ºC	48.6ºC	47.5ºC

Table 4.3 Pools T_{bot} that resulted from setting the bath temperature for circular quartz pools of different depth

case	T_{bath}	T_{bot}		
		Shallow	Medium	Deep
1	-10ºC	4ºC	-0.9ºC	-4ºC
2	0ºC	11.9ºC	7.3ºC	4.3ºC
3	10ºC	19.6ºC	14.3ºC	12.3ºC
4	20ºC	27.7ºC	22.8ºC	20.6ºC
5	30ºC	34.7ºC	30.5ºC	29.3ºC
6	40ºC	43.3ºC	40.1ºC	37.7ºC
7	50ºC	50.1ºC	47.5ºC	46.8ºC

4.2 Burning Rate

The fuel mass loss rate per unit area of the pool or mass flux (burning rate), $\dot{m}''_b$, of the square pool with respect to the bottom boundary temperature for two side wall materials of quartz and aluminum is shown in Fig. 4.2. The burning rate of the aluminum pool is less than the quartz pool at lower bottom boundary temperatures then rising to 10% more than the quartz pool burning rate at higher bottom temperatures.

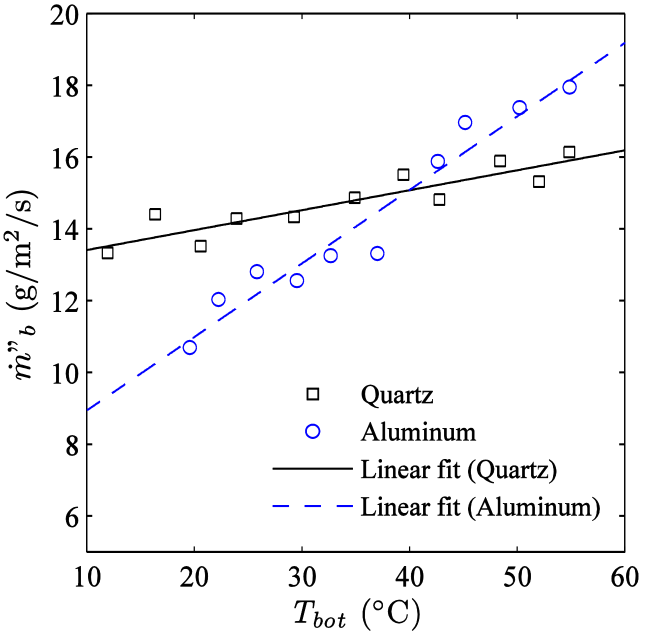

Fig. 4.2 Methanol burning rates in aluminum and quartz square pools as a function of bottom boundary temperature

The relationships between burning rate, $\dot{m}''_b$, of the circular pool and the imposed pool bottom temperature, T_{bot}, for different wall materials namely copper, stainless steel and quartz are shown in Fig. 4.3. For any prescribed T_{bot} the $\dot{m}''_b$ increases with decreasing wall thermal conductivity (*i.e.*, from copper to quartz). This result is counterintuitive as walls with higher thermal conductivity would be expected to transfer more energy from hot products to the liquid (the reason for this outcome is discussed in Sec. 4.5).

Fig. 4.4 shows the mass flux of the circular pool with different depths of L = 6 mm, L = 12 mm, and L = 18 mm as functions of pool bottom temperature. It is shown in Fig. 4.4 that the methanol mass flux increases with the pool depth at any specific bottom temperature. As explained in Sec. 3.4, the uncertainty (95%

confidence interval) in the mass loss rate, $\dot{m}_b$, is around ±0.2 mg/s which is equivalent to ±0.03 g/(m^2s) uncertainty in the burning rate, $\dot{m}_b''$. This uncertainty is essentially smaller than the symbol size, so it is neglected in Fig. 4.2, Fig. 4.3, and Fig. 4.4.

From Fig. 4.2, Fig. 4.3, and Fig. 4.4, it is apparent that the burning rate, $\dot{m}_b''$, increases with increasing pool bottom temperature, T_{bot}. The fitted lines to the experimental data depict that the increases in the burning rate with bottom boundary temperatures are essentially linear over the range of boundary temperatures studied. Given the connection between the rate that energy is made available for evaporating the fuel and the burning rate, these results are intuitive. When the inlet fuel temperature is raised then less of the energy that arrives at the pool by various means of heat transfer is needed to raise the fuel's temperature to the liquid surface temperature, and hence more is available for evaporating the fuel and the burning rate will be higher. The linearity of the burning rate with the base temperature then may be explained by assuming a constant specific heat capacity for the liquid fuel within the temperature range considered here.

The dependency of $\dot{m}_b''$ on T_{bot} however is not the same for different pools. It is apparent in Fig. 4.3 that the methanol $\dot{m}_b''$ increases by 70% as the base is heated from 20°C to 55°C while the quartz pool $\dot{m}_b''$ increases only by 20% for changing the T_{bot} from 11°C to 55°C. Moreover, in Fig. 4.4, $\dot{m}_b''$ increases by 25%, 18%, and 13% for copper, stainless steel, and quartz pools, respectively from 0°C to 50°C and as the pool becomes shallower the mass flux gets more sensitive to bottom temperature variations (*i.e.*, 20% versus 4% increase in $\dot{m}_b''$ for shallow vs deep pool). The trends can be explained by having a good understanding of heat transfer within the liquid fuel and between the liquid fuel and the pool wall.

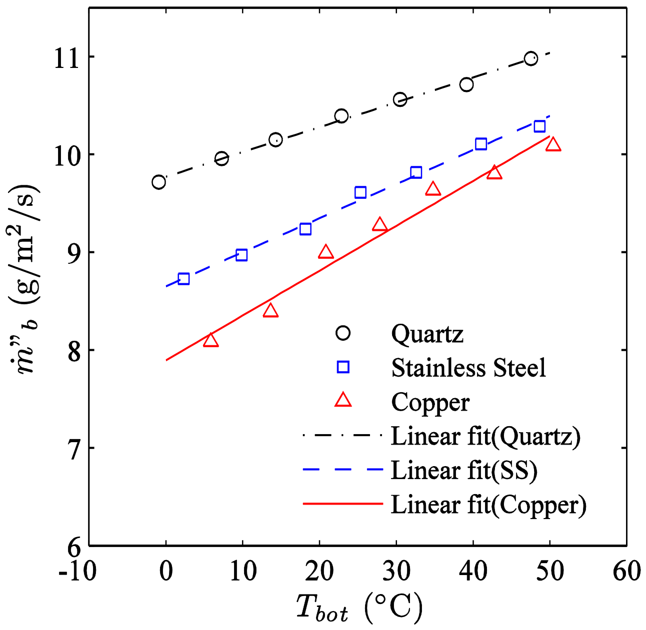

Fig. 4.3 Mass burning rate of methanol pool fire with respect to the bottom boundary temperature and different pool wall materials

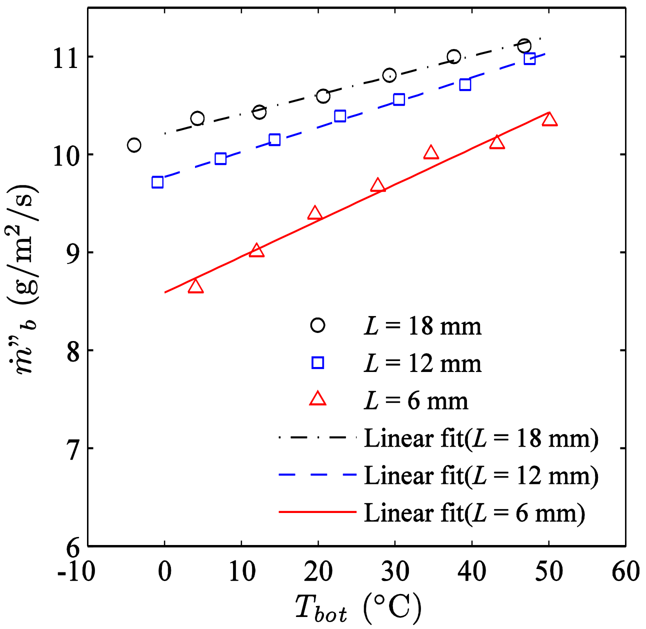

Fig. 4.4 Mass burning rate of methanol pool fire with respect to the bottom boundary temperature and different pool depth

It can be seen from a comparison between Fig. 4.2 and Fig. 4.3 that slightly different results were obtained for the square versus the round pool by altering the pool wall materials. While the line of mass flux vs. T_{bot} for the aluminum vessel crossed the trend line of quartz pool in Fig. 4.2, the copper pool $\dot{m}''_b$ is always lower than the $\dot{m}''_b$ of the quartz pool over the range of 0°C < T_{bot} < 50°C. This result could be due to the differences in the burner designs that would affect the heat transfer from the wall to the liquid layer. Besides the difference in geometry, the base of the square pool was in direct contact with the lower part of the pool wall. This can affect the heat transfer from the vessel wall to the liquid fuel that is one of the most important pathways for the size of the pools considered in this study. The wall was separated from the base by O-rings and an air gap in the circular pools.

The burning rate of the flammable liquids has been measured and reported in the literature since the 1950s. Wide ranges of fuels (*i.e.*, hydrocarbon liquids and alcohols) and pool sizes were considered to expand the experimental data. Among the fuels, methanol was very common probably due to its clean flame that generates a low level of smoke, ease of use and availability. Methanol mass burning rate, $\dot{m}''_b$, as a function of pool diameter, *d*, from some of the experimental studies (as indicated in the figure legend) is presented in Fig. 4.5. The measured burning rates from the current study on the square and circular pools are also included for comparison. It should be noted that for the square pool, the equivalent diameter calculated as $2W/\pi^{1/2}$ (W is the width of the pool) was used in Fig. 4.5.

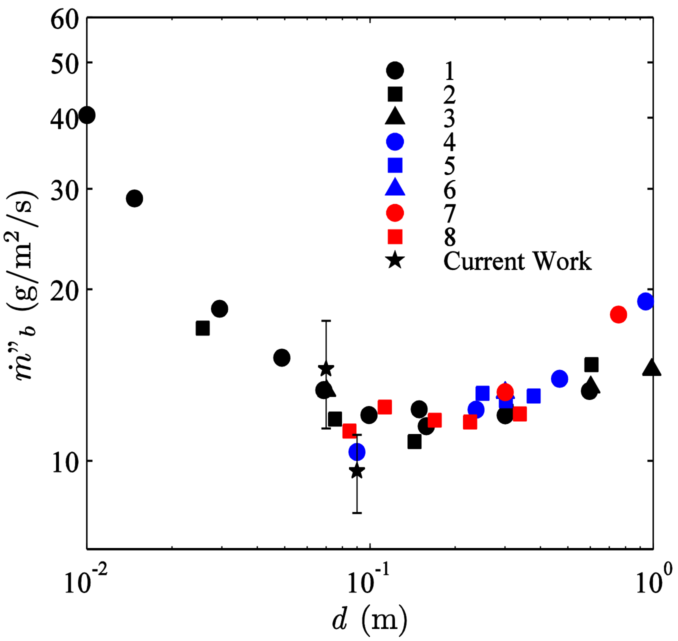

Fig. 4.5 Methanol mass burning rate as a function of pool diameter in comparison with the data from the literature; the numbers in the legend are the reference associated with the data: 1: [19], 2: [104], 3: [113], 4: [103], 5: [109], 6: [108], 7: [101], and 8: [114] .

In previous studies, pool fires were commonly described by only the pool diameter and the fuel type. Therefore, for a methanol pool with a diameter of 90 mm (*i.e.*, circular pool) only one value was reported in the literature regardless of its variations with the test parameters (*i.e.*, wall materials and liquid-side boundary conditions) used in this study. The range of the burning rate measured in the present work was indicated by the range bars plotted with the data. As it is apparent in Fig. 4.5, the experimental results are in good agreement with the data from the literature.

This figure also can elucidate why even after normalizing the burning rate, $\dot{m}''_b$ of the square quartz pool was larger than that for the circular quartz pool. As explained in Sec. 2.4 (Fig. 2.9), when the heat transfer from the pool wall to the liquid fuel is important, mass flux, $\dot{m}''_b$,decreases with the pool diameter increasing. That is, the mass flux itself is inherently a function of the pool diameter. The square pool characteristic diameter ($2W/\pi^{1/2}$) is smaller than the circular pool diameter.

4.3 Flame Height

The visible flame height was measured from the flame images. When methanol pool is burning, the produced flame is translucent blue and is hard to observe in natural light. Therefore, the flame images were taken in a darkened lab and against a black background to reduce the unwanted light. A series of typical successive photographs of the flame in the circular pool acquired under this condition is shown in Fig. 4.6. It should be noted that these photos were taken every 5 seconds.

As described in Sec. 2.3.1, the visible fire includes the persistent flame zone and the intermittent zone [60]. The conical region above the fuel surface is the persistent flame zone which can be distinguished by the bright boundary which is the location of the flame sheet (where the combustion is the most probable). It can be seen that the flame is very bright at the base at the pool rim where it is expected that combustion mostly occurs [61]. Above this conical flame zone that maintains its structure is the intermittent zone which is fluctuating as a result of large-scale toroidal vortices that form around the base of the flame and move upward [82, 83] as described in Sec. 2.3.1.

In every flame photograph the flame height was determined from the pool rim to the tip of the visible flame. The results from 120 images of the flame were statistically analyzed to find the height that the flame maintains in at least half of the images. For the remainder of this chapter, this value is referred to as the flame height, l_f.

The flame height, l_f, variations with respect to the bottom boundary temperature, T_{bot}, for different pool materials and for different pool depths are illustrated in Fig. 4.7 and Fig. 4.8, respectively. The flame height is expected to be strongly coupled with the fuel burning rate. Therefore, as it is apparent in Fig. 4.7 and Fig. 4.8, the flame height, l_f, increases with the bottom temperature, T_{bot}, and for a prescribed T_{bot} the flame becomes taller as the pool gets deeper and the wall thermal conductivity deceases.

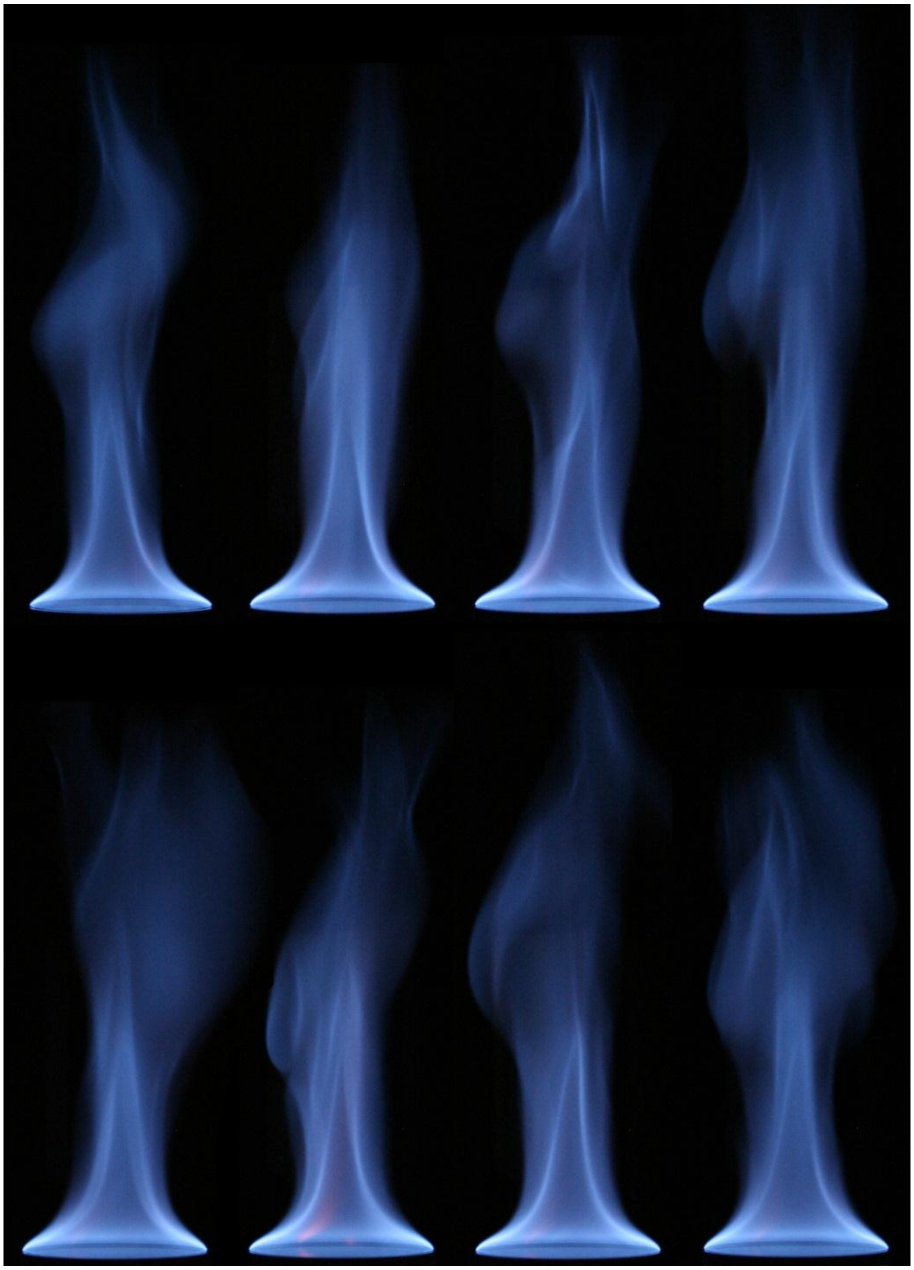

Fig. 4.6 A series of successive photographs of flame established above the methanol pool

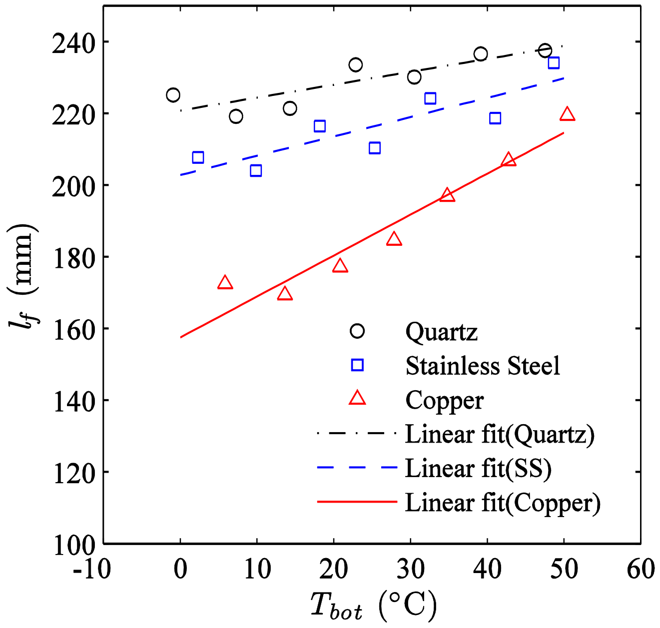

Fig. 4.7 Flame height of methanol pool fire with respect to the bottom boundary temperature and different pool wall materials

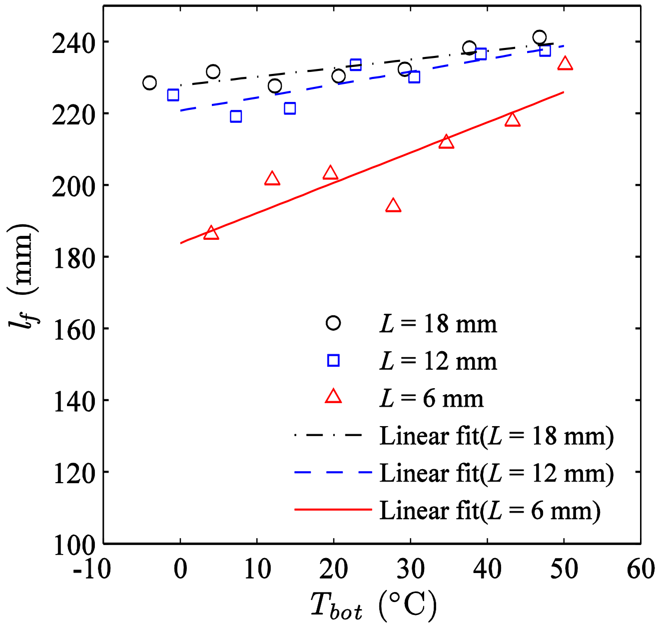

Fig. 4.8 Flame height of methanol pool fire with respect to the bottom boundary temperature and different pool depth

Similar to burning rate, the sensitivity of the flame height to the pool bottom temperature is not the same for all the burners. l_f increases by 27%, 13% and 9% for copper, stainless steel, and quartz pools, respectively by increasing the bottom temperature from 0ºC to 50ºC. For the same T_{bot} variation, the flame enlarges by 25% for the shallow pool (*i.e.*, L = 6 mm) while a relatively trivial increase of 6% in the flame height occurs for the deep pool (*i.e.*, L = 18 mm).

The results for the flame height, shown in Fig. 4.7 and Fig. 4.8, are strongly coupled with the fuel-burning rate. The relationship between the flame height and the burning rate is depicted in Fig. 4.9 by square symbols. The triangle and the circle symbols represent the height that the flame maintains in 90% and 10% of the collected images, respectively. These three data sets, can actually quantify the spatial flickering behavior of the flame relative to the flame height (*i.e.*, median value). The experimental results are also compared with three correlations selected from the equations listed in Table 2.1: Eq. (2.17) [65] solid line, Eq. (2.23) [97] dash line, and Eq. (2.19) [94] dash-dot line.

The increase in the flame height with the burning rate seen in Fig. 4.9 is associated with the time (or space) needed to entrain oxygen into the reaction zone of the flame. When the rate of fuel vapor emitted from the pool, $\dot{m}''_b$, is increased, a larger / taller flame will result in order to provide the required oxygen for combustion.

As it can be seen in Fig. 4.9, all three correlations predict flame height value within the limits that are established with the tip of visible flame locations in 90% to 10% of the images. However, on the left side of the graph (*i.e.*, $\dot{m}''_b < 9.5$ g/(m^{2}s)) Eq. (2.19) and on the right side (*i.e.*, $\dot{m}''_b \geq 9.5$ g/(m^{2}s)) Eq. (2.17) have better agreement with the experimental flame heights, respectively. Eq. (2.23) predicts the flame height with a discrepancy of up to 10% for the entire range of the considered $\dot{m}''_b$.

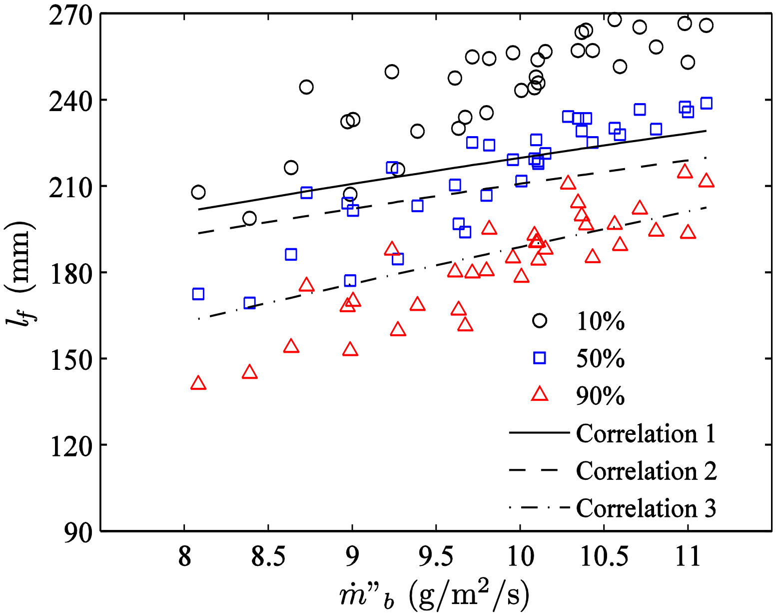

Fig. 4.9 Flame height with respect to burning rate in comparison with the correlations from the literature. Correlations 1 [65], 2 [97], and 3 [94] are presented in Table 2.1.

4.4 Wall Temperature Distributions

In order to understand the effects of the pool wall material, the thermal structure of the medium circular pool walls were measured in this study. When the vaporized fuel is ignited above a flammable liquid pool, the rim of the pool is heated by being in proximity with the flame and combustion products. Heat is conducted downward through the wall and after a transient stage the steady-state wall thermal structure is established.

The wall temperature variations with time for the first 10 min after ignition for three different vertical positions, *y*, along the pool wall made of different materials (*i.e.*, copper, stainless steel and quartz) are shown in Fig. 4.10. The steady-state wall temperature profiles with respect to the vertical distance upward, $T_w(y)$, from the bottom of the pool, $y = 0$ mm are presented in Fig. 4.11, Fig. 4.12, and Fig. 4.13 for the copper, stainless steel, and quartz pool, respectively. The numbers in the graph legends are associated with the test cases as listed in Table 4.2.

From Fig. 4.10, it is apparent that the steady temperature fields are established within the pool wall in less than 10 min. The transient period depends on the wall material and the vertical locations. As it is shown in Fig. 4.10a, the temperature along the entire height of the copper wall rises uniformly to its steady state value. When the wall material is changed to one with lower thermal conductivity (*i.e.*, stainless steel and quartz), the wall temperature rises non-uniformly through its height. The temperature increase is larger and occurs faster at the top region of the wall in comparison with the lower part (especially for the quartz pool).

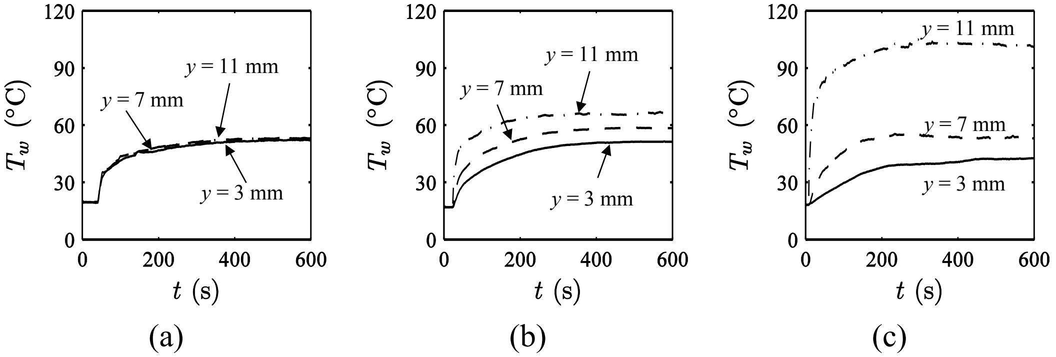

Fig. 4.10 (a) Copper, (b) stainless steel and (c) quartz wall temperture variations with time at different verical locations when the bottom temperature is according to case 4 in Table 4.2

The steady-state wall temperatures are the values averaged over a 10-minute period of data collection following a 20-minute transient stage after the ignition (to make sure that the steady-state thermal structure is established along the entire wall). The range of measured value deviation from the averaged wall temperature are not included in Fig. 4.11, Fig. 4.12, and Fig. 4.13 either to avoid clutter in the data presentations or due to being smaller than the symbol size. The standard deviation of the wall temperature data at different vertical locations are mostly smaller than ±0.25ºC for the copper pool and smaller than ±1ºC for the stainless steel and quartz pools. The largest deviation was ±2ºC. The wall temperature measurements were repeated three times (for case 4) and the uncertainty of the measured values was found to be within ±5ºC (90% confidence).

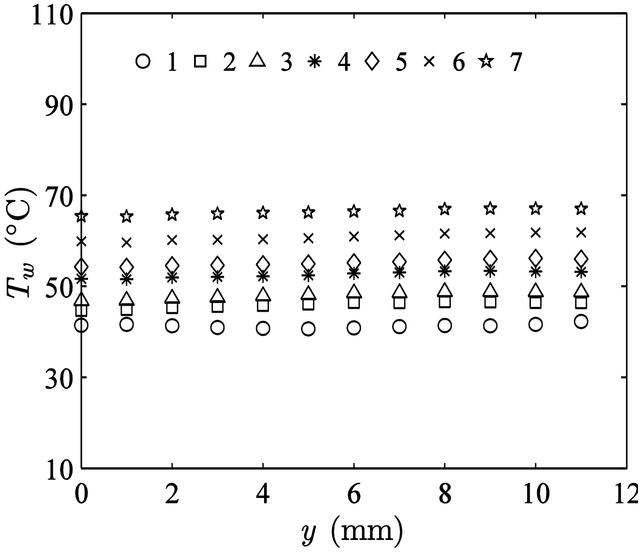

Fig. 4.11 Wall temperature distributions for the copper pool with respect to vertical location from the pool bottom; the numbers in the legends correspond to the cases listed in Table 4.2. The bottom temperature increases from 1 to 7

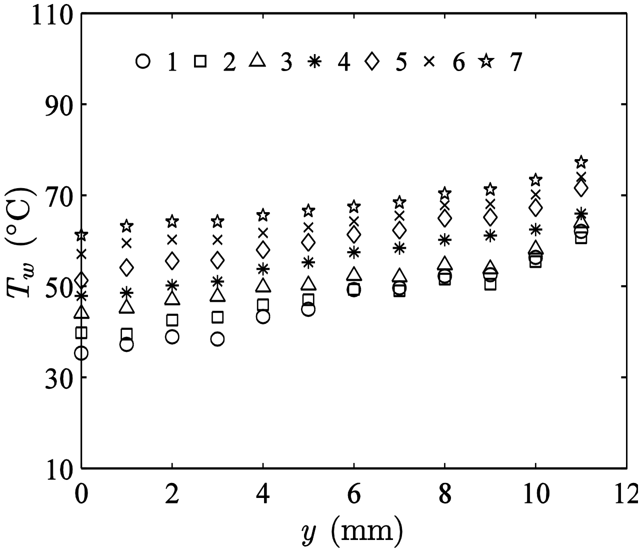

Fig. 4.12 Wall temperature distributions for the stainless steel pool with respect to vertical location from the pool bottom; the numbers in the legends correspond to the cases listed in Table 4.2. The bottom temperature increases from 1 to 7

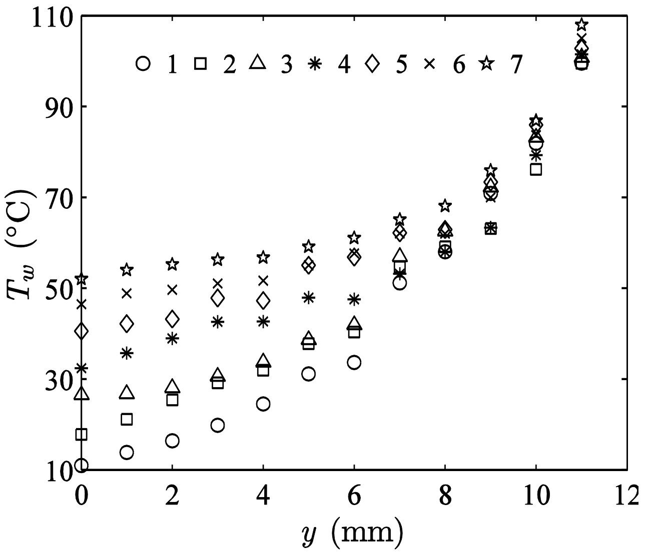

Fig. 4.13 Wall temperature distributions for the quartz pool with respect to vertical location from the pool bottom; the numbers in the legends correspond to the cases listed in Table 4.2. The bottom temperature increases from 1 to 7

As it is illustrated in Fig. 4.11, Fig. 4.12, and Fig. 4.13 the walls made of different materials adopt significantly different thermal structures while being in close proximity with the flame at the top and cool liquid at the bottom. From comparison of the wall temperature distributions, $T_w(y)$, it can be concluded that for highly conductive wall, copper, $T_w(y)$ is almost invariant throughout its height, while the low conductive wall, quartz, has a rapid temperature increase within the last 4 mm close to the top edge. The stainless steel $T_w(y)$ increases from bottom to top almost linearly. These trends agree well with the wall temperature profiles shown in [106].

Finally, it can be seen that for the two metals, the temperature near the pool lip is affected by the set bottom boundary temperature, while the quartz pool's lip seems to be unaffected by the bottom temperature. From Fig. 4.13, it can be seen that the quartz wall temperature profiles at different bottom temperatures are converging monotonically to the same value for the wall rim temperature regardless of T_{bot}.

The thermal structures along the pool wall can be explained knowing that the top rim of the wall is near the flame and heat transfers from the hot gases to the wall. As the heat is conducted downward through the wall, part of it transfers convectively to the adjacent fluids which are quiescent ambient air and liquid fuels on the outer and inner sides, respectively. Therefore, the problem consists of a system including solid wall, liquid fuel and ambient air. This phenomenon was not quantitatively modeled in this study. The heat conduction through the wall may simply be assumed one-dimensional, but boundary conditions at the top and the bottom edge of the wall are unknown. Therefore, a qualitative explanation is presented here.

One of the three heat transfer pathways of conduction through the wall, convection from the wall inner surface to the liquid fuel and convection from the wall outer surface to the ambient air will dominant according to the relative thermal resistance and the local temperature difference. Comparing the convection to the ambient air and the convection to the liquid fuel, the latter is always the largest since the thermal resistance of the liquid is smaller. The convective heat transfer coefficient of liquids are usually one to two orders of magnitude larger than those for gases [63].

The importance of the convection from the wall surface to the liquid fuel over the conduction through the wall downwards is the Biot number, *Bi*. It can be expressed as the ratio of the thermal resistance inside the wall to the resistance at its surface as [63]:

$$Bi = hL_c / k_w \tag{4.1}$$

where h (kJ/(m^{2}K)) is the convective heat transfer coefficient of the liquid fuel in contact with the wall surface, L_c (m) is the characteristic length equal to the ratio of the wall volume to its surface area wetted with the fuel and k_w (kJ/(mK)) is the wall thermal conductivity. For the different pools considered here only the wall thermal conductivity changes with altering the wall material (the wall properties were assumed temperature independent). The *Bi* number for the copper pool is two orders of magnitude smaller than the quartz pool *Bi* number.

When *Bi* is small, it means that heat is preferred to be conducted downward through the wall. Thus, a uniform temperature distribution, similar to the one shown in Fig. 4.11 for the copper pool, is established within the wall. A non-uniform temperature field, as shown for the quartz pool in Fig. 4.13, is associated with the case of large *Bi* number. That is, in the quartz pool instead of being conducted through the wall, heat is mostly convected from the inner surface of the wall to the liquid fuel within the top region of the wall where ΔT is high (this heat transfer is quantified in Sec. 5.1). This phenomenon and the low thermal conductivity of the quartz wall result in a rapid temperature drop downwards along the quartz wall.

4.5 Temperature Distributions within the Liquid Fuel

In order to understand and quantify the energy transport in the liquid phase, steady state temperature distributions within the liquid fuel are required. Therefore, the fuel temperatures were measured across the central cross-sectional plane of the pool from the pool wall to the central axis for different burners. For different bottom temperatures, the resulting two-dimensional temperature maps and the vertical profiles along the central axis of the pools are presented here. It should be noted that in the temperature distributions presented in this section, the inner surface of the wall is located at x = 0 mm and the central axis is at x = 35 mm for square and at x = 45 mm for circular pools.

Spatial distribution plots of the liquid temperature for the two square pools (quartz and aluminum) are shown in Fig. 4.14. When the circulating water temperature was set to 20°C the mean bottom temperatures of 24°C and 29°C were recorded for quartz and aluminum pools, respectively. The reason for this difference remains unclear, but, as shown in Fig. 4.14 it could be related to how the liquid thermally stratifies itself differently for the two different types of pool wall materials.

The first notable observation seen in Fig. 4.14 is that the fuel adopted a two-layered thermal structure, one layer being nearly uniform and the other having a relatively steep gradient, and that the ordering of these layers is dependent on the wall material. For the quartz pool, the temperature gradient was much larger (~5°C/mm) within the bottom half of the pool compared to that within the top half (~0.5°C/mm). The top layer, which was almost of a uniform temperature, is being described as "thermally well-mixed". For the same planar section of the aluminum pool the temperature distribution within the liquid fuel shows a large temperature gradient layer at the top, which is as much as 4°C/mm, while the lower part of the pool ($y < 10$ mm) is now a thermally well-mixed layer.

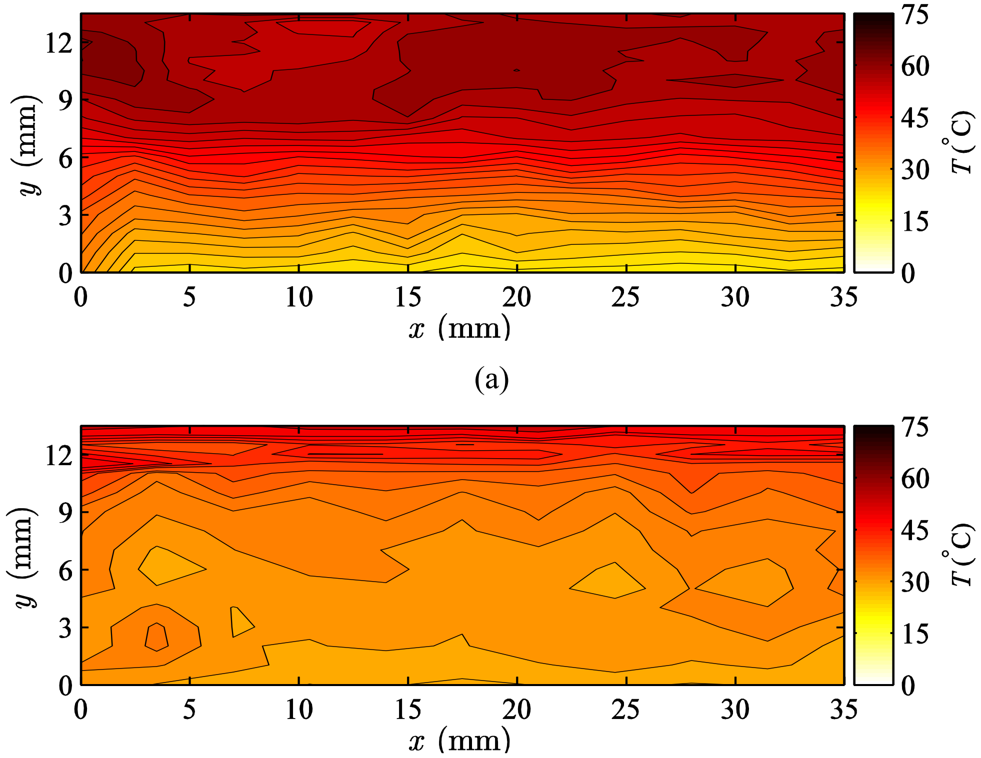

(a)

(b)

Fig. 4.14 Temperature distributions within the liquid phase for (a) quartz square pool with bottom temperature of 24°C and (b) aluminum square pool when the base temperature was 29°C

Note that the last data points in Fig. 4.14 are 0.5 mm beneath the liquid-vapor interface. While this point is unimportant for the quartz pool because the liquid in this region is uniform in temperature, there are significant changes occurring in that region of the aluminum pool. As a result, the fuel surface temperature is 4-5°C higher within the quartz vessel than that for the aluminum one. According to the literature [12], the surface temperature is expected to be a few degrees less than the fuel boiling point of 64°C, which is in agreement with the data presented for the quartz pool.

The liquid fuel temperature profiles along the central axis of the square pool are shown in Fig. 4.15 and Fig. 4.16, where the quantitative values can be easily seen rather than in the 2-D maps. The liquid temperatures in this section are normalized as:

$$\theta = (T - T_{bot})/(T_s - T_{bot}) \tag{4.2}$$

where T is the measured temperature and T_s is the liquid surface temperature. The vertical coordinate is also scaled against the pool depth, L as:

$$y^* = y/L \tag{4.3}$$

The use of dimensionless variables of θ and y^* allows a more effective way to follow the trends of results especially when temperature profiles of different pools at different bottom temperatures are compared against each other.

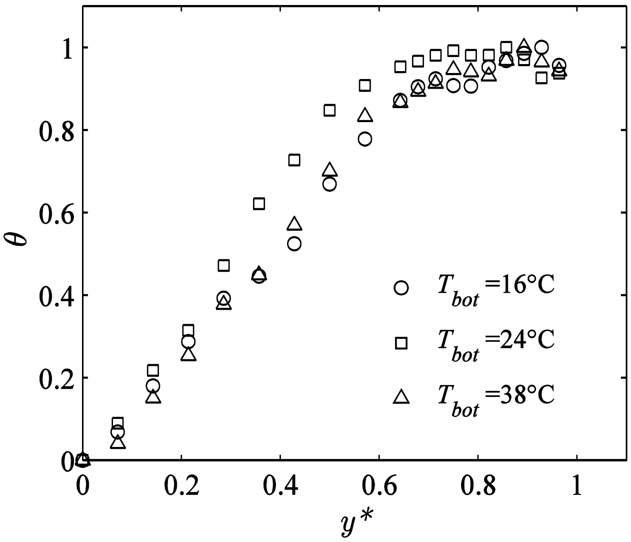

Fig. 4.15 Normalized liquid temperature distributions along the quartz square pool central axis with respect to normalized vertical location for different bottom temperatures

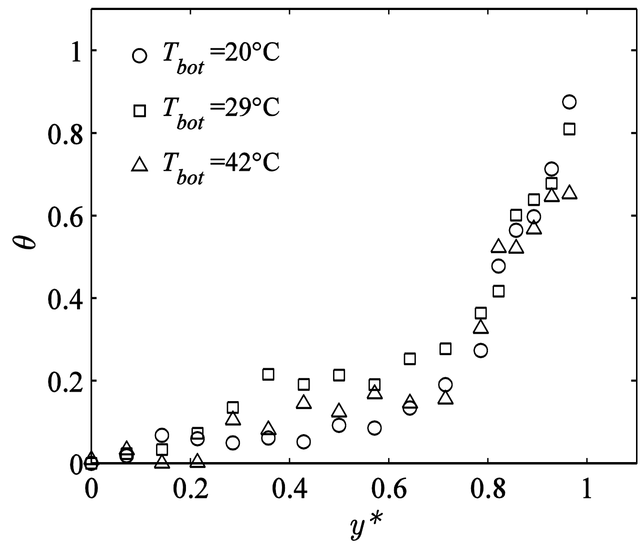

Fig. 4.16 Normalized liquid temperature distributions along the aluminum square pool central axis with respect to normalized vertical location for different bottom temperatures

Within the quartz pool, the temperature of the upper quarter of the fuel is almost uniform and equal to the highest temperature observed in the liquid phase. The temperature then shows a rapid decrease in the lower three quarters of the fuel layer. An opposite trend can be seen for the aluminum pool. The variation in temperature is less than 20% of the pool surface-bottom temperature difference within the first 0.6-0.7 of the pool depth and then it rises significantly to surface temperature within the remainder of the pool.

Two-dimensional temperature maps for different boundary temperatures, as listed in Table 4.2, are shown in Fig. 4.17, Fig. 4.18, and Fig. 4.19 for copper, stainless steel, and quartz circular pools, respectively. The non-dimensional central temperature profiles within different pools are shown in Fig. 4.20, Fig. 4.21, and Fig. 4.22 for copper, stainless steel, and quartz circular pools, respectively.

For the circular pool, the same as square pool, the liquid surface temperature is a few degrees (~3-4°C) below the expected boiling point of methanol. It is also apparent that the isothermal lines are mostly horizontal. This suggests that heat transfer mostly occurs in the *y*-direction especially in the central region. Therefore, the temperature is almost constant in the *x*-direction except for the regions near the wall ($x < 10$ mm). In the vicinity of the wall the isothermal lines are not horizontal due to the heat transfer between the wall and the liquid fuel. The slope of the isothermal lines is positive or negative depending on the heat transfer direction.

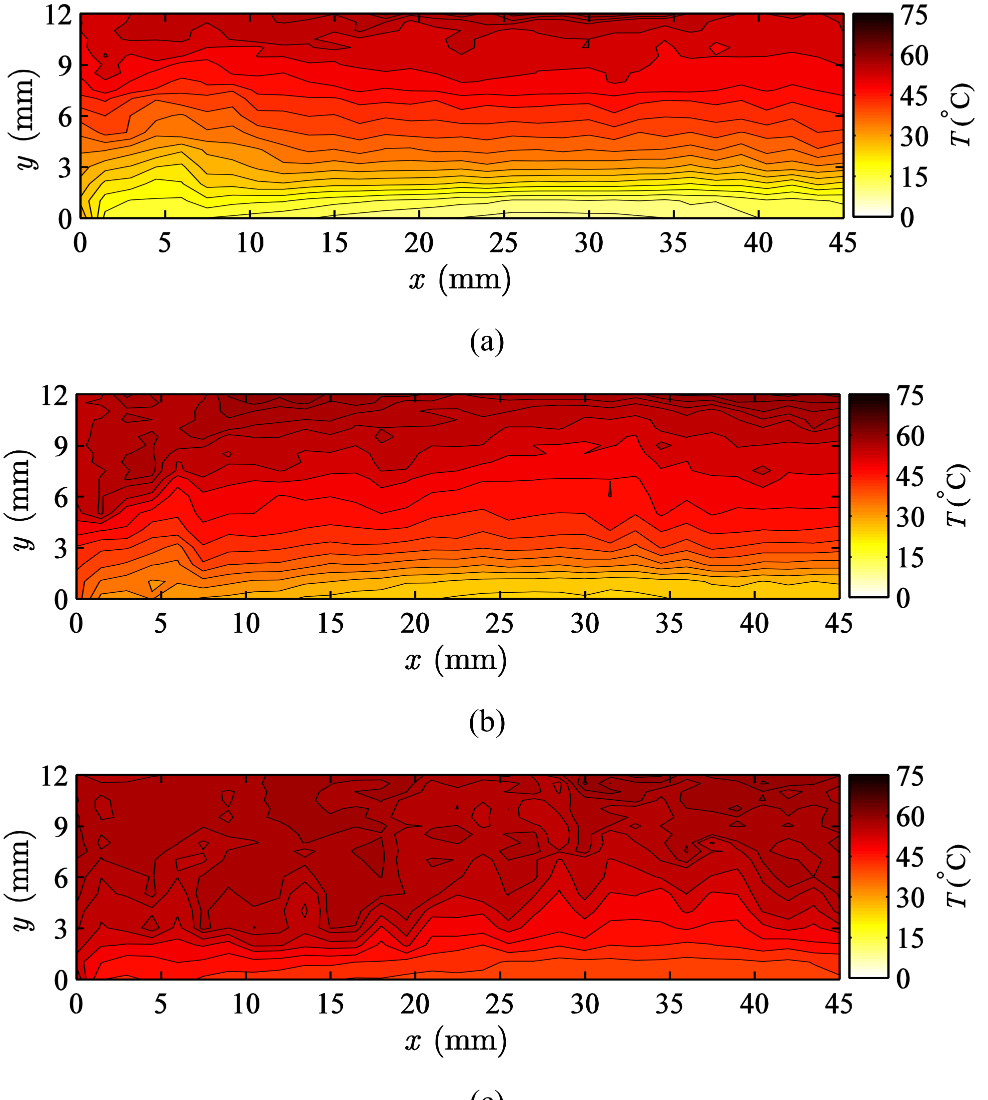

(a)

(b)

(c)

Fig. 4.17 Temperature distributions within the liquid phase for the copper pool when (a) T_{bot} =13.5ºC , (b) T_{bot} =28ºC, (c) T_{bot} =43ºC

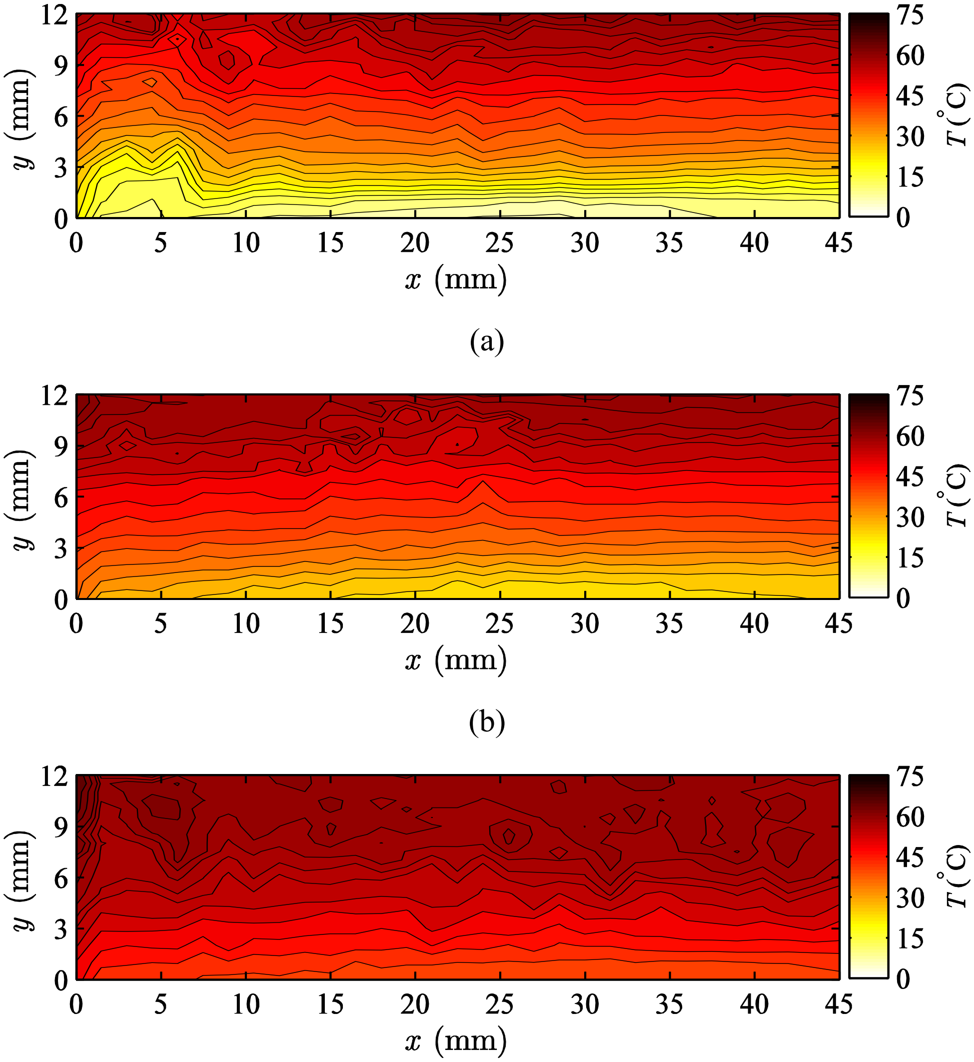

(a)

(b)

(c)

Fig. 4.18 Temperature distributions within the liquid phase for the stainless steel pool when (a) T_{bot} =10ºC , (b) T_{bot} =25ºC, (c) T_{bot} =41ºC

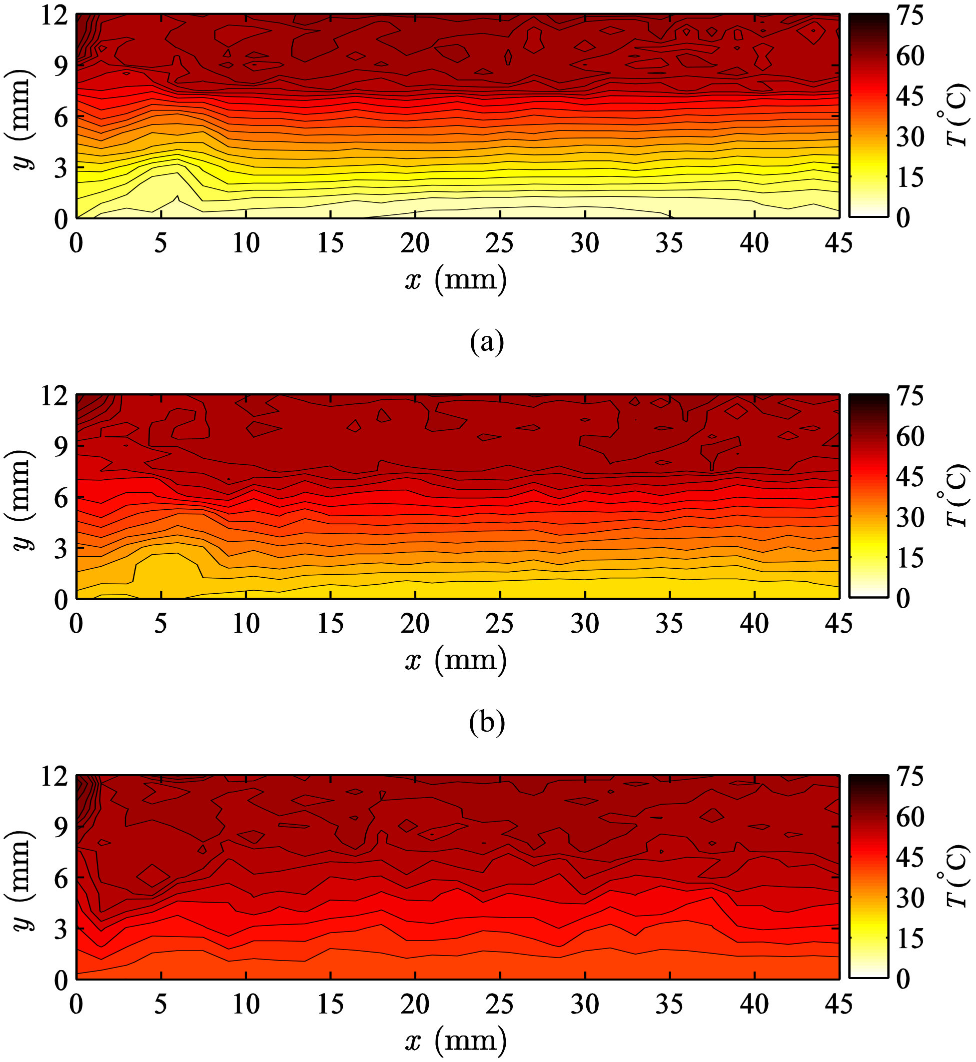

(a)

(b)

(c)

Fig. 4.19 Temperature distributions within the liquid phase for the circular medium quartz pool when (a) T_{bot} =7ºC , (b) T_{bot} =23ºC, (c) T_{bot} =39ºC

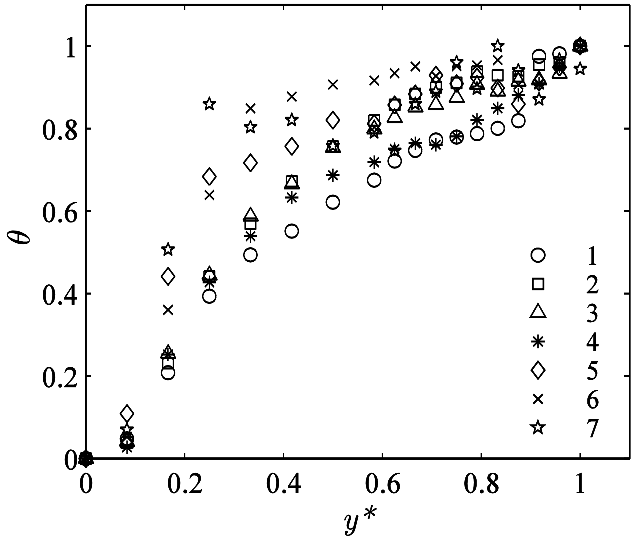

Fig. 4.20 Normalized liquid temperature distributions along the pool central axis for the copper pool with respect to normalized vertical location; the numbers in the legends correspond to the cases listed in Table 4.2

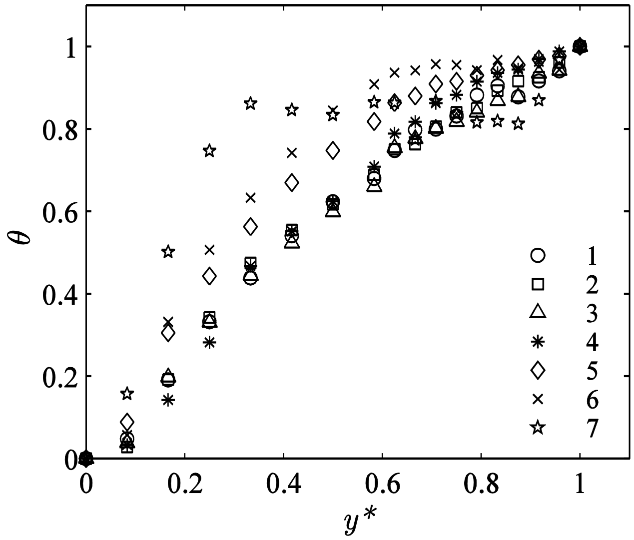

Fig. 4.21 Normalized liquid temperature distributions along the pool central axis for the stainless steel pool with respect to normalized vertical location; the numbers in the legends correspond to the cases listed in Table 4.2

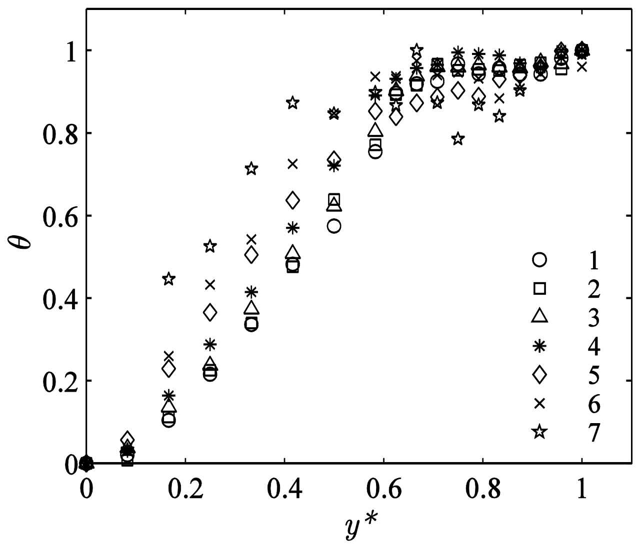

Fig. 4.22 Normalized liquid temperature distributions along the pool central axis for the quartz pool with respect to normalized vertical location; the numbers in the legends correspond to the cases listed in Table 4.2

When the wall material is altered the heat transfer through the wall and from the wall to the liquid fuel are affected (as described in Sec. 4.4). As a result, the thermal structure within the liquid fuel changes. It is apparent in Fig. 4.20, Fig. 4.21, and Fig. 4.22 that the trends of the liquid temperature profiles, $\theta(y^*)$, within different vessels become similar at higher bottom temperatures. This two-layer thermal structure includes a relatively steep temperature gradient region at the bottom and an almost uniform temperature region at the top, which is similar to the trends observed in the square quartz pool. However, while this structure is maintained for the quartz pool, it is changed significantly for the steel and copper pools at lower bottom temperatures.

The reason for the variation in liquid thermal structure with bottom temperature for metallic vessels may also be explained from the energy transfer between the wall and the liquid phase. This heat transfer is in the form of convection. Therefore, the local wall heat flux, $\dot{q}''(y)$, is proportional to the local characteristic temperature difference between the wall and liquid bulk [182]. That is, $\Delta T(y) = T_w(y) - T_l(y)$, where $T_w(y)$ is the wall temperature and $T_l(y)$ is the liquid temperature at the center of the pool both at the same vertical positions. To establish an understanding of wall heat flux distributions, $\Delta T(y)$ is shown in Fig. 4.23 against the vertical location, y.

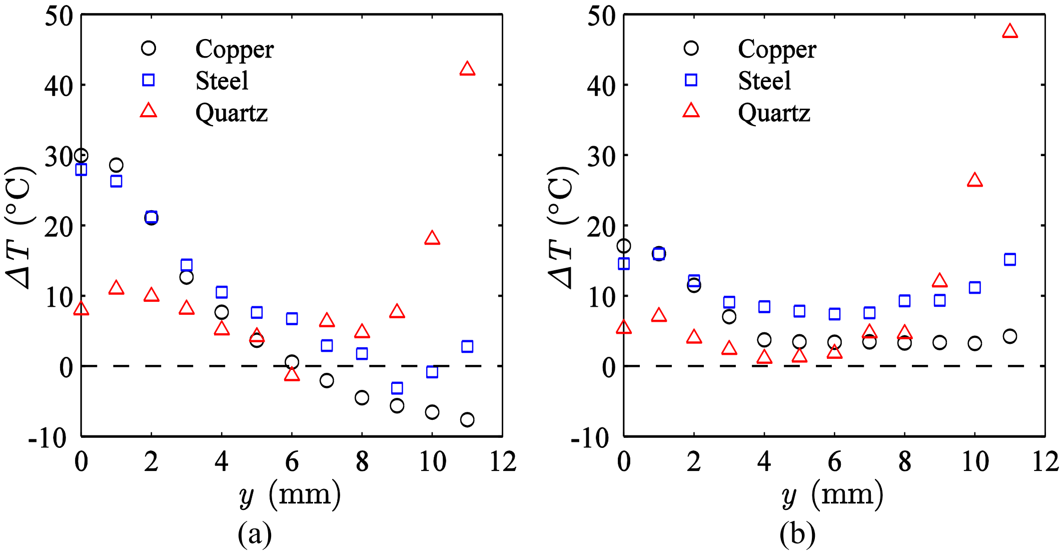

Fig. 4.23 Characteristic wall-liquid temperature difference versus vertical location and for different pool walls when the boundary condition is according to (a) case 2 (T_{bath} = 0°C) and (b) case 6 (T_{bath} = 40°C) listed in Table 4.2

It is apparent that heat transfer from the copper wall to the liquid mostly occurs in the lower region, $y < 6$ mm, where $\Delta T(y)$ is positive and large. This heat transfer from the wall to the lower region of the liquid layer at low bottom temperatures, *e.g.*, case 2, cools the wall to a lower temperature than the liquid temperature in the top region. Therefore, the copper wall gains heat from the hot fuel at the top region and acts as an energy sink. Nakakuki [142] showed that by taking heat from the liquid layer the thickness of the uniform-temperature layer can be reduced. This altering of the uniform layer is in agreement with current results as shown in Fig. 4.20 and Fig. 4.21 where at lower bottom temperatures more heat is taken from the liquid by the cooler wall, which results in a thinner uniform-temperature layer. By increasing T_{bot} to case 6, Fig. 4.23b, less heat is taken from the wall in the lower region. Therefore, the wall becomes hotter than the liquid, and the uniform-temperature layer is formed below the liquid surface within metallic pools.

For the quartz pool, it is apparent in Fig. 4.23 that there is a positive and large $\Delta T(y)$ for the first 4 mm below the surface. The large temperature difference drops rapidly downward. Therefore, while a profound amount of heat transfers to the fuel within the first few millimeters of the wall at the top, insignificant heat transfer occurs along the lower region of the wall. Due to the substantial temperature difference between the fuel and the wall, there is a potential for convective currents to be established in the top region which keeps that part of liquid fuel thermally well-mixed. It is also apparent in Fig. 4.19 that a thermal boundary layer was established on the liquid-wall interface in the quartz pool. Moreover, it can be seen in Fig. 4.23 that the quartz $\Delta T(y)$ is almost independent from T_{bot} , whereas the strong dependency of the wall heat transfer on T_{bot} for the copper pool is seen. That may explain the change in the copper pool thermal structure with T_{bot} while the trends for the quartz pool remain invariant.

It may also be possible to elucidate the reason for observing a completely different trend in the liquid temperatures within the aluminum square pool. As mentioned in Sec. 2.5 a three-zone thermal structure could be established within relatively deep pools [139]. The liquid was hot at the top of the layer below the interface as a result of flame heat feedback. Due to the relatively colder base (compared with the liquid surface) the liquid within the bottom region of the deep pool was cold. While the top and bottom zones had uniform temperatures, there was a region between them in which liquid temperature decreased from the hot-zone to the cold-zone temperature. In the square pool, the wall was also cooled by the base (they were in direct contact). This effect may be nominal for the quartz pool since the quartz wall does not conduct heat from the flame to the base. However, due to the thermal conductivity of the aluminum wall, it is expected (based on the observation for copper circular pool) that the wall temperature significantly drops below the liquid temperature. Therefore, a significant amount of heat can be taken from the liquid by the cold wall and could completely diminish the uniform-temperature layer. Nakakuki [142] proposed that when the outer surface of the pool wall was cooled with water, the thickness of the hot-zone decreased.

The two-dimensional temperature maps and normalized profiles at the central axis for circular quartz pools of different depths are presented in Fig. 4.24 and Fig. 4.26 for the shallow pool (L = 6 mm) and in Fig. 4.25 and Fig. 4.27 for the deep pool (L = 18 mm). The impacts of having the prescribed boundary temperatures at different distances below the pool surface on the liquid phase thermal structure can be examined in these figures if they are compared with the results presented for the medium quartz pool (L = 12 mm) in Fig. 4.19 and Fig. 4.22.

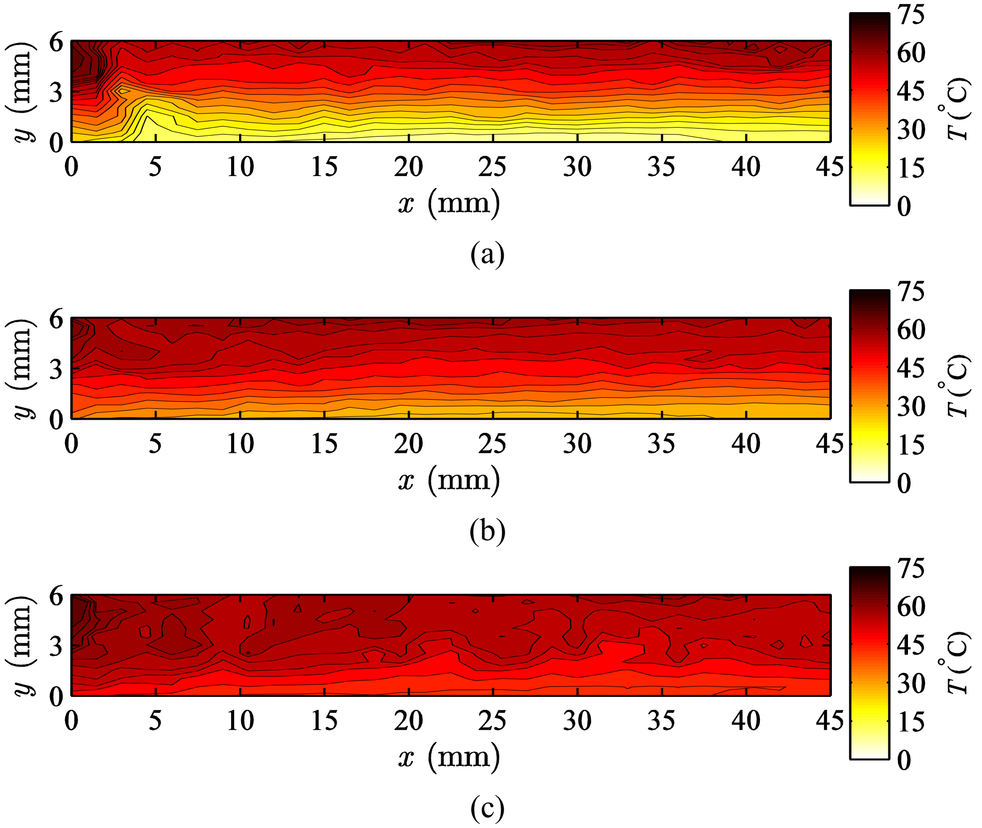

Fig. 4.24 Temperature distributions within the liquid phase of the shallow quartz pool when (a) T_{bot} =12ºC , (b) T_{bot} =28ºC, (c) T_{bot} =43ºC

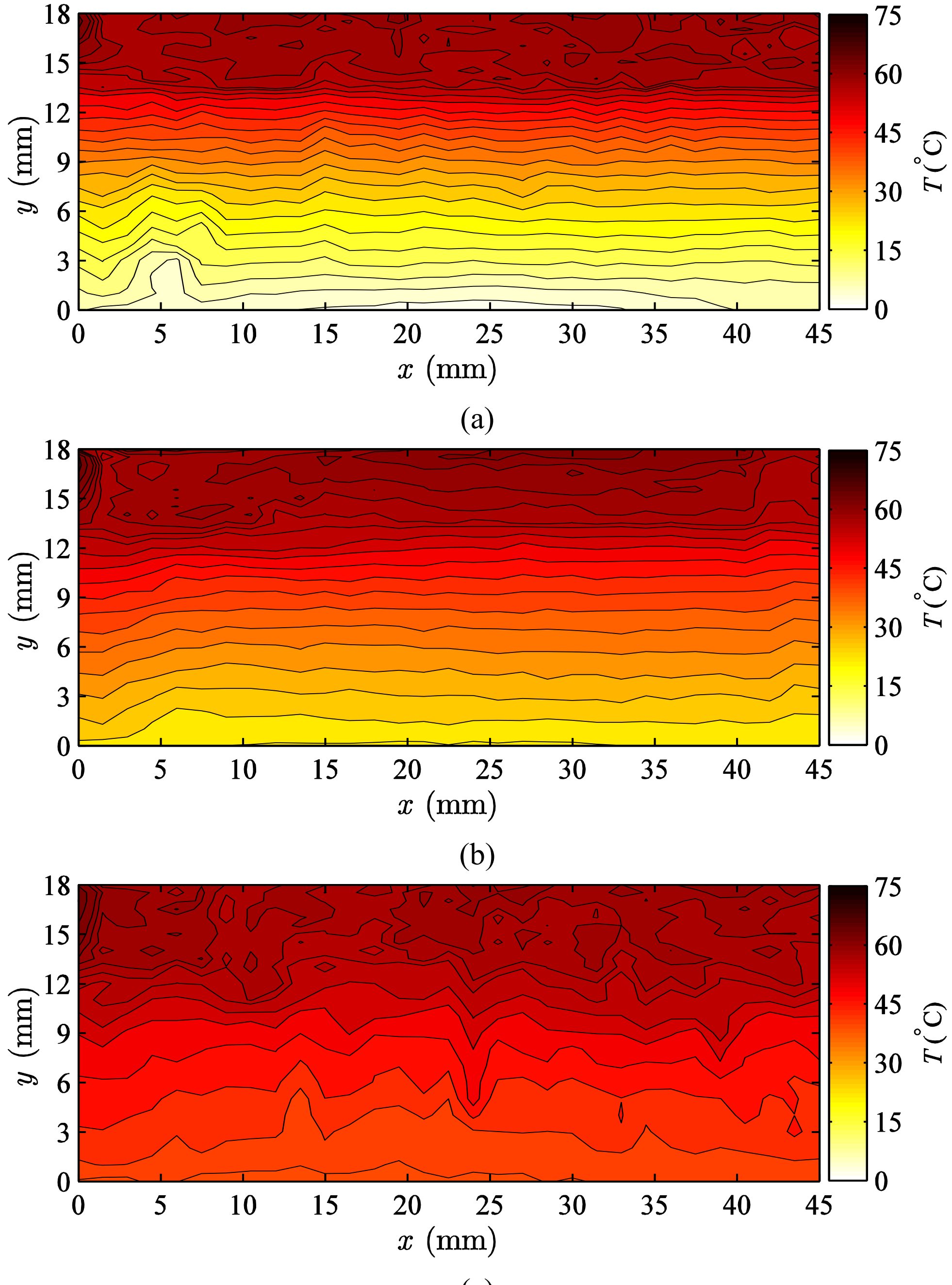

(a)

(b)

(c)

Fig. 4.25 Temperature distributions within the liquid phase of the deep quartz pool when (a) T_{bot} =4ºC , (b) T_{bot} =21ºC, (c) T_{bot} =38ºC

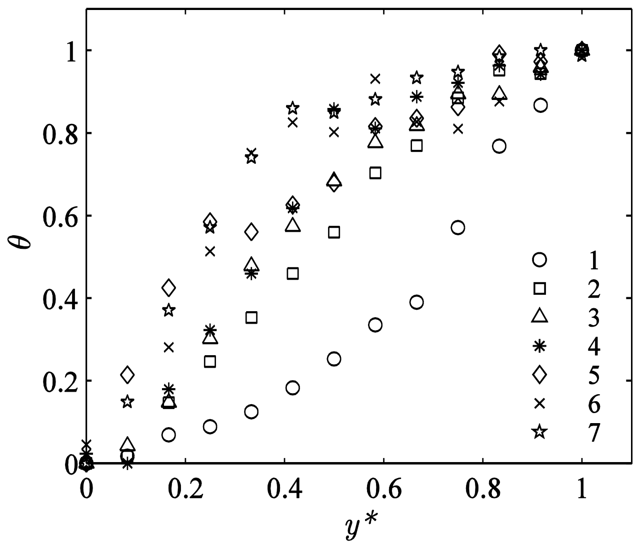

Fig. 4.26 Normalized liquid temperature distributions along the pool central axis for the shallow quartz pool with respect to normalized vertical location; the numbers in the legends correspond to the cases listed in Table 4.3

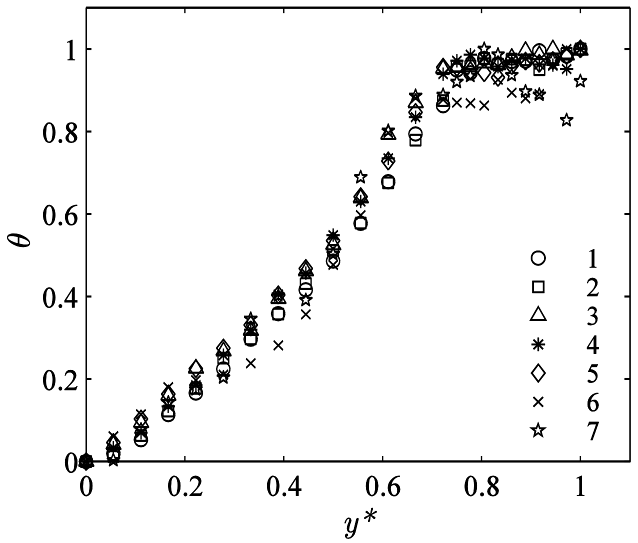

Fig. 4.27 Normalized liquid temperature distributions along the pool central axis for the deep quartz pool with respect to normalized vertical location; the numbers in the legends correspond to the cases listed in Table 4.3

It is apparent that while the two-layer thermal structures can be clearly recognized in the medium and deep pools, liquid temperature increases through the shallow pool differently especially at lower bottom temperatures. At lower bottom temperatures, the liquid temperature rise is almost linear and as T_{bot} increases the temperature rise occurs faster in the lower part and slower within the upper region. That is, the thermal structure approaches the two-layer pattern as the bottom temperature increases for the shallow pool. The existence of a thermal boundary layer at the liquid-wall interface a few millimeters below the pool surface is also apparent in Fig. 4.24 and Fig. 4.26. This means that the wall heat transfer pattern should be the same as that for the medium quartz pool, which was a large amount of heat transfer within the top region (the first few millimeters) and no significant wall heat flux in the lower region.

In summary, it can be concluded that in general, a two-layer temperature structure including a uniform-temperature layer and a relatively steep temperature gradient layer can be observed within the liquid phase. The uniform-temperature layer is usually established below the liquid surface and above the other layer. Therefore, the top region of the liquid pool is at a temperature equal to the liquid pool surface temperature, and the liquid temperature decreases vertically through the lower layer from the surface temperature to T_{bot}. This general liquid thermal structure is influenced by the test parameters (*i.e.*, pool bottom boundary temperature, pool wall thermal conductivity, and pool depth). The effect of lowering T_{bot} (from 50ºC to 0ºC) is diminishing of the uniform-temperature layer thickness and this effect becomes more profound when the pool wall thermal conductivity increases (from that of quartz to that of copper) or when the pool becomes shallower (from L = 18 mm to L = 6 mm). It is also found that when the pool was deeper than a certain depth (between 12 and 18 mm in this case) the thickness of the uniform-temperature layer becomes independent from T_{bot} variations. It is also observed that the combination of the test parameters sometimes could result in a complete disappearance of the uniform-temperature layer. For example, at the coldest T_{bot}, the uniform-temperature layer was no longer observed in either the copper pool or the shallow quartz pool.

The temperature data presented in this section is the average of 100 samples. The range of the liquid temperature variation is estimated from the standard deviation of the sample population. The distributions of standard deviation in the liquid temperature within the different pools when the bottom temperature was imposed by setting the bath to 0°C are shown in Fig. 4.28.

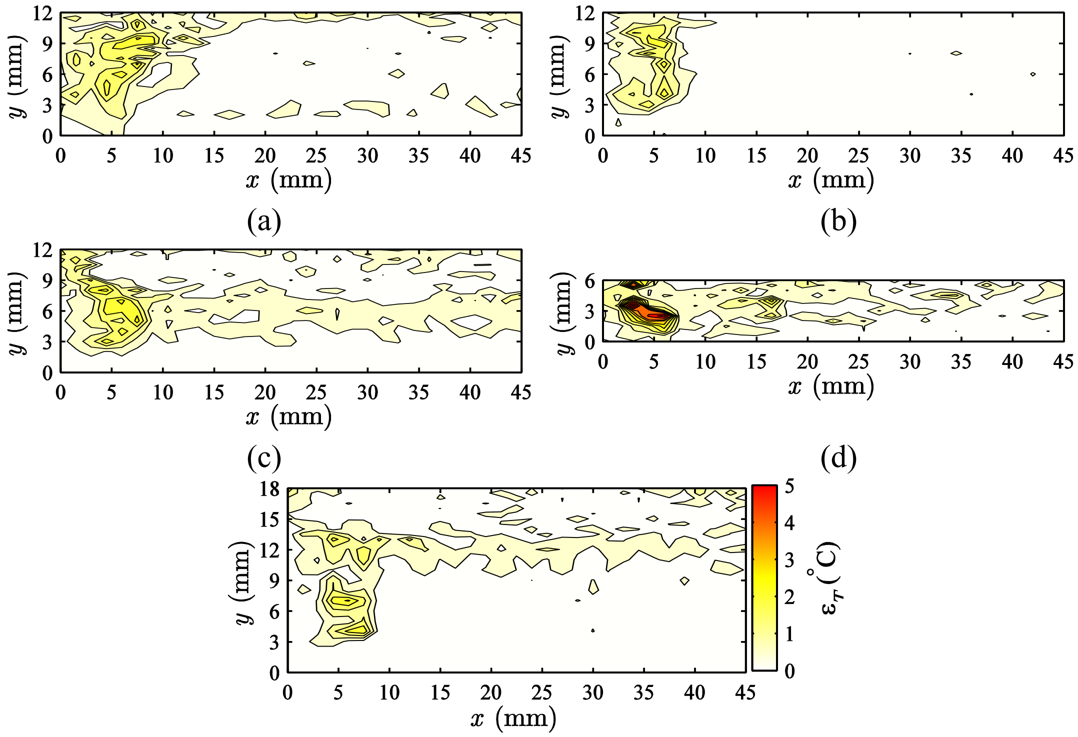

(a) (b) (c) (d) (e)

Fig. 4.28 Standard deviation in temperature measurements within the liquid phase of (a) copper, (b) stainless steel, (c) quartz, (d) shallow, and (e) deep pools when the bottom temperatures were imposed by a bath temperature of 0°C.

It is apparent in Fig. 4.28 that the largest values of the temperature standard deviation are associated with the regions near the wall (x < 10 mm) especially in the shallow pool where the standard deviation can be as large as 5°C. As the standard deviation of the liquid temperature is less than 0.5°C elsewhere, it can be suggested that the liquid temperature variations near the wall may be not related to the uncertainty of the measurement technique. These large deviation values near the wall could be due to the transport phenomena in that region. The motion of cool or warm parcels of fluids over the thermocouple junction may cause fluctuations in temperature readings. However, this justification requires more information about the liquid flow field, which is presented in next section.

4.6 Velocity Distributions within the Liquid Fuel

The velocity fields within the quartz pools with different depths were measured using PIV across a field of view of 30 mm×L (L = 6, 12, and 18 mm) from the pool wall. In the presented results in this section, the inner surface of the wall is located at x = 0 mm. As it is mentioned in Sec. 3.7, the results illustrated in this section are the mean values of 500 instantaneous velocity fields and are associated with the flow distributions within the pool 20 min after ignition.

The mean velocity vector field and the velocity magnitude maps are illustrated in Fig. 4.29, Fig. 4.30, and Fig. 4.31 for shallow, medium and deep pools, respectively. The measured 2D mean velocity vector field overlaid with the computed vorticity, ω, of the liquid fuel within the shallow, medium and deep pools are shown in Fig. 4.32, Fig. 4.33, and Fig. 4.34, respectively. Each figure shows results for several bottom temperatures as indicated in the figure captions. Also, for clearer presentation only every fourth vector is displayed. For the shallow pool the large temperature gradient induced between the pool top and bottom affected the quality of particle images. Therefore, only the result for T_{bot} = 43°C is presented that had a relatively small temperature gradient.

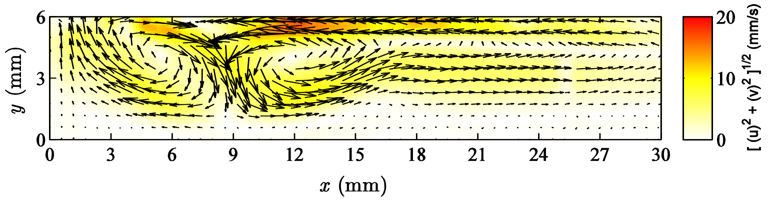

Fig. 4.29 Vector maps of the average velocity field with a background color map of the velocity magnitude within the liquid phase of the shallow quartz pool (L = 6 mm) when T_{bot} is 43°C

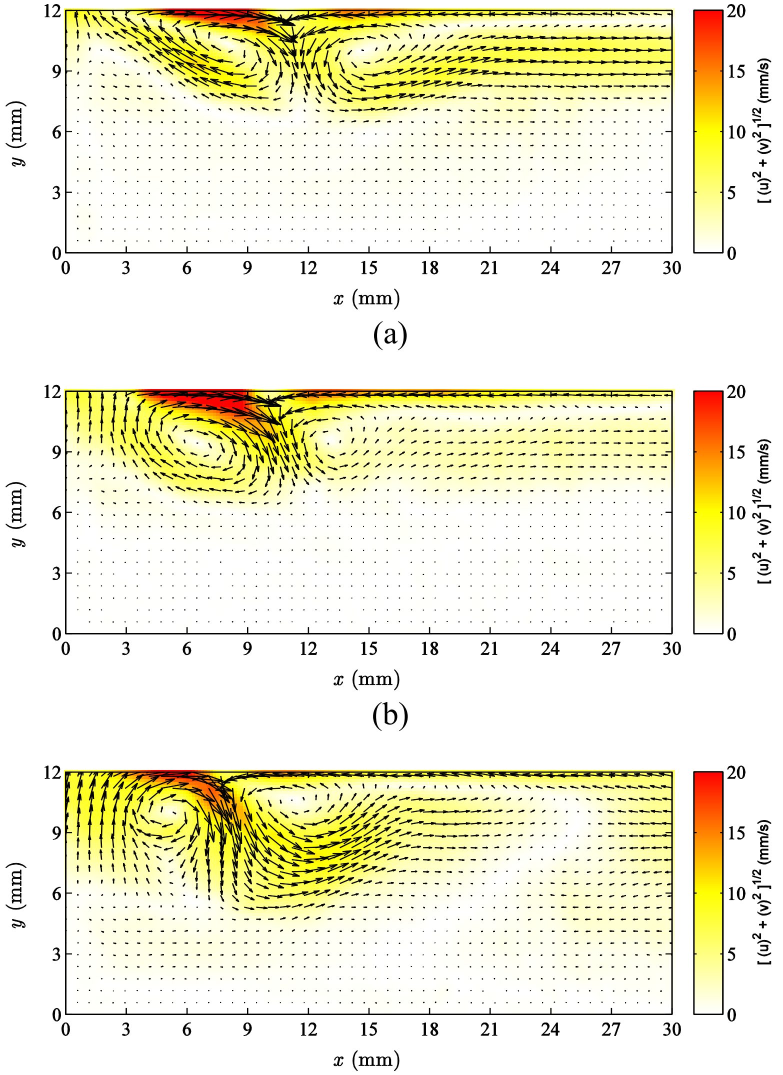

(a)

(b)

(c)

Fig. 4.30 Vector maps of the average velocity field with a background color map of the velocity magnitude within the liquid phase of the medium quartz pool (L = 12 mm) when (a) T_{bot} =7ºC , (b) T_{bot} =23ºC, (c) T_{bot} =39ºC

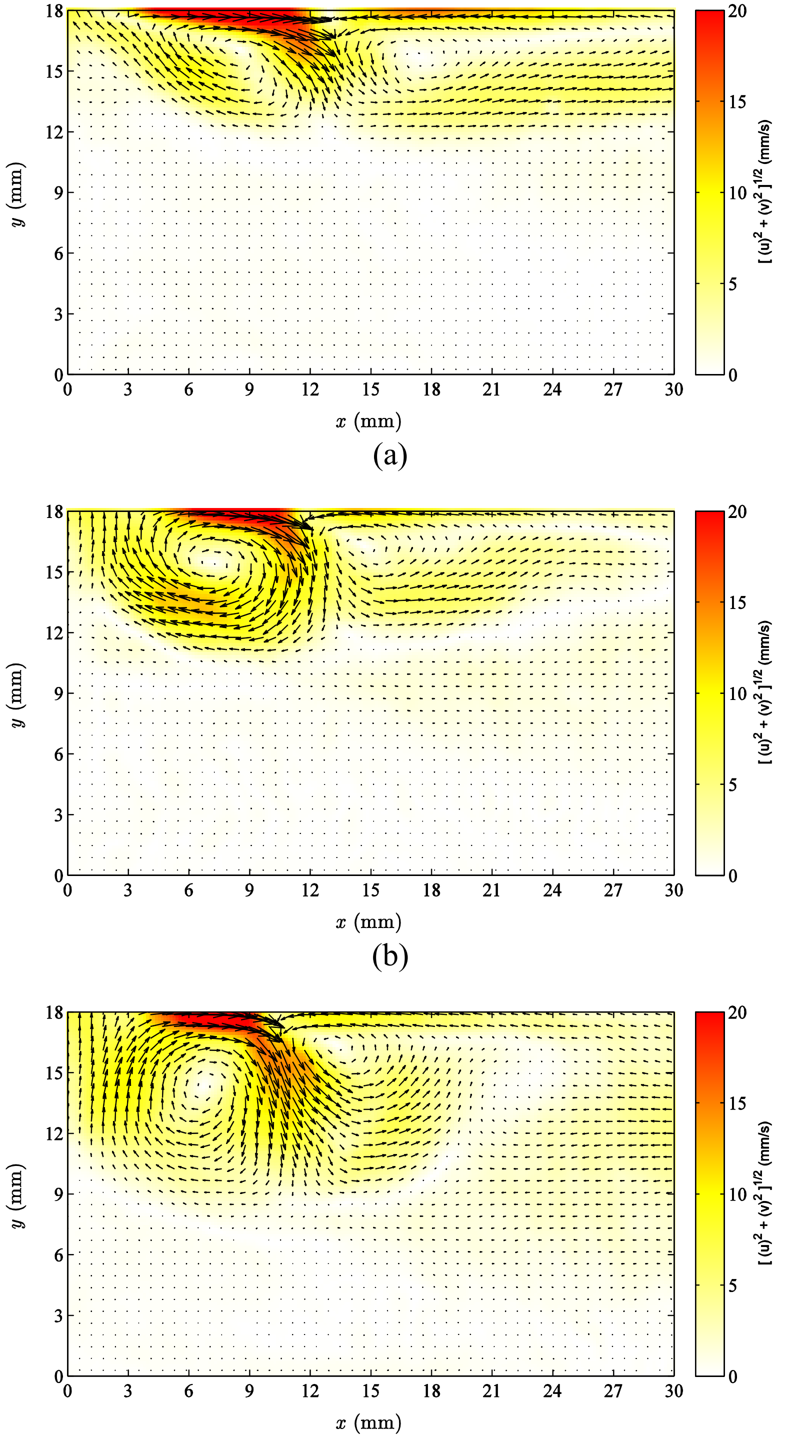

(a)

(b)

(c)

Fig. 4.31 Vector maps of the average velocity field with a background color map of the velocity magnitude within the liquid phase of the deep quartz pool (L = 18 mm) when (a) T_{bot} =4ºC , (b) T_{bot} =21ºC, (c) T_{bot} =38ºC

The velocity fields show the existence of large-scale mixing motion in the top layer of the liquid fuel with two strong counter-rotating vortices located adjacent to the pool wall. The velocity magnitude can be as large as 20 mm/s in this region and as it can be seen in the velocity fields the maximum velocity occurs on the fuel surface. It should be noted that as it can be seen in Fig. 4.32, Fig. 4.33, and Fig. 4.34 there are other small vortices immediately below the main vortices rotating in opposite direction. As only every fourth vectors are presented in these figures not all of the features in velocity vector field may be clearly seen. To address this, zoomed-in views of these vortices are presented in Appendix C. In contrast to the top layer of the liquid, the bottom layer is seen to have a low velocity (magnitude less than 2 mm/s) and no discernible vorticity. It worth emphasizing that due to the axisymmetric characteristic of the round pools, the same phenomena are expected at the other side of the pool central axis.

Two main vortices, as shown in the results, recirculate fluid in the top region of the liquid layer. The first vortex, close to the pool wall, rotates clockwise directing fluid away from the wall toward the center of the pool on the upper side of the vortex and toward the wall from the bulk pool on the lower side of the vortex. Potential driving mechanisms for this vortex can be a buoyancy force on the fluid next to the wall and thermocapillary stress along the fuel surface.

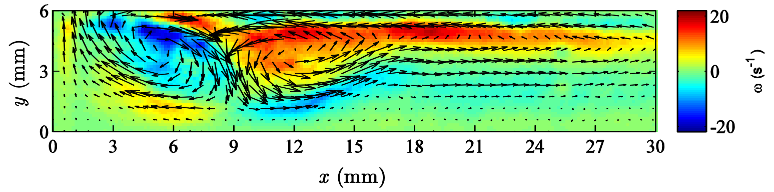

Fig. 4.32 Vector maps of the average velocity field with a background color map of the mean vorticity field within the liquid phase of the shallow quartz pool (L = 6 mm) when T_{bot} is 43°C

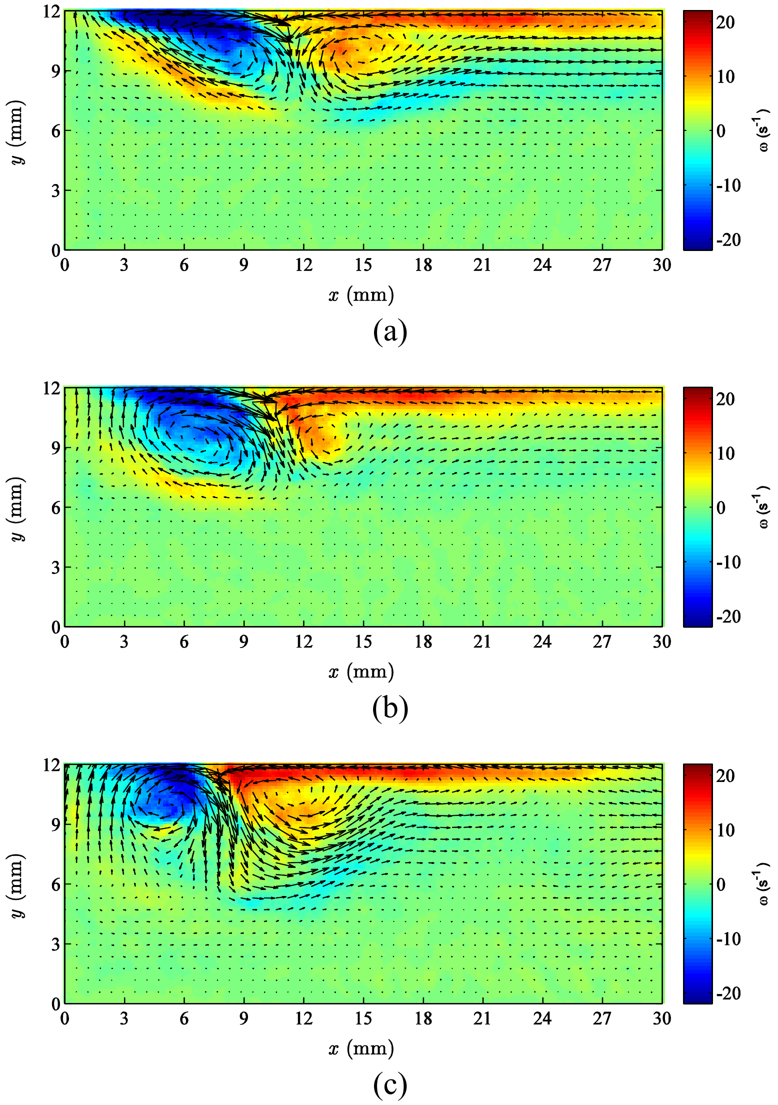

(a)

(b)

(c)

Fig. 4.33 Vector maps of the average velocity field with a background color map of the mean vorticity field within the liquid phase of the medium quartz pool (*L* = 12 mm) when (a) T_{bot} =7ºC , (b) T_{bot} =23ºC, (c) T_{bot} =39ºC

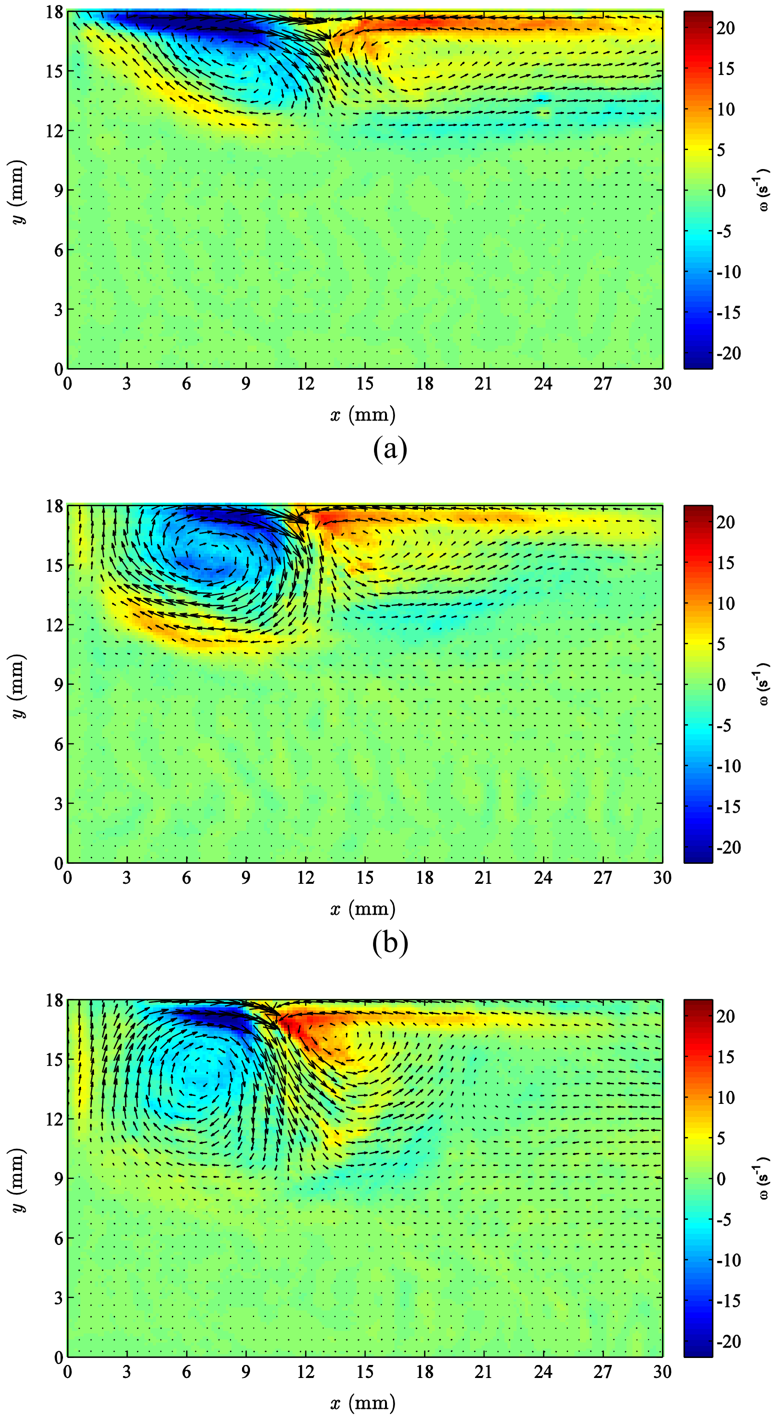

(a)

(b)

(c)

Fig. 4.34 Vector maps of the average velocity field with a background color map of the mean vorticity field within the liquid phase of the deep quartz pool (L = 18 mm) when (a) T_{bot} =4ºC , (b) T_{bot} =21ºC, (c) T_{bot} =38ºC

According to the measured wall temperature distributions presented in Sec. 4.4, for the quartz pool, the wall rim is much hotter than the liquid fuel because of its proximity to the base of the flame. Therefore, a thermal boundary layer is established on the top region of the wall inner surface. Due to the temperature gradient within the wall thermal boundary layer, buoyancy forces are generated. Therefore, the liquid fuel in contact with the hot upper portion of the wall will rise toward the liquid-vapor interface and a buoyant flow will be created upwards. Once this buoyant flow reaches the top of the liquid layer it must be diverted radially inward to the pool's center in order to remain part of the pool. If the is disturbed from being horizontal, surface tension forces at the fuel interface pull downward on the upward buoyant flow and as the liquid is confined from one side by the pool wall, the flow is turned toward the pool center. Along with the need for continuity in the liquid, those two motions of upwards at the wall and then inwards support the creation of this vortex.

Another potential mechanism for creating this wall vortex could be a gradient in thermocapillary stress. If the surface tension is not uniform at the free surface, the region with higher surface tension pulls the fluid toward itself and causes fluid motion. Since surface tension is a decreasing function with increasing temperature, colder free surfaces pull the fluid from hotter regions. As discussed in Sec. 2.5 this phenomenon is pronounced in the flame spread stage of pool fires. The flame raises the local temperature of the liquid beneath itself to near boiling, while fuel in the non-burning region remains cool. For a room temperature methanol pool in the fire-spread stage there could be a 45ºC temperature difference establishing the stress difference to cause liquid motion that accelerates the flame spread over the fuel surface. In the current situation of steady-state burning the temperatures nearest to the surface while remaining immersed in the fuel are nearly uniform in the radial direction. Considering the wall vortex to be on the order of 12 mm (from the inner wall surface to the point the flow direction was changed downward), there is at most 3-4ºC temperature difference, which limits the variation of the surface tension to 3×10^{-4} N/m.

The second vortex has a counter-clockwise rotation driving fluid from the central region of the pool along the surface to form a stagnation point when it meets the wall vortex. The origins of this second vortex is less clear in whether it is simply fluid responding to viscous shear stress due to the existence of the vortex nearer the wall or whether there are separate forces on the fluid that need to be taken into account. The local evaporation of small scale non-luminous pool fires (*e.g.*, methanol) is believed to be highest close to the wall that can cause fluid motion from the pool center to the wall [19]. However, more investigations are required to determine the driving mechanisms of these vortices.

Both vortices contribute strongly to energy transfer in the upper part of the liquid pool. The wall vortex transfers heat from the wall to the liquid. As shown in Sec 4.5, the local temperature difference between the wall and the liquid fuel was substantial near the top of the pool (up to 50ºC). As a result, the buoyant flow (natural convection) was established within the top region of the pool to transfer heat from the wall to the liquid fuel.

It is apparent in Fig. 4.29-Fig. 4.34 that the thickness of the mixing motion layer and the size of the recirculation zone increase with increases in the pool depth and bottom boundary temperature. In general, these two parameters (pool depth and bottom temperatures) have the same effects on the vortical structures. Within the pool, the vortical structures are countered by shear stress which is proportional to the liquid viscosity which is a strong function of temperature. The viscosity of the liquid methanol changes by a factor of four within the temperature range of 0ºC to 60ºC [35]. By making the bottom of the pool cooler (*i.e.*, decreasing T_{bot}) or bringing the cold bottom closer to the fuel top region where the vortical structures exist (*i.e.*, decreasing the pool depth), a liquid with a greater viscosity would be at the boundary of the mixing motion layer. Therefore, the size of the vortices decreases at lower bottom temperatures and fuel depths.

Another potential mechanism can be the effect of buoyancy stratification within the liquid fuel similar to its effect in the flame spread stage [148]. The liquid temperature is higher at the top region and lower at the bottom due to the flame heat feedback from above. As a result, the liquid phase is buoyantly stable, and any vertical motion within this stable system is resisted by the buoyancy forces. By increasing the temperature difference between the liquid surface and the pool bottom (*i.e.*, by lowering T_{bot}) or decreasing the pool depth, the vertical temperature gradient increases. Therefore, the stabilizing buoyancy effect becomes stronger, and the vortical structures are prevented from further penetration through the thermally stabilized liquid layer. However, these explanations are still qualitative and more investigations are required to characterize different effects involved in this phenomenon.

As mentioned before, the results presented in Fig. 4.29-Fig. 4.34 are the mean value of 500 instantaneous velocity fields. The RMS (root mean square) deviation of these sample populations from the averaged velocity fields of different pools are shown in Fig. 4.35. It can be seen that the velocity fields are more stable for the deeper pool and the deviation increases as the pool become shallower. It is also apparent that the velocity fields are more unsteady in the regions where vortices exist. These velocity variations could be associated with the temporal and spatial unsteadiness of the flow field within the liquid phase especially where the vortical structures occurred. Although the flow distribution may be considered steady in general, at any point within the liquid phase, the magnitude and the direction of the velocity vectors change continuously. In a data set (500 flow fields), the vortical structures were maintained in the instantaneous velocity maps, but they were shifted slightly through the data set. The smaller error in the deep pool may mean that the velocity fields within the deep pool were more stable than that within the shallow pool. The RMS deviation within the deep pool was less than 3 mm/s while it was ~8 mm/s in the shallow pool.

A source of uncertainty for velocity measurements in an environment with large temperature gradient (or density gradient) is the distortion due to the refraction index variation. The temperature variation from the bottom of the pool to the pool surface is significant and can be as large as 9ºC/mm in the shallow pool. The scattered light rays from the particles are refracted as they pass through the parcels of fluid with different refractive index. Therefore the detected particle locations from the images are different from the actual locations of the particles

[183]. The quantity of the uncertainty in the velocity measurements due to this effect is unknown here, which limits the presented results to be qualitative flow visualization.

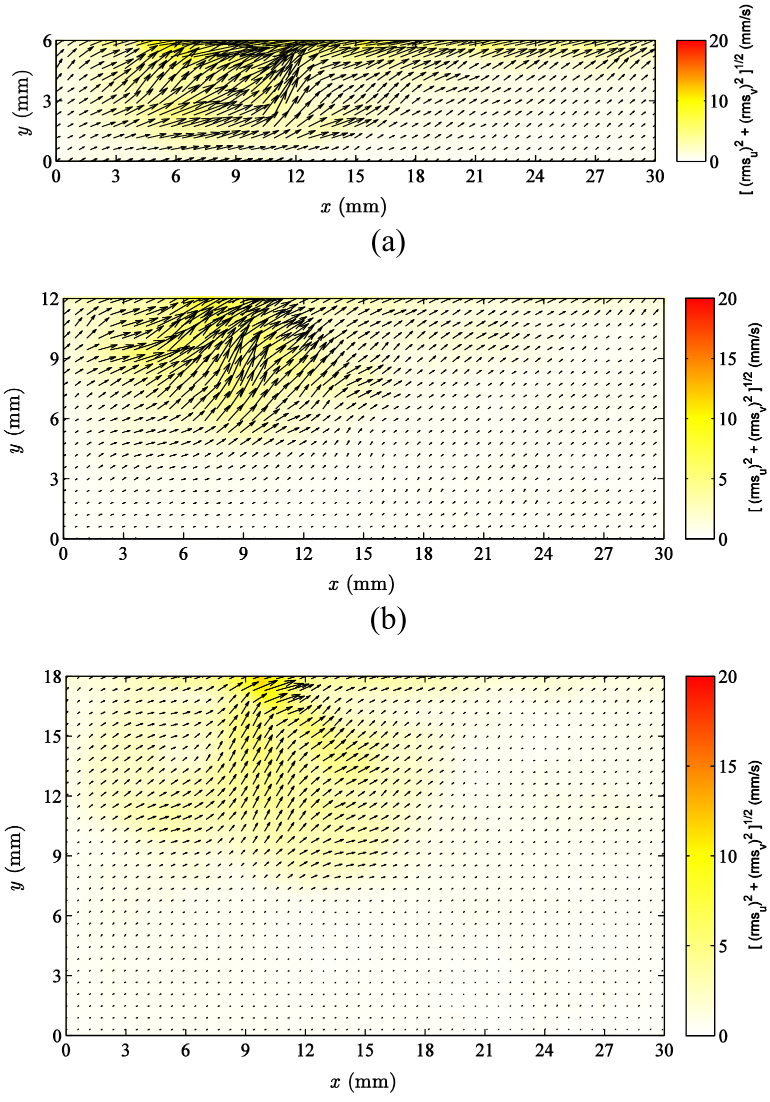

(a)

(b)

(c)

Fig. 4.35 Vector maps of the RMS deviation in velocity field with a background color map of the error magnitude within the liquid phase of (a) shallow, (b) medium and (c) deep quartz pool when T_{bot} results from setting T_{bath} = 40ºC

4.7 Conclusion

In this chapter, the experimental results for the variables of interest including burning rate, flame height, wall and liquid temperature distributions, and velocity field within the liquid phase of pool fire were presented. It was shown that typically two-layer thermal structures including a uniform temperature layer below the liquid surface and a steep gradient layer at the lower region were established within the liquid phase. Also, the velocity measurements within the liquid phase showed two strong vortices within the upper layer (uniform temperature) of the liquid fuel.

The general responses of the measured variables to the change of test parameters (*i.e.*, pool bottom temperature, pool depth and wall material) were as the following:

- Burning rate and flame height increased with an increase in the bottom temperature and the pool depth and a decrease in the wall thermal conductivity.
- The temperature distributions along the wall were strong functions of the wall thermal conductivity and varied from a uniform distribution for the copper pool to significantly non-uniform one for the quartz pool.
- It was shown qualitatively that while the copper wall heat transfer to the liquid fuel might be affected by the bottom temperature, the quartz wall heat transfer remained almost invariant.
- The configuration and the thickness of the two layers of temperature distribution within the liquid fuel were shown to be functions of the test parameters.

The energy transport phenomena within the liquid phase are studied and quantified in the next chapter in order to further investigate and justify the experimental results.

5. Heat Transfer within the Liquid Phase

In this chapter the experimental results collected in this study and presented in Chapter 4 are used to develop an energy model to investigate the heat transfer within the liquid phase of the pool fire. The approach here is to estimate the heat feedback from the flame and hot combustion products to the liquid phase, and then to provide quantitative insight into how energy is distributed within the liquid fuel. Fuel burning rate, as the pool fire characteristic that is affected by different transport phenomena, burning conditions and parameters, is used to evaluate the energy model estimations in this chapter.

5.1 Pool Wall Heat Flux

One of the main heat transfer pathways for a pool fire of the size being investigated here is the heat transfer from the hot products through the pool wall and into the liquid fuel. The local wall heat flux to the liquid fuel, $\dot{q}''_w(y)$, results from two-dimensional heat conduction through the wall material and a complex interaction with the liquid (natural convection). The experimental data gives vertically resolved internal wall $T_w(y)$ and liquid $T_l(y)$ temperatures 0.5 mm on each side from the solid-liquid interface, as shown in Fig. 5.1. The local heat flux can be estimated from the temperature gradient at the liquid-wall surface in the *x*-direction [182] as:

$$\dot{q}''_w(y) = \frac{T_w(y) - T_l(y)}{R_w + R_l} \tag{5.1}$$

where $R_w = \Delta x / k_w$ and $R_l = \Delta x / k_l$ are the wall and the liquid thermal resistances, and $\Delta x = 0.5$ mm. For the case of pool with the copper wall R_l is three orders of magnitude larger than R_w, while R_l is one order of magnitude large than R_w for the quartz pool. These relative magnitudes of thermal resistances indicate that the internal wall temperatures are reasonable estimations of the actual interface temperature especially for the copper. In addition, the numerical model of Nakakuki [106] showed that the calculated temperature of the innermost node of the wall was equal to that of the outermost node at the same vertical position for 1-2 mm thick copper, glass (Pyrex) and stainless steel pool walls.

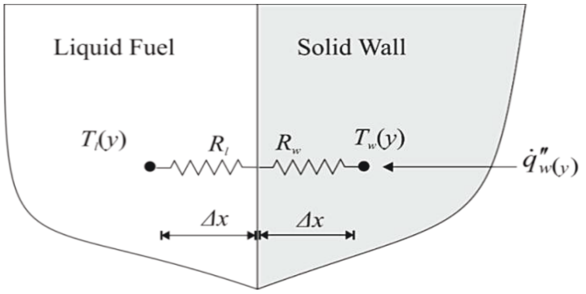

Fig. 5.1 Schematic diagram of the wall heat flux at the solid-liquid interface

The local wall heat fluxes to the liquid pool at different vertical positions are shown in Fig. 5.2 for the 12 mm deep pool with different pool wall materials and bottom boundary temperatures, T_{bot} (case 2 is the coldest and case 6 is the hottest as shown in Table 4.2). According to Eq. (5.1), and as it is illustrated in Fig. 5.1, when heat is transferred from the wall to the liquid fuel, its sign is positive and vice versa the negative sign means that heat transfers from the liquid to the wall.

It is apparent in Fig. 5.2, except within the top region of the copper pool ($y > 6$ mm) where heat flux can be negative indicating that the heat transfer is from the wall to the liquid fuel elsewhere irrespective of the pool wall material. It was shown in Fig. 4.23 (Sec. 4.5) that the characteristic temperature difference between the wall and the liquid fuel also depicted similar behaviors.

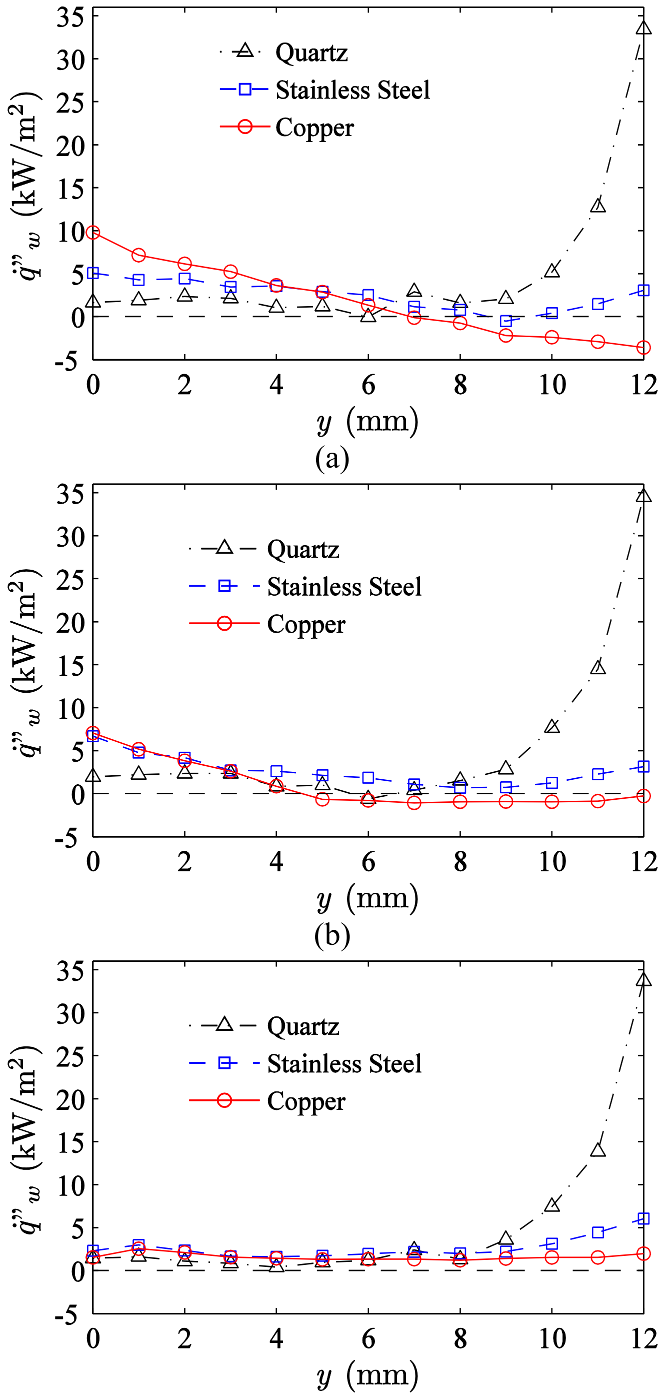

(a)

(b)

(c)

Fig. 5.2 Local wall heat flux with respect to vertical location for different pool wall materials (12 mm deep pool) when the boundary condition, T_{bot} , is according to (a) case 2 (coldest), (b) case 4, and (c) case 6 (hottest) listed in Table 4.2

The trend of the local heat flux $\dot{q}''_w(y)$ along the copper wall changes significantly by changing the boundary temperatures. It should be remembered that according to the wall temperature results presented in Sec. 4.4, the temperature of the copper wall is constant at different vertical positions and it changes uniformly by altering T_{bot}. As shown in Fig. 5.2a, at low T_{bot} the local wall heat flux decreases almost linearly with the vertical position, *y*, from 10 kW/m^2 to -4 kW/m^2. In this case, $\dot{q}''_w(y)$ is positive and relatively large within the lower region of the copper wall (*y* < 6 mm). As a result, the wall temperature drops to a value less than the liquid temperature for the top half of the wall, and the heat transfer direction switches from the liquid to the wall.

By increasing T_{bot} to case 4, Fig. 5.2b, the magnitude of the wall heat flux in both regions of the copper wall (*i.e.*, top and bottom halves) decreases. That is, less heat is transferred within the lower part since the liquid fuel is now warmer. Eventually, when the bottom temperature is high enough (*e.g.*, case 6 as shown in Fig. 5.2c), the wall heat flux becomes mostly positive throughout the length of the copper wall. Therefore, heat transfers from the wall to the liquid pool. The wall heat flux in this case is almost constant and around 1.8 kW/m^2 through the entire wall. The wall heat transfer strong dependency on T_{bot} may help to explain the relatively large variations of $\dot{m}''_b$ and l_f versus T_{bot} (shown in Sec. 4.2 and Sec. 4.3) for the copper pool.

Also, from Fig. 5.2 it is apparent that the wall heat flux trends for the quartz pool remains almost invariant as T_{bot} changes from case 1 to 3. This common trend includes a positive and relatively large heat flux of ~34 kW/m^2 at the top edge of the wall that drops rapidly within the first 4 mm. Deeper into the pool, the wall heat flux is almost constant (~1-2 kW/m^2) during the remainder of the wall length (*y* < 8 mm). The independency of the quartz wall heat transfer to the bottom temperature may explain the relatively low rates of change of $\dot{m}''_b$ and l_f with respect to T_{bot} for the quartz pool shown in Sec. 4.2 and Sec. 4.3.

Finally, the stainless steel wall heat flux is always between the values for the copper and the quartz pool in Fig. 5.2. That is, for the lower region, the stainless steel's $\dot{q}''_w(y)$ is lower than that of copper and at the top region it is lower than that of quartz.

The average wall heat flux can be determined by integrating the local values over the whole surface as

$$\langle \dot{q}''_w \rangle = \int_0^L \frac{1}{L} \dot{q}''_w(y)dy \qquad (5.2)$$

where $\langle \dot{q}''_w \rangle$ is the average wall heat flux in kW/m^2, and L is the pool depth. The averaged wall heat fluxes for different pools and bottom temperatures are shown in Fig. 5.3. The fitted lines (solid for copper, dashed for stainless steel, and dashed/dot for quartz) in Fig. 5.3 are to clarify the variation of $\langle \dot{q}''_w \rangle$ with T_{bot} trends. It is apparent that the averaged wall heat flux is the lowest for the high-thermal-conductive wall, copper, and the highest, for quartz with the lowest thermal conductivity. This is due to the large temperature difference between the wall and the liquid fuel in the quartz pool.

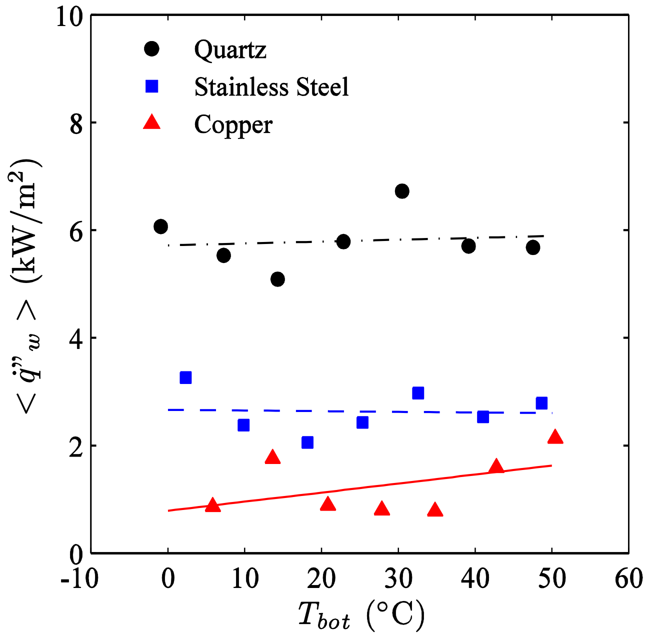

Fig. 5.3 Averaged wall heat flux with respect to the bottom temperature for different pool wall materials

5.2 Liquid Phase Energy Balance

In this section the wall heat transfer estimated in Sec. 5.1 is used in a model based on conservation of energy in the liquid phase to predict the mass burning rate, $\dot{m}''_b$. Such a model provides quantitative estimate for different heat transfer pathways to the liquid phase so that they can be evaluated against the measured burning rate (presented in Sec. 4.2).

A schematic diagram of the liquid phase energy balance is shown in Fig. 5.4. In this figure, the control volume (CV) containing only the liquid phase and the different energy fluxes into and out of the CV are illustrated. The energy fluxes are per unit pool surface area (*i.e.*, $A_p = \pi d^2/4$). Liquid fuel that enters into the CV carries an enthalpy per unit area of $\dot{m}''_b h_i$ into the CV, and the vaporized fuel leaves the volume at the pool surface with an enthalpy per unit area of $\dot{m}''_b h_o$. The difference between these two enthalpy fluxes is the required heat for the liquid fuel to warm up from the inlet temperature, T_i, to the surface temperature, T_s, and fuel evaporation, which is:

$$\dot{q}''_l = \dot{m}''_b \left(c_{p,l} (T_s - T_i) + \Delta H_v \right) \tag{5.3}$$

where $c_{p,l}$ (kJ.g^{-1}.K^{-1}) is the liquid specific heat, and ΔH_v (kJ/g) is the fuel heat of evaporation at T_s.

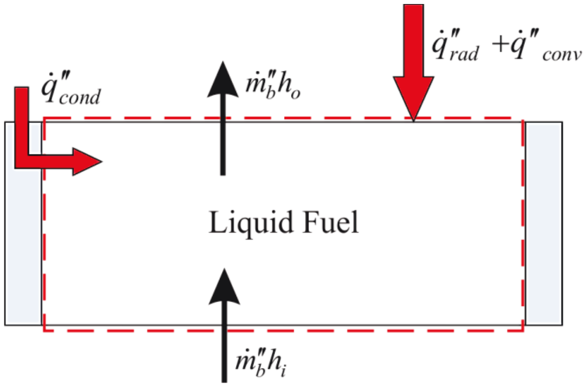

Fig. 5.4 Schematic diagram of the energy balance of liquid fuel of pool fire, showing a control volume containing the liquid fuel and different energy fluxes at its surfaces

According to the law of conservation of energy under steady-state conditions, the energy for the fuel heating and evaporation, $\dot{q}''_l$, must be balanced with the summation of the heat fluxes through the CV boundaries. In general, heat transfers from the flame and hot combustion products to the liquid pool in the forms of conduction, $\dot{q}''_{cond}$, (meaning a pathway that involves convection from the hot product gases or radiation to the solid wall and then its conduction through the solid until being convected into the liquid), direct convection, $\dot{q}''_{conv}$, and radiation, $\dot{q}''_{rad}$, from the flame to the liquid.

For small-scale pools (d < 0.1 m) the conduction heat pathway is expected to be important. Moreover, for smaller diameters of the medium pool regime (*i.e.*, 0.1 m ≤ d < 1 m) convection is expected to dominate and since the current pool is 0.09 m in diameter, convection needs to be included. Radiation is only considered important for large pools or those with luminous and soot-forming flames, but in order to avoid any assumption the radiation is also included for the given small methanol flame in this study.

As a result, under steady state condition, the energy balance of the liquid phase to create the fuel vapor, which is subsequently burned, yields:

$$\dot{q}''_l = \dot{q}''_{cond} + \dot{q}''_{conv} + \dot{q}''_{rad} \tag{5.4}$$

where $\dot{q}''_{cond}$, $\dot{q}''_{conv}$, and $\dot{q}''_{rad}$ (kW/m^2) are the conductive, convective and radiative heat transfers per unit surface area of the pool, respectively.

The convective heat transfer from the flame to the fuel surface was studied by Orloff and de Ris [126, 132]. The procedure presented in [126] to estimate the convective heat flux is applied here to calculate $\dot{q}''_{conv}$ as:

$$\dot{q}''_{conv} = \alpha \left[\frac{\Delta H_c (\chi_a - \chi_r) r}{\chi_a} - c_{p,\infty} (T_s - T_\infty) \right] E(\beta) \tag{5.5}$$

where $E(\beta) = \beta / [\exp(\beta) - 1]$, $\beta = \dot{m}''_b / \alpha$,and α is a constant that according to [126] equals to 8 (g.m^{-2}.s^{-1}) for pools without lips. The remainder of the parameters in Eq. (5.5) are the properties of methanol pool fire which are listed in Table 5.1. An empirical correlation was developed in [103] for radiative heat flux as:

$$\dot{q}''_{rad} = 68.3 \times Y_s^{1/4}\left[1-\exp\left(-\left(\frac{4}{3}\Delta H_v d\right)^{3/2}\right)\right] \tag{5.6}$$

The parameters used in Eq. (5.6) can be found in Table 5.1.

Table 5.1 Methanol pool fire properties used in Eqs. (5.5) and (5.6)

Property	Symbol	Value
Heat of combustion	ΔH_c	19.9 kJ/g [103]
Combustion efficiency	χ_a	1 [21]
Radiative heat release fraction	χ_r	0.2 [20, 113]
fuel/air stoichiometric mass ratio	r	0.156
Specific heat capacity of air	$c_{p,\infty}$	1.2×10^{-3} kJ/(gK)
Pool surface temperature	T_s	59ºC
Ambient temperature	T_∞	25ºC
Smoke yield	Y_s	0.001 (g/g) [50, 103]

According to Eq. (5.5), the convective heat flux from the flame and hot products to the liquid surface is a function of burning rate. The variation of the estimated $\dot{q}''_{conv}$ with respect to the mass flux, $\dot{m}''_b$, is apparent in Fig. 5.5 that shows a decrease in $\dot{q}''_{conv}$ with increasing the burning rate. This outcome can be due to the expansion of the fuel-rich volume immediately above the fuel surface when more fuel is evaporated [131]. The fuel vapor temperature is relatively low and cools the combustion gases. That is, more fuel vapor takes more heat from the gases above the liquid surface and decreases the convection heat feedback. Another reason could be the presence of Stefan flow (upward flow of the fuel vapor from the pool surface) [184] which at higher burning rates pushes the hot products further away from the fuel surface.

The conduction heat flux, $\dot{q}''_{cond}$, is equal to the averaged wall heat flux from Eq. (5.2) that is scaled to the heat flux per unit area of pool surface as:

$$\dot{q}''_{cond} = \left(A_w / A_p\right)\left\langle \dot{q}''_w \right\rangle \tag{5.7}$$

where $A_w = \pi dL$ and $A_p = \pi d^2/4$ are the wall and pool areas, respectively.

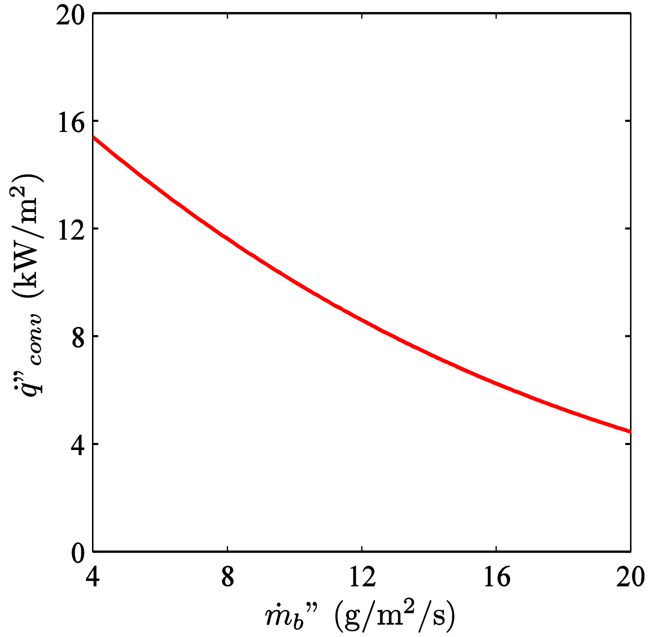

Fig. 5.5 Estimated convective heat feedback according to the method presented in [126] with respect to the pool fire burning rate

With estimates for the convection, radiation, and conduction pathways that bring energy to the liquid pool to both warm up and evaporate the fuel it is possible to estimate the mass burning rate from liquid phase energy balance as:

$$\dot{m}_b'' = \frac{\dot{q}''_{cond} + \dot{q}''_{conv} + \dot{q}''_{rad}}{\left(c_{p,l}\left(T_s - T_i\right) + \Delta H_v\right)} \tag{5.8}$$

It should be noted that for the range of the measured burning rate in this study ($8 \le \dot{m}_b'' \le 11$ g/(m^{2}s)), $\dot{q}''_{conv}$ decreases by around 2.3 kW/m^2. That is, as the correlation for $\dot{q}''_{conv}$ was itself a function of burning rate, an iterative procedure was used to estimate $\dot{m}_b''$ from Eq. (5.8).

In Fig. 5.6, the estimated burning rates, based on the liquid phase energy balance, are compared against the measured values for three different pool wall materials (*i.e.*, copper, stainless steel, and quartz), and for seven boundary temperatures ranging from 0ºC to 50ºC (listed in Table 4.2). The dashed and dashed/dotted lines in Fig. 5.6, respectively, denote ±5% and ±10% deviation from a one-to-one correspondence shown with solid line. As it can be seen the estimated $\dot{m}_b''$ are mostly within the ±5% deviation bound from the measured values (all values are within ±10% deviation bound). The good agreement with experimental data verifies that the model presented in this section based on liquid phase energy balance is a reasonably appropriate predicting tool for the burning rate of the studied pool fires. According to this approach, the heat for the fuel evaporation is mainly provided by the convection from the flame and the heat that is conducted through the wall and then convected to the liquid phase. The radiative heat flus is only ~5% relative to convective heat flux.

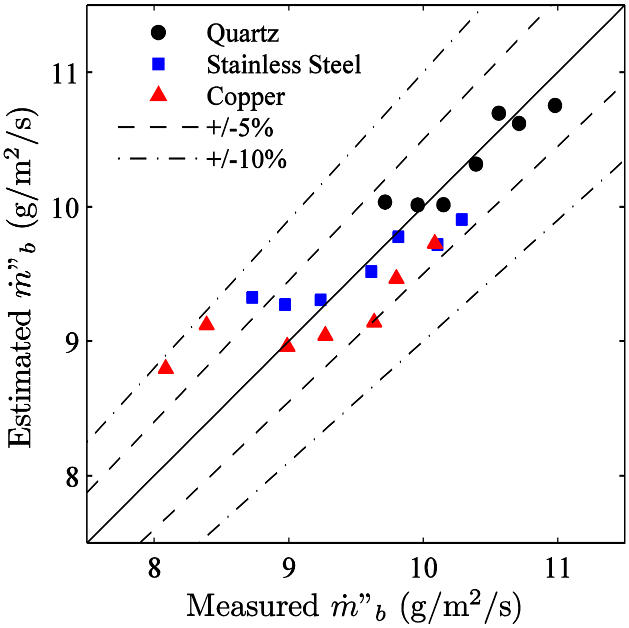

Fig. 5.6 Estimated methanol steady burning rate in comparison with the measured values for all the cases listed in Table 4.2

The ratios of conduction to convection pathway from the model, $\dot{q}''_{cond}/\dot{q}''_{conv}$, are illustrated in Fig. 5.7 for different pools (*i.e.*, copper, stainless steel, quartz) and different bottom temperatures. The lines are fitted to the values only to clarify the trends. It is apparent that among the three pools, this ratio is the largest for the quartz pool and the smallest for the copper pool for any boundary condition. For the quartz pool, the relative magnitude of the conduction to convection is 30% whereas it can be as low as 4% for the copper pool. That is, when the wall heat conductivity is low a larger portion of the required heat for the fuel evaporation is transferred from the conduction pathway (25% for the quartz pool) in comparison with the highly conductive wall (4-9% for the copper pool).

The decrease in heat conduction results in a lower burning rate for the copper pool. Due to this lower burning rate, less cool fuel vapor is emitted from the copper pool surface in comparison to the quartz pool. Consequently, as shown in Fig. 5.5, the convective heat flux from the flame to the liquid within the copper pool is ~1 kW/m^2 greater than that for the quartz pool.

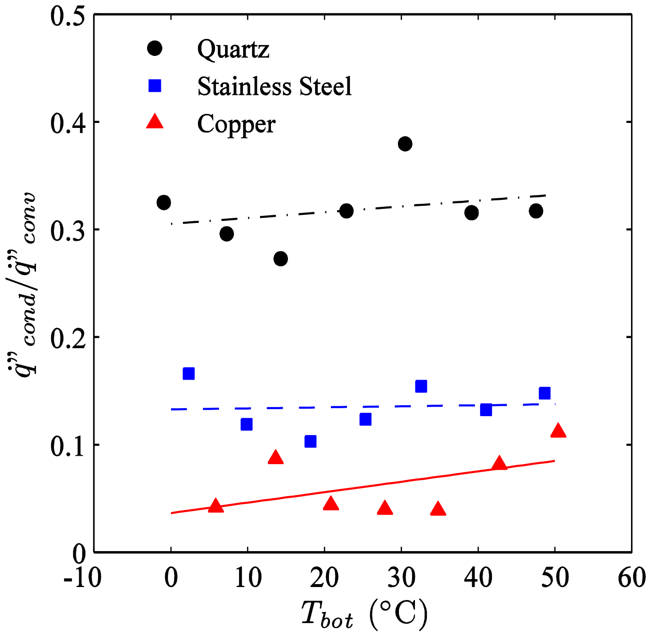

Fig. 5.7 Ratio of conduction to convection heat fluxes in respect to T_{bot} and for different wall materials

5.3 Thermal Structure within the Liquid Phase

So far in this chapter, a method has been presented to estimate the flame heat feedback to the liquid pool. Then, the mass burning rate of pool fire has been predicted from the energy balance of the liquid phase. That method was based on a CV that contained the whole liquid layer, so the complexity of the transport phenomena within the liquid was avoided. In this section, the thermal structure of the liquid phase is investigated analytically and is compared with the measured results. Here only quartz pools (*i.e.*, shallow, medium and deep pools) are considered for which more information including their flow fields is available.

According to the results presented in this study, there is a strong correlation between the temperature and velocity field variations within the liquid fuel in pool fires. The liquid thermal structure within the quartz pool is two-dimensional, steady and locally must comply with the law of conservation of energy following:

$$\rho_l c_{p,l}\left(\vec{V}.\vec{\nabla} T\right) = k_l \vec{\nabla}^2 T + \Phi + \dot{Q}''' \tag{5.9}$$

where all the properties (*e.g.*, density and thermal conductivity) are associated with the liquid fuel, and $\vec{V}$ and T are the two-dimensional velocity and temperature fields within the liquid, respectively. Φ (kW/m^3) is the energy dissipated by viscous stress and is included in Eq. (5.9) to keep the generic form of the law of conservation of energy, but it is neglected in this analysis. $\dot{Q}'''$ (kW/m^3) is the sensible energy generated within the liquid fuel. Since the fluid within the liquid phase is non-reacting, the internal energy generation must be equal to zero (*i.e.*, $\dot{Q}''' = 0$). Finally, in Eq. (5.9), $\vec{\nabla}$ is the vector differential operator defined as:

$$\vec{\nabla} = \left(\frac{\partial}{\partial x}, \frac{\partial}{\partial y}\right) \tag{5.10}$$

The mean velocity vector field and the temperature distributions for medium and deep pools with boundary temperatures of 7°C and 4°C (Case 2 in Table 4.3), respectively, are superimposed in Fig. 5.8. It is apparent that the vortices essentially only exist within the upper near-uniform temperature layer. From the wall heat flux profiles for the quartz pool (Sec. 5.1) it can be seen that the heat transfer from the wall to the liquid phase mostly occurs within the near-uniform temperature layer in the top region of the pool. Within this layer, the vortices contribute to heat transfer from hot surfaces (*i.e.*, the pool's wall and the liquid interface) to the bulk of the liquid fuel and keep the upper region at almost a constant temperature.

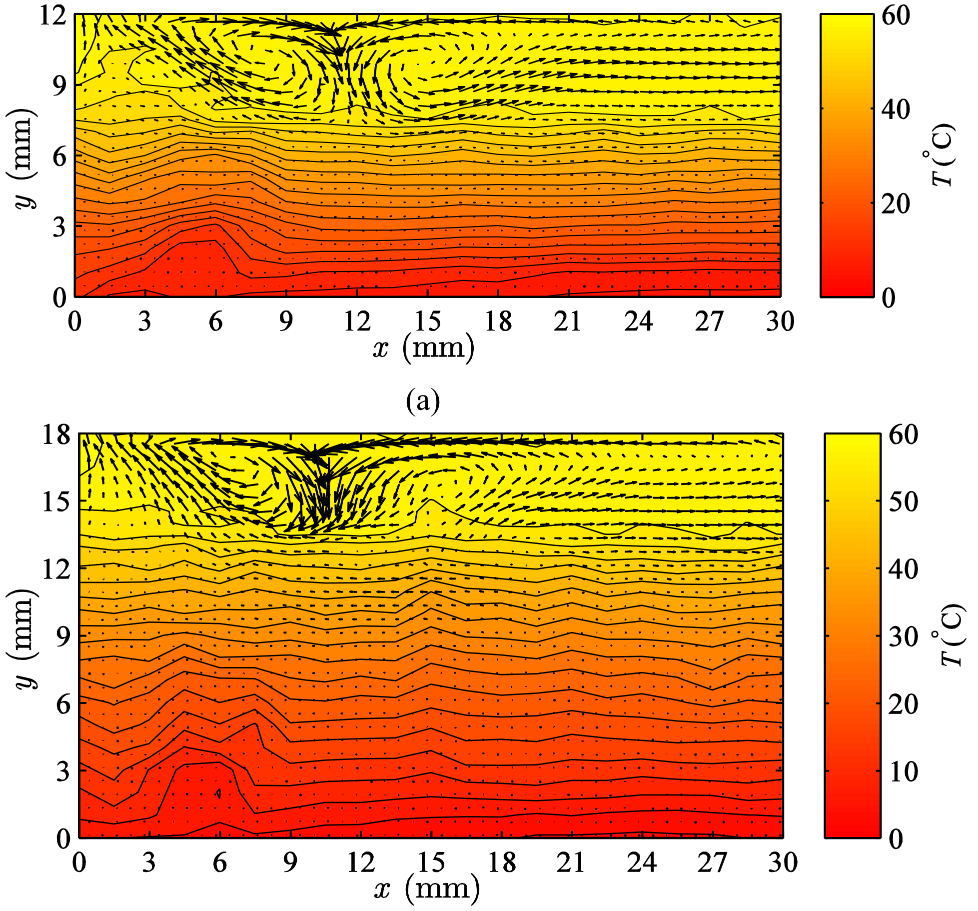

(a)

(b)

Fig. 5.8 Vector maps of the average velocity field (every 4th computed vector shown) with a background color map of the temperature distributions within the liquid phase of (a) the medium pool and (b) the deep pool when the bottom temperatures were imposed by a bath temperature of 0°C

Beneath this layer where the velocity is low, as shown in Fig. 5.8, the isotherms are almost horizontal (except a region near the wall $x < 6$ mm). The temperature difference between the liquid phase and the wall decreases in the lower region due to the rapid temperature drop vertically through the quartz walls. The wall heat flux profiles and the absence of a thermal boundary layer near the wall indicate that a relatively small heat transfer occurs from the wall to the liquid fuel in the lower region. Therefore, the driving force for convective motion is reduced deeper in the pool. As a result, without the propensity to mix, for the lower part of the pool, the liquid temperature variation is due to vertical heat conduction within an almost stable fluid.

It can be concluded that the energy distribution mechanism within the upper layer of the liquid fuel is two-dimensional and is primarily by convection. In the lower region of the liquid phase, energy transfer is mostly one-dimensional in the vertical direction by conduction due to the temperature gradient and convective transport due to the slow vertical fluid motion. These differences in the two layers of the liquid provide a natural partitioning in the system's energy transfer where the upper layer is relatively complex and difficult to quantify and the lower layer is relatively simple.

According to the experimental results in this study and as suggested in the literature [139], the temperature within the upper layer is uniform and equal to the surface temperature (~60°C). Therefore, in this analysis the liquid temperature within this layer is set to the surface temperature. For the rest of the pool depth with a thickness of δ from the bottom of the pool to the boundary between the upper and the lower region, the temperature distribution of the liquid fuel can be obtained from a one-dimensional model based on the conservation of energy. Within this region it can be assumed that the horizontal temperature variations in the *x*-direction are negligible as:

$$\frac{\partial T}{\partial x} \approx 0 \tag{5.11}$$

This assumption can be justified by the horizontal isothermal lines that are apparent in the lower region of the pool.

As a result, within the lower region (*i.e.*, $0 < y < \delta$), the conservation of energy is simplified to:

$$\rho_l c_{p,l} v \frac{dT}{dy} = k_l \frac{d^2 T}{dy^2} \tag{5.12}$$

Substituting $\dot{m}''_b = \rho_l c_{p,l}$, and using the non-dimensional temperature, θ, defined in Eq. (4.2) and vertical location normalized with respect to the thickness of the lower region ($y^+ = y/\delta$) Eq. (5.12) becomes:

$$\frac{d^2\theta}{dy^{+2}} - Pe\,\frac{d\theta}{dy^{+}} = 0 \tag{5.13}$$

where *Pe* is the Peclet number defined as:

$$Pe = \frac{c_{p,l}\dot{m}''_b\delta}{k_l} \tag{5.14}$$

The Peclet number indicates the importance of the heat convection (second term in Eq. (5.13)) to the heat conduction (first term) in the lower region.

As *Pe* approaches zero, the problem can be assumed to be one-dimensional conduction through a stationary liquid. However, the *Pe* number is around 1-2 for the pools studied here. An increasing *Pe* means that the convection effects become increasingly important. The convection heat transfer in this case can increase the heat transfer through the lower layer by ~50-100% compared to the one-dimensional conduction model. The fluid motion brings the cold liquid from the bottom of the pool to a distance closer to the fuel surface, so the temperature gradient immediately underneath of the uniform-temperature layer increases. Consequently, the heat transfer through the bottom layer increases with the *Pe*. More discussion on the effect of vertical fluid motion on the thermal structure within the lower liquid layer can be found in Appendix D.

Using the following boundary conditions to solve Eq. (5.13),

$$\begin{aligned}\theta(0) &= 0\\ \theta(1) &= 1\end{aligned} \tag{5.15}$$

the solution would be as:

$$\theta(y^{+}) = \frac{\exp(Pe\,.y^{+}) - 1}{\exp(Pe) - 1} \tag{5.16}$$

Having the temperature within the upper layer equal to the surface temperature the solution can be extended to the entire pool depth as:

$$\begin{cases} T(y) = \left(T_s - T_{bot}\right)\left\{\dfrac{\exp(Pe\,.\,y/\delta) - 1}{\exp(Pe) - 1}\right\} + T_{bot} & y < \delta \\ T(y) = T_s & y > \delta \end{cases} \tag{5.17}$$

The thickness of the lower layer, δ, is required for this solution to be complete. The estimation of this quantity requires the analysis of the transport phenomena within the uniform-temperature layer, which as mentioned earlier is 2D and complex. Therefore, to avoid this complexity and derive a solution, Eq. (5.17) was compared with the experimental data and the thickness value that gave the least root-mean-square (RMS) difference at any specific condition was determined. For the three circular pools of different depths (*i.e.*, shallow, medium, and deep), the RMS difference obtained from these comparisons using different values for δ are shown Fig. 5.9.

The values of δ that gave the lowest RMS difference for the comparison between the experiments and the solution, Eq. (5.17), and the thickness of the uniform-temperature layer are presented in Fig. 5.10 with respect to the bottom temperature. Based on the results presented in Fig. 5.10, the liquid phase of the pool fire may be classified to two regimes namely thin and thick liquid layer. In the first regime the thickness of the uniform-temperature layer is affected by the bottom temperature, while a thick liquid layer is independent from T_{bot} .

It is apparent in Fig. 5.10 that δ decreases with bottom temperature increasing in the pools with 6 mm and 12 mm depth (*i.e.*, the shallow and medium pools). According to the results, these variations are also almost linear and happen at a same rate with respect to T_{bot} . It can be seen that the slopes of the dashed line ($\delta = -0.07\,T_{bot} + 8.93$, R^2 = 0.888) and the solid line ($\delta = -0.07\,T_{bot} + 6.03$, R^2 = 0.986) that represent the variations in the thickness of the lower layer versus the bottom temperature for medium and shallow pools, respectively, are almost identical. As a result, the thickness of the uniform-temperature layer (*i.e.*, L-δ) increases as the bottom of the pool becomes hotter. This result puts the shallow and medium pools into the thin liquid layer category.

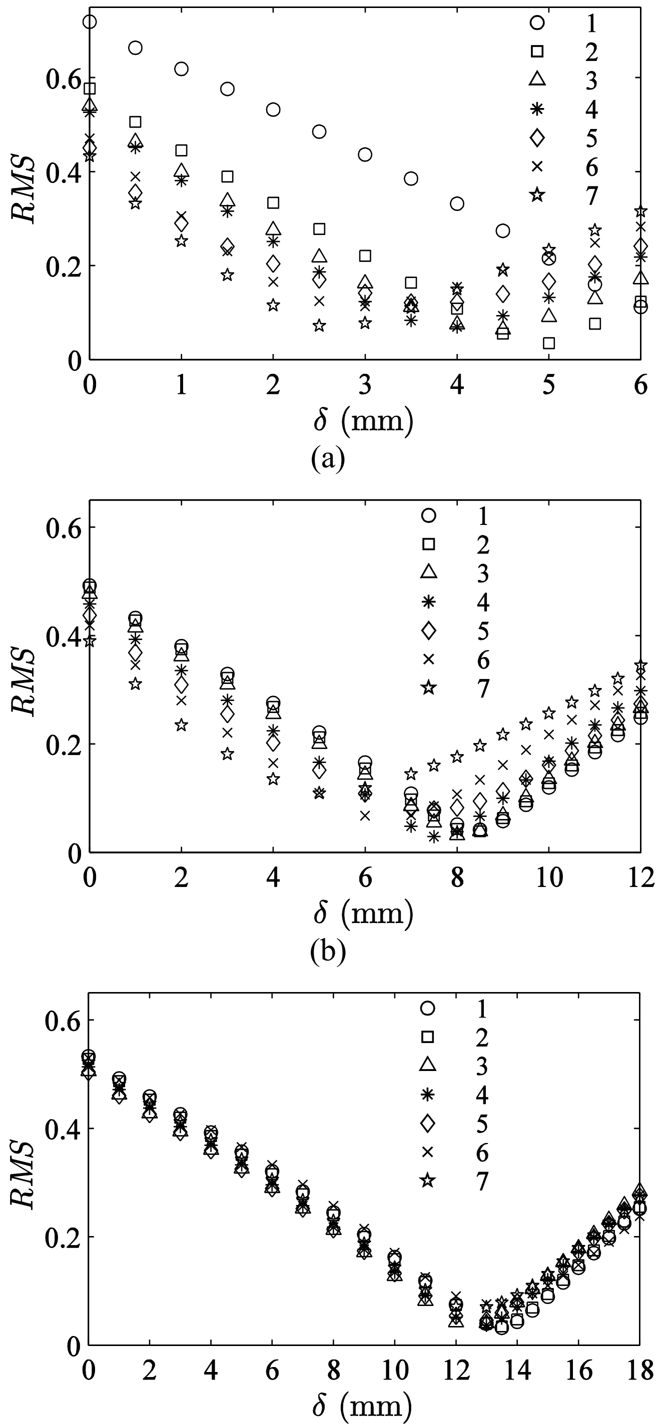

(c)

Fig. 5.9 The RMS difference of the analytical solution in comparison with the experimental results for liquid temperature with respect to the thickness used in the solution to predict the liquid thermal structure within (a) shallow, (b) medium, and (c) deep pool; the numbers in the legends are according to Table 4.3

As it can be seen in Fig. 5.10, the lower layer thickness, δ, is almost invariant with respect to T_{bot} for the deep pool (L = 18 mm). Therefore, the deep pool can be classified as a thick liquid layer, and for this specific pool geometry, it can be concluded that the transition from the thin to the thick layer regime happens at a pool depth between 12 mm and 18 mm. The pool diameter may also play a role in this classification so further investigation involving various pool diameters is required to characterize the pool depth at which the liquid phase pattern changes in general.

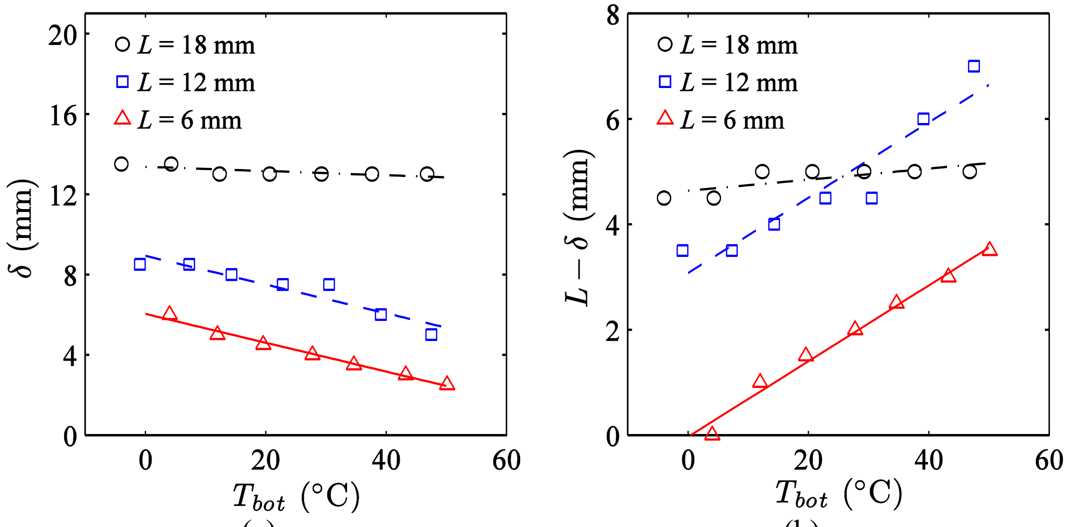

(a) (b)

Fig. 5.10 The thickness of (a) the lower layer and (b) the uniform-temperature layer with respect to the bottom temperature

As discussed in Sec. 4.6, a thermally stratified region is established beneath the uniform-temperature layer within the pool. This lower region is stable due to the buoyancy that resists any effects, such as liquid motion, that disturbs the thermal stratification. In the thin liquid layer regime (*i.e.*, medium and shallow pools in this case), the spread of the uniform-temperature layer which may be established as a result of mixing motion (*i.e.*, counter-rotating vortices) is prevented by the thermally stratified layer within the pool. Buoyancy effects increase with the temperature gradient within the pool due to either an increase in temperature difference between the pool bottom and surface or a decrease in the pool depth. When the temperature gradient is very large, there are also possibilities for the uniform-temperature layer to disappear completely as it was observed for the lowest bottom temperature in the shallow pool. In this case the average temperature gradient is 9°C per millimeter. By increasing the pool depth from the thin to the thick layer regime, the thermally stratified region is established adequately further away from the liquid surface that it no longer affects the uniform-temperature layer extension. Therefore, the thickness of this layer remains constant.

Using the thickness, δ, the temperature profiles within the liquid fuel are calculated and their comparisons against the measured values are illustrated in Fig. 5.11, Fig. 5.12, and Fig. 5.13. In these figures the lines are the calculated temperature profiles according to Eq. (5.17) using the model for δ, the symbols are experimental data, and the error bars represent the 95% confidence bounds for the data. It is apparent that the comparison is in a reasonably good agreement with the measured liquid temperature within the pools of different depth and at different boundary temperatures.

Except for the case of the shallow pool at its lowest boundary condition (Fig. 5.11a) where the largest difference between the solution and experimental data is around 10°C, the discrepancies are less than 2-3°C for all the presented cases. For the shallow pool at the lowest bottom temperature, the uniform temperature layer completely disappears and the thermally stratified layer starts right below the liquid surface. For this condition, the liquid surface temperature was also influenced by the bottom temperature and was recorded to be 3-4°C lower than the typical surface temperature (*i.e.*, ~60°C). The agreement for this case could be improved by using a lower surface temperature, which was avoided to keep the solution consistent for all cases.

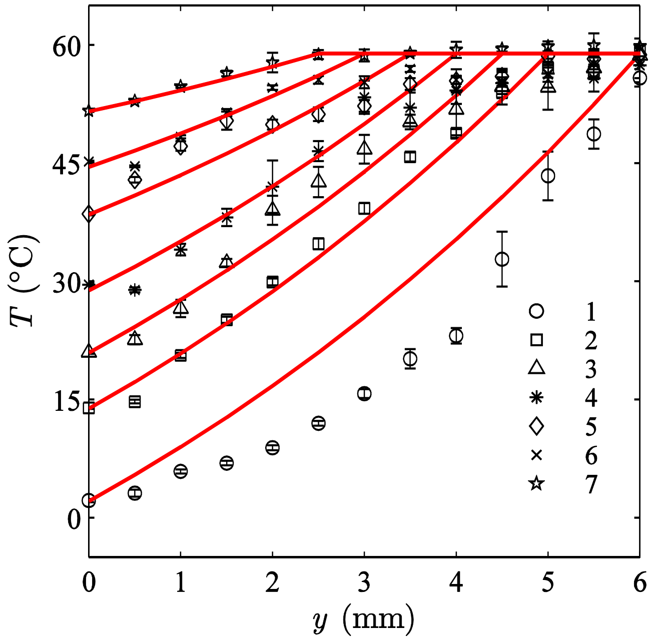

Fig. 5.11 Measured temperatures within the shallow pool (symbols) compared to the solution (lines). The numbers are according to Table 4.3

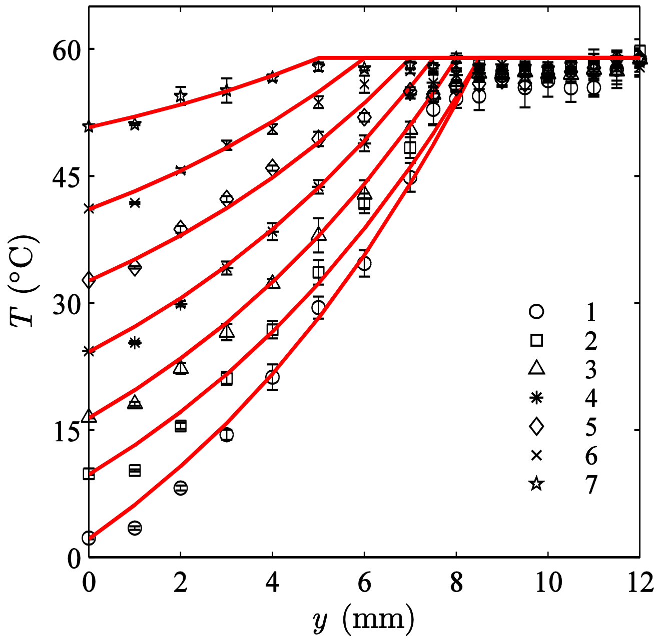

Fig. 5.12 Measured temperatures within the medium pool (symbols) compared to the solution (lines). The numbers are according to Table 4.3

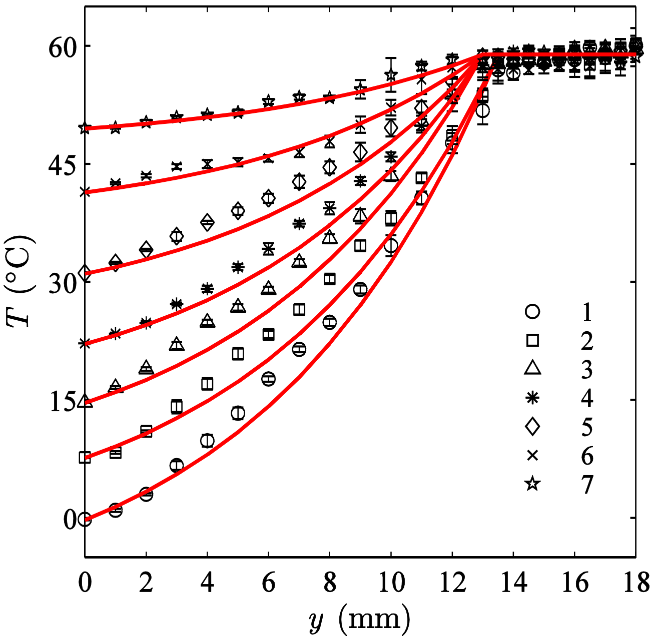

Fig. 5.13 Measured temperatures within the deep pool (symbols) compared to the solution (lines). The numbers are according to Table 4.3

5.4 Energy Transfer to the Sub-layer

Having the liquid temperature distributions from the model presented in the previous section, the heat transfer to the liquid bottom layer of the circular quartz pool of different depths is predicted here. The model then is validated against the measured burning rate, to evaluate the physics considered for the liquid phase. The analysis is again based on conservation of energy but this time the control volume only contains the uniform temperature layer established at the upper region of the liquid pool as shown in Fig. 5.14. It is worth emphasizing that the thickness of the CV (shown with dashed line) is variable, and equals the pool depth, L, minus the thickness of the lower region, δ, as determined in the previous section.

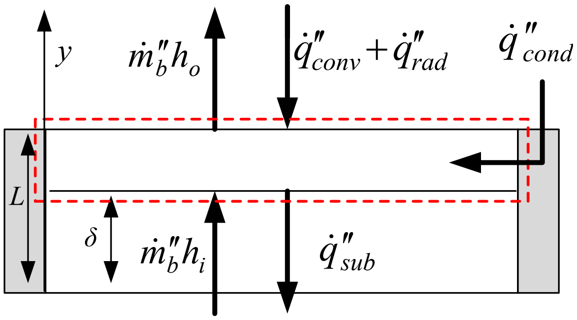

Fig. 5.14 Schematic diagram of a control volume containing the uniform-temperature layer at the top region of the liquid phase and different energy transfer mechanisms at its surfaces

The energy balance of the CV shown in Fig. 5.14 per unit area of the pool requires:

$$\dot{m}''_b (h_o - h_i) = \dot{q}''_{conv} + \dot{q}''_{rad} + \dot{q}''_{cond} - \dot{q}''_{sub} \tag{5.18}$$

where h_i and h_o (kJ/g) are the enthalpy of the liquid at the inlet and outlet of the CV, respectively, and $\dot{q}''_{sub}$ (kW/m^2) is the heat transfer from the uniform temperature layer to its cooler sub-layer. This heat transfer can be calculated from the derivative of the solution for the liquid temperature in the lower liquid layer given by Eq. (5.17) as:

$$\dot{q}''_{sub} = -k_l \left. \frac{dT}{dy} \right|_{y=\delta} \tag{5.19}$$

$\dot{q}''_{conv}$, $\dot{q}''_{rad}$ and $\dot{q}''_{cond}$ are the flame heat feedback in forms of convection, radiation and conduction, respectively. The convection and radiation heat pathways are determined using Eqs. (5.5) and (5.6), respectively. The conduction is determined from the wall heat flux distributions calculated in Sec. 5.1. as:

$$\dot{q}''_{cond} = \frac{4(L-\delta)}{d} \int_{\delta}^{L} \dot{q}''_w(y)\, dy \tag{5.20}$$

It is important to note that here as the CV only contains the upper layer, the wall heat transfer is determined within the first *L*-*δ* from the top edge of the pool wall (*i.e.*, from $y = \delta$ to $y = L$). It is also assumed that the wall heat flux distribution within the top region, $\dot{q}''_w(y)$, is the same for all three quartz pools (*i.e.*, shallow, medium and deep pools). Showing that the quartz wall heat flux profiles are almost independent from the bottom temperature in Fig. 5.2, this assumption is reasonable.

As the temperature within the CV remains constant, the sensible enthalpy of the liquid does not change and the enthalpy difference between the inlet and outlet equals to the heat of evaporation. Therefore, the burning rate can be determined as

$$\dot{m}''_b = \frac{\dot{q}''_{conv} + \dot{q}''_{rad} + \dot{q}''_{cond} - \dot{q}''_{sub}}{\Delta H_v} \tag{5.21}$$

The correlation for convection and the temperature solution are also functions of burning rate, so an iterative procedure was used to calculate $\dot{m}''_b$. The burning rates for the shallow, medium and deep pools calculated from Eq. (5.21) in comparison with the measured values are illustrated in Fig. 5.15.

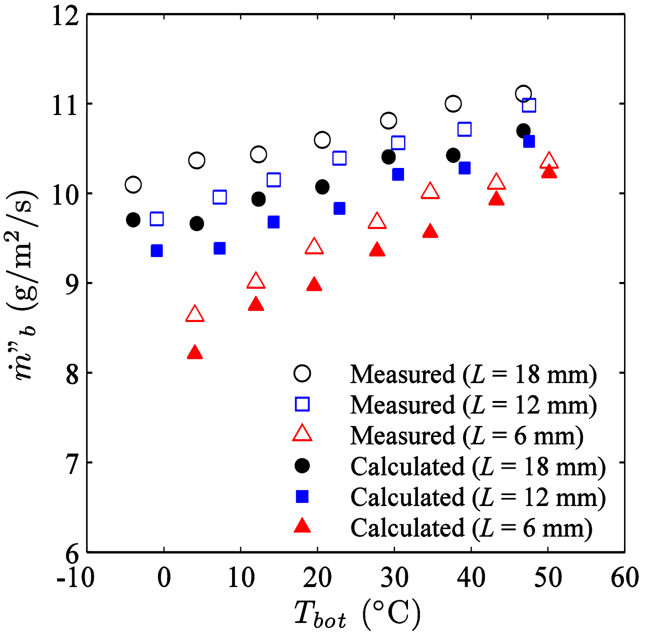

Fig. 5.15 Calculated methanol burning rate with respect to the bottom temperature in comparison with the measured values for shallow, medium and deep quartz pool. The convection heat feedback was determined according to [126]

It is apparent in Fig. 5.15 that the calculated $\dot{m}''_b$ variations with T_{bot} follow almost exactly the same trends as the measured ones do. However, the calculations underestimate the burning rate in the worst case with 0.5 g/(m^{2}s), which means that less than 0.6 kW/m^2 worth of heat flux is missed in this analysis (less than 6% of $\dot{q}''_{conv}$). This discrepancy is independent from the pool depth and the bottom temperature, suggesting it should be associated with the direct heat feedback from the flame to the liquid surface. Therefore, it may be due to the correlations used for convection and radiation heat pathway in this model.

Ditch et al. [103] proposed that the convective heat flux is almost constant and is equal to 12.5 kW/m^2. When this value was used for $\dot{q}''_{conv}$ in Eq. (5.21), the burning rate was re-calculated and the results are shown in Fig. 5.16. In comparison with Fig. 5.15 the calculated values are now in the range of the experimental results, especially at lower boundary temperatures, but the slopes of the variations do not agree as well as those shown in Fig. 5.15. It can be concluded that the comparison could be very close if an accurate model for the convection heat feedback was available.

Finally, the change in the heat flux to the sub-layer, $\dot{q}''_{sub}$, calculated from Eq. (5.19) with respect to T_{bot} for shallow, medium and deep pools are presented in Fig. 5.17. The heat flux to the sub-layer can be elucidated by the sensible energy that is required by the cooler liquid to warm up from the inlet temperature to the pool surface temperature. It is apparent that $\dot{q}''_{sub}$ can be as large as 3 kW/m^2, which is equivalent to ~20% of the total flame heat feedback to the pool. Therefore, in order to establish an exact energy balance of the pool fire, the sensible energy within the liquid phase must be accounted for.

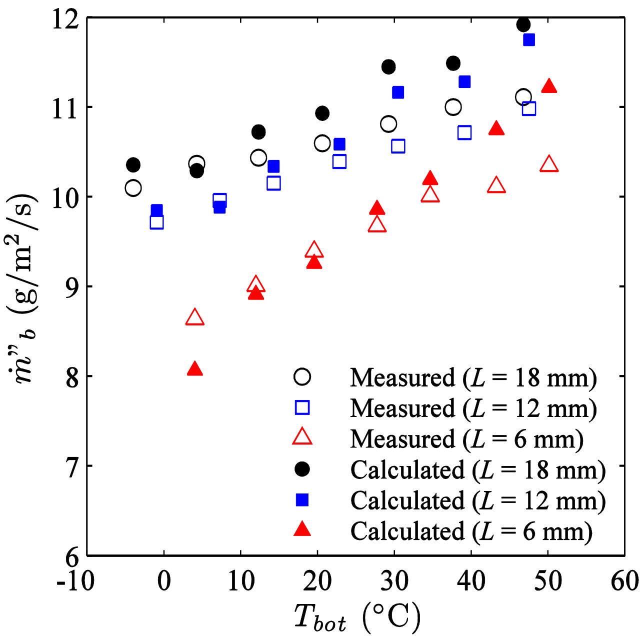

Fig. 5.16 Calculated methanol burning rate with respect to the bottom temperature in comparison with the measured values for shallow, medium and deep quartz pools. A constant value as suggested in [103] was used for $\dot{q}''_{conv}$

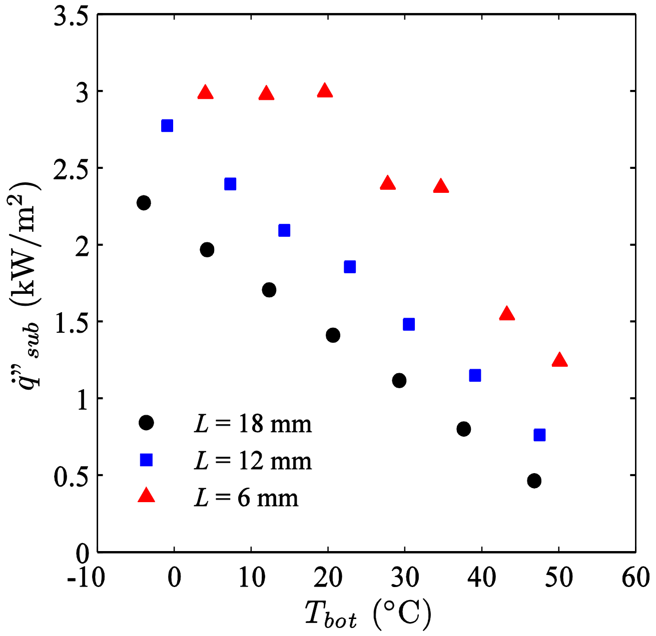

Fig. 5.17 The calculated heat flux to the sub-layer from the bottom of the CV shown in Fig. 5.14 with respect to the bottom temperature in shallow, medium and deep quartz pools

Fig. 5.17 also highlights the causes for the fuel burning rate reduction as the bottom temperature is lowered or when the pool becomes shallower. Considering the CV around the uniform temperature layer the sensible enthalpy difference of the flow into and out of the CV is constant. Only the heat lost from the bottom of the CV to the lower liquid layer, $\dot{q}''_{sub}$, is variable. According to Eq. (5.19) , this heat flux is proportional to the temperature gradient within the lower region, and increases as a result of either larger $T_s - T_{bot}$ or smaller δ. Therefore, due to the higher heat flux to the sub-layer at lower T_{bot} (T_s is constant) or in shallower pool, there is a lower amount of energy available for the fuel evaporation and consequently the burning rate reduces.

5.5 Conclusion

In this chapter, a systematic energy analysis of the liquid phase of pool fire was presented to explore and quantify different heat transfer pathways from the flame and hot products to the liquid pool. The wall heat flux was estimated from the measured temperature gradient at the wall-liquid interface. The convective and radiative heat pathways were calculated using the correlations from the literature. This model predicted the steady-state burning rate of the medium pool with different wall materials (copper, stainless steel, and quartz) within 10% of the measured burning rate. The model suggested that the required sensible and latent energy of the liquid fuel was provided mainly by direct convection from the flame and combustion products to the liquid surface and also by the heat transferred through the wall into the liquid pool (conduction). The importance of the conduction pathway increased with a decrease in the wall thermal conductivity.

The liquid temperature distributions within the quartz pool with different depths were also driven analytically, which were in reasonably good agreement with the measured profiles. According to this analysis, liquid motion was important even within the lower region of the liquid phase where no significant mixing motions were observed. Using this solution in the energy model for the liquid phase, it was found that the sensible energy change within the pool was noticeable and should be included in the energy analysis of the system.

6. Conclusion and Future Works

This study was aimed to help understand the transport processes involved within the liquid phase of pool fires. The phenomena of interest were mainly those that transfer energy to the liquid pool from the flame and those that redistribute this energy within the liquid fuel in a steady-state laboratory-scale methanol pool fire. After reviewing the literature, the key variables for this investigation were identified. An experimental apparatus was designed and constructed to have well-defined boundary conditions on the liquid-side. Appropriate testing methods were developed to collect data including the burning rate, flame height, as well as the temperature and velocity within the pool. The experimental results were analyzed to explore the effects of changes in the liquid-side boundary conditions (*i.e.*, bottom temperature, wall material and pool depth) and to develop models for better understanding of small-scale pool fires.

The highly controlled experimental setup enabled establishing steady-state steady-flow burning condition by maintaining a constant fuel level to the top edge within the pool during the tests. Furthermore, it allowed well-prescribed liquid pool parameters including the pool bottom temperature (*i.e.*, 0ºC to 50ºC), wall thermal conductivity (*i.e.*, wall made of copper, stainless steel, and quartz), and depth (*i.e.*, 6, 12, and 18 mm). The tests were conducted under quiescent environment conditions at the atmospheric pressure and typical room temperature (~22°C) by using two burners: a square burner with a width of 70 mm and a circular burner with a diameter of 90 mm, all with 2.5 mm thick walls.

The experimental results for the measured variables were presented and their trends with respect to the pool parameters were discussed in this thesis, which are summarized here. The measured burning rate and the flame height have been compared to data and correlations from the literature, and good agreement was shown. From the experimental results, the general effects of various test parameters on methanol pool fires were observed as the following: the burning rate, $\dot{m}''_b$, and the flame height, l_f, increased by increasing the bottom temperature, T_{bot}, increasing the pool depth, L, and by lowering the pool wall thermal conductivity.

The rates of these variations were also functions of the test parameters. For example, while $\dot{m}''_b$ and l_f rose by 25% and 27% for the copper pool over the range of T_{bot}, these variations were found to be 13% and 9% for the quartz pool (quartz had a thermal conductivity two orders of magnitude smaller than that for the copper wall). Moreover, $\dot{m}''_b$ and l_f increased by 20% and 25% for the shallow pool (*i.e.*, $L = 6$ mm) by increasing T_{bot} from around 0ºC to 50ºC, but the rates of increase were lowered to 4% and 6% for the deep pool (*i.e.*, $L = 18$ mm) over the same range of T_{bot}. Therefore, it may be concluded that the sensitivity of the pool fire variables (*i.e.*, burning rate and flame height) to the liquid-side boundary condition, T_{bot}, increases for shallower pools or those with higher wall thermal conductivity.

The temperature measurements at different vertical positions within the pool walls revealed that the different pool walls adopted different thermal structures as a result of being in proximity with the flame and hot combustion products at the top and cool liquid at the bottom. The temperature within the copper wall was constant over the pool full depth and in the range of 40ºC to 66ºC depending on T_{bot}, while the stainless steel wall temperature increased almost linearly from the bottom to the top. For the quartz pool, the top region of the wall near the flame was significantly hotter than the other two pool wall materials (~110ºC at 1 mm below the rim), dropping rapidly through the top 1/3 of the wall to become almost the same temperature as the liquid in the lower region.

The temperature distributions within the liquid fuel showed that, in general, a two-layer thermal structure was developed within the pool at steady-state. The top layer below the fuel surface was almost uniform while the lower layer had a relatively steep temperature gradient. However, this general structure was affected strongly by the boundary conditions experienced by the pool. It was shown that while above a certain pool depth (*e.g.*, the deep pool) the thickness of the uniform-temperature layer was independent from the bottom temperature. In contrast, this thickness decreased by 60% as T_{bot} was reduced from 50ºC to 0ºC in the shallow and medium pools. In the shallow pool, this layer could be made to vanish at the lowest T_{bot}. The two-layer thermal structure was also formed within the copper, stainless steel and quartz pools at higher boundary temperatures. However, as the bottom temperature decreased to its minimum, this layer diminished and eventually completely disappeared in the copper and stainless steels pools. That is, the sensitivity of the thickness of the uniform-temperature layer to T_{bot} was also increased with an increase in the wall thermal conductivity.

The velocity field, measured by 2-component PIV, within the liquid phase revealed the presence of large mixing motions within the liquid pool. Two main vortices were detected. One vortex close to the wall associated with the buoyant flow near the hot burner walls was seen as responsible for transferring heat away from the hot wall. The other vortex was counter-rotating and participated in transporting this energy toward the pool's center. Both vortices were observed to be only present in the top region of the liquid layer. The presence of these vortical structures appears to be the reason for the near-uniform temperature seen in the top layer of liquid thermal structure. In the lower region of the pool, no significant motion was observed (other than vertical motion needed to keep the pool level fixed, which is of the order of 1 mm/min), which allowed the steeper temperature gradient in the lower part of the liquid fuel thermal structure to be established.

The local wall heat flux as a function of vertical location (pool depth) was estimated from the vertical liquid and wall temperature gradients measured in this study. The results showed that most of the heat transfer from the quartz wall to the liquid occurred in a few millimeters of the top region. Moreover, the copper wall at the lower bottom boundary conditions actually extracts heat from the liquid near the top, while in the lower region the heat transfer was from the warm wall to the cooler liquid fuel. Overall wall heat transfer was also higher for the quartz pool compared to the metallic pools (*i.e.*, stainless steel and copper). As a result, the burning rate (and flame height) increased when the pool wall thermal conductivity dropped. The higher sensitivity of $\dot{m}_b''$ and l_f to bottom temperature for the copper pool was attributed to the variations in copper wall heat flux with respect to T_{bot} while the quartz wall heat flux is almost independent from T_{bot} .

An energy balance analysis was also presented that used the estimated wall heat flux to predict the burning rate within ±10% of the measured values. The model suggested that there were two main heat transfer pathways for the methanol pool fires investigated here. These pathways were direct convection from the flame and hot products to the liquid surface and the heat that was conducted through the pool wall and then transferred to the liquid with natural convection. However, the proportions of these heat pathways, the ratio of conduction to convection, changed with pool wall materials from 4%-10% for the copper pool to 26%-37% for the quartz pool. The radiation was estimated to be around 5% relative to the convection heat pathway.

An analysis for the temperature within the liquid layer was developed based on the conservation of energy. According to this analysis, the liquid phase was divided vertically into two layers each with different patterns of energy transfer. The upper and lower layers contained the uniform-temperature and relatively steep gradient regions, respectively. The temperature within the upper layer was set to the liquid surface temperature, and it was assumed that the energy model for the lower layer was one-dimensional conduction and convection normal to the pool surface. Therefore, the solution of the energy equation showed that the liquid temperature increased exponentially from T_{bot} at the bottom of the pool to the fuel surface temperature, T_s, at the bottom of the uniform temperature layer. The analytical solution was compared to the measured temperature distributions at different vertical locations within the pool and a good agreement (discrepancy less than 3ºC) was observed. This comparison supported the hypothesis applied in the analytical solution development that the heat transfer in the lower region was not only in the form of conduction but also in the form of convection. The *Pe* number was 1-2 for the pools investigated in this study, so it was shown that convection was important even in the region without large-scale mixing motions (*i.e.*, the lower region of the pool with relatively steep temperature gradient).

Finally, another energy balance analysis was presented to predict the mass burning rate. This model included the flame heat feedback (in the forms of convection, radiation and conduction) and sensible and latent heat requirements for liquid fuel evaporation. The solution for the liquid temperature was used to quantify the sensible heat requirement within the pool for preheating the liquid fuel to the surface temperature. The model predictions for methanol burning rate were in good agreement with the measured values (the agreement depended on the accuracy of the correlation used for the convective flame heat feedback from the literature). After the model validation was confirmed, it was shown that the sensible heat requirement within the pool could be as large as 20% of the overall heat transfer from the flame to the liquid pool. Therefore, in order to establish an accurate energy balance of the system, the liquid sensible energy had to be accounted for. It was also found that this sensible energy increased with lowering the pool depth and bottom temperature. This resulted in less available energy for the fuel evaporation, which eventually led to the burning rate, $\dot{m}''_b$, (and consequently flame height) reduction.

In conclusion, some recommendations for future research on pool fire are proposed based on the current study.

- A fuel with a non-luminous flame (*i.e.*, methanol), which generated very low level of thermal radiation, was studied here. Other fuels especially those with high tendency to produce soot can be investigated to find the effects of the radiation on the liquid phase.
- Various pool geometries including different pool diameters and shapes can be studied. The importance of the liquid phase phenomena is mostly ignored for the larger pools, and this assumption requires evaluation.
- From the literature and the observation during the data collection, it was seen that the burning rate could be different if a gap was allowed between the liquid surface and pool rim (*i.e.*, freeboard). This effect needs to be investigated to characterize the mechanisms involved.
- In this study, two different regimes were detected for the liquid thermal structure behavior to the pool depth and bottom temperature variations. In

the first regime the uniform temperature layer was affected by the bottom temperature (denoted as a thin liquid layer) and in the second regime the pool is sufficiently deep that the uniform temperature layer remained unaffected (a thick liquid layer). More pool depths, sizes, and fuels need to be investigated to characterize these regimes.

- A marching method was used for liquid temperature measurements, which was limited to the steady-state condition. If instantaneous temperature fields could be measured, the transient trends of the temperature fields within the liquid phase could be captured. Such an investigation allows a better understanding of the transport phenomena that resulted in uniform temperature layer formation.
- More accurate PIV measurement is required in order to quantify the velocity vectors within the liquid phase. The out-of-plane motion may be important, which suggests that a 3D technique (*e.g.*, Stereo PIV) would be better.
- It would be also interesting to investigate the effects of wind on the liquid phase. This can change the distribution of the heat transfer from the flame to the liquid and can affect the burning rate and flame structure, but its effects on the transport phenomena within the liquid are underrepresented.

References

[1] The Buncefield Incident 11 December 2005: The final report of the major incident investigation board, 2008.

[2] B. Zheng, G-.h. Chen, Storage tank fire accidents, Process Safety Progress, 30(3) (2011) 291-293.

[3] http://www.cbc.ca/.

[4] Alberta fire commissioner's statistical report, 2012.

[5] M.S. Wijayasinghe, T.B. Makey, Cooking oil: a home fire hazard in Alberta, Canada, Fire Technology, 33(2) (1997) 140-166.

[6] A health and safety guideline for your workplace: Flammable liquid storage, Industrial Accident Prevention Association, 2008.

[7] Handling and storage of flammable materials at the work site, Government of Alberta, 2009.

[8] National Fire Protection Association, Flammable and combustible liquids code, NPFA No. 30, 2003.

[9] National Fire Protection Association, Life safety code, NPFA No. 101, 2006.

[10] National Fire Protection Association, Standard for the installation of sprinkler systems, NPFA No. 13, 1999.

[11] D.T Gottuk, J.L. Scheffey, F.W. Williams, J.E. Gott, R.J. Tabet, Optical fire detection (OFD) for military aircraft hangars: final report on OFD performance to fuel spill fires and optical stresses, Naval Research Laboratory, 2000.

[12] D. Drysdale, Introduction to fire dynamics, 2nd ed., John Wiley & Sons, New York, 1998.

[13] P. Joulain, The behavior of pool fires: state of the art and new insights, Proceedings of the Combustion Institute, 27 (1998) 2691-2706.

[14] P. Joulain, Review Artide: Convective and radiative transport in pool and wall fires: 20 years of research in poitiers, Fire Safety Journal, 26 (1996) 99-149.

[15] D.B. Spalding, The combustion of liquid fuels, Symposium (International) on Combustion, 4(1) (1953) 847-864.

[16] J. Armendáriz, M. Matalon, Evaporation and combustion of thin films of liquid fuels, The Journal of Fluid Mechanics, 435 (2001) 351-376.

[17] H.C. Hottel, Review: Certain laws governing the diffusive burning of liquids, Fire Research Abstracts and Reviews, 1 (1959) 41-43.

[18] V.I. Blinov, G.N. Khudiakov, The burning of liquid pools, Doklady Akademi Nauk SSSR, 113 (1957) 1094-1098.

[19] K. Akita, T. Yumoto, Heat transfer in small pools and rates of burning of liquid methanol, Symposium (International) on Combustion, 10 (1965) 943-948.

[20] A. Hamins, M. Klassen, J. Gore, S. Fischer, T. Kashiwagi, Heat feedback to the fuel surface in pool fires, Combustion Science and Technology, 97(1-3) (1994) 37-62.

[21] A. Hamins, T. Kashiwagi, R. Buch, Characteristics of pool fire burning, in: Fire resistance of the Industrial Fluids, ASTM STP 1284, American Society for Testing and Material, Philadelphia, 1996, pp. 15-41.

[22] A. Nakakuki, Liquid fuel flames in laminar flame regions, Combustion and Flame, 23 (1974) 337-346.

[23] K.B. McGrattan, H.R. Baum, R.G. Rehm, Large eddy simulation of smoke movement, Fire Safety Journal, 30(2) (1998) 161-178.

[24] J. Zhang, S. Dembele and J.X. Wen, Investigation of turbulence models for CFD simulations of gas and liquid pool fires, Journal of Fire Sciences, 27 (2009) 157-182.

[25] V. Novozhilov, H. Koseki, U. Kingdom, CFD prediction of pool fire burning rates and flame feedback, Combustion Science and Technology, 176(8) (2004) 1283-1307.

[26] S.Hostikka, K. Mcgrattan, A. Hamins, Numerical modeling of pool fires using LES and finite volume method for radiation, in: Fire Safety Science-the seventh international symposium, 2003, pp. 383-394.

[27] K. Prasad, C. Li, K. Kailasanath, C. Ndubizu, R. Ananth, P.A. Tatem, Numerical modeling of methanol liquid pool fires, Combustion Theory and Modelling, 3(4) (1999) 743-768.

[28] K. Prasad, C. Li, K. Kailasanath, C. Ndubizu, R. Ananth and P.A. Tatem, Numerical modeling of fire suppression using water mist. 3. Methanol liquid pool fire model, Report NRL/MR/6410-98-8102, Naval Research Laboratory Report, 1998.

[29] K. Prasad, C. Li, K. Kailasanath, Numerical modeling of fire suppression using water mist. 4. suppression of liquid methanol pool fires, Report NRL/MR/6410-98-8303, Naval Research Laboratory, 1998.

[30] A. Vali, D.S. Nobes, L.W. Kostiuk Effects of altering the liquid phase boundary conditions of methanol pool fires, Experimental Thermal and Fluid Science, 44 (2013) 786-791.

[31] A. Vali, D.S. Nobes, L.W. Kostiuk, Transport Phenomena within the Liquid Phase of a Laboratory-Scale Circular Methanol Pool Fire, Combustion and Flame, 161(4) (2014) 1076-1084.

[32] T. Steinhaus, S. Welch, R.O. Carvel, J.L. Torero, Large-scale Pool Fires, Thermal Science, 11(2) (2007) 101-118.

[33] M.G. Zabetakis, Flammability characteristics of combustible gases and vapours, Report Bulletin 627, US Bureau of Mines, 1965.

[34] K.K. Kuo, Priciples of combustion, 2nd ed., John Wiley & Sons, New Jersey, 2005.

[35] D.W. Green, R.H. Perry, Chemical engineers' handbook, McGraw-Hill, 2008.

[36] V. Babrauskas, R.D. Peacock, Heat release rate: The single most important variable in fire hazard, Fire Safety Journal, 18(3) (1992) 255-272.

[37] A. Tewarson, Heat release rate in fires, Fire and Materials, 4(4) (1980) 185-191.

[38] R.P. Lindstedt, M.P. Meyer, A dimensionally reduced reaction mechanism for methanol oxidation, Proceedings of the Combustion Institute, 29(1) (2002) 1395-1402.

[39] M.D. Smooke, V. Giovangigli, Numerical modeling of axisymmetric laminar diffusion flames by a parallel boundary value method, International Journal of High Performance Computing Applications, 5(4) (1991) 34-49.

[40] B.J. McBride, S. Gordon, M.A. Reno, Coefficients for calculating thermodynamic and transport properties of individual species, NASA Technical. Memorandum. 4513, 1993.

[41] S. Yalamanchilia, W.A. Sirignanoa, R. Seiserb, K. Seshadrib, Reduced methanol kinetic mechanisms for combustion applications, Combustion and Flame, 142(3) (2005) 258-265.

[42] D. Aronowitz, R.J. Santoro, F.L. Dryer, I. Glassman, Kinetics of the oxidation of methanol: Experimental results semi-global modeling and mechanistic concepts, Proceeding of the Combustion Institute, 17(1) (1979) 633-644.

[43] C.K. Westbrook, F.L. Dryer, Simplified reaction mechanisms for the oxidation of hydrocarbon fuels in flames, Combustion Science and Technology, 27 (1981) 31-43.

[44] A. Tewarson, Heat release rates from samples of polymethlmethacrylate and polystyrene burning in normal air, Fire and Materials, 1(3) (1976) 90-96.

[45] J.A. Koski, L.A. Gritzo, L.A. Kent, Actively cooled calorimeter weasurements and environment characterization in a large pool fire, Fire and Materials, 20 (1996) 69-78.

[46] V. Babrauskas, Heat Release Rates, in: SFPE Handbook of Fire Protection Engineering, National Fire Protection Association, Quincy, Massachusetts, 2002, pp. 3.1-3.37.

[47] V. Babrauskas, The Cone Calorimeter, in: SFPE Handbook of Fire Protection Engineering, National Fire Protection Association, Quincy, Massachusetts, 2002, pp. 3.63-63.81.

[48] M. Janssens, Calorimetry, in: SFPE Handbook of Fire Protection Engineering, National Fire Protection Association, Quincy, Massachusetts, 2002, pp. 3.38-33.62.

[49] I. Glassman, Soot formation in combustion processes, Proceeding of the Combustion Institute, 22(1) (1989) 295-311.

[50] A. Tewarson, Smoke Point Height and Fire Properties of Materials, Report NISTGCR-88-555, National Institute of Standards and Technology, Gaithersburg, MD, 1988.

[51] J.D. Ris, Fire radiation - a review, Symposium (International) on Combustion, 17 (1979) 1003-1016.

[52] H.C. Hottel, W.R. Hawthorne, Diffusion in laminar flame jets, Symposium on Combustion and Flame, and Explosion Phenomena, 3(1) (1949) 254-266.

[53] E.E. Zukoski, T. Kubota and B. Cetegen, Entrainment in fire plumes, Fire Safety Journal, 3(3) (1981) 107-121.

[54] B.J. McCaffrey, Flame height, in: SFPE Handbook of Fire Protection Engineering, National Fire Protection Association, Quincy, Massachusetts, 1995, pp. 2.1-2.8.

[55] E.E. Zukoski, Fluid dynamic aspects of room fires, in: Fire Safety Science-Proceedings of the first International Symposium, 1985, pp. 1-30.

[56] B.M. Cetegena, E. E. Zukoskia, T. Kubotaa Entrainment in the Near and Far Field of Fire Plumes, Combustion Science and Technology, 39 (1984) 305-331.

[57] G. Cox, R. Chitty, Some source-dependent effects of unbounded fires, Combustion and Flame, 60(3) (1985) 219-232.

[58] V. Babrauskas, Estimating large pool fire burning rates, Fire Technology, 19(4) (1983) 251-261.

[59] B.J. McCaffrey, Purely Buoyant Diffusion Flames: Some Experimental Results, Report NBSIR 79-1910

National Bureau of Standards, Washington, D.C., 1979.

[60] P.K. Raj, Large LNG fire thermal radiation—modeling issues and hazard criteria revisited, Process Safety Progress, 24(3) (2005) 192-202.

[61] R. Chitty, G. Cox, A method for measuring combustion intermittency in fires, Fire and Materials, 3(4) (1979) 238-242.

[62] A. Bouhafid, J.P. Vantelon, P. Joulain, On the flame structure at the base of a pool fire, Symposium (International) on Combustion, 22(1) (1989) 1291-1298.

[63] F.P. Incropera, D.P. Dewitt, Fundamentals of heat and mass transfer, 5th ed., John Wiley & Sons, New York, 2002.

[64] M.A. Delichatsios, Air entrainment into buoyant jet flames and pool fires, Combustion and Flame, 70 (1987) 33-46.

[65] B.J. McCaffrey, Purely buoyant diffusion flames: some experimental results,Report NBSIR 79-1910, National Bureau of Standards, 1979.

[66] G. Cox, R. Chitty, A study of the deterministic properties of unbounded fire plumes, Combustion and Flame, 39(2) (1980) 191-209.

[67] H.C. Kung, P. Stavrianidis, Buoyant plumes of large-scale pool fires, Symposium (International) on Combustion, 19(1) (1982) 905-912.

[68] E. Gengembre, P. Cambray, D. Karmed and J.C. Bellet, Turbulent Diffusion Flames with Large Buoyancy Effects, Combustion Science and Technology, 41(1-2) (1984) 55-67.

[69] G. Heskestad, Peak gas velocities and flame heights of buoyancy-controlled turbulent diffusion flames, Symposium (International) on Combustion, 18 (1981) 951–960.

[70] H. Koseki, T. Yumoto, Burning characteristics of heptane in 2.7m square dike fires, Fire Safety Science-Proceedings of the second international symposium (1989) 231-240.

[71] L. Audouin, G. Kolb, J. L. Torero, J. M. Most, Average centreline temperatures of a buoyant pool fire obtained by image processing of video recordings, Fire Safety Journal, 24 (1995) 167-187.

[72] F. Tamanini, Direct measurements of the longitudinal variation of burning rate and product yield in turbulent diffusion flames, Combustion and Flame, 51 (1983) 231-243.

[73] H. Koseki, Combustion properties of large liquid pool fires, Fire Technology, 25(3) (1989) 241-255.

[74] E.J. Weckman, A.B. Strong, Experimental investigation of the turbulence structure of medium-scale methanol pool fires, Combustion and Flame, 105 (1996) 245-266.

[75] G. Heskestad, Fire plumes, flame height, and air entrainment, in: SFPE Handbook of Fire Protection Engineering, National Fire Protection Association, Quincy, Massachusetts, 2002, pp. 2.1-2.17.

[76] X.C. Zhou, J. P. Gore, Measurements and prediction of air entrainment rates of pool fires, Symposium (International) on Combustion, 26(1) (1996) 1453-1459.

[77] J. Richard, J.P. Garo, J.M. Souil, J.P. Vantelon, On the flame structure at the base of a pool fire interacting with a water mist, Experimental Thermal and Fluid Science, 27 (2003) 439-448.

[78] W.E. Mell, K.B. McGrattan and H.R. Baum, Numerical simulation of combustion in fire plumes, Proceeding of the Combustion Institute, 26 (1996) 1523-1530.

[79] S. Venkatesh, A. Ito and K. Saito, Flame base structure of small-scale pool fires, Proceeding of the Combustion Institute, 26 (1996) 1437-1443.

[80] J.M. Most, P. Mandin, J. Chen and P. Joulain, Influence of gravity and Pressure on pool fire-type diffusion flames, Proceeding of the Combustion Institute, 26 (1996) 1311-1317.

[81] A. Hamins, J.C. Yang and T. Kashiwagi, An experimental investigation of the pulsation frequency of flames, Symposium (International) on Combustion, 24 (1992) 1695-1702.

[82] E.J. Weckman, A. Sobiesiak, The oscillatory behaviour of medium-scale pool fires, symposium (International) on Combustion, 22 (1988) 1299-1310.

[83] W.M.G. Malalasekera, H.K. Versteeg and K. Gilchrist, A review of research and an experimental study on the pulsation of buoyant diffusion flames and pool fires, Fire and Materials, 20 (1996) 261-271.

[84] B.M. Cetegen, K.D. Kasper, Experiments on the oscillatory behavior of buoyant plumes of helium and helium-air mixtures, Physics of Fluids, 8(11) (1996) 2974-2984.

[85] P.H. Thomas, R. Baldwin, and A.J.M. Heselden, Buoyannt diffusion flames: some measurements of air entrainment, heat transfer, and flame merging symposium (International) on Combustion, 10 (1965) 983-996.

[86] A. Ito, T. Konishi and K. Saito, Scale Effects on Flame Structure in Medium-Size Pool Fires, in: K. Saito (Ed.) Progress in Scale Modeling, Springer Science+Business Media, 2008, pp. 99-107.

[87] B.M. Cetegen, T. A. Ahmed, Experiments on the periodic instability of buoyant plumes and pool fires, Combustion and Flame, 93 (1993) 157-184.

[88] P.J. Pagni, Pool vortex shedding frequencies, in: L.M. Trefethen, R.L. Panton (Ed.) Some unanswered questions in fluid mechanics, ASME, New York, 1989, pp. 26.

[89] K. Prasad, C. Li, K. Kailasanath, C. Ndubizu, R. Ananth, P.A. Tatem, Numerical modeling of methanol liquid pool fires, Combust Theor Model, 3(4) (1999) 743-768.

[90] P.H. Thomas, C.T. Webster, M.M. Raftery, Some experiments on buoyant diffusion flames, Combustion and Flame, 5 (1961) 359-367.

[91] H.A. Becker, D. Hang, Visible length of vertical free turbulent diffusion flames, Combustion and Flame, 32 (1978) 115-137.

[92] P.H. Thomas, The size of flames from natural fires, Symposium (International) on Combustion, 9 (1963) 844-859.

[93] G.T. Kalghatgi, Lift-off heights and visible lengths of vertical turbulent jet diffusion flames in still air, Combustion Science and Technology, 41(1-2) (1984) 17-29.

[94] E.E. Zukoski, B.M. Cetegen, T. Kubota, Visible structure of buoyant diffusion flames, Symposium (International) on Combustion, 20 (1984) 361-366.

[95] F.R. Steward, Prediction of the height of turbulent diffusion buoyant flames, Combustion Science and Technology, 2(4) (1970) 203-212.

[96] W.R. Hawthorne, D.S. Weddell, H.C. Hottel, Mixing and combustion in turbulent gas jets, Symposium on Combustion and Flame, and Explosion Phenomena, 3(1) (1949) 266-288.

[97] J.A. Fay, Model of large pool fires, J. Hazard. Mater., B136 (2006) 219-232.

[98] G. Heskestad, Luminous heights of turbulent diffusion flames, Fire Safety Journal, 5 (1983) 103-108.

[99] Z.-H. Li, Y. He, H. Zhang, J. Wanga,, Combustion characteristics of n-heptane and wood crib fires at different altitudes, Proceedings of the Combustion Institute, 32(2) (2009) 2481-2488.

[100] H. Hayasaka, Unsteady burning rates of small pool fires, in: Fifth International Symposium on Fire Safety Science, 1997, pp. 499-510.

[101] D. Burgess, M. Hertzberg in: J.M.B. N.H. Afgan (Ed.) Heat Transfer in Flames, Wiley, New York, 1974, pp. 413–430.

[102] K.S. Mudan, Thermal radiation hazards from hydrocarbon pool fires, Progress in Energy and Combustion Science, 10(1) (1984) 59-80.

[103] B. D. Ditch, J. L. de Ris, T. K. Blanchat, M. Chaos, R.G. Bill Jr., S. B. Dorofeev, Pool fires - an empirical correlation, Combustion and Flame, 160 (2013) 2964-2974.

[104] D.S. Burgess, A. Strasser, J. Grumer, Diffusive burning of liquids in open trays, Fire Research Abstracts and Reviews, 3 (1961) 177-192.

[105] V. Babrauskas, Estimating large pool fire burning rates, Fire Technol, 19(4) (1983) 251-261.

[106] A. Nakakuki, Heat transfer in small scale pool fires, Combustion and Flame, 96(3) (1994) 311-324.

[107] J.L. De Ris, P.K. Wu, G. Heskestad, Radiation fire modeling, Proceedings of the Combustion Institute, 28(2) (2000) 2751-2759.

[108] D.J. Rasbash, Z.W. Rogowski, G.W.V. Stark, Properties of fires of liquids, Fuel, 31 (1956) 94-107.

[109] R.C. Corlett, T.M. Fu, Some recent experiments with pool fires, Pyrodynamics, 4 (1966) 253-269.

[110] J.M. Souil, J.P. Vantelon,P. Joulain, W.L. Grosshandler Experimental and theoretical study of thermal radiation from freely burning kerosene pool fires, Progress in Astronautics and Aeronautics, 105(1) (1986) 388-401.

[111] H. Koseki, T. Yumoto, Air entrainment and thermal radiation from heptane pool fires, Fire Technology, 24(1) (1988) 33-47.

[112] H. Koseki, G. W. Mulholland, The effect of diameter on the burning of crude oil pool fires, Fire Technology, 27(1) (1991) 54-65.

[113] M. Klassen, J.P. Gore, Structure and Radiation Properties of Pool Fires, Report NIST-GCR-94-651, National Institute of Standards and Technology, Gaithersburg, MD, 1994.

[114] J.A.R. Woods, B.A. Fleck, L.W. Kostiuk, Effects of traverse air flow on burning rates of rectangular methanol pool fires, Combustion and Flame, 146 (2006) 379-390.

[115] J.M. Chatris, J. Quintela, J. Folch, E. Planas, J. Arnaldos, J. Casal, Experimental study of burning rate in hydrocarbon pool fires, Combustion and Flame, 126 (2001) 1373-1383.

[116] E.G. Eddings, S. Yan, W. Ciro, A.F. Sarofim Formulation of a surrogate for the simulation of jet fuel pool fires, Combustion Science and Technology, 177(4) (2005) 715-739.

[117] B. Chen, S. Lu, C. Li, Q. Kang, M. Yuan, Unsteady burning of thin-layer pool fires, Journal of Fire Sciences, 30(1) (2011) 3-15.

[118] J. Gore, M. Klassen, A. Hamins, T. Kashiwagi, Fuel property effects on burning rate and radiative transfer from liquid pool flames, in: Third International Symposium on Fire Safety Science, 1997, pp. 395-404.

[119] A. Bouhafid, J.P. Vantelon, J.M. Souil, G. Bosseboeuf, F.X. Rongere, Characterisation of thermal radiation from freely burning oil pool fires, Fire Safety Journal, 15(5) (1989) 367-390.

[120] B.Z. Dlugogorcki, M. Wilson, Effect of lip height on properties of small scale pool fires, in: Fire Safety Science-Proceedings of the Fourth international symposium, 1995, pp. 129-140.

[121] A. Hamins, K. Konishi, P. Borthwick, T. Kashiwagi, Global properties of gaseous pool fires, Symposium (International) on Combustion, 26(1) (1996) 1429-1436.

[122] G. Heskestad, A fire products collector for calorimetry into the MW range, Technical Report, J.I. OC2EI.RA, Factory Mutual Research Corporation, Norwood, MA, 1981.

[123] A. Tewarson, Physico-chemical and combustion/pyrolysis properties of polymeric materials,Report NBS-GGR-80-295, National Bureau of Standards, 1980.

[124] A. Hamins, M. Kassen, J. Gore, T. Kashiwagi, Estimate of flame radiance via a single location measurement in liquid pool fires, Combustion and Flame, 86 (1991) 223-228.

[125] J.M. Souil, P. Joulain, E. Gengembre, Experimental and theoretical study of thermal radiation from turbulent diffusion flames to vertical target surfaces, Combustion Science and Technology, 41(1-2) (1984) 69-81.

[126] L. Orloff, J. de Ris, Froude modeling of pool fires, Symposium (International) on Combustion, 19 (1982) 885-895.

[127] G.H. Markstein, Relationship between smoke point and radiant emission from buoyant turbulent and laminar diffusion flames, Symposium (International) on Combustion, 20(1) (1985) 1055-1061.

[128] L. Orloff, J. de Ris, M.A. Delichatsios, Radiation from buoyant turbulent diffusion flames, Combustion Science and Technology, 84(1-6) (1992) 177-186.

[129] M. A. Delichatsios, L. Orloff, M.M. Delichatsios, The effects of fuel sooting tendency and the flow on flame radiation in luminous turbulent jet flames, Combustion Science and Technology, 84(1-6) (1992) 199-215.

[130] P.L. Blackshear Jr., K.A. Murty, Some effects of size, orientation, and fuel molecular weight on the burning of fuel-soaked wicks, Symposium (International) on Combustion, 11(1) (1967) 545-552.

[131] K.C. Adiga, D.E. Ramaker, P.A. Tatem, F.W. Williams, Modeling thermal radiation in open liquid pool fires, Fire Safety Science-Proceedings of the second international symposium (1989) 241-250.

[132] J. de Ris, L. Orloff, A dimensionless correlation of pool burning data, Combustion and Flame, 18(3) (1972) 381-388.

[133] M.G. Zabetakis, D.S. Burgess, Research on the hazards associated with the production and handling of liquid hydrogen, US Bureau of Mines RI5707, Pittsburgh, PA, 1961.

[134] A. Shinotake, S. Koda, K. Akita, An experimental study of radiative properties of pool fires of an intermediate scale, Combustion Science and Technology, 43(1-2) (1985) 85-97.

[135] F. Jiang, J.L. de Ris, H. Qi, M.M. Khan, Radiation blockage in small scale PMMA combustion, Proceedings of the Combustion Institute, 33 (2011) 2657-2664.

[136] M.A. Brosmer, C.L. Tien, Radiative energy blockage in large pool fires, Combustion Science and Technology, 51(1-3) (1987) 21-37.

[137] P.L. Blackshear Jr., K.A. Murty, Heat and mass transfer to, from, and within cellulosic solids burning in air, Symposium (International) on Combustion, 10(1) (1965) 911-923.

[138] A. Nakakuki, Heat transfer mechanisms in liquid pool fires, Fire Safety Journal, 23 (1994) 339-363.

[139] V.I. Blinov, G.N. Khudiakov, Diffusion burning of liquids, NTIS No. AD296762, 1961.

[140] K. Hasegawa, Experimental study on the mechanism of hot zone formation in open-tank fires, in: Fire Safety Science- Proceeding of the Second International Symposium, 1988, pp. 221-230.

[141] T. Inamura, K. Saito, K.A. Tagavi, A study of boilover in liquid pool fires supported on water. part II: Effects of in-depth radiation absorption, Combustion Science and Technology, 86(1-6) (1992) 105-119.

[142] A. Nakakuki, Heat transfer in hot-zone-forming pool fires, Combustion and Flame, 109(3) (1997) 353-369.

[143] B. Kozanoglu, F. Ferrero, M. Munoz, J. Arnaldos, J. Casal, Thermal analysis of thin layer boilover, Heat Mass Transfer, 44 (2008) 1549-1555.

[144] B. Kozanoglu, F. Ferrero, M. Munoz, J. Arnaldos, J. Casal, Velocity of convective currents in boilover, Chemical Engineering Science, 61 (2006) 2550-2556.

[145] K. Sefiane, C. Ward, Recent advances on thermocapillary flows and interfacial conditions during the evaporation of liquids, Advances in Colloid and Interface Science, 134-135 (2007) 201-223.

[146] A. Ito, K. Saito, T. Inamura, Holographic interferometry temperature measurements in liquids for pool fires supported on water, Journal of Heat Transfer, 114(4) (1992) 944-949.

[147] J. Straub, The role of surface tension for two-phase heat and mass transfer in absence of gravity, Experimental Thermal and Fluid Science, 9 (1994) 253-273.

[148] H.D. Ross, Ignition of and flame spread over laboratory-scale pools of pure liquid fuels, Progress in Energy and Combustion Science, 20(1) (1994) 17-63.

[149] F.A. Williams, Mechanisms of fire spread, Symposium (International) on Combustion, 16(1) (1977) 1281-1294.

[150] K. Akita, Some problems of flame spread along a liquid surface, Symposium (International) on Combustion, 14(1) (1973) 1075-1083.

[151] W.A. Sirignano, I. Glassman, Flame spreading above liquid fuels: Surface-tension-driven flows, Combustion Science and Technology, 1(4) (1970) 307-312.

[152] H.D. Ross, F.J. Miller, Detailed experiments of flame spread across deep butanol pools, Symposium (International) on Combustion, 26(1) (1996) 1327-1334.

[153] R.J. Murad, J. Lamendola, H. Isoda, M. Summerfield, A study of some factors influencing the ignition of a liquid fuel pool, Combustion and Flame, 15(3) (1970) 289-298.

[154] I.G. Namyatov, S.S. Minaev, V.S. Babkin, V.A. Bunev, A.A. Korzhavin, Diffusion combustion of a liquid fuel film on a metal substrate, Combustion, Explosion and Shock Waves, 36(5) (2000) 562-570.

[155] K.E. Torrance, R.L. Mahajan, Fire spread over liquid fuels: Liquid phase parameters, Symposium (International) on Combustion, 15(1) (1975) 281-287.

[156] F.J. Miller, H. D. Ross,, Further observations of flame spread over laboratory-scale alcohol pools, Symposium (International) on Combustion, 24(1) (1992) 1703-1711.

[157] D.N. Schiller, H.D. Ross, W.A. Sirignano, Computational analysis of flame spread across alcohol pools, Combustion Science and Technology, 118(4-6) (1996) 203-255.

[158] J. Cai, Feng Liu, W.A. Sirignano, Three-dimensional structures of flames over liquid fuel pools, Combustion Science and Technology, 175(11) (2003) 2113-2139.

[159] M. I. Hassan, K. Kuwana, K. Saito, T. Hirano, PIV measurements of flow structures created by a pulsating flame spread over 1-propanol, Fire Safety Science-Proceedings of the Seventh International Symposium (2003) 153-160.

[160] K.E. Torrance, Subsurface flows preceding flame spread over a liquid fuel, Combustion Science and Technology, 3(3) (1971) 133-143.

[161] F.J. Higuera, Steady thermocapillary-buoyant flow in an unbounded liquid layer heated nununiformly from above, Physics of Fluids, 12(9) (2000) 2186-2197.

[162] D. Schwabe, J. Metzger, Coupling and separation of buoyant and thermocapillary convection, Journal of Crystal Growth, 97(1) (1989) 23-33.

[163] A.E. Gill, The boundary-layer regime for convection in a rectangular cavity, Journal of Fluid Mechanics, 26(3) (1966) 515-536.

[164] A. Nakakuki, Heat transfer in pool fires at a certain small lip height, Combustion and Flame, 131 (2002) 259-272.

[165] B.Z. Dlugogorski, M.T. Wilson, , Effect of ullage on properties of small-scale pool fires, Developments in Chemical Engineering and Mineral Processing, 8(1-2) (2000) 149–166.

[166] G. Magnus, Tests on combustion velocity of liqluid fuels and temperature distribution in flames and beneath surface of burning liquid, International Symposium on the Use of Models in Fire Research, National Academy of Sciences, Washington, (1961).

[167] L. Orloff, Simplified radiation modeling of pool fires, Symposium (International) on Combustion, 18(1) (1981) 549-561.

[168] J.P. Garo, H. Koseki, J.P. Vantelon, A.C. Fernandez Pello, Combustion of liquid fuels floating on water, International Journal of Thermal Sciences, 11(2) (2007) 119-140.

[169] B. Chena, S-.X. Lua, C-.H. Li, Q-.S. Kang, V. Lecoustrec, Initial fuel temperature effects on burning rate of pool fire, J. Hazard. Mater., 188 (2011) 369-374.

[170] V. Babrauskas, Effect of Environmental Variables, in: V. Babrauskas, S.J. Grayson (Ed.) Heat Release in Fires, Elsevier Applied Science, New York, NY, 1992, pp. 307-325.

[171] J. Fang, R. Tu, J.-F. Guan, J.-J. Wang, Y.-M. Zhang, Influence of low air pressure on combustion characteristics and flame pulsation frequency of pool fires, Fuel, 90(8) (2011) 2760-2766.

[172] J. Yin, W. Yao, Q. Liu, Z. Zhou, N. Wu, H. Zhang, C.-H. Lin, T. Wu, O.C. Meier, Experimental studyof n-Heptane pool fire behavior in an altitude chamber, International Journal of Heat and Mass Transfer, 62 (2013) 543-552.

[173] L. Hu, S. Liu, Y. Xu, D. Li, A wind tunnel experimental study on burning rate enhancement behavior of gasoline pool fires by cross air flow, Combustion and Flame, 158(3) (2011) 586-591.

[174] L.H. Hua, S. Liu, W. Peng,R. Huo, Experimental study on burning rates of square/rectangular gasoline and methanol pool fires under longitudinal air flow in a wind tunnel, J. Hazard. Mater., 169 (2009) 972–979.

[175] L. Hu, S. Liu, L. Wu, Flame radiation feedback to fuel surface in medium ethanol and heptane pool fires with cross air flow, Combustion and Flame, 160(2) (2013) 295-306.

[176] T.G. Beckwith, R.D. Marangoni, J.H. Lienhard V, Mechanical Measurements, 6th ed., Pearson Education Inc., Upper Saddle River, NJ, 2007.

[177] B.N. Taylor, C.E. Kuyatt, Guidelines for evaluating and expressing the uncertainty of NIST measurement results, National Institute of Standards and Technology,Technical Note 1297, 1993.

[178] J.A.R. Woods, Effects of crossflow on burning rates of rectangular methanol pool fires, MSc Thesis, University of Alberta, Edmonton, AB, 2005.

[179] J. Westerweel, Fundamentals of digital particle image velocimetry, Measurement Science and Technology, 8 (1997) 1379-1392.

[180] M.Raffel, C.E. Willert, S.T. Wereley, J. Kompenhans, Particle Image Velocimetry A Practical Guide, 2 ed., Springer-Verlag Berlin Heidelberg, 1998.

[181] Product-Manual for DaVis 7.2 , Flow Master, , LaVision GmbH, Anna-Vandenhoeck-Ring 19, D-37081 Göttingen, Germany, 2007.

[182] L.M. Jiji, Heat Convection, Springer, Netherlands, 2006.

[183] S.B. Dalziel, M. Carr, J.K. Sveen, P.A. Davies, Simultaneous synthetic schlieren and PIV measurements for internal solitary waves, Messurement Science and Technology, 18 (2007) 533-547.

[184] J. Benitez, Principles and modern applications of mass transfer operations, 2nd ed., John Willey & Sons, Inc, 2009.

[185] S. Yaltkaya, R. Aydin, Experimental investigation of temperature effect on the refractive index of dye laser liquids, Turkish Journal of Physics, 26 (2002) 41-47.

APPENDIXES

In Appendix A, the properties of methanol, the fuel used in this study, can be found. The manufacturing drawings of the experimental rig designed in this study are shown in Appendix B. Zoomed-in views of the velocity vector fields within the liquid pool especially in the top region and adjacent to the wall are shown in Appendix C. Lastly, an analysis for heat transfer through a liquid layer is presented in Appendix D, which helps understanding the model presented in Chapter 5 for the liquid phase thermal structure.

Appendix A: Methanol Properties

In this appendix the properties of methanol, the fuel used in this study, are presented [35]. The thermo-physical properties listed here are for the standard condition (*i.e.*, 25ºC and 101.3 kPa) unless otherwise stated.

Molecular weight	32.04 g/mol
Critical temperature	512.5 K
Critical pressure	8.084 MPa
Boiling point	64.6ºC
Freezing point	-97.6ºC
Flash point	11ºC
Flammability limit (volumetric)	6%-36.5%
Thermal expansion	0.0015 1/ ºC
Heat of combustion	22.7 kJ/g (HHV) 19.9 kJ/g (LHV)
Refractive index [185]	1.325 $n = -0.00042\ T + 1.33512$ (T in ºC)
Vapor pressure	16.96 kPa $P_v = \exp\left[C_1 + C_2/T + C_3 \ln T + C_4 T^{C_5}\right]$ Pa where $\begin{array}{ccccc} C_1 & C_2 & C_3 & C_4 & C_5 \\ 81.768 & -6876 & -8.7078 & 7.19\times10^{-6} & 2 \end{array}$
Heat of evaporation	1.17 kJ/g 1.1 kJ/g (at 64.6ºC)

$\Delta H_v = C_1(1-T_r)^{C_2+C_3Tr+C_4T_r^2}$ J/kmol

where

C_1	C_2	C_3	C_4
5.239e-7	0.3682	0	0

Density

786.6 kg/m^3

$\rho = C_1 \big/ C_2^{[1+(1+T/C_3)^{C_4}]}$ kmol/m^3

where

C_1	C_2	C_3	C_4
2.288	0.2685	512.64	0.2453

Heat capacity

2.53 kJ/(gK)

$C_p = C_1 + C_2T + C_3T^2 + C_4T^3$ J/(kmolK)

where

C_1	C_2	C_3	C_4
1.06×10^5	-3.62×10^2	0.938	0

Viscosity

5.44×10^{-4} Pa.s

$\mu = \exp\,[C_1 + C_2/T + C_3 \ln T]$ Pa.s

where

C_1	C_2	C_3
-25.317	1789.2	2.069

Surface tension

22.07×10^{-3} N/m

22.6×10^{-3} N/m (at 20ºC)

20.96×10^{-3} N/m (at 40ºC)

19.41×10^{-3} N/m (at 60ºC)

Thermal conductivity

0.2 W/(mK)

$k = C_1 + C_2T$ W/(mK)

where

C_1	C_2
0.2837	-0.000281

Appendix B: Experimental Apparatus Drawings

In this appendix the manufacturing drawings of the burners (*i.e.*, the square and circular pools) are presented. These drawings were developed in SolidWorks software. First are the drawings for the square burner followed by the circular burner's drawings.

Square Burner

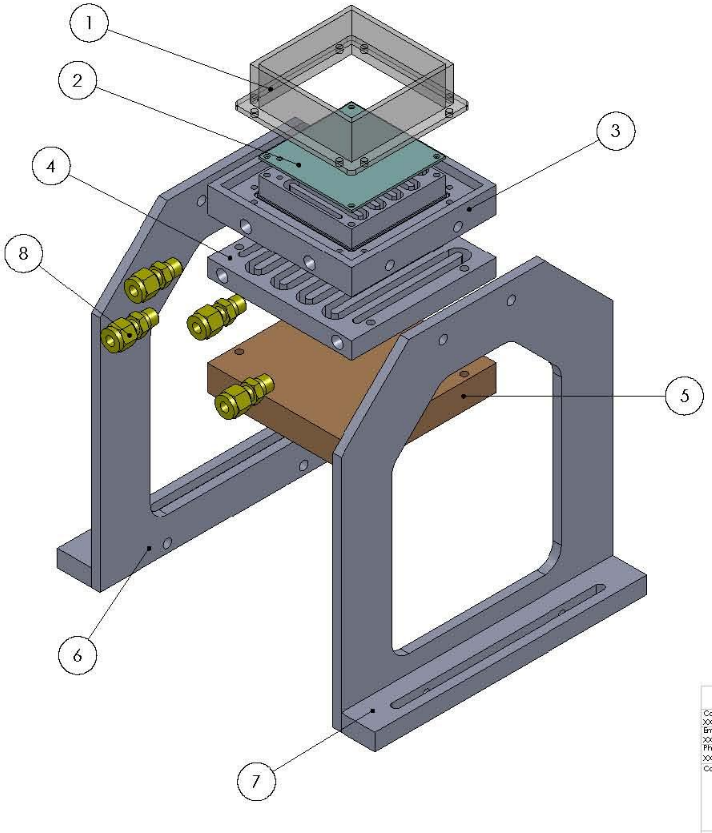

ITEM NO.	PART TITLE	DESCRIPTION	QTY.
1	container		1
2	porous plate		1
3	exchanger_Fuel		1
4	exchanger_water		1
5	plate5		1
6	support1		2
7	support2		2
8	Male Connector (Tappered Thread)_SS-400-1-2_1_4 x 1_8_Swagelok Company__10F25_3D04B8	Male Connector (Tappered Thread)	4

Nobes Lab
Contact:
XXX
Email:
XXX
Phone:
XXX
Comments:

UNLESS OTHERWISE SPECIFIED:
DIMENSIONS ARE IN INCHES
TOLERANCES:
FRACTIONAL±
ANGULAR: MACH± BEND ±
TWO PLACE DECIMAL ±
THREE PLACE DECIMAL ±
INTERPRET GEOMETRIC TOLERANCING PER:
MATERIAL:
XXXXX
Lab Location:
XXX
DO NOT SCALE DRAWING

	NAME
DRAWN	xxxxx
CHECKED	xxxxx
ENG APPR.	xxx
Speed Code	xxxxx
MecE Job #	xxx
File Name:	pool fire_exploded

vali
2/17/2014 3:30:15 PM
Monday, February 17, 2014

The Department of Mechanical Engineering
UNIVERSITY OF ALBERTA
TITLE:

SIZE B
Project: XXXXX
REV XXX
SCALE: 1:5
Mass: xxxxx
SHEET 1 OF 1

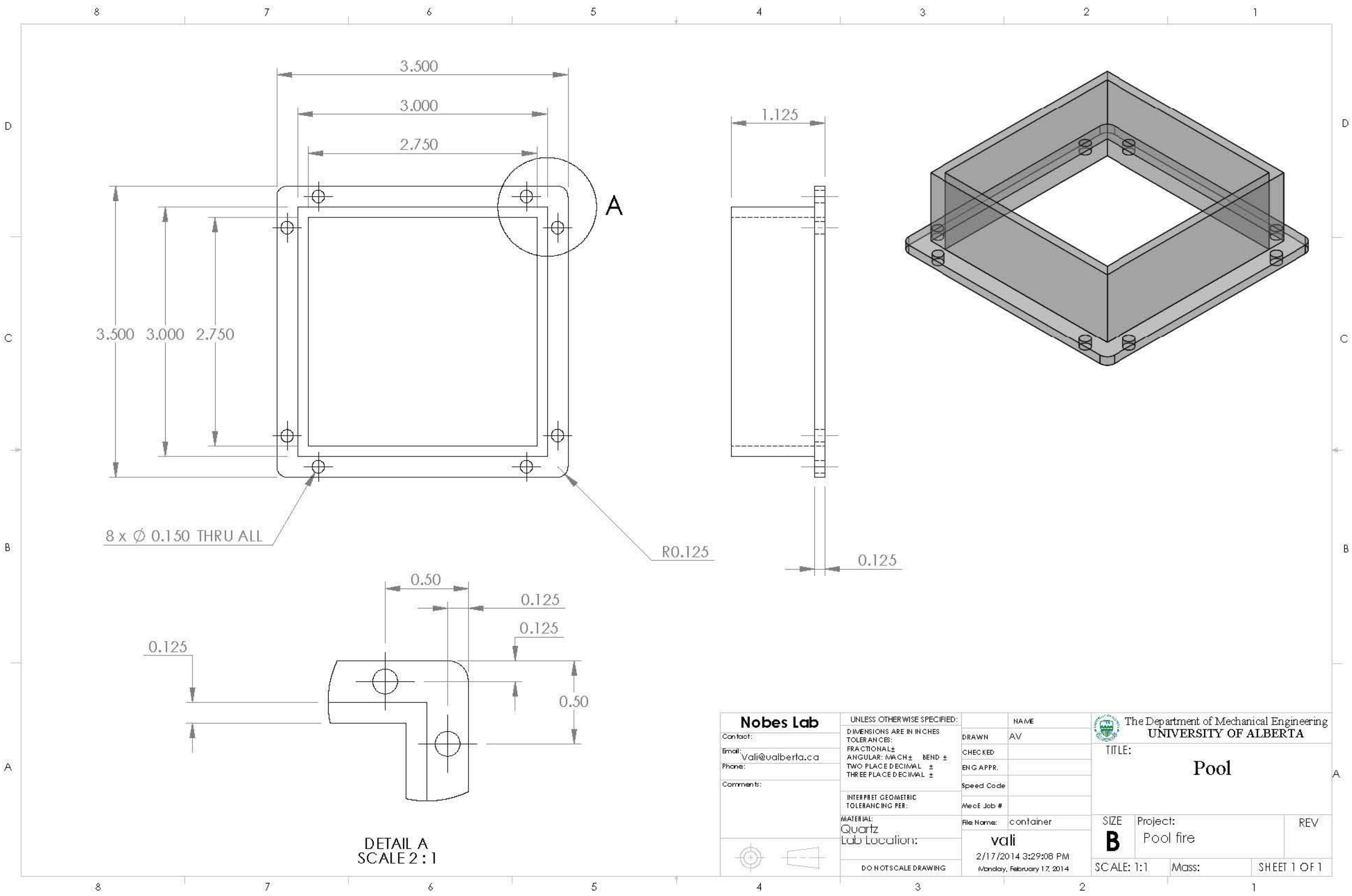

Nobes Lab
Contact:
Email: Vali@ualberta.ca
Phone:
Comments:

UNLESS OTHERWISE SPECIFIED:
DIMENSIONS ARE IN INCHES
TOLERANCES:
FRACTIONAL±
ANGULAR: MACH± BEND ±
TWO PLACE DECIMAL ±
THREE PLACE DECIMAL ±
INTERPRET GEOMETRIC TOLERANCING PER:
MATERIAL:
Quartz
Lab Location:
DO NOT SCALE DRAWING

	NAME
DRAWN	AV
CHECKED	
ENG APPR.	
Speed Code	
MecE Job #	
File Name:	container

vali
2/17/2014 3:29:08 PM
Monday, February 17, 2014

The Department of Mechanical Engineering
UNIVERSITY OF ALBERTA
TITLE:
Pool
SIZE B
Project: Pool fire
REV
SCALE: 1:1
Mass:
SHEET 1 OF 1

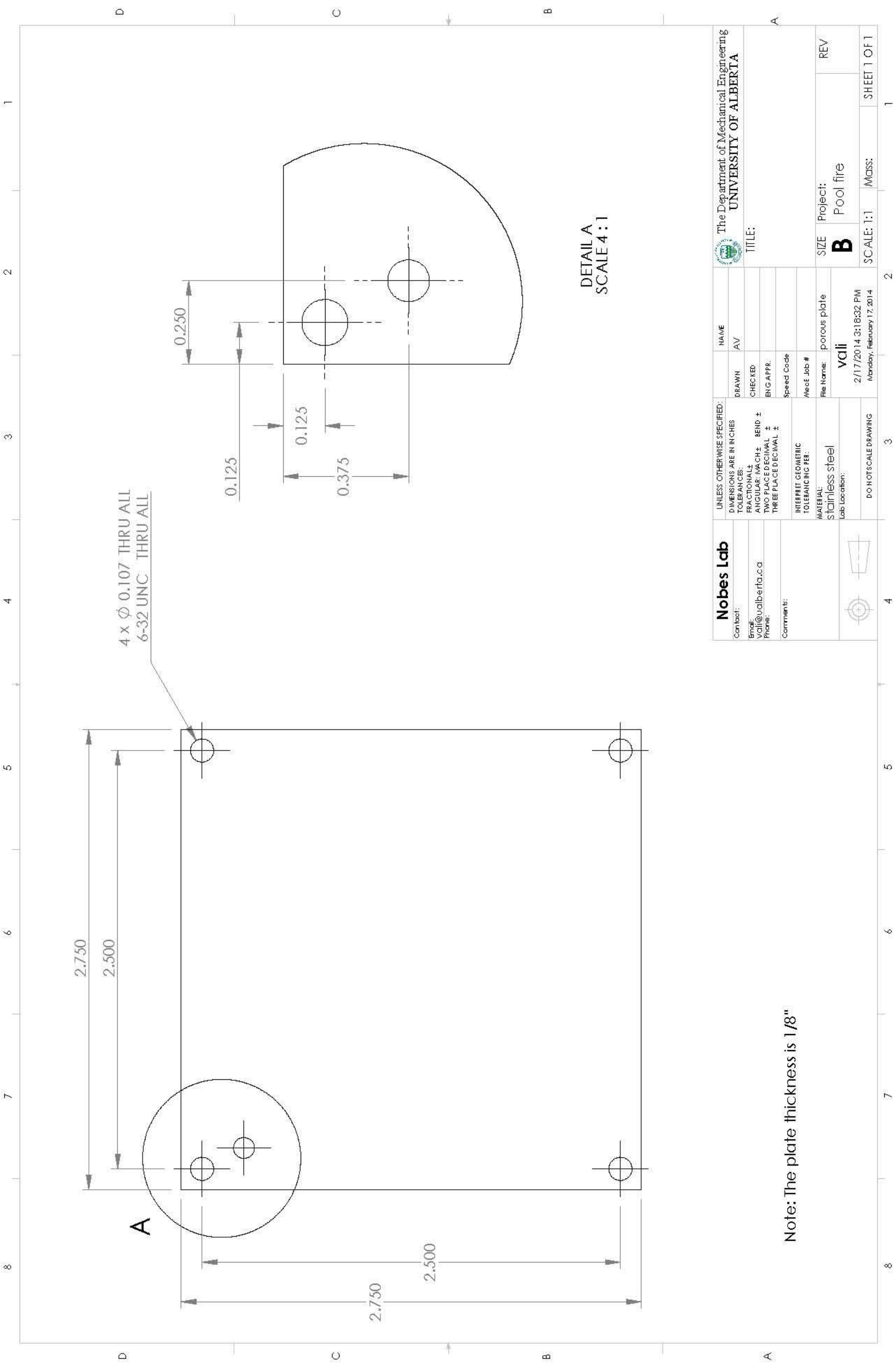
4 x ∅ 0.107 THRU ALL
6-32 UNC THRU ALL
A
2.750
2.500
2.500
2.750
0.250
0.125
0.125
0.375
DETAIL A
SCALE 4 : 1
Note: The plate thickness is 1/8"
Nobes Lab
Contact:
Email:
vali@ualberta.ca
Phone:
Comments:
UNLESS OTHERWISE SPECIFIED:
DIMENSIONS ARE IN INCHES
TOLERANCES:
FRACTIONAL±
ANGULAR: MACH± BEND ±
TWO PLACE DECIMAL ±
THREE PLACE DECIMAL ±
INTERPRET GEOMETRIC
TOLERANCING PER:
MATERIAL:
stainless steel
Lab Location:
DO NOT SCALE DRAWING
NAME
DRAWN AV
CHECKED
ENG APPR.
Speed Code
MecE Job #
File Name: porous plate
vali
2/17/2014 3:18:32 PM
Monday, February 17, 2014
The Department of Mechanical Engineering
UNIVERSITY OF ALBERTA
TITLE:
SIZE
B
Project:
Pool fire
REV
SCALE: 1:1
Mass:
SHEET 1 OF 1
A
B
C
D
1
2
3
4
5
6
7
8

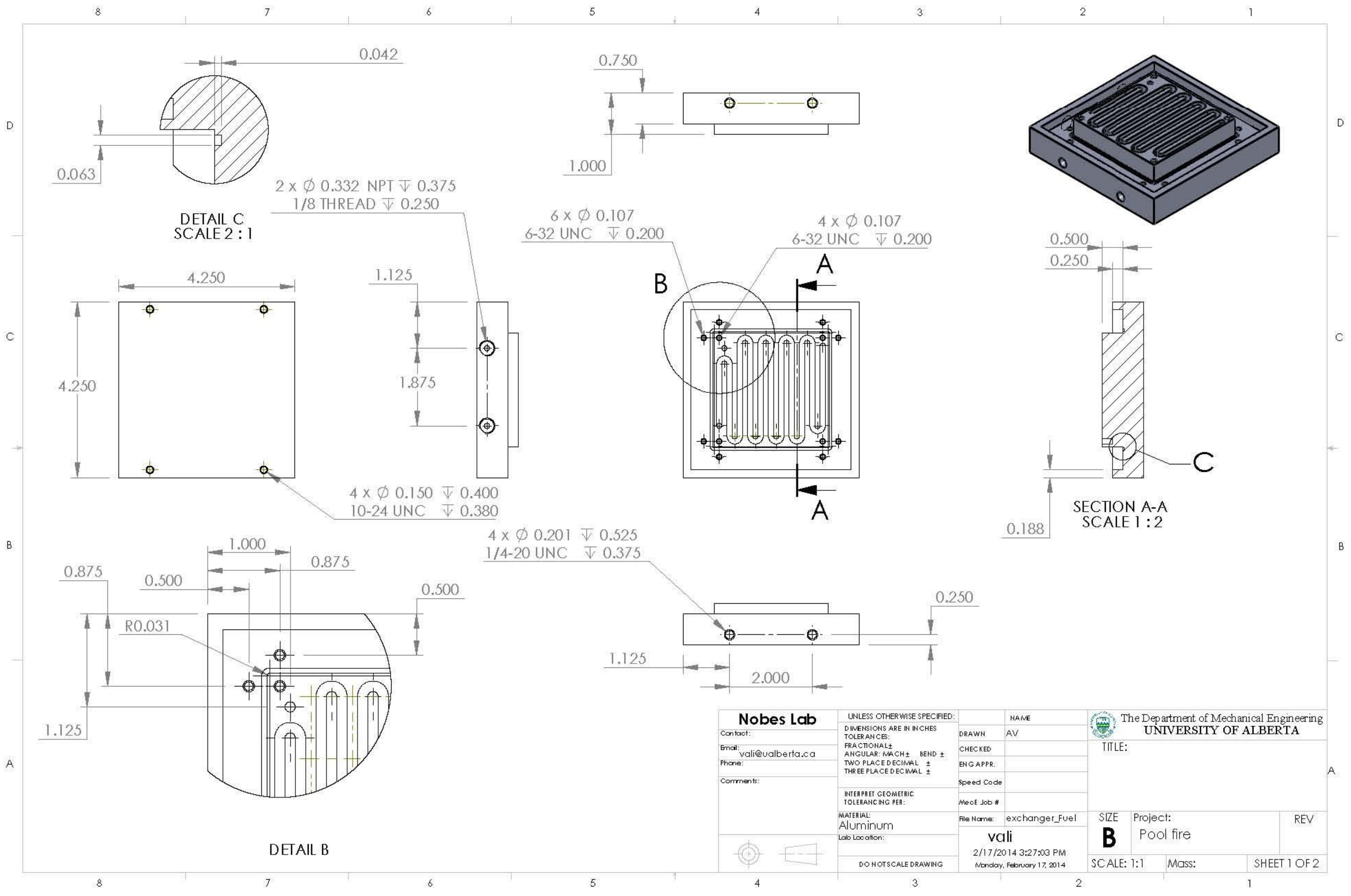
0.042
0.063
DETAIL C
SCALE 2 : 1
2 x ∅ 0.332 NPT ↧ 0.375
1/8 THREAD ↧ 0.250
0.750
1.000
6 x ∅ 0.107
6-32 UNC ↧ 0.200
4 x ∅ 0.107
6-32 UNC ↧ 0.200
A
B
0.500
0.250
C
SECTION A-A
SCALE 1 : 2
0.188
4.250
4.250
1.125
1.875
4 x ∅ 0.150 ↧ 0.400
10-24 UNC ↧ 0.380
4 x ∅ 0.201 ↧ 0.525
1/4-20 UNC ↧ 0.375
1.000
0.875
0.875
0.500
0.500
R0.031
1.125
0.250
1.125
2.000
DETAIL B
Nobes Lab
Contact:
Email: vali@ualberta.ca
Phone:
Comments:
UNLESS OTHERWISE SPECIFIED:
DIMENSIONS ARE IN INCHES
TOLERANCES:
FRACTIONAL±
ANGULAR: MACH± BEND ±
TWO PLACE DECIMAL ±
THREE PLACE DECIMAL ±
INTERPRET GEOMETRIC TOLERANCING PER:
MATERIAL: Aluminum
Lab Location:
DO NOT SCALE DRAWING
NAME
DRAWN AV
CHECKED
ENG APPR.
Speed Code
MecE Job #
File Name: exchanger_Fuel
vali
2/17/2014 3:27:03 PM
Monday, February 17, 2014
The Department of Mechanical Engineering
UNIVERSITY OF ALBERTA
TITLE:
SIZE B
Project: Pool fire
REV
SCALE: 1:1
Mass:
SHEET 1 OF 2

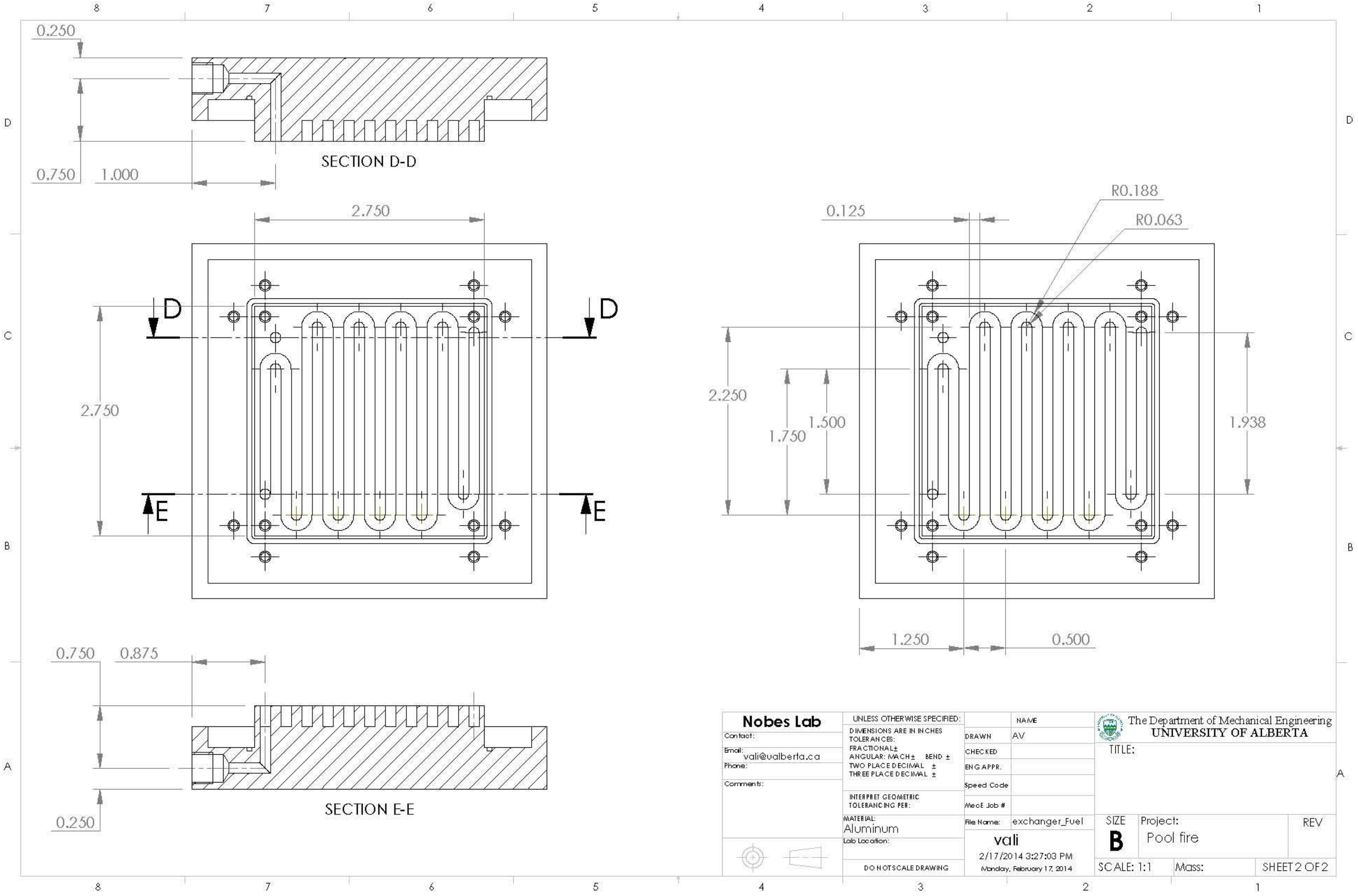
0.250
0.750
1.000
SECTION D-D
2.750
2.750
D
D
E
E
0.750
0.875
0.250
SECTION E-E
0.125
R0.188
R0.063
2.250
1.750
1.500
1.938
1.250
0.500
Nobes Lab
Contact:
Email: vali@ualberta.ca
Phone:
Comments:
UNLESS OTHERWISE SPECIFIED:
DIMENSIONS ARE IN INCHES
TOLERANCES:
FRACTIONAL±
ANGULAR: MACH± BEND ±
TWO PLACE DECIMAL ±
THREE PLACE DECIMAL ±
INTERPRET GEOMETRIC TOLERANCING PER:
MATERIAL:
Aluminum
Lab Location:
DO NOT SCALE DRAWING
NAME
DRAWN AV
CHECKED
ENG APPR.
Speed Code
MecE Job #
File Name: exchanger_Fuel
vali
2/17/2014 3:27:03 PM
Monday, February 17, 2014
The Department of Mechanical Engineering
UNIVERSITY OF ALBERTA
TITLE:
SIZE
B
Project:
Pool fire
REV
SCALE: 1:1
Mass:
SHEET 2 OF 2

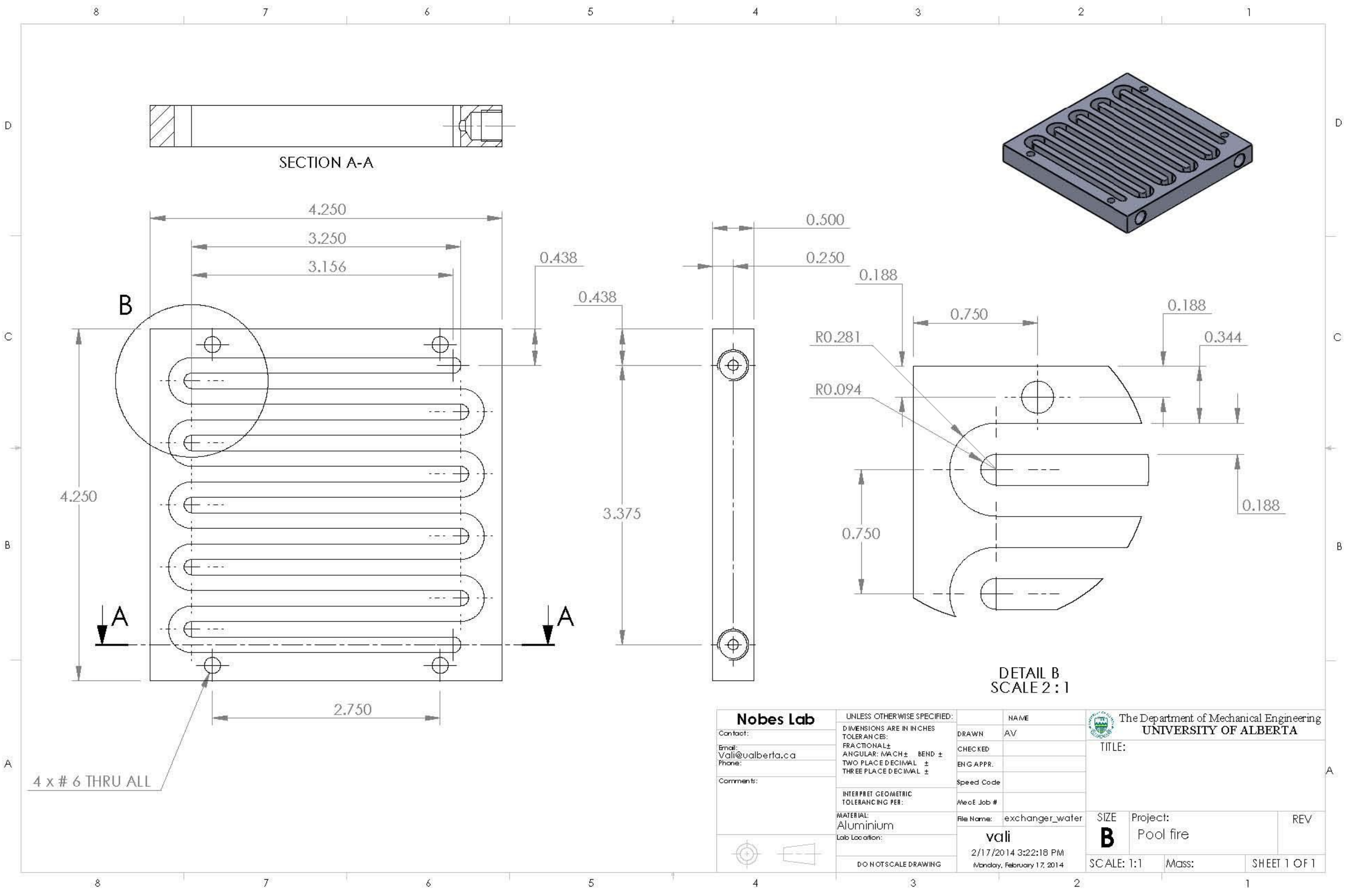
SECTION A-A
4.250
3.250
3.156
0.438
0.438
0.500
0.250
B
A
A
4.250
3.375
2.750
4 x # 6 THRU ALL
0.188
0.750
R0.281
R0.094
0.188
0.344
0.188
0.750
DETAIL B
SCALE 2 : 1
Nobes Lab
Contact:
Email: Vali@ualberta.ca
Phone:
Comments:
UNLESS OTHERWISE SPECIFIED:
DIMENSIONS ARE IN INCHES
TOLERANCES:
FRACTIONAL±
ANGULAR: MACH± BEND ±
TWO PLACE DECIMAL ±
THREE PLACE DECIMAL ±
INTERPRET GEOMETRIC
TOLERANCING PER:
MATERIAL:
Aluminium
Lab Location:
DO NOT SCALE DRAWING
NAME
DRAWN AV
CHECKED
ENG APPR.
Speed Code
MecE Job #
File Name: exchanger_water
vali
2/17/2014 3:22:18 PM
Monday, February 17, 2014
The Department of Mechanical Engineering
UNIVERSITY OF ALBERTA
TITLE:
SIZE
B
Project:
Pool fire
REV
SCALE: 1:1
Mass:
SHEET 1 OF 1
1
2
3
4
5
6
7
8
A
B
C
D

Circular Burner

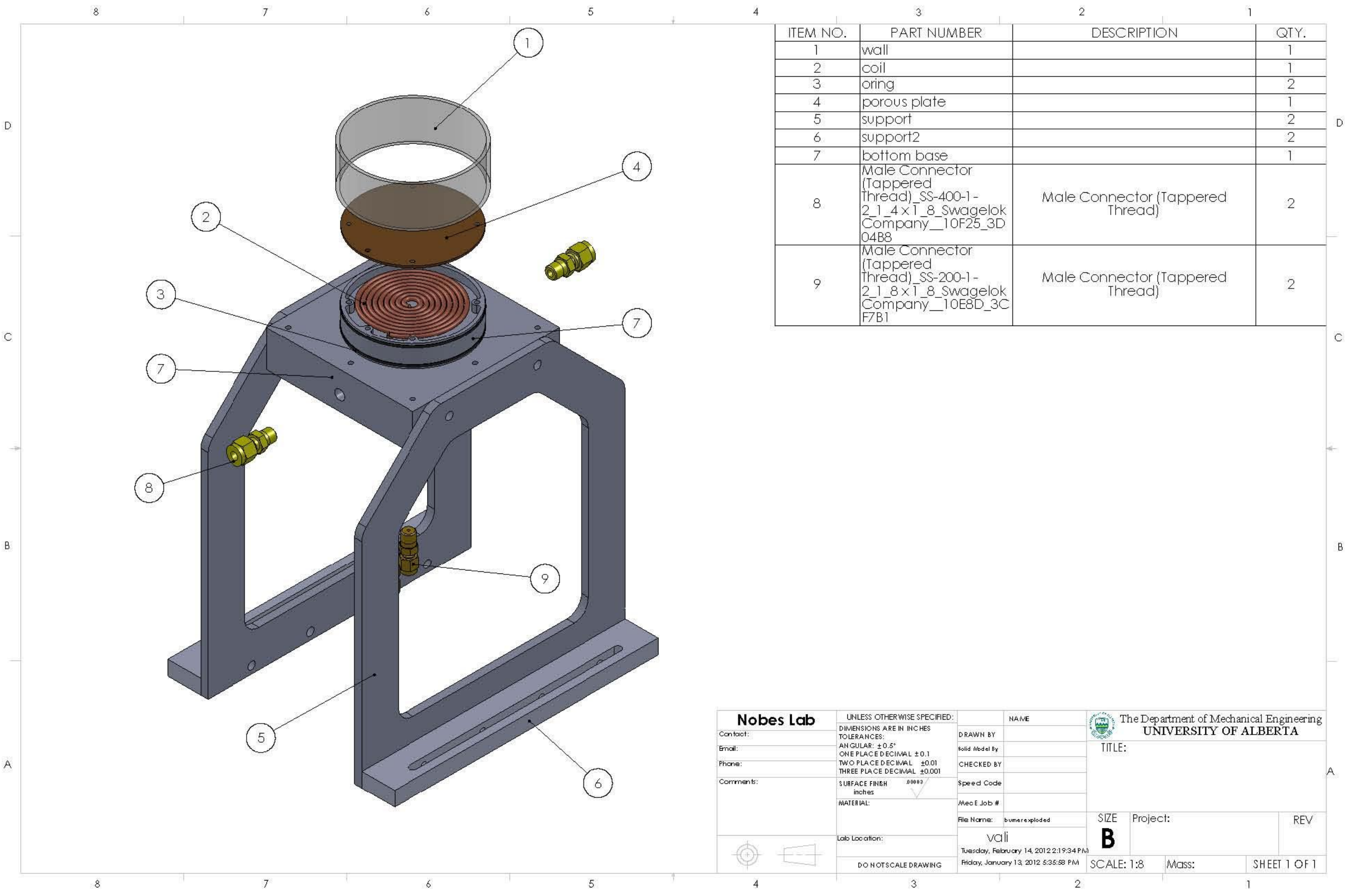

ITEM NO.	PART NUMBER	DESCRIPTION	QTY.
1	wall		1
2	coil		1
3	oring		2
4	porous plate		1
5	support		2
6	support2		2
7	bottom base		1
8	Male Connector (Tappered Thread)_SS-400-1-2_1_4 x 1_8_Swagelok Company__10F25_3D04B8	Male Connector (Tappered Thread)	2
9	Male Connector (Tappered Thread)_SS-200-1-2_1_8 x 1_8_Swagelok Company__10E8D_3CF7B1	Male Connector (Tappered Thread)	2

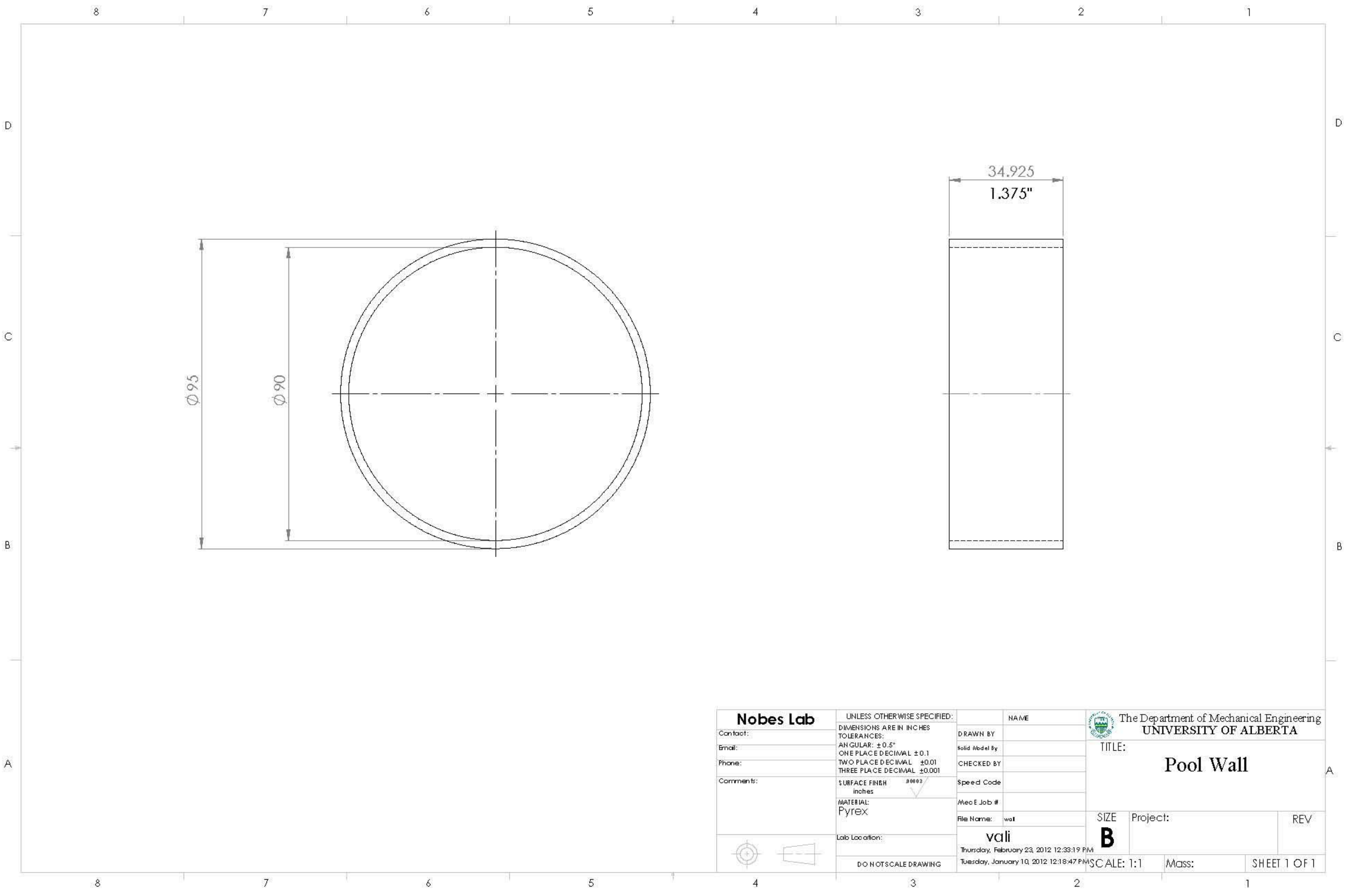

Nobes Lab
Contact:
Email:
Phone:
Comments:

UNLESS OTHERWISE SPECIFIED:
DIMENSIONS ARE IN INCHES
TOLERANCES:
ANGULAR: ±0.5°
ONE PLACE DECIMAL ±0.1
TWO PLACE DECIMAL ±0.01
THREE PLACE DECIMAL ±0.001
SURFACE FINISH inches .00003
MATERIAL: Pyrex
Lab Location:
DO NOT SCALE DRAWING

NAME
DRAWN BY
Solid Model By
CHECKED BY
Speed Code
MecE Job #
File Name: wall
vali
Thursday, February 23, 2012 12:33:19 PM
Tuesday, January 10, 2012 12:18:47 PM

The Department of Mechanical Engineering
UNIVERSITY OF ALBERTA
TITLE: Pool Wall
SIZE B
Project:
REV
SCALE: 1:1
Mass:
SHEET 1 OF 1

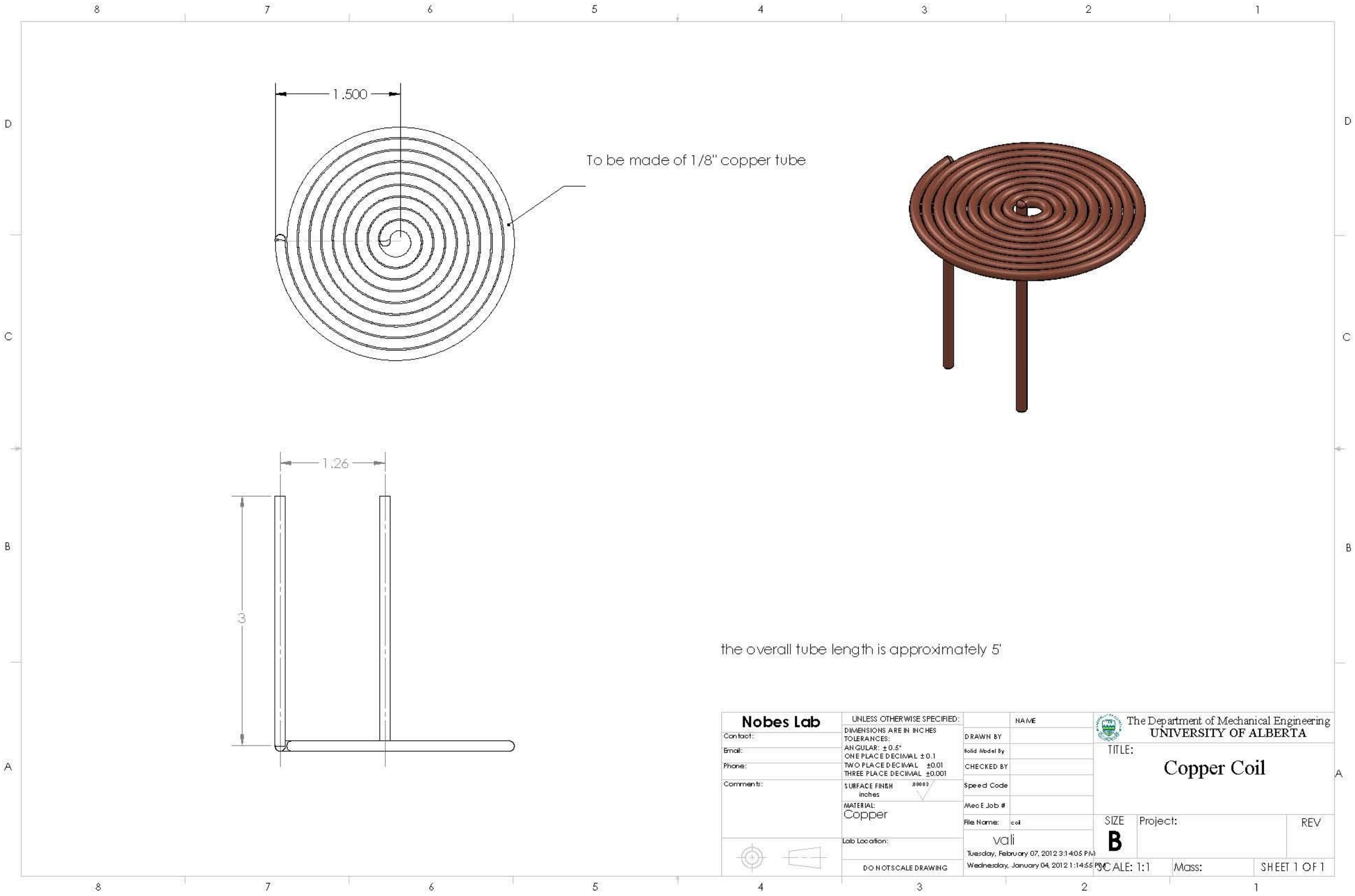

the overall tube length is approximately 5'

Nobes Lab
Contact:
Email:
Phone:
Comments:

UNLESS OTHERWISE SPECIFIED:
DIMENSIONS ARE IN INCHES
TOLERANCES:
ANGULAR: ±0.5°
ONE PLACE DECIMAL ±0.1
TWO PLACE DECIMAL ±0.01
THREE PLACE DECIMAL ±0.001
SURFACE FINISH .00003
inches
MATERIAL:
Copper
Lab Location:
DO NOT SCALE DRAWING

NAME
DRAWN BY
Solid Model By
CHECKED BY
Speed Code
MecE Job #
File Name: coil
vali
Tuesday, February 07, 2012 3:14:05 PM
Wednesday, January 04, 2012 1:14:55 PM

The Department of Mechanical Engineering
UNIVERSITY OF ALBERTA
TITLE:
Copper Coil
SIZE
B
Project:
REV
SCALE: 1:1
Mass:
SHEET 1 OF 1

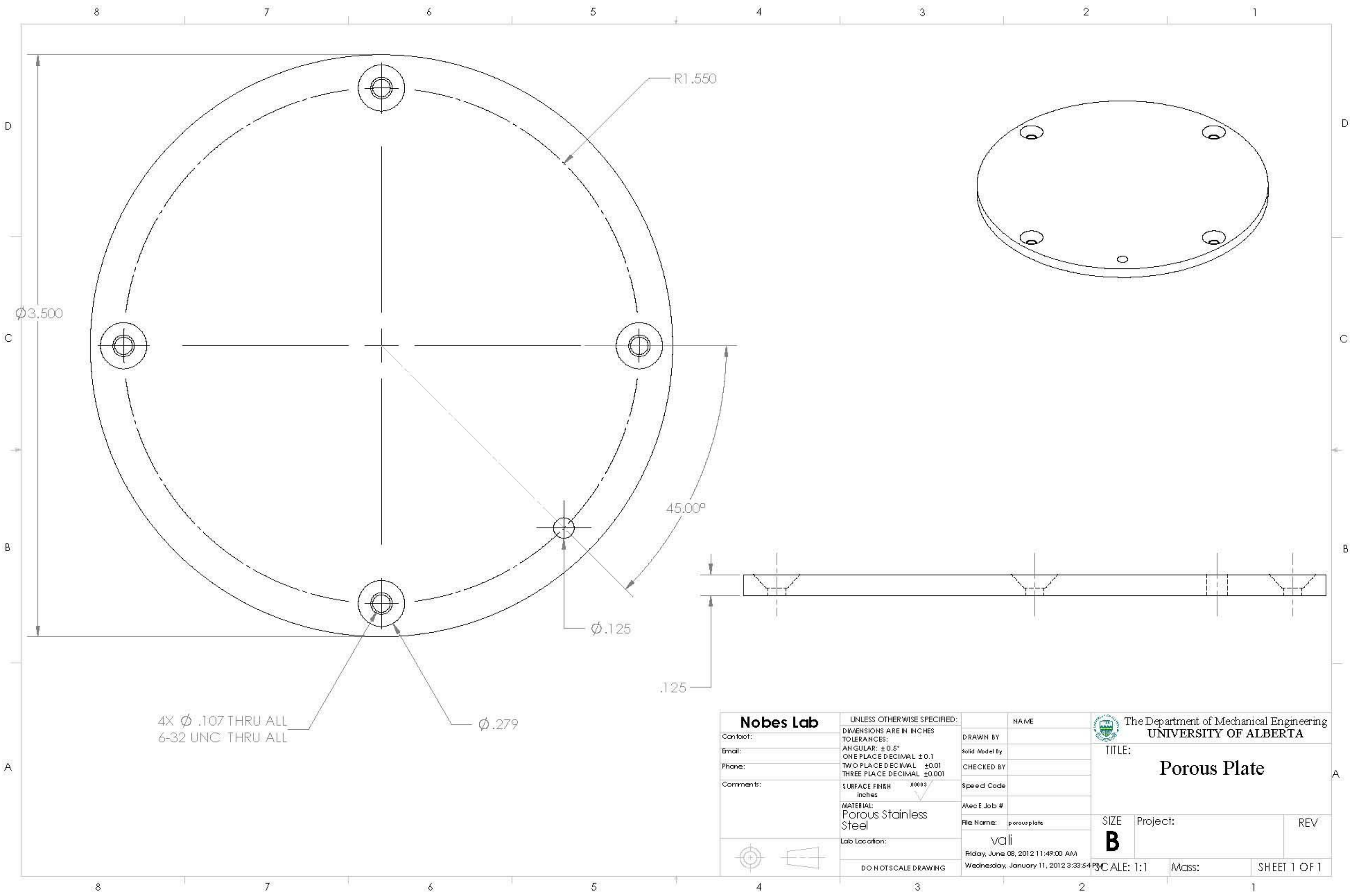

Nobes Lab

Contact:

Email:

Phone:

Comments:

UNLESS OTHERWISE SPECIFIED:

DIMENSIONS ARE IN INCHES
TOLERANCES:
ANGULAR: ±0.5°
ONE PLACE DECIMAL ±0.1
TWO PLACE DECIMAL ±0.01
THREE PLACE DECIMAL ±0.001

SURFACE FINISH .00003 inches

MATERIAL: Porous Stainless Steel

Lab Location:

DO NOT SCALE DRAWING

	NAME
DRAWN BY	
Solid Model By	
CHECKED BY	
Speed Code	
MecE Job #	
File Name:	porousplate

vali
Friday, June 08, 2012 11:49:00 AM
Wednesday, January 11, 2012 3:33:54 PM

The Department of Mechanical Engineering
UNIVERSITY OF ALBERTA

TITLE: Porous Plate

SIZE: B

Project:

REV

SCALE: 1:1

Mass:

SHEET 1 OF 1

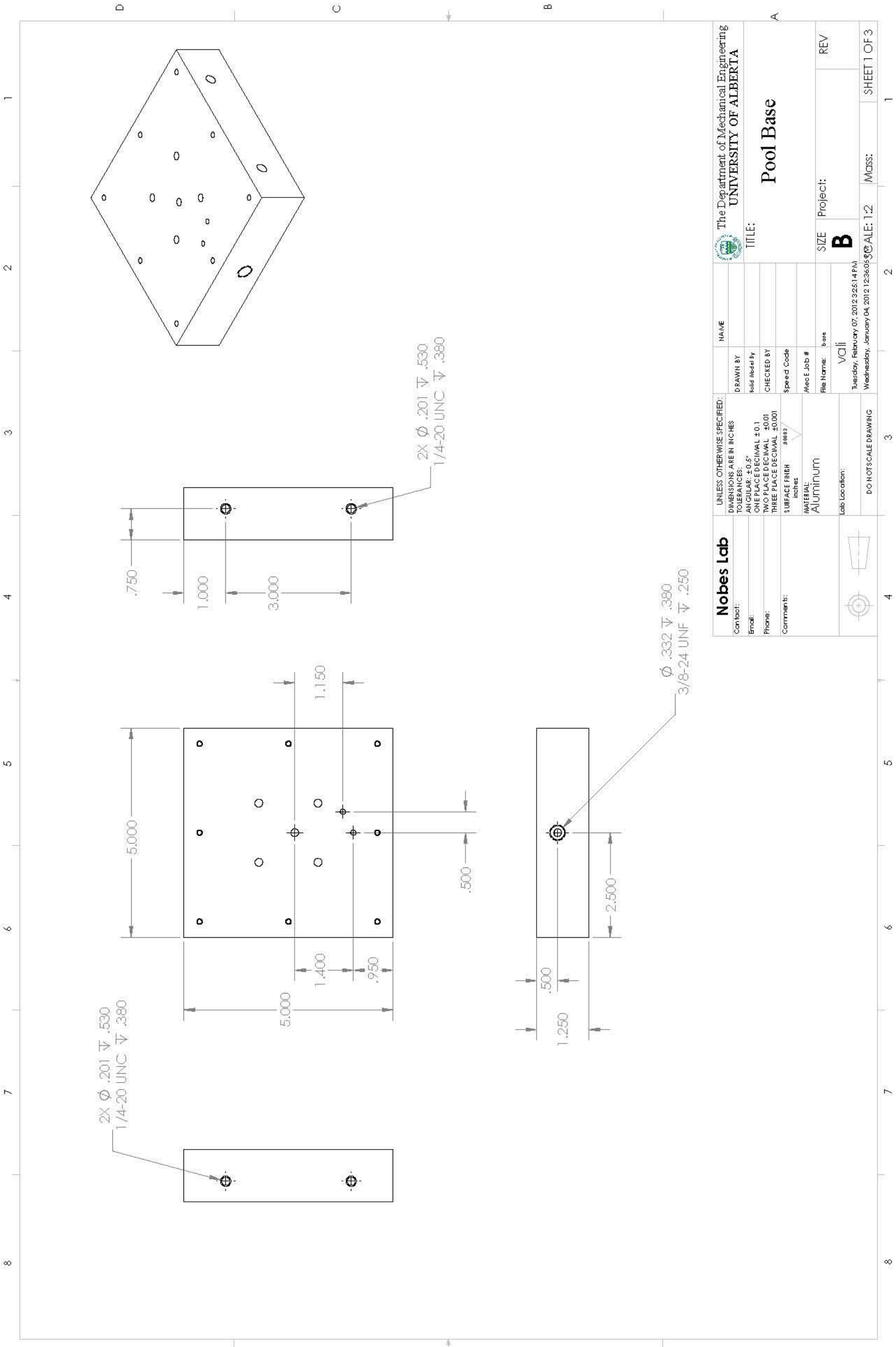
2X Ø .201 ↧ .530
1/4-20 UNC ↧ .380
.750
1.000
3.000
1.150
5.000
.500
1.400
.950
5.000
Ø .332 ↧ .380
3/8-24 UNF ↧ .250
2.500
.500
1.250
2X Ø .201 ↧ .530
1/4-20 UNC ↧ .380
Nobes Lab
Contact:
Email:
Phone:
Comments:
UNLESS OTHERWISE SPECIFIED:
DIMENSIONS ARE IN INCHES
TOLERANCES:
ANGULAR: ±0.5°
ONE PLACE DECIMAL ±0.1
TWO PLACE DECIMAL ±0.01
THREE PLACE DECIMAL ±0.001
SURFACE FINISH inches .0003
MATERIAL: Aluminum
Lab Location:
DO NOT SCALE DRAWING
NAME
DRAWN BY
Solid Model By
CHECKED BY
Speed Code
MecE Job #
File Name: base
vali
Tuesday, February 07, 2012 3:25:14 PM
Wednesday, January 04, 2012 12:36:05 PM
The Department of Mechanical Engineering
UNIVERSITY OF ALBERTA
TITLE:
Pool Base
SIZE
B
Project:
REV
SCALE: 1:2
Mass:
SHEET 1 OF 3
A
B
C
D
1
2
3
4
5
6
7
8

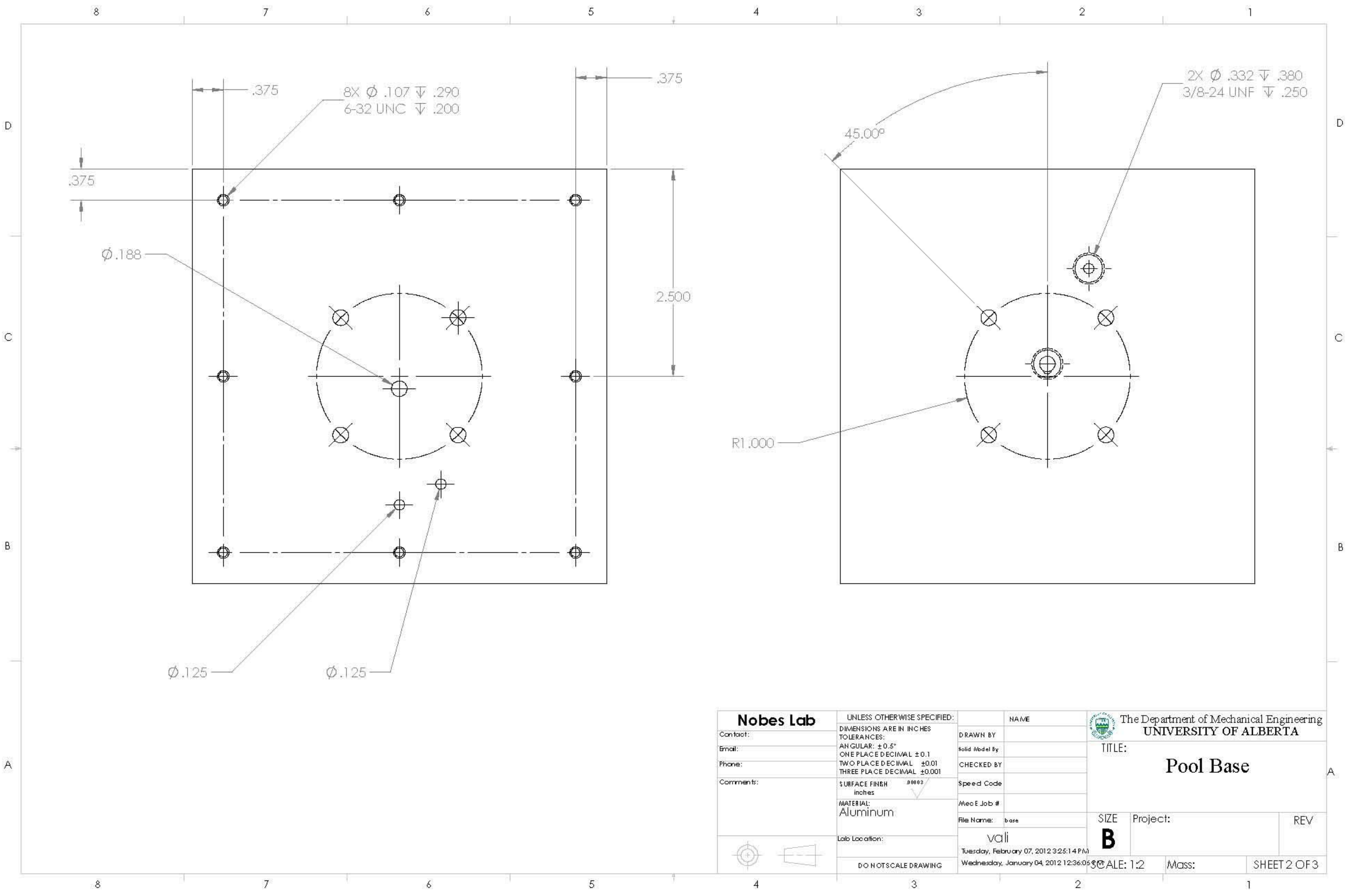
.375
8X Ø .107 ↧ .290
6-32 UNC ↧ .200
.375
.375
Ø.188
2.500
Ø.125
Ø.125
45.00°
2X Ø .332 ↧ .380
3/8-24 UNF ↧ .250
R1.000
Nobes Lab
Contact:
Email:
Phone:
Comments:
UNLESS OTHERWISE SPECIFIED:
DIMENSIONS ARE IN INCHES
TOLERANCES:
ANGULAR: ±0.5°
ONE PLACE DECIMAL ±0.1
TWO PLACE DECIMAL ±0.01
THREE PLACE DECIMAL ±0.001
SURFACE FINISH inches
.00003
MATERIAL:
Aluminum
Lab Location:
DO NOT SCALE DRAWING
NAME
DRAWN BY
Solid Model By
CHECKED BY
Speed Code
MecE Job #
File Name: base
vali
Tuesday, February 07, 2012 3:25:14 PM
Wednesday, January 04, 2012 12:36:05 PM
The Department of Mechanical Engineering
UNIVERSITY OF ALBERTA
TITLE:
Pool Base
SIZE
B
Project:
REV
SCALE: 1:2
Mass:
SHEET 2 OF 3
8
7
6
5
4
3
2
1
D
C
B
A

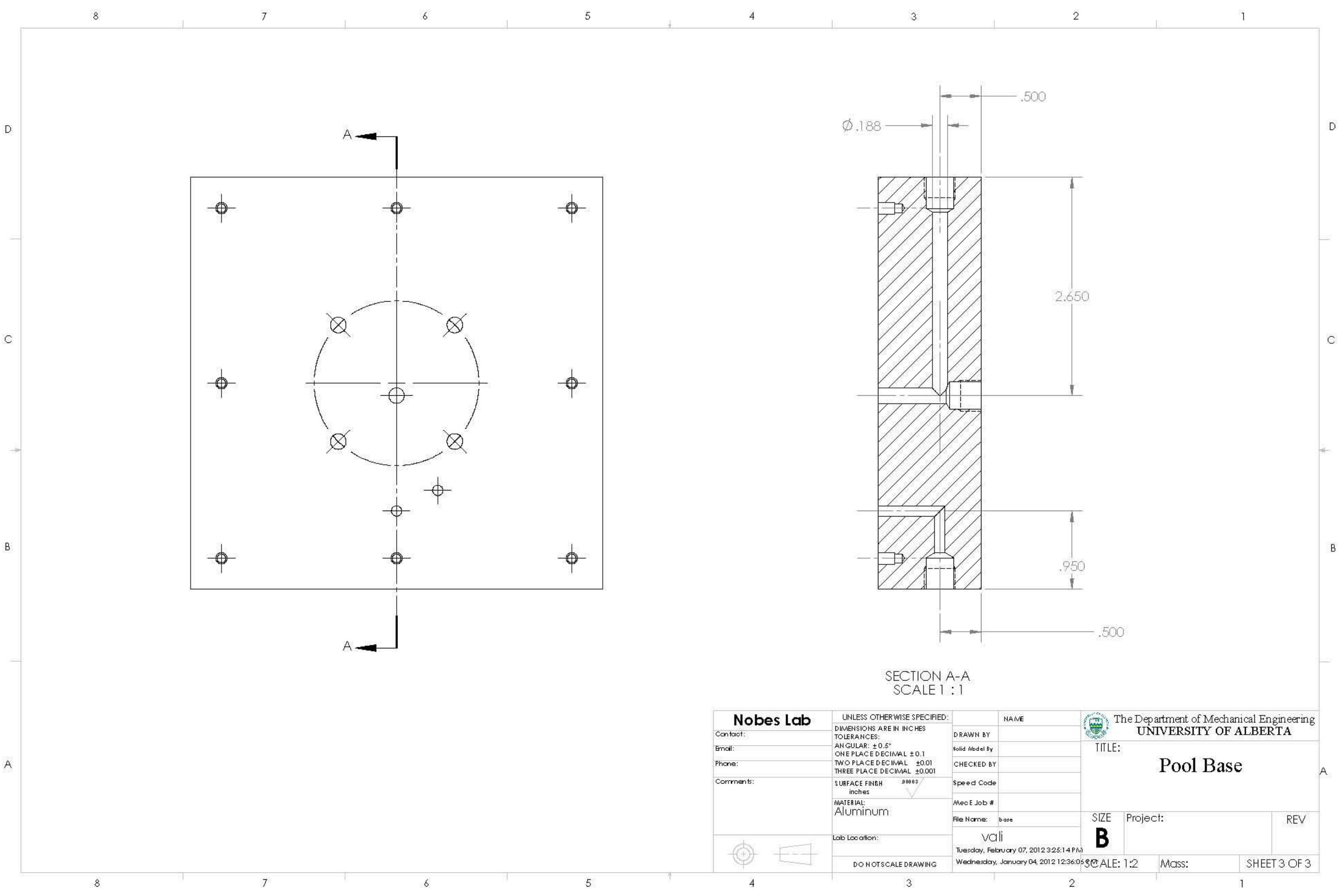
A
A
Ø.188
.500
2.650
.950
.500
SECTION A-A
SCALE 1 : 1
Nobes Lab
Contact:
Email:
Phone:
Comments:
UNLESS OTHERWISE SPECIFIED:
DIMENSIONS ARE IN INCHES
TOLERANCES:
ANGULAR: ±0.5°
ONE PLACE DECIMAL ±0.1
TWO PLACE DECIMAL ±0.01
THREE PLACE DECIMAL ±0.001
SURFACE FINISH inches .00003
MATERIAL: Aluminum
Lab Location:
DO NOT SCALE DRAWING
NAME
DRAWN BY
Solid Model By
CHECKED BY
Speed Code
MecE Job #
File Name: base
vali
Tuesday, February 07, 2012 3:25:14 PM
Wednesday, January 04, 2012 12:36:05 PM
The Department of Mechanical Engineering
UNIVERSITY OF ALBERTA
TITLE:
Pool Base
SIZE
B
Project:
REV
SCALE: 1:2
Mass:
SHEET 3 OF 3
8
7
6
5
4
3
2
1
D
C
B
A

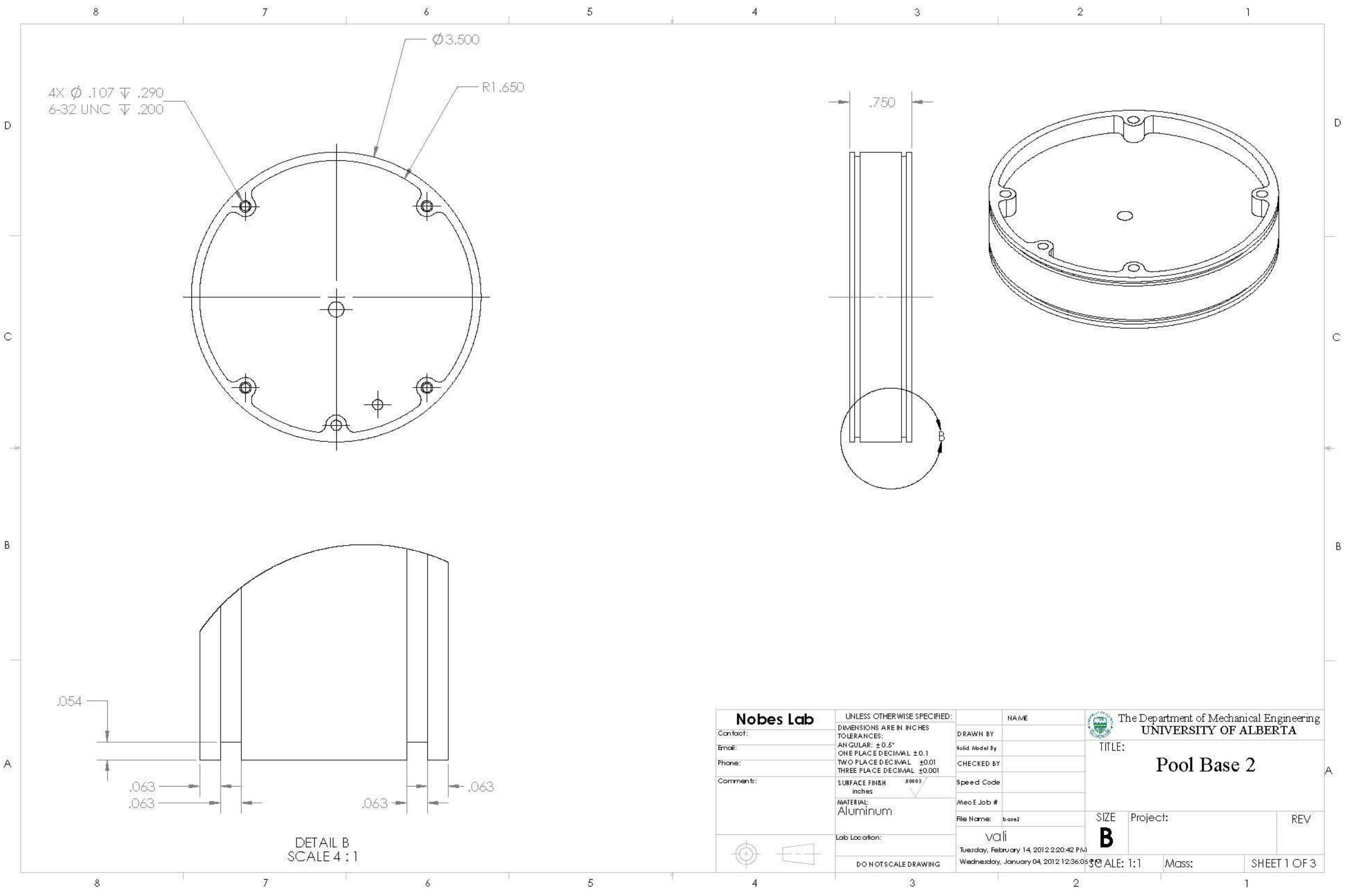
Ø3.500
4X Ø .107 ↧ .290
6-32 UNC ↧ .200
R1.650
.750
B
.054
.063
.063
.063
.063
DETAIL B
SCALE 4 : 1
Nobes Lab
Contact:
Email:
Phone:
Comments:
UNLESS OTHERWISE SPECIFIED:
DIMENSIONS ARE IN INCHES
TOLERANCES:
ANGULAR: ±0.5°
ONE PLACE DECIMAL ±0.1
TWO PLACE DECIMAL ±0.01
THREE PLACE DECIMAL ±0.001
SURFACE FINISH inches
.00003
MATERIAL:
Aluminum
Lab Location:
DO NOT SCALE DRAWING
NAME
DRAWN BY
Solid Model By
CHECKED BY
Speed Code
MecE Job #
File Name: base2
vali
Tuesday, February 14, 2012 2:20:42 PM
Wednesday, January 04, 2012 12:36:05 PM
The Department of Mechanical Engineering
UNIVERSITY OF ALBERTA
TITLE:
Pool Base 2
SIZE
B
Project:
REV
SCALE: 1:1
Mass:
SHEET 1 OF 3
8
7
6
5
4
3
2
1
D
C
B
A

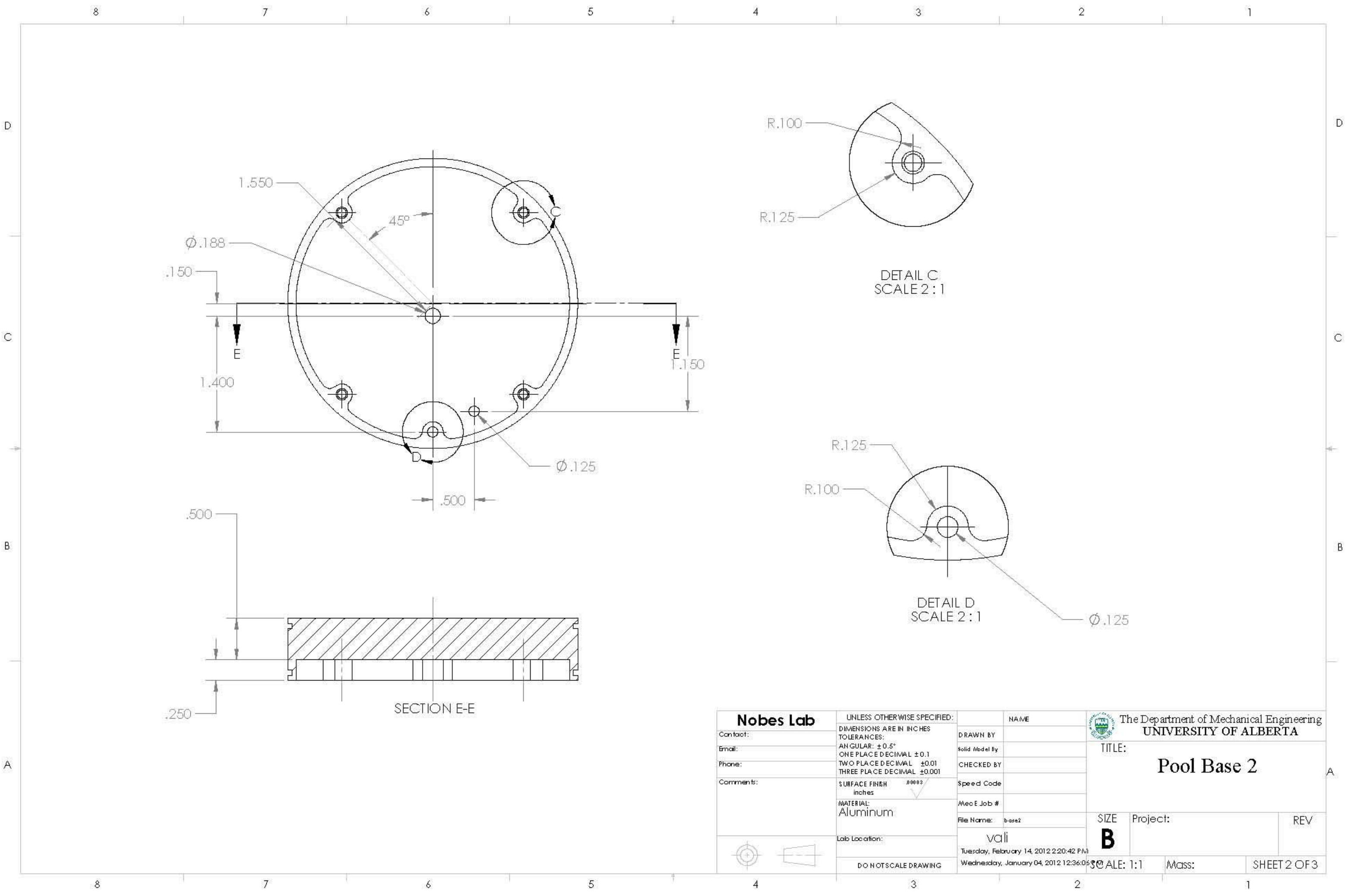

8
7
6
5
4
3
2
1
D
C
B
A
1.550
45°
Ø.188
.150
E
E
1.150
1.400
C
D
Ø.125
.500
.500
.250
SECTION E-E
R.100
R.125
DETAIL C
SCALE 2 : 1
R.125
R.100
DETAIL D
SCALE 2 : 1
Ø.125
Nobes Lab
Contact:
Email:
Phone:
Comments:
UNLESS OTHERWISE SPECIFIED:
DIMENSIONS ARE IN INCHES
TOLERANCES:
ANGULAR: ±0.5°
ONE PLACE DECIMAL ±0.1
TWO PLACE DECIMAL ±0.01
THREE PLACE DECIMAL ±0.001
SURFACE FINISH inches
.00003
MATERIAL:
Aluminum
Lab Location:
DO NOT SCALE DRAWING
NAME
DRAWN BY
Solid Model By
CHECKED BY
Speed Code
MecE Job #
File Name:
base2
vali
Tuesday, February 14, 2012 2:20:42 PM
Wednesday, January 04, 2012 12:36:05 PM
The Department of Mechanical Engineering
UNIVERSITY OF ALBERTA
TITLE:
Pool Base 2
SIZE
B
Project:
REV
SCALE: 1:1
Mass:
SHEET 2 OF 3

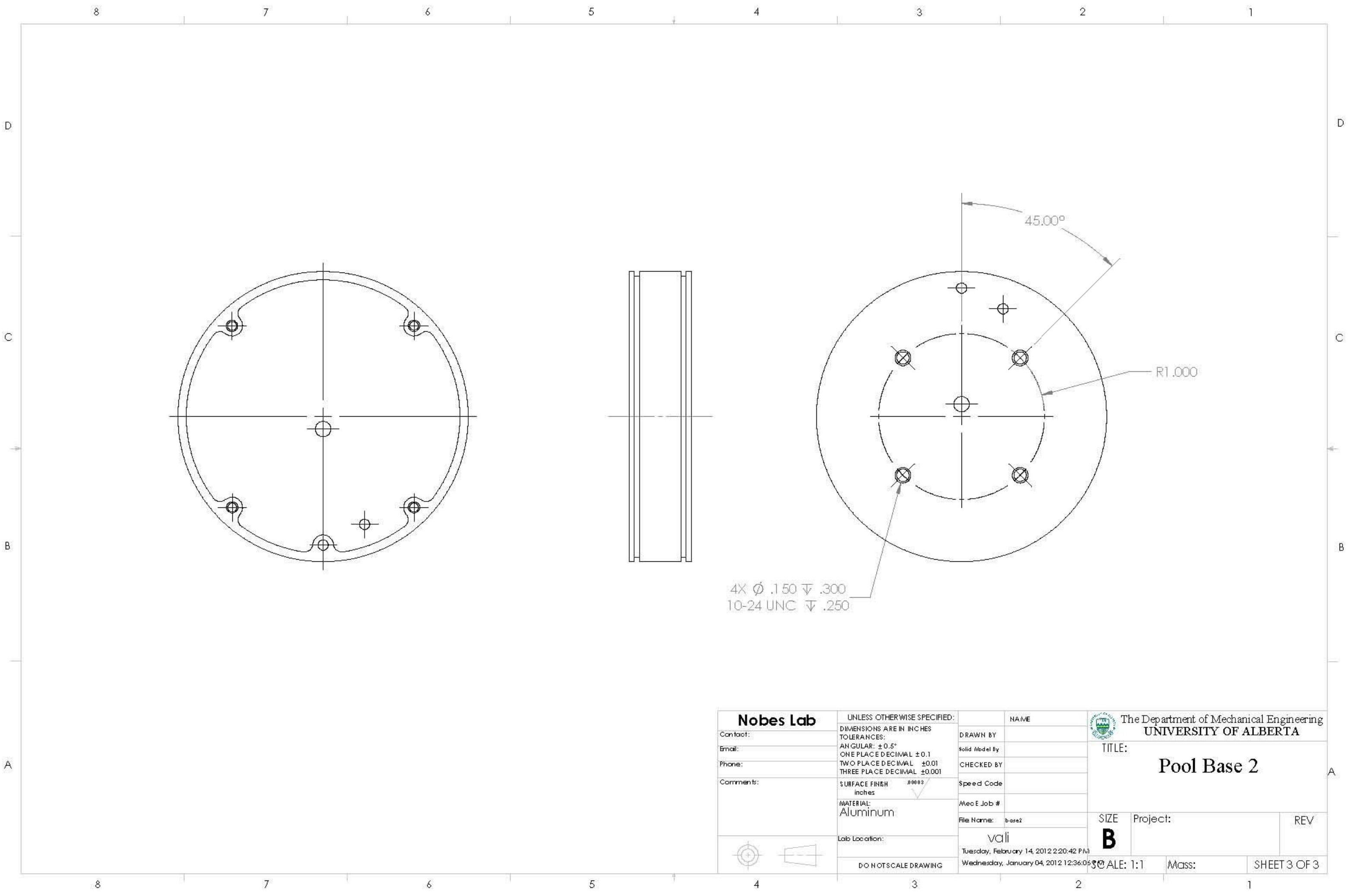
45.00°
R1.000
4X Ø .150 ↧ .300
10-24 UNC ↧ .250
Nobes Lab
Contact:
Email:
Phone:
Comments:
UNLESS OTHERWISE SPECIFIED:
DIMENSIONS ARE IN INCHES
TOLERANCES:
ANGULAR: ±0.5°
ONE PLACE DECIMAL ±0.1
TWO PLACE DECIMAL ±0.01
THREE PLACE DECIMAL ±0.001
SURFACE FINISH inches .00003
MATERIAL:
Aluminum
Lab Location:
DO NOT SCALE DRAWING
NAME
DRAWN BY
Solid Model By
CHECKED BY
Speed Code
MecE Job #
File Name: base2
vali
Tuesday, February 14, 2012 2:20:42 PM
Wednesday, January 04, 2012 12:36:05 PM
The Department of Mechanical Engineering
UNIVERSITY OF ALBERTA
TITLE:
Pool Base 2
SIZE
B
Project:
REV
SCALE: 1:1
Mass:
SHEET 3 OF 3
1
2
3
4
5
6
7
8
A
B
C
D

Appendix C: Velocity Vector Fields within the Liquid Fuel

In addition to the main vortices, there are smaller vortices that are difficult to observe due to the size and the number of the velocity vectors as shown in Sec. 3.7. In this appendix the same results are presented but here the data images have been optimized to show smaller scale features which are mainly small vortices.

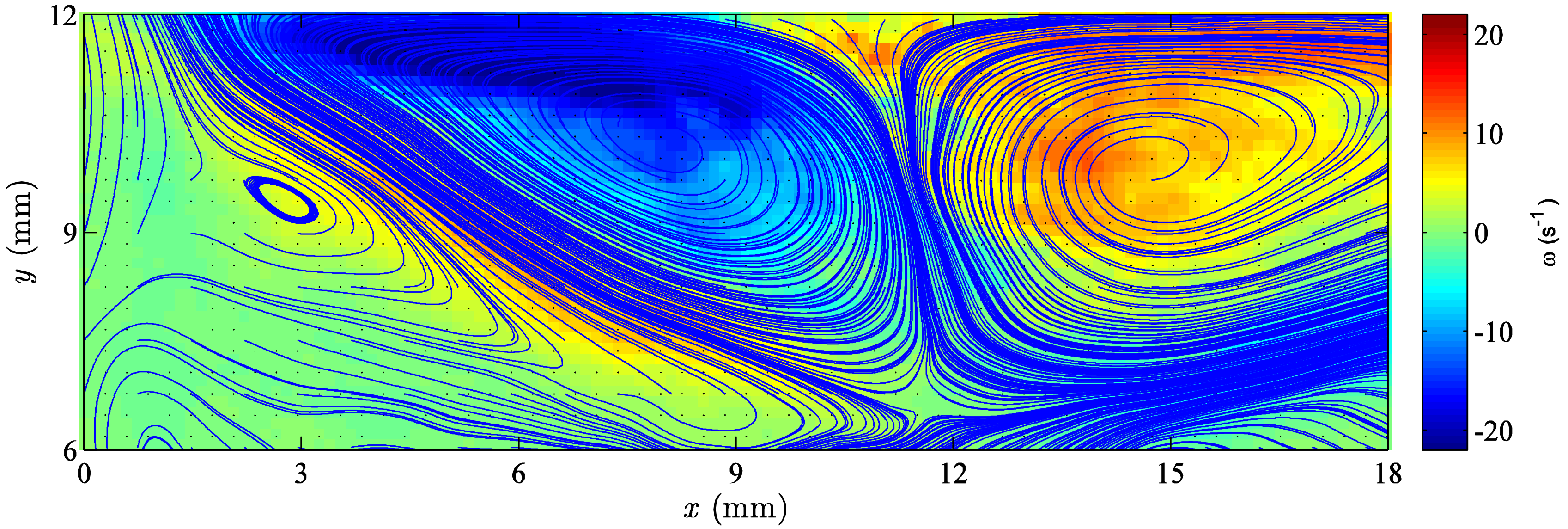
12
9
6
y (mm)
0
3
6
9
12
15
18
x (mm)
20
10
0
-10
-20
ω (s^{-1})

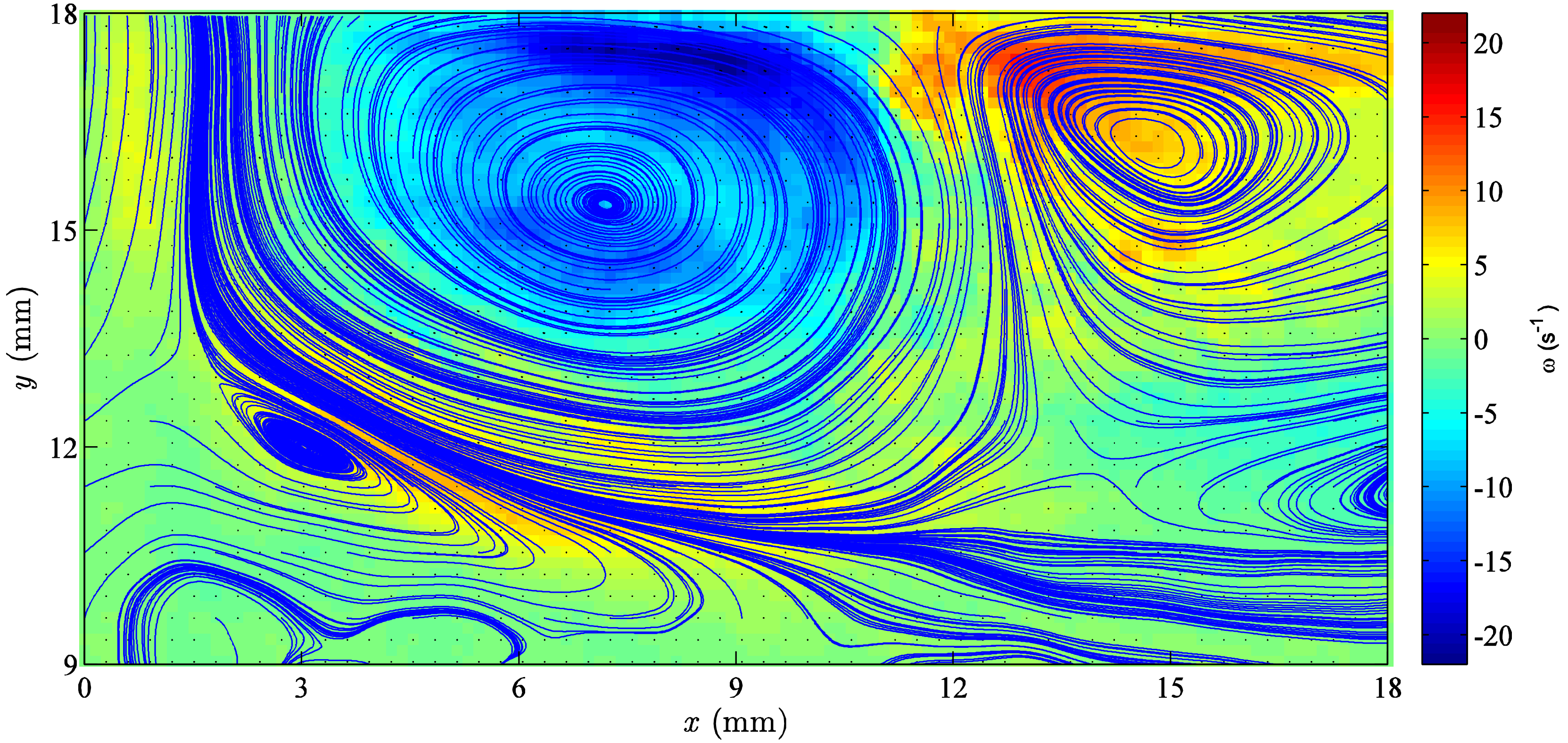
18
15
12
9
y (mm)
0
3
6
9
12
15
18
x (mm)
20
15
10
5
0
-5
-10
-15
-20
ω (s^{-1})

Appendix D: 1D Thermal Structure of a Liquid Layer

This appendix contains supplementary information for modeling the one-dimensional energy transfer within a liquid layer. The interested problem here is shown schematically in Fig. D.1. The control volume, CV, (shown by the dashed line) contains a layer of liquid with a thickness of Y within a one-dimensional liquid flow with a characteristic velocity of U. The liquid enters to the CV at temperature T_1 from the bottom and leaves the top of the CV at T_2. Here it is assumed that $T_2 > T_1$ just to make it analogous to the liquid phase of pool fire. The both sides (*i.e.*, left and right) of the CV are adiabatic boundary conditions.

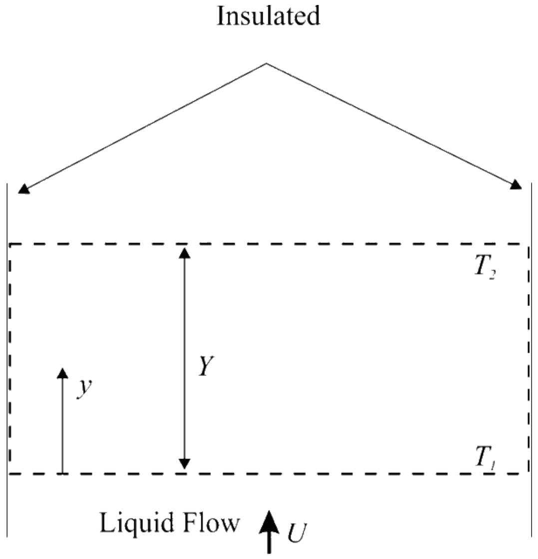

Fig. D.1 Schematic diagram of the 1D energy transfer problem in the liquid

The 1D conservation of energy equation within the liquid layer is:

$$\rho_l c_{p,l} U \frac{dT}{dy} = k_l \frac{d^2 T}{dy^2} \tag{D.1}$$

The liquid temperature, T, and vertical coordinate, y, are normalized as:

$$\theta = \frac{T - T_1}{T_2 - T_1} \tag{D.2}$$

$$y^* = \frac{y}{Y} \tag{D.3}$$

Therefore, the dimensionless form of Eq. (D.1) becomes:

$$Pe\frac{d\theta}{dy^*} = \frac{d^2\theta}{dy^{*2}} \tag{D.4}$$

where *Pe* is the Peclet number defined as:

$$Pe = \frac{\rho_l c_{p,l} UY}{k_l} \tag{D.5}$$

The solution to the differential equation, Eq. (D.4), using the boundary conditions of the problem is shown for different values of the *Pe* number in Fig. D.2. As it can be seen, when the *Pe* number is zero the temperature distribution within the liquid layer becomes linear which means the energy is transferred through the liquid only by conduction. This case is associated with no liquid flow (*i.e.*, $U = 0$), and as the liquid characteristic velocity increases, (*i.e.*, increasing *Pe*), the temperature profiles more change from the case that is dominated by heat conduction.

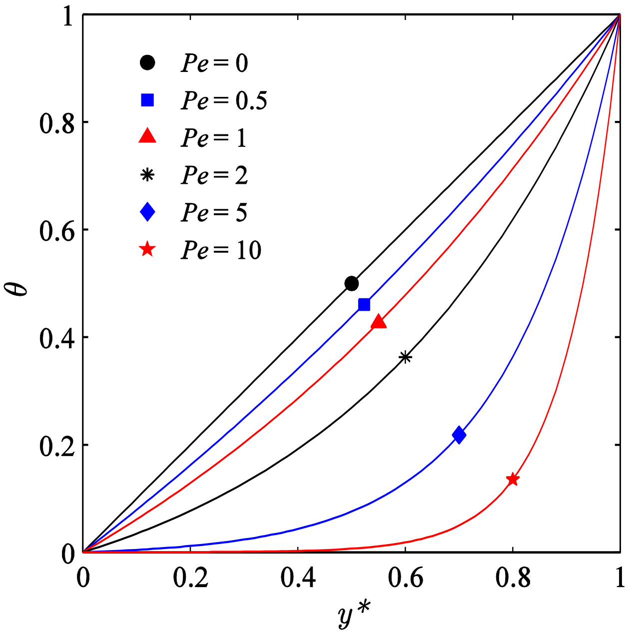

Fig. D.2.Temperature distributions of a liquid layer for different values of the *Pe* number

In order to show the effect of fluid motion on the energy transfer within the liquid layer the heat flux from the top surface of the CV through the liquid layer, $\dot{q}''_{top}$, as:

$$\dot{q}''_{top} = -k_l \left. \frac{dT}{dy} \right|_{y=Y} \tag{D.6}$$

is calculated and illustrated in Fig. D.3 for different values of the *Pe* number relative to the case that *Pe* is zero (*i.e.*, conduction energy transfer within a stagnant liquid), $\dot{q}''_{top,c}$. It is apparent that the transport of energy with fluid motion when *Pe* is around 1-2 (*i.e.*, the pools investigated in this study) should be taken into account. The energy transfer within the liquid layer is combination of conduction and convection.

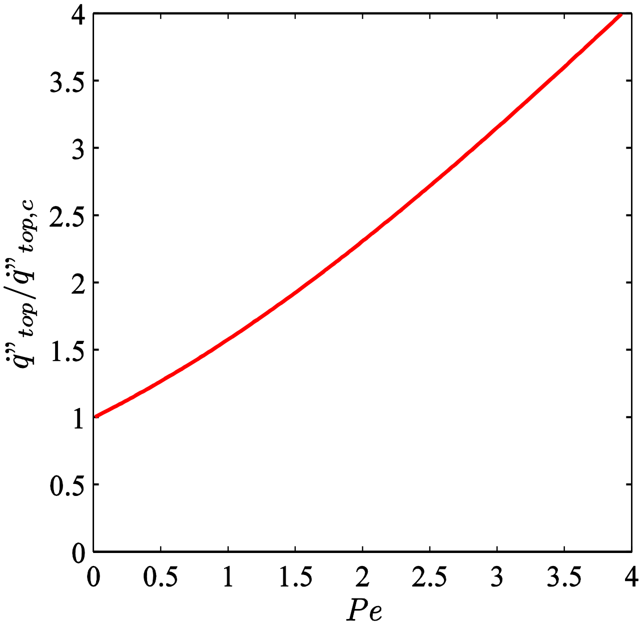

Fig. D.3. The ratio of the heat flux from the top of the control volume to the heat flux within a still liquid layer (no fluid motion) with respect to the *Pe* number